From outcrop analogue to flow simulation: modelling heterogeneity in shallow-marine reservoirs

Gavin Henry Graham

Imperial College London

Department of Earth Science & Engineering

A dissertation submitted in partial fulfilment of the requirements for the degree of Doctor of Philosophy of Imperial College London

February, 2014

This work is dedicated with pride to my parents.....

Declaration of originality

I hereby declare that this thesis, *'From outcrop analogue to flow simulation: modelling heterogeneity in shallow-marine reservoirs'*, is entirely my own work under the supervision of Dr. Gary J. Hampson and Prof. Matthew D. Jackson and performed in the Department of Earth Science and Engineering at Imperial College London. All other material in this thesis has been given full acknowledgement where appropriate. This work has not been previously submitted, in whole or in part, to any other academic institution for a degree, diploma, or any other qualification.

Gavin Henry Graham

Department of Earth Science and Engineering

Imperial College London

Copyright declaration

'The copyright of this thesis rests with the author and is made available under a Creative Commons Attribution Non-Commercial No Derivatives licence. Researchers are free to copy, distribute or transmit the thesis on the condition that they attribute it, that they do not use it for commercial purposes and that they do not alter, transform or build upon it. For any reuse or redistribution, researchers must make clear to others the licence terms of this work.'

Abstract

Shallow-marine reservoirs are typically complex, containing hierarchically arranged heterogeneity in inter-well volumes, at scales that are challenging to represent in reservoir models. Permeability contrasts associated with clinoforms are one such heterogeneity, but at present there are no modelling tools available to automate the generation of multiple three-dimensional (3D) clinoform surfaces. Consequently, clinoforms are rarely incorporated in models of shallow-marine reservoirs, even when their potential impact on flow is recognized. A numerical algorithm that generates multiple 3D clinoforms is presented. The algorithm is validated via construction of 3D, surface-based reservoir models of: (1) fluvial-dominated delta-lobe deposits exposed at outcrop (Cretaceous Ferron Sandstone Member, Utah, USA); and (2) a deltaic reservoir using a sparse subsurface dataset (Jurassic Sognefjord Formation, Troll Field, Norwegian North Sea).

We use a suite of 3D reservoir models constructed with the clinoform-modelling algorithm and outcrop-analogue data (Cretaceous Ferron Sandstone Member, Utah) to quantify the impact of clinoforms on fluid flow in the context of: (1) other uncertainties in reservoir characterisation, such as the impact of bed-scale heterogeneity on vertical permeability; and (2) reservoir engineering decisions, including oil production rate. Clinoforms are difficult to identify using production data, but our results indicate that they can significantly influence hydrocarbon recovery and their impact can be larger than that of other geological heterogeneities and of reservoir engineering decisions.

Vertical permeability within distal delta-front facies comprising interbedded sandstones and shales is found to be an important influence on sweep within clinothems. However, it is difficult to characterize these intervals from subsurface datasets. A digital outcrop modelling method is presented and applied to capture the geometry and architecture of sandbodies in such deposits in an outcrop analogue (G2 parasequence, Grassy Member, Blackhawk Formation, Utah, USA). We use the resulting digital outcrop model to make a preliminary interpretation of 3D gutter cast geometry.

Acknowledgements

I would like to express my sincere gratitude to my PhD supervisors Dr. Gary J. Hampson and Prof. Matthew D. Jackson. Their insightful direction and encouragement were integral to the completion of this thesis. It has been a pleasure to work with them both and I look forward to our collaboration continuing into the future.

Funding for this work is gratefully acknowledged from the United Kingdom Natural Environment Research Council (NERC) and ExxonMobil Upstream Research Company. Roxar are thanked for providing the academic use of RMS® software as well as Schlumberger for providing the academic use of Petrel® and Eclipse 100 software.

I have had the great pleasure to work with many colleagues during the course of this project. I would specifically like to thank, Fahad A. Dilib, Dr. Peter J. R. Fitch, Dr. Berit Legler and Benoît Y.G. Massart for a combination of: assistance during fieldwork; collaboration; friendship; and support. I would also like to thank Gregory S. Benson of ExxonMobil Upstream Research Company, who has been wonderful in providing mentorship as well as guidance even when he was under no requirement to do so.

Last, but by no means least, I would like to thank my family: my parents Alaisdair and Sheila Graham – I could not have done this without your strength; my grandparents John and Agnes Graham - for contributions they felt were minor but kept me going; Phoebe - for her love and patience; and my late grandparents John Angus and Annie Campbell - they would have been very proud to have seen this completed thesis. Finally, I would like to thank the congregation at London City Presbyterian Church who have been of great comfort and support during my time in London.

Contents

Declaration of originality **3**

Copyright declaration **4**

Abstract **5**

Acknowledgements **6**

Contents **7**

List of Figures **13**

List of Tables **27**

1 Introduction **29**

1.1 Classification of shallow-marine shoreline systems 29

1.2 Geological heterogeneity in shallow-marine reservoirs 31

1.3 Conventional approaches to reservoir modelling 34

1.4 Surface-based reservoir modelling 37

1.5 Thesis aims and objectives 40

1.6 Thesis structure 41

1.7 Journal articles and conference presentations 43

2 Three-dimensional modelling of clinoforms within shallow-marine reservoirs: Part 1. Concepts and application **46**

2.1 Summary 46

2.2 Introduction 47

2.3 Conceptual framework for clinoform modelling 52
2.3.1 Bounding surfaces that define rock volume 52
2.3.2 Plan-view clinoform geometry 55
2.3.3 Cross-sectional clinoform geometry 59
2.3.4 Spacing and progradation direction of clinoform surfaces 61
2.3.5 Stochastic modelling of clinoforms 62
2.4 Example 1: Ferron Sandstone reservoir analogue 63
2.4.1 Geological setting 63
2.4.2 Model construction 66
2.4.3 Geological model results 73
2.4.4 Production strategy 75
2.4.5 Simulation results 77
2.5 Example 2: Troll West reservoir sector model 79
2.5.1 Geological setting 79
2.5.2 Model construction 82
2.5.3 Geological model results 87
2.5.4 Production strategy 90
2.5.5 Simulation results 92
2.6 Discussion 94
2.7 Conclusions 96

3 Three-dimensional modelling of clinoforms within shallow-marine reservoirs: Part 2. Impact on fluid flow and hydrocarbon recovery in fluvial-dominated deltaic reservoirs 98

3.1 Summary 98
3.2 Introduction 99

3.3 Geological heterogeneity in fluvial-dominated deltaic reservoirs 102
3.4 Geological heterogeneity investigated in this study 106
3.4.1 Presence of channelized fluvial sandbodies 106
3.4.2 Permeability anisotropy in distal delta-front heteroliths 110
3.4.3 Barrier coverage along clinoform surfaces 110
3.4.4 Permeability of channelized sandbodies 112
3.5 Production strategy 112
3.6 Design of simulation experiments 113
3.7 Model construction 114
3.7.1 Geological framework for clinoform-bearing models of the Ferron Sandstone outcrop analogue 114
3.7.2 Modelling the geometry and distribution of clinoform surfaces 115
3.7.3 Modelling heterogeneity along clinoform surfaces 118
3.7.4 Modelling reservoir structure 120
3.7.5 Rock and fluid properties 121
3.8 Results 122
3.8.1 Stacked delta-lobe deposits with channelized fluvial sandbodies either present or absent 123
3.8.2 Stacked delta-lobe deposits with channelized fluvial sandbodies always present 125
3.9 Discussion 126
3.9.1 Impact of clinoform-surface character, distribution and associated uncertainty 127
3.9.2 Impact of channelized sandbodies 132
3.9.3 Impact of bed-scale heterogeneity in distal delta-front

heteroliths 137
3.9.4 Impact of reservoir engineering decisions 139
3.9.5 Implications for reservoir monitoring and management. . 140
3.9.6 Closing summary 143
3.10 Conclusions 144

4 Three-dimensional digital outcrop modelling using stereophotogrammetry: Application to improved characterization of sandbody connectivity in thinly bedded intervals of wave-dominated shallow-marine reservoirs 146

4.1 Summary 146
4.2 Introduction 147
4.3 Storm event beds and gutter casts 151
4.4 Geological setting and study area 155
4.5 Data collection 157
4.5.1 Georeferencing 159
4.5.2 Stereophotogrammetry 164
4.6 Digital outcrop model construction 166
4.7 Digital outcrop model results 169
4.8 Preliminary analysis of gutter cast geometry and spatial distribution 172
4.8.1 Description 172
4.8.2 Interpretation 174
4.9 Reservoir implications and future applications 177
4.10 Discussion 179
4.11 Conclusions 182

5 Discussion and conclusions 184

5.1 Discussion 184

5.1.1 Surface-based modelling of heterogeneity in shallow-marine reservoirs 184

5.1.2 Quantifying the impact of heterogeneity on fluid flow and hydrocarbon recovery in fluvial-dominated deltaic reservoirs 185

5.1.3 Three-dimensional digital outcrop modelling using stereophotogrammetry 186

5.1.4 Surface-based modelling for flow simulation: future directions 187

5.2 Recommendations for future work 192

5.3 Conclusions 193

Bibliography 196

Appendix A 222

A1 Clinoform-modelling algorithm 222

A.1.1 Generating clinoform surfaces 224

A.1.2 Modelling heterogeneity along clinoform surfaces 235

A2 Stochastic input parameters algorithm 244

Appendix B 251

B1 Example Eclipse® data file 251

Appendix C **259**

C1 Photomodeler Scanner® workflow 259

C1.1 Camera calibration 260

C1.2 Triangulation 261

C1.3 Dense point cloud 262

C1.4 Georeferencing 264

C1.5 Export 266

List of Figures

Figure 1.1: **30**
Classification of shallow-marine shoreline systems based on the long term movement of the shoreline and the key depositional processes (modified after Boyd et al., 1992).

Figure 1.2: **32**
Generic hierarchy of heterogeneities within shoreface-shelf reservoirs (standplain Fig. 1.1) across a range of lengthscales: (A) a parasequence set; (B) a single parasequence; (C) a package of beds bounded by clinoform discontinuity surfaces (bedset); (D) hummocky-cross stratification; and (E) micropsopic laminations. Note the heterogeneity associated with clinoform surfaces (after Sech et al., 2009 and references therein).

Figure 1.3: **36**
(A) Object-based modelling approach to capture channelized sandbodies in a non-reservoir (mudstone) background on a fine-scale cell-based grid. Channelized sandbodies have a 'stair-step' geometry limited by grid resolution. (B) Object-based modelling approach to capture channelized sandbodies in a non-reservoir (mudstone) background on a coarser-scale cell-based grid. Many of the smaller channelized sandbodies are below the grid resolution so are not captured, while connectivity is not preserved in the larger sandbodies, as the cell-face contacts that are captured in the fine-scale model in (A) have been lost. (C) Surface-based model; each channelized sandbody is defined by an upper and lower surface. Channelized sandbodies are shown in colour while the non-reservoir background and associated grid-cells are not shown (modified after Jackson et al., in press).

Figure 1.4: **37**
Generic example of surface hierarchy, developed according to rules that define which surfaces can truncate previously modelled surfaces. Structural surfaces are typically at the top of the hierarchy as they truncate other surfaces (surfaces 1 and 2). Stratigraphic surfaces are typically next in the hierarchy, as these are often truncated by faults but truncate facies boundaries (surfaces 3-5). Sedimentological surfaces are typically at the base of the hierarchy (surfaces 6-11). This hierarchy may be modified for a given reservoir model as in some cases, structural surfaces may be truncated by stratigraphic surfaces (modified after Jackson et al., in press).

Figure 2.1: **48**
(A) Outcrop view of delta-front clinoforms in the Ferron Sandstone Member at the Ivie Creek amphitheatre, north of I-70, east-central Utah, USA (corresponding to parasequences 1.5 and 1.6 of Deveugle et al., 2011). Note the dipping nature of the delta-front sandstones and shales, and the erosional contact with an overlying distributary channel sandstone. (B) Corresponding outcrop interpretation showing clinoform surfaces within the delta-front deposits. (C) Corresponding line drawing highlighting approximately 25 clinoforms, shown as black lines on a white background. CP = Coastal plain heteroliths, DC = Distributary channel sandstone, PD = Prodelta shales. Photographs and line drawings have no vertical exaggeration.

Figure 2.2: **53**
Examples of clinoforms produced by the clinoform-modelling algorithm conditioned to different bounding surfaces and clinoform geometries. (A) Bounding surfaces represent post-depositional folding of the original (depositional) geometries of the clinoform surface and the top and base bounding surfaces. (B) Bounding surfaces represent a clinoform within a volume truncated at its top, for example by a channel (Fig. 2.1). (C) Bounding surfaces represent a clinoform downlapping on to irregular sea-floor topography. (D) Height function (Eq. 2.1). (E) Shape function (Eq. 2.7) demonstrating that increasing the exponent, P, increases the dip angle of clinoforms.

Figure 2.3: **56**
Generalized, first-order approximations of the plan-view geometry of clinoforms in different depositional environments: (A) Nayarit Coast, Mexico, representative of a wave-dominated strandplain; (B) Nile Delta, Egypt, representative of a wave-dominated delta; and (C) Wax Lake Delta, Louisiana, USA, representative of a fluvial-dominated delta. (Images modified after Google Earth, 2013).

Figure 2.4: **58**
(A) A user specifies the widths and lengths of the top ellipse (solid line) and base ellipse (dashed line) relative to the clinoform origin. The clinoform surface is created in the volume between the top (solid line) and base (dashed line) ellipses. (B) At a point on the clinoform surface, we calculate the radius relative to the clinoform origin (black arrow, $r_c(x,y)$), the radius of the base ellipse (black arrow, $r_{max}(x,y)$) and the radius of the top ellipse (black arrow, $r_{min}(x,y)$). (C) Plan view of four adjacent clinoforms. The user specifies the overall progradation direction of the clinoform surfaces relative to north as well as the coordinates of the initial insertion point, p_O. (D) Conceptual depositional-dip-oriented cross-section view of clinoform surfaces. Clinoform spacing, S, is defined as the

distance between the top truncation points of two adjacent clinoform surfaces. Clinoform length, L, is defined as the distance between the top and base truncations by the user-specified bounding surfaces along a single clinoform surface.

Figure 2.5: **65**

(A) Palaeogeographic reconstruction of the late Cretaceous “Last Chance” and “Vernal” delta systems of the Ferron Sandstone Member of the Mancos Shale in present-day Utah (after Cotter, 1976). The location of Deveugle et al.'s (2011) model (Fig. 2.5D) and a regional cross section (Fig. 2.5B) are highlighted. (B) Schematic regional cross section through the “Last Chance” delta system of the Ferron Sandstone Member and its eight component shallow-marine tongues (numbered PSS1 to PSS8, using the nomenclature of Deveugle et al., 2011), from southwest (palaeolandward) to northeast (palaeoseaward) (after Anderson and Ryer, 2004). (C) Detailed cross section through the lowermost shallow-marine tongues (PSS1 in Fig. 2.5B) and associated coastal-plain strata (after Garrison Jr. and van den Bergh, 2004). The tongue is subdivided into constituent parasequences (after Deveugle et al., 2011). Parasequence 1.6 is modelled in this study. (D) Map showing distribution of facies-association belts at the top of PS 1.6, in Deveugle et al.’s (2011) model area. The area of the model constructed in this study (Figs. 2.7-2.10) lies within the dashed lines.

Figure 2.6: **68**

(A) Interpreted line drawing of clinoforms at the Junction Point section of Ivie Creek Amphitheatre (Fig. 2.5D) (modified after Forster et al., 2004). Data from 104 clinoforms were collected to condition the clinoform-modelling algorithm. Frequency distributions of values measured from outcrop data for (B) clinoform length (Fig. 2.4D), and (C) clinoform spacing (Fig. 2.4D) which are used as input parameters in the clinoform-modelling algorithm.

Figure 2.7: **70**

Surfaces generated by the clinoform-modelling algorithm for the model of part of parasequence PS1.6 of the Ferron Sandstone Member (Fig. 2.5C, D). (A) Single 3D clinoform surface generated by the clinoform modelling algorithm. (B) 3D dip cross section showing the concave upward geometry of the clinoform surfaces, and (C) 3D strike section of the model showing surfaces that exhibit bidirectional dips. Not all surfaces used in the model of part of Ferron Sandstone Member (Fig. 2.8) are shown.

Figure 2.8: **71**
Surface-based model of part of parasequence PS1.6 of the Ferron Sandstone Member (Fig. 2.5C, D), a fluvial-dominated delta lobe. (A) 3D view of the model superimposed on a digital elevation map of the study area, with no vertical exaggeration and orientations of regional depositional dip and strike shown. (B) Plan-view section of model showing curved clinoform surfaces, consistent with the geometry of fluvial-dominated delta lobes. (C) 2D dip section and (D) 2D strike section through the model, showing details of the complex internal architecture. Red lines indicate facies boundaries and blue lines parasequence-bounding flooding surfaces. Black lines represent clinoform surfaces.

Figure 2.9: **72**
View of Figure 2.8C showing grid layering that conforms to the architecture of the clinoform surfaces, facies association boundaries and parasequence-bounding flooding surfaces.

Figure 2.10: **76**
(A) Plan view facies association map of the Ferron Sandstone Member extracted from our reservoir model (Fig. 2.5D), showing location of injector and producer wells, and the cross-section illustrated in (B-D). The colour scheme is the same as in Figures 2.5D and 2.8A. (B) Depositional-dip-oriented cross-section showing the internal facies architecture of the modelled parasequence with the location of barriers along the clinoforms shown as black lines. (C, D) The same depositional-dip-oriented cross-section showing water saturation after 5 years of production where water has been injected down depositional dip, from east to west, for models with (C) 0% barrier coverage along clinoforms, and (D) 90% barrier coverage along clinoforms. Note oil is bypassed below clinoform surfaces in (D).

Figure 2.11: **78**
(A) Recovery factor (solid lines) and water cut (dashed lines) as function of time in the simulation model of part of parasequence 1.6 of the Ferron Sandstone Member. Curves in black denote results for the model with 0% barrier coverage along clinoforms, and curves in gray denote the model with 90% barrier coverage along clinoforms. Note the significant decrease in recovery factor for the model with 90% barrier coverage along clinoforms. (B) Oil (solid lines) and water (dashed lines) production rate as a function of time. In the models with 90% barrier coverage along clinoforms, the target production rate is not met and water breakthrough occurs earlier than in models where barriers are not present along clinoforms.

Figure 2.12: **80**
(A) Palaeogeographic reconstruction of gross depositional environments in the central and northern North Sea during the early-to-mid Kimmeridgian (modified from Fraser et al., 2003), marked by retreat and drowning of the "Troll delta" system ("series-6" of the Sognefjord Formation; Dreyer et al., 2005). (B) Simplified outline of the Troll Field, highlighting major blocks bounded by normal faults that post-date deposition of the Sognefjord Formation. The location of the modelled area and a stratigraphic cross section across Troll West (Fig. 2.12C) are shown. (C) Schematic cross section through the "Troll delta" system of the Sognefjord Formation in Troll West, from west (palaeoseaward) to east (palaeolandward). Major shallow-marine tongues (labelled "series-1" to "series-6", using the nomenclature of Dreyer et al., 2005) and their component parasequences are shown (after Gibbons et al., 1993).

Figure 2.13: **84**
Normal distributions, shown as black lines, for (A) clinoform length (Fig. 2.4D), and (B) clinoform spacing (Fig. 2.4D) generated from published seismic data from the Sognefjord Formation (Figures 3 and 12 in Dreyer et al., 2005). Columns in grey represent the values for clinoform length and spacing drawn at random from the normal distribution and used to populate the Troll sector model.

Figure 2.14: **88**
Surfaces generated by the clinoform-modelling algorithm for the Troll sector model. (A) 3D dip cross-section of clinoform surfaces in the model demonstrating their concave upwards geometry, and (B) 3D view of clinoform surfaces in the model showing close to linear clinoforms in plan-view within fault-bounded compartment. Not all surfaces used in the Troll sector model (Fig. 2.15) are shown.

Figure 2.15: **89**
(A) Plan view facies association map of the Sognefjord Formation in our Troll West sector model, showing the location of compartmentalizing faults and a horizontal well. Cross sections along (B) depositional dip and (C) depositional strike, showing bounding flooding surfaces (blue), surfaces representing facies-association boundaries (red), and clinoforms generated by the modelling algorithm (black) for all parasequences in the model volume.

Figure 2.16: **91**
(A) Plan view facies association map of the Sognefjord Formation extracted from our Troll West sector model, showing the location of the horizontal well and the cross-section shown in (B-D). (B) Depositional-dip-oriented cross-section

showing the internal facies architecture of the modelled parasequences with the location of barriers along the clinoforms shown as black lines. (C, D) The same depositional-dip-oriented cross-section showing water saturation after 1000 days of production, for models with (C) 0% barrier coverage along clinoforms, and (D) 90% barrier coverage along clinoforms.

Figure 2.17: **93**

(A) Oil, (B) water, and (C) gas production rates, and (D) cumulative oil production as a function of time in the simulation model of the Sognefjord Formation in a fault-bounded sector of the Troll Field (Fig. 2.12B), for production from a single horizontal well through gas cap expansion and aquifer influx (Fig. 2.16). In the models with 90% barrier coverage along clinoforms, free gas breakthrough is delayed (Fig. 2.17C) and liquid production is decreased (Fig. 2.17A, B, D) relative to the models lacking barriers along clinoforms.

Figure 3.1: **103**

Generic hierarchy of heterogeneities within fluvial-dominated deltaic reservoirs across a range of lengthscales. Plan view maps with corresponding cross-sections oriented along depositional dip are shown for three orders of stratigraphic cycle: (A) vertically stacked shallow-marine tongues within a basinward-thinning wedge; (B) an individual shallow-marine tongue comprising compensationally stacked delta-lobe deposits; and (C) an individual delta-lobe deposit. Sedimentological heterogeneity at smaller lengthscales is shown for: (D) an upward-coarsening clinothem succession consisting of gravity-flow sandstone beds bounded by clinoform surfaces within the distal delta front (dDF) facies-association belt; (E) internal structure of an individual gravity-flow sandstone bed; and (F) microscopic lamination.

Figure 3.2: **107**

(A) Palaeogeographic reconstruction of the late Cretaceous “Last Chance” and “Vernal” delta systems of the Ferron Sandstone Member of the Mancos Shale in present-day Utah (after Cotter, 1976). The location of a regional cross section shown in (B) is highlighted, as well as the location of the plan view facies-association maps in Fig. 3.3A-E. (B) Detailed regional cross section through the lowermost shallow-marine tongue of the “Last Chance” delta system of the Ferron Sandstone Member (parasequence set 1 of Deveugle et al., 2011) (after Garrison Jr. and van den Bergh, 2004). Four delta-lobe deposits (parasequences 1.4, 1.5, 1.6, and 1.7 of Deveugle et al., 2011) are modelled in this study.

Figure 3.3: **109**
(A-E) Maps showing the distribution of facies-association belts at the top of parasequences 1.4, 1.5, 1.6, and 1.7 and in the overlying coastal-plain interval (after Deveugle et al. 2011), with the area of the models described in this paper shown by dashed lines. The regional palaeogeographic and stratigraphic context of the maps is illustrated in Figure 3.2.

Figure 3.4: **111**
(A, D) Maps showing the distribution of facies-association belts at the top of shallow-marine deposits in models of stacked delta-lobe parasequences, and associated model cross-sections illustrating facies architecture along (B, E) regional depositional dip and (C, F) regional depositional strike. Two models are shown, either (A-C) lacking or (D-F) containing channelized fluvial sandbodies that truncate the underlying delta-lobe parasequences.

Figure 3.5: **113**
3D perspective view showing the simulated production scheme used in the models of several stacked delta-lobe deposits (parasequences 1.4-1.7 and overlying coastal-plain deposits of Deveugle et al., 2011; Fig. 3.3A-E) illustrated using maps of facies-association belts at the top of the model volumes. A structural dip of 8° is applied to all models, which results in simulated waterflooding in a range of directions relative to the local depositional dip (i.e. azimuthal orientation) of each delta-lobe parasequence (Fig. 3.3A-E). In all models, production is simulated using a line drive of four injection wells located down structural dip of six production wells.

Figure 3.6: **119**
(A) 3D clinoform surface from parasequence 1.5 in the reservoir-scale model of the Ferron Sandstone (Figs. 3.2B, 3.3B), generated using the clinoform modelling algorithm described in Chapter 2. (B) The frequency function (Eq. 3.1) used to place elliptical barriers along each clinoform surface. (C) Extent of overlapping elliptical barriers along 3D clinoform surface in part A. The barriers cover 80% of the clinoform surface. (D) The barrier-covered clinoform surface in part C is translated into a transmissibility multiplier grid property in x, y, and/or z directions, depending on the orientation of the clinoform. The transmissibility multiplier is modified for cells in the grid layer above the clinoform surface. Grid cells in red are assigned a transmissibility multiplier of 1 and are open to flow, whereas grid cells in purple are assigned a transmissibility multiplier of 0 and act as a barrier to flow.

Figure 3.7: **124**
Average percentage change in oil recovery (green bars) and total volume of water produced (blue bars) in models of stacked delta-lobe deposits, observed when each factor in the experimental design is varied from setting 1 to setting 2 (Table 3.1), for: (A) models that either contain or lack channelized fluvial sandbodies (i.e. set 1 of simulation experiments in Table 3.1); and (B) models that contain channelized fluvial sandbodies of varying permeability (i.e. set 2 of simulation experiments in Table 3.1). If the bars lie to the right then the change is positive and more oil is recovered or more water is produced. For example, if the models contain a 90% barrier to flow along clinoforms (setting 2), oil recovery decreases by c. 5% and increases the total water produced in the models by c. 55% compared with models containing clinoforms with 0% barrier coverage (setting 1). The effects of individual factors and combinations of factors are displayed, where these are considered significant (i.e. >0.5% change in recovery factor, >1% change in total water produced).

Figure 3.8: **128**
Maps and cross-sections illustrating models of stacked delta-lobe deposits that either (left column) lack or (right column) contain channelized fluvial sandbodies which erode down from overlying coastal-plain deposits. (A) Maps of facies-association belts near the top of the models (parasequence 1.7, Fig. 3.3D, with overlying coastal-plain deposits, Fig. 3.3E, removed) showing location of injection and production wells, and the cross-sections illustrated in parts B-E. (B) Depositional-dip-oriented cross-sections showing the internal facies architecture of the modelled parasequences, with barriers covering 90% of each clinoform surface shown as black lines and the location of parasequence-bounding flooding surfaces shown as dashed black lines. (C) Depositional-dip-oriented cross-sections showing water saturation after 10 years of production for models that lack barriers to flow along clinoforms with a target oil production rate over 10 years of 350 S m^3/day (2200 bbl/day). Earlier water breakthrough occurs locally in the model lacking channelized fluvial sandbodies (left). (D) Corresponding cross-sections showing water saturation after 10 years of production with a target oil production rate over 10 years of 350 S m^3/day (2200 bbl/day) for models that have a 90% barrier to flow along clinoforms. Early water breakthrough occurs in both models locally when a 90% barrier to flow along clinoforms is present.

Figure 3.9: **130**
(A) Map of facies-association belts at the top of a single delta-lobe deposit extracted from our reservoir model (parasequence 1.6 in Figs. 3.3C, 3.4), showing location of injection and production wells, and the cross-sections illustrated in

parts B-E. (B) Depositional-dip-oriented cross-section showing the internal facies architecture of the modelled parasequence; barriers along clinoforms are not shown. Depositional-dip-oriented cross-sections showing water saturation after 15 years of production where water has been injected via waterflooding down depositional dip with a target oil production rate over 20 years of 175 S m^3/day (1100 bbl/day), from east to west, with 90% barrier coverage along clinoform surfaces, for models with clinoform spacing of: (C) 100 m, (D) 50 m, and (E) 25 m.

Figure 3.10: **131**

Change in (A) recovery factor and (B) time of water breakthrough with increasing barrier coverage for models of a single delta-lobe deposit (parasequence 1.6 in Figs. 3.3C, 3.4, 3.10) with different spacings of clinoform surfaces. Waterflooding is up structural dip and down depositional dip, with a target oil production rate over 20 years of 175 S m^3/day (1100 bbl/day). For 70% barrier coverage a range of values is given for recovery factor and date of water breakthrough. While the trend used to place barriers along clinoforms and the overall percentage of the surface that acts as a barrier to flow is honoured, the local position of barriers along clinoforms changes with each stochastic realization.

Figure 3.11A: **133**

Maps and cross-sections illustrating models of stacked delta-lobe deposits that either (left column) lack or (right column) contain channelized fluvial sandbodies that erode down from overlying coastal-plain deposits. (A) Maps of facies-association belts near the top of the models (parasequence 1.7, Fig. 3.3D, with overlying coastal-plain deposits, Fig. 3.3E, removed) showing location of injection and production wells, and the cross-sections illustrated in parts B-E. (B) Depositional-dip-oriented cross-sections showing the internal facies architecture of the modelled parasequences with barriers covering 90% of each clinoform surface shown as black lines and parasequence-bounding flooding surfaces as dashed lines. (C) Corresponding cross-section showing water saturation after 10 years of production with a target oil production rate over 10 years of 350 S m^3/day (2200 bbl/day). Sweep is improved locally in the model containing channelized fluvial sandbodies (right). (D-E) shown on next page.

Figure 3.11B: **134**

Cross-sections illustrating models of stacked delta-lobe deposits that either (left column) lack or (right column) contain channelized fluvial sandbodies that erode down from overlying coastal-plain deposits (location maps shown in part (A) on previous page). (D) Depositional-dip-oriented cross-sections showing the internal facies architecture of the modelled parasequences with barriers covering 90% of each clinoform surface shown as black lines and parasequence-bounding

flooding surfaces showed as dashed lines. Note that barriers near the top of the clinoforms (left) have been replaced by channelized fluvial sandbodies (right). (E) Corresponding cross-section showing water saturation after 10 years of production. Sweep is improved, and earlier water breakthrough occurs locally in the model containing channelized fluvial sandbodies (right).

Figure 3.12: **136**

(A) Map of facies-association belts near the top of the model of stacked delta-lobe deposits containing channelized fluvial sandstones (with coastal-plain deposits, Fig. 3.3E, removed), showing the location of injection and production wells. Maps of water saturation after 10 years of production, with a target oil production rate over 10 years of 350 S m^3/day (2200 bbl/day) for: (B) model containing 0% barrier coverage along clinoform surfaces and channelized fluvial sandbody permeability (k_h) of 1 × (1793) mD, and (C-D) models containing 90% barrier coverage along clinoform surfaces with channelized fluvial sandbody permeability (k_h) of (C) 1 × (1793) mD, and (D) 5 × (1793) mD. Sweep efficiency is reduced when the permeability of channelized fluvial sandbodies is 5 × (1793) mD.

Figure 3.13: **138**

Maps and cross-sections illustrating models of stacked delta-lobe deposits that either have zero vertical permeability or non-zero vertical permeability in distal delta-front facies in the presence of a 90% barrier to flow along clinoforms, in models that either (left column) lack or (right column) contain channelized fluvial sandbodies. (A) Maps of facies-association belts near the top of the models (parasequence 1.7, Fig. 3.3D, with overlying coastal-plain deposits, Fig. 3.3E, removed) showing location of injection and production wells, and the cross-sections illustrated in parts in B-D. (B) Depositional-dip-oriented cross-section showing the internal facies architecture of the modelled parasequences with barriers covering 90% of each clinoform surface shown as black lines and parasequence-bounding flooding surfaces showed as dashed lines. (C, D) Depositional-dip-oriented cross-section showing water saturation after 20 years of production, with a target oil production rate over 20 years of 175 S m^3/day (2200 bbl/day), where there is (C) zero vertical permeability in dDF deposits, and (D) non-zero vertical permeability (k_v of 7 mD) in dDF deposits. Sweep is improved locally in the models containing low vertical permeability (k_v of 7 mD) in dDF deposits.

Figure 3.14A: **139**

(A) Map of facies-association belts near the top of the model of stacked delta-lobe deposits containing channelized fluvial sandstones (with coastal-plain

deposits, Fig. 3.3E, removed), showing the location of injection and production wells. (B) Maps of water saturation for models containing 90% barrier coverage along clinoform surfaces and non- zero vertical permeability (k_v of 7 mD) in dDF deposits, with a low target oil production rate over 20 years of 175 S m^3/day (1100 bbl/day) (left column) and a higher target oil production rate over 10 years of 350 S m^3/day (2200 bbl/day) (right column). (C-D) shown on next page.

Figure 3.14B: **140**

(C) Depositional-dip-oriented cross-section showing the internal facies architecture of the modelled parasequences with barriers covering 90% of each clinoform surface shown as black lines and parasequence-bounding flooding surfaces showed as dashed lines (facies key and location map shown in part (A) on previous page). (D) Depositional-dip-oriented cross-sections showing water saturation at the end of production using the low target oil production rate (left column) and the higher target oil production rate (right column). Sweep efficiency is reduced when producing at the higher oil production rate.

Figure 3.15: **141**

(A, B) Cross-sections of facies-association belts along the structural crest of two models containing multiple, stacked delta-lobe deposits (with coastal-plain deposits, Fig. 3.3E, removed), showing the location of production wells: (A) 0% barrier to flow along clinoforms, non-zero vertical permeability (k_v of 7 mD) in dDF deposits, and no channelized fluvial sandbodies; and (B) 90% barrier to flow along clinoforms, zero vertical permeability in dDF deposits, and channelized fluvial sandbodies present. Pressure and water-saturation profiles along the labelled well in both models are shown in parts E-I. (C, D) Corresponding cross-sections showing water saturation after 10 years of production with a target oil production rate over 10 years of 350 S m^3/day (2200 bbl/day). (E-I) Facies-association successions, stratigraphic surfaces and pressure and water-saturation profiles after 10 years of production along production well (labelled in parts A-D), with dashed lines denoting clinoform surfaces and black lines representing parasequence bounding flooding surfaces. Well data extracted from five models are shown, with increasing heterogeneity from left to right: (E) 0% barrier to flow along clinoforms, non-zero vertical permeability (k_v of 7 mD) in dDF deposits, and no channelized fluvial sandbodies; (F) 0% barrier to flow along clinoforms, non-zero vertical permeability (k_v of 7 mD) in dDF deposits, and no channelized fluvial sandbodies; (G) 90% barrier to flow along clinoforms, zero vertical permeability (k_v of 7 mD) in dDF deposits, and no channelized fluvial sandbodies; (H) 90% barrier to flow along clinoforms, non-zero vertical permeability (k_v of 7 mD) in dDF deposits, and no channelized fluvial sandbodies; and (I) 90% barrier to flow

along clinoforms, zero vertical permeability in dDF deposits, and channelized fluvial sandbodies present.

Figure 4.1: **148**
Outcrop view of distal lower shoreface deposits in the G2 parasequence of the Grassy Member, Blackhawk Formation, north of Green River, east-central Utah, USA (Figs. 4.4, 4.5). Note the irregular geometries of the sandstone beds. Photograph has no vertical exaggeration.

Figure 4.2: **152**
(A) Generalised depositional model of a shoreface fronting a wave-dominated delta, highlighting the position of distal lower shoreface deposits relative to the mean fair weather wave base and mean storm wave base (modified after Howell et al., 2008a). (B) Schematic cross-section oriented along depositional strike illustrating heterogeneity within an upward-coarsening succession (bedset) of distal lower shoreface deposits bounded by clinoform surfaces (modified after Sech et al., 2009). Note the presence of gutter casts within the distal lower shoreface.

Figure 4.3: **154**
Previous interpretations of gutter cast geometry in (A-B) plan view, and (C-D) cross-section (modified after Myrow, 1992). Gutter casts are interpreted to be straight (left) or sinuous (right) channelized scours that are continuous along their axes.

Figure 4.4: **156**
(A) Location of the Mesaverde Group outcrop belt, which contains the Blackhawk Formation, in the Wasatch Plateau and Book Cliffs (after Hampson et al. 2012). The inset map (top left) shows the location of the outcrop belt on the western margin of the late Cretaceous Western Interior Seaway (after Kauffman & Caldwell, 1993). (B) Palaeogeographic map for the G2 parasequence of the Grassy Member, Blackhawk Formation with study area highlighted (Fig. 4.5). Dashed lines represent the maximum progradational extent for a particular facies belt (after O'Bryne and Flint, 1995). (C) Summary stratigraphic cross-section through the Star Point Sandstone, Blackhawk Formation and lower Castlegate Sandstone in the Book Cliffs (after Hampson et al., 2012 and references therein). The tops of the lower Castlegate Sandstone and Castlegate Sandstone are used as local datum surfaces in the cross-section. Shallow-marine parasequences are numbered in the Star Point Sandstone (KSp070-010), in the Spring Canyon (SC4-7), Aberdeen (A1-4), Kenilworth (K1-5), Sunnyside (S1-3),

Grassy (G1-4) and Desert (D1-2) Members of the Blackhawk Formation, and in the Castlegate Sandstone (C1-3).

Figure 4.5: **158**
Basemap of the study area, highlighting the sub-vertical cliff face walls in which the G2 parasequence of the Grassy Member is exposed. The georeferencing stations used to capture and spatially position outcrop data using the stereophotogrammetric technique are shown.

Figure 4.6: **160**
Outcrop data collection and digital outcrop modelling workflow.

Figure 4.7: **165**
(A) Example of stereophotogrammetry outcrop data collection technique in plan-view and (B) oriented in front of the outcrop face. Camera stations one and eight are positioned first and cross-checked to ensure that the stereoline is parallel to the outcrop face and that the camera lens in each position are oriented perpendicular to the stereoline. Each outcrop target should appear in at least three photographs. Camera position one and eight only capture the outcrop target and a small proportion of the outcrop face, but ensure that the targets at the edge of the outcrop appear in sufficient images that these parts of the outcrop can be triangulated.

Figure 4.8: **170**
(A) Photograph of distal lower shoreface deposits in one of the studied cliff faces (located in Fig. 4.5). (B) Corresponding part of digital outcrop model point cloud with inset map view highlighting the 3D aspect of the point cloud. There is no vertical exaggeration in either image.

Figure 4.9: **171**
(A) Part of the digital outcrop model comprising 12 point clouds. Note the white rectangles at the base of the digital outcrop model, which house the reflective targets at their centre (located in Fig. 4.5). (B) One point cloud extracted from Figure 4.9A is made up of 761636 individual points. Note yellow points at the base of the point cloud, which are the calculated positions of the outcrop targets (Eq. 4.4, 4.5, 4.6, 4.7), which show close correspondence with the original positions on the outcrop face (white rectangles) (located in Fig. 4.5). (C) Closer view of individual point cloud in Figure 4.9B, highlighting the dense point cloud created with less than 2 mm spacing between points. Point clouds are shown with no vertical exaggeration.

Figure 4.10: **173**
(A-G) 2D cross-sections of gutter casts from selected photopans (located in Fig. 4.5), illustrating the range of distributions, geometries, and internal structure of gutter casts in the study area.

Figure 4.11: **177**
Flute cast geometry in (A) plan view, (B) flow-perpendicular cross-section, and (C) flow-parallel cross-section (modified after Allen, 1982). This 3D geometry can account for many of 2D cross-sections through gutter casts observed in the study area.

Figure 5.1: **189**
(A) Object-based modelling approach to capture channelized sandbodies in a non-reservoir (mudstone) background on a fine-scale cell-based grid. Channelized sandbodies have a 'stair-step' geometry limited by grid resolution. Channelized sandbodies are shown in colour while the non-reservoir background and associated grid-cells are not shown. (B) Surface-based model to capture channelized sandbodies in a non-reservoir (mudstone) background; each channelized sandbody is defined by an upper and lower surface. (C) Close up view of part of the surface-based model shown in (B), meshed with tetrahedral elements. The element shape and size is adapted to capture the varying size of the channelized sandbodies; the non-reservoir background is not meshed as it does not contribute to flow. The complex sandbody architecture is well preserved with efficient use of mesh elements (compare Fig. 5.1A and Fig. 5.1C) (modified after Jackson et al., in press).

Figure 5.2: **190**
Comparison of numerical solutions obtained using an adaptive mesh in a heterogeneous model, with those obtained using conventional methods. (A) View highlighting the distribution of heterogeneity in models (C) and (D). Purple denotes high permeability while grey denotes low permeability. Permeability for cartesian model in (B) not shown. Water saturation at a snapshot in time (0.2 pore-volumes injected (PVI) in (B) cartesian grid, (C) cornerpoint grid and (D) adaptive, unstructured mesh. Note the variation in water saturation profiles between models (B) and (C) with model (D), arising from numerical dispersion affecting the movement of water which significantly alters the time to water breakthrough and oil recovery at breakthrough (modified after Jackson et al., 2013).

List of Tables

Table 2.1: **54**
Nomenclature for parameters used in the clinoform-modelling algorithm.

Table 2.2: **67**
Clinoform modelling parameters used in the clinoform-bearing model of the Ferron Sandstone Member reservoir analogue.

Table 2.3: **74**
Reservoir, fluid and rock properties used in the model of the Ferron Sandstone Member reservoir analogue (after Farrell and Abreu, 2006; Deveugle et al., 2011).

Table 2.4: **83**
Clinoform modelling parameters used in the clinoform-bearing sector model of the Sognefjord Formation reservoir, Troll Field.

Table 2.5: **90**
Reservoir, fluid and rock properties used in the sector model of the Sognefjord Formation reservoir, Troll Field.

Table 3.1: **108**
Factors investigated in simulation experiments. Four factors investigate uncertain parameters in reservoir characterization which correspond to three lengthscales of heterogeneity in the hierarchy described for fluvial-dominated deltaic reservoirs (Fig. 3.1B-D). One further factor investigates engineering decisions. The right hand column shows the values of factors varied (grey boxes) and held constant (white boxes) in each set of simulation experiments.

Table 3.2: **117**
Values of parameters used in the clinoform-modelling algorithm described in Chapter 2 for models of the Ferron Sandstone Member reservoir analogue.

Table 3.3: **121**
Reservoir, rock and fluid properties used in models of the Ferron Sandstone Member reservoir analogue.

Table 4.1: **162**
Nomenclature for parameters used in georeferencing digital outcrop models.

Table 4.2: **180**
Summary of the strengths and weaknesses of the stereophotogrammetry-based method of digital outcrop model construction relative to LIDAR-based methods.

Chapter 1

Introduction

1.1 Classification of shallow-marine shoreline systems

Shallow-marine systems form important reservoirs and host significant reserves of hydrocarbons in many major oil and gas provinces worldwide (Tyler and Finley, 1991). Examples include Jurassic Brent Group Reservoirs in the North Sea, offshore United Kingdom and Norway (e.g., Husmo et al., 2003); Tertiary reservoirs in the Niger Delta province, offshore Nigeria (e.g., Larue and Legarre, 2004); Miocene reservoirs in the Baram Delta Province, offshore Brunei Darussalam (e.g., Hodgetts et al., 2001); and Triassic reservoirs in the Prudhoe Bay of Alaska, USA (e.g., Begg et al., 1992). The shallow-marine realm is defined as the part of the depositional system that exists between the landward influence of marine processes and the seaward influence of continental, mainly fluvial processes and can be classified in a number of ways (Fig. 1.1) (Boyd et al., 1992; Howell et al., 2008b). Shallow-marine systems are divided into two broad categories: progradational or retrogradational (Howell et al., 2008b). Progradational systems represent shoreline movement through sediment supply from fluvial processes or by longshore drift that is greater than the rate of accommodation available through sea-level rise or subsidence (Van Wagoner et al., 1990). The converse, in which there is a relative sea-level rise or a reduction in sediment supply, results in retrogradational systems. This study focuses on progradational shallow-marine systems

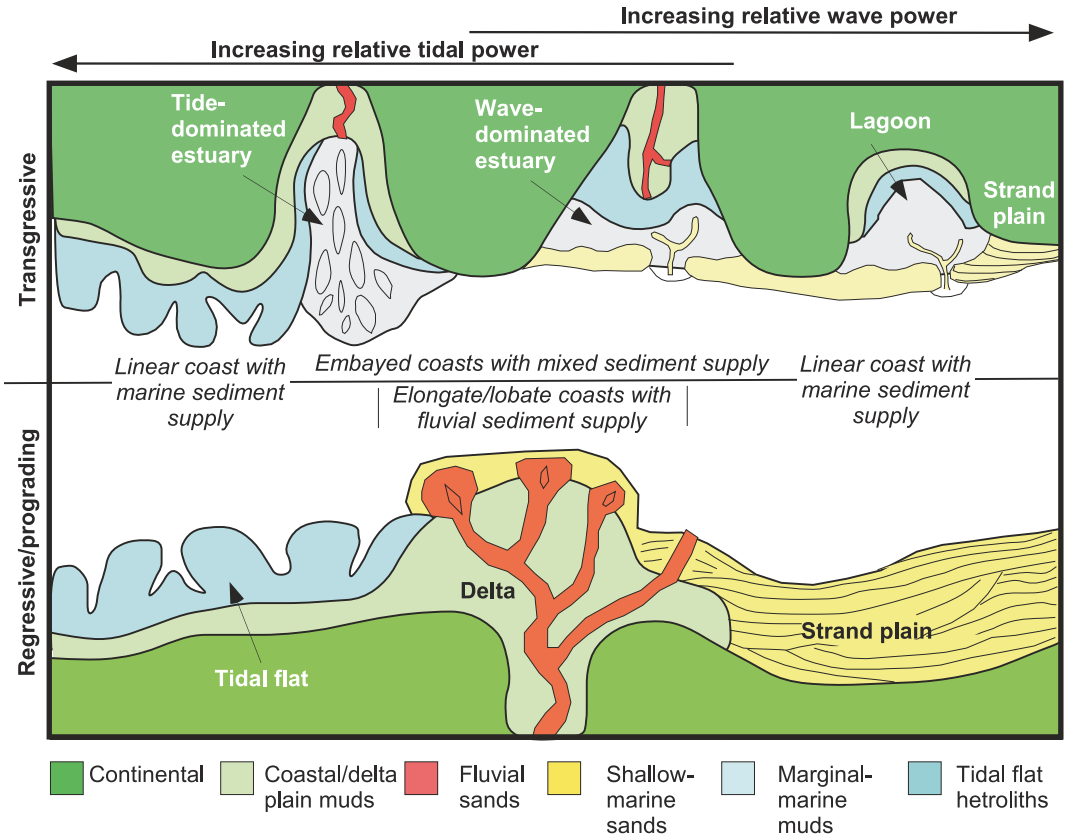


Figure 1.1. Classification of shallow-marine shoreline systems based on the long term movement of the shoreline and the key depositional processes (modified after Boyd et al., 1992).

such as deltaic and strandplain shorelines, which are further classified by placing a progradational shallow-marine system within a ternary diagram according to relative influence of fluvial, tide or wave processes (Galloway, 1975; Ainsworth et al., 2011; Vakarelov and Ainsworth, 2013). While basinal energy in the form of tides or waves, and fluvial energy are important controls on the characteristics of shallow-marine systems, they are further influenced by the nature of the sediment supply and tectonic-physiographic setting. The geometry and spatial distribution of facies formed by these processes results in complex facies architecture and distributions of geological heterogeneities within shallow-marine reservoirs.

1.2 Geological heterogeneity in shallow-marine reservoirs

Within shallow-marine reservoirs, heterogeneities are hierarchically arranged over a range of lengthscales (Fig. 1.2) (e.g., Kjønsvik et al., 1994; Sech et al., 2009; Fig. 3.1). By way of illustration, a generic hierarchy of heterogeneities within shoreface. reservoirs (corresponding to "strandplain" in Fig. 1.1) is used here to show the hierarchical arrangement of common heterogeneities within shallow-marine reservoirs. At the field scale (c. 10 km) shallow-marine strata comprise a number of vertically stacked, shallow-marine tongues (parasequence sets of Van Wagoner et al., 1990) that interfinger with coeval offshore shales in a palaeoseaward direction, and with coeval coastal-plain deposits in a palaeolandward direction (Fig. 1.2A).

Shallow-marine parasequence sets can be further subdivided into multiple smaller deltaic or shoreface tongues (parasequences of Van Wagoner et al., 1990). Parasequences can exhibit complex stacking patterns and are often bounded by laterally continuous low permeability flooding surfaces which can compartmentalize shallow-marine reservoirs (e.g., Ainsworth et al., 1999) (Fig. 1.2B). The top of each shallow-marine tongue and their associated coastal-plain deposits can be locally eroded by channelized sandbodies of different types (e.g. deltaic distributary channel fills, fluvial channel fills, incised valley fills) that may be genetically unrelated to the deposits they cut into, but which can form high permeability thief zones for fluid flow if they contain continuous, coarse-grained sandstones (e.g., Deveugle et al., 2011).

Within parasequences, the geometry and distribution of clinoform surfaces control intraparasequence facies and permeability architecture in several ways (Fig. 1.2B) (Hampson, 2000, Hampson et al., 2008) (bedsets of Van Wagoner et al., 1990).

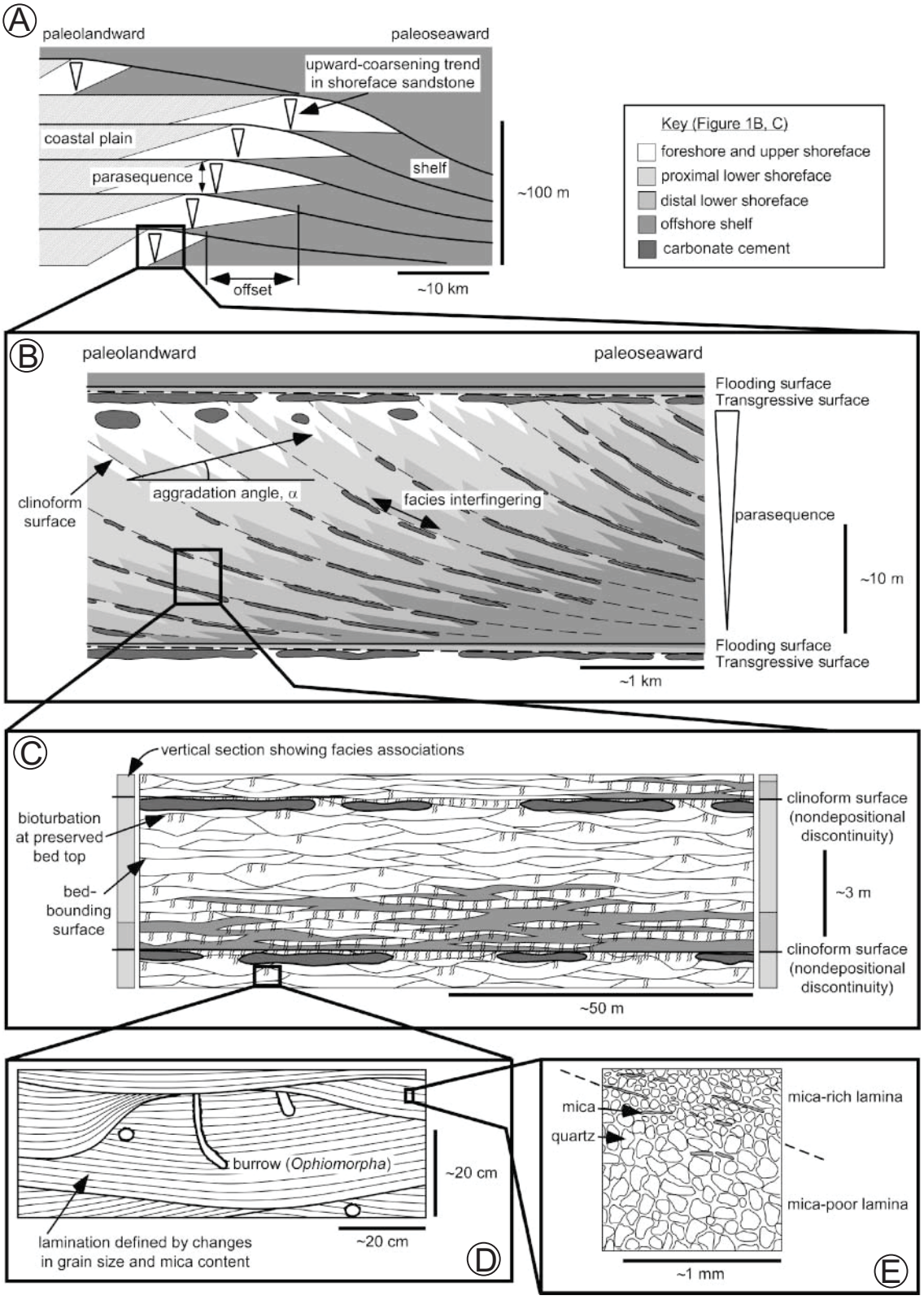


Figure 1.2. Generic hierarchy of heterogeneities within shoreface-shelf reservoirs (standplain Fig. 1.1) across a range of lengthscales: (A) a parasequence set; (B) a single parasequence; (C) a package of beds bounded by clinoform discontinuity surfaces (bedset); (D) hummocky-cross stratification; and (E) micropsopic laminations. Note the heterogeneity associated with clinoform surfaces (after Sech et al., 2009 and references therein).

Clinoforms are often associated with laterally discontinuous barrier or baffles to flow and have been previously identified as a key control on fluid-flow and hydrocarbon recovery within shallow-marine reservoirs (e.g., Wehr and Brasher, 1996; Ainsworth et al., 1999; Dutton et al., 2000; Howell et al., 2008a, 2008b; Jackson et al., 2009; Enge and Howell, 2010; see Chapter 3). The nature of the heterogeneity associated with the clinoform surfaces is dependent on the depositional environment. Subsurface datasets indicate that calcite-cemented concretions are one such barrier or baffle to flow along clinoforms in wave-dominated shoreface systems (Jennette and Riley, 1996; Wehr and Brasher, 1996; Morris et al., 2006). The dominant source of calcite cement in shallow-marine sandstones is carbonate fossils contained within the sandstones (e.g. Fürsich, 1982; Hudson and Andrews, 1987; Saigal and Bjørlykke, 1987; Bryant et al., 1988). Typically, calcite cement distribution reflects local diffusional diagenetic redistribution of carbonate shell material whose location was controlled by the depositional environment (Bjørkum and Walderhaug, 1990; Walderhaug and Bjørkum, 1998). If the supply of carbonate shell material was exhausted at relatively early stage of fluid migration, the calcite-cemented concretions tend not to merge, whereas if the amount of carbonate shell material is large, the concretions may merge and form continuous calcite-cemented layers (Bjørkum and Walderhaug, 1990). Mudstone and siltstone drapes along clinoforms are more common in fluvial-dominated systems (Howell et al., 2008b), and are interpreted to have been deposited during quieter periods of sediment and water discharge (Howell et al., 2008a). Furthermore, clinoforms may also be marked by dislocations of facies types that are associated with major contrasts in reservoir properties (such as porosity, permeability, capillary pressure, and mobile oil saturation) (e.g., Kjønsvik et al., 1994; Wehr and Brasher, 1996; Larue and Legarre, 2004), where

variable bed-scale successions within facies types can make it difficult to predict reservoir properties using conventional techniques (Fig. 1.2C) (e.g., Worthington, 2000). Smaller-scale heterogeneities in shallow-marine reservoirs include sedimentary structures, and the degree and type of bioturbation present within beds (Fig. 1.2D), and grain size and sorting characteristics, which control pore geometries at the microscopic scale (Fig. 1.2E).

1.3 Conventional approaches to reservoir modelling

Fluid distribution and flow and are ultimately controlled by facies architecture and geologic heterogeneity (e.g., Weber, 1986; Weber and van Geuns, 1990; Kjønsvik et al., 1994; Wehr and Brasher, 1996; Jackson and Muggeridge 2000; White et al., 2004; Jackson et al., 2005, 2009). It is therefore essential to define geological heterogeneity and reservoir character prior to production, in order to accurately predict likely hydrocarbon recovery and drainage patterns. However in most subsurface reservoirs, the geological data used to constrain reservoir architecture and facies distribution are far from optimal. Low-resolution but extensive 3D seismic reflection data can only resolve the large scale architecture of the reservoir which can be used to identify key reservoir faults and reservoir zonation schemes. Detailed, but widely-spaced 2D core and well-log data typically sample less than 0.1% of the reservoir (North and Prosser, 1993), but provide no information away from wells and may not even represent a suitable Representative Elementary Volume (REV) for the reservoir. Geological modellers therefore rely on geostatistics as a substitute for geological data to distribute facies away from high-resolution well data. Geostatistical algorithms are then conditioned to, and qualitatively checked against, a prior interpretation of the depositional architecture and

stratigraphy of the reservoir that drives reservoir model construction. Two approaches are commonly adopted for stochastically distributing facies within reservoir models: object- and pixel-based techniques.

Object based techniques (or Boolean models) simulate the distribution of geological features that are discrete in nature on a predefined cell-based grid (e.g., Haldorsen and Damsleth, 1990). Geobodies are stochastically distributed and conditioned to both user defined parameters describing object geometries and trends and available subsurface data. Object-based techniques are commonly used to represent geobodies such as channels, point-bars and lobes in fluvial settings (e.g., Deutsch and Wang, 1996; Colombera et al., 2012). With pixel-based techniques each node on a grid is assigned a single value of the variable being modelled (e.g. facies type), which is dependent on both the value assigned to a neighbouring cell and the initial user defined constraints on the distribution of the variable. Pixel-based methods utilise either: two-point statistic variograms (e.g., sequential-indicator simulation (SISIM); Journel and Gomez-Hernandez, 1993; truncated Gaussian simulation (TGSIM); Matheron et al., 1987) or multiple-point statistics that extract geometrical characteristics, relationships and spatial distributions from predefined 3D training images (e.g., Multiple Point Statistics, MPS; Strebelle, 2002). However, object- and pixel-based approaches to reservoir modelling are populated on a cell-based grid and are often not able to capture key heterogeneities. This is because the underlying grid is defined prior to property distribution, and limits the spatial distribution and complexity of geometries that can be represented in the model (Fig. 1.3A) (Deutsch, 2002; Jackson et al., in press). So while geostatistical approaches can give mathematically plausible answers, at best, they average finer scale aspects of reservoir architecture and, at worst, may not be

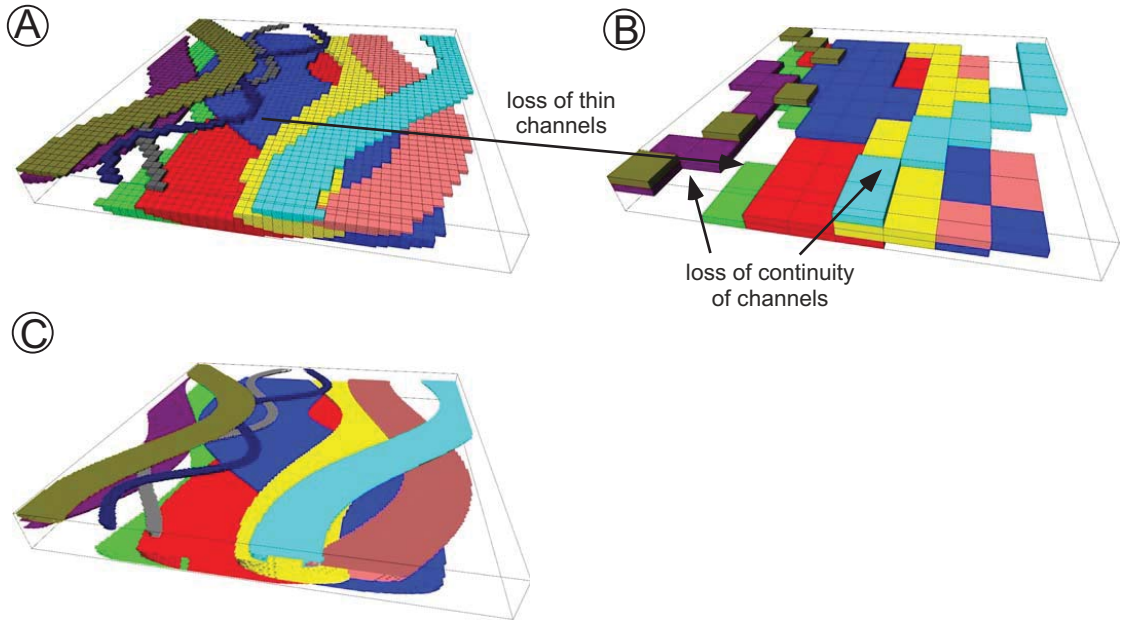


Figure 1.3. (A) Object-based modelling approach to capture channelized sandbodies in a non-reservoir (mudstone) background on a fine-scale cell-based grid. Channelized sandbodies have a 'stair-step' geometry limited by grid resolution. (B) Object-based modelling approach to capture channelized sandbodies in a non-reservoir (mudstone) background on a coarser-scale cell-based grid. Many of the smaller channelized sandbodies are below the grid resolution so are not captured, while connectivity is not preserved in the larger sandbodies, as the cell-face contacts that are captured in the fine-scale model in (A) have been lost. (C) Surface-based model; each channelized sandbody is defined by an upper and lower surface. Channelized sandbodies are shown in colour while the non-reservoir background and associated grid-cells are not shown (modified after Jackson et al., in press).

geologically correct or even feasible (Larue and Legarre, 2004). While fine-scale reservoir (geological or static) models can allow key geometries and heterogeneities to be represented, they comprise a large number of grid cells. Fine-scale models then become computationally inefficient for multiple fluid-flow simulation experiments over a range of realisations. Therefore, properties such as porosity and permeability modelled on the fine-scale cell-based grid are typically upscaled onto a coarser cell-based grid for fluid-flow simulation experiments. However, a coarser cell-based grid further limits the spatial distribution and complexity of geometries of heterogeneities that can be represented in models (e.g. Fig. 1.3B). Alternatively, streamline simulation methods can be used on

these fine-scale reservoir models (e.g., Batycky et al., 1997) which are computationally less expensive, but make a number of simplifying assumptions to the underlying flow physics that may be violated in many reservoir and production scenarios (Jackson et al., in press; discussed in Chapter 3).

1.4 Surface-based reservoir modelling

Surface-based modelling has been introduced more recently as a method for reservoir model construction (e.g., Deutsch et al., 2001; Pyrcz et al., 2005; Zhang et al., 2009, Sech et al., 2009; Enge and Howell, 2010). Surface-based modelling utilises surfaces to represent key geological heterogeneity prior to generating a grid for flow simulation (Sech et al., 2009; Jackson et al., in press). Any structural, stratigraphic and sedimentological heterogeneity to be modelled are incorporated in reservoir models using a hierarchy of surfaces (Fig. 1.4) (Jackson et al., in press).

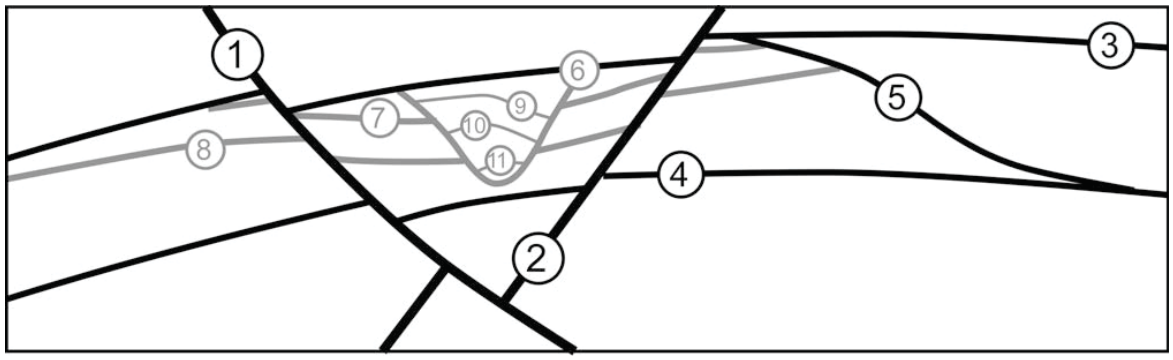


Figure 1.4. Generic example of surface hierarchy, developed according to rules that define which surfaces can truncate previously modelled surfaces. Structural surfaces are typically at the top of the hierarchy as they truncate other surfaces (surfaces 1 and 2). Stratigraphic surfaces are typically next in the hierarchy, as these are often truncated by faults but truncate facies boundaries (surfaces 3-5). Sedimentological surfaces are typically at the base of the hierarchy (surfaces 6-11). This hierarchy may be modified for a given reservoir model as in some cases, structural surfaces may be truncated by stratigraphic surfaces (modified after Jackson et al., in press).

Surfaces are used to define discrete volumes, in which petrophysical properties remain constant (Jackson et al., in press). The advantage of a surface-based modelling approach is that it allows the grid for flow simulation to be defined at the last stage of modelling so that geological model resolution is not limited by grid resolution. Surfaces for reservoir models can be generated in a number of ways. Outcrop analogue data has long been used to provide high resolution quantitative data on the geometry and distribution of heterogeneities to bridge the resolution gap between seismic and well-data. Such outcrop data have traditionally been used in a qualitative way, to gain generic geological insights into a particular reservoir type (e.g., Van Wagoner et al., 1990), or in a quantitative way, such as to characterise geobody dimensions and geometries (e.g., Reynolds, 1999; White and Willis, 2000). Over the last decade, several techniques have been developed to aid digital capture of outcrop data, with the aim of improving the accuracy, efficiency and repeatability of data collection. Data for digital outcrop models can be collected by referencing 2D photomontages of 2D outcrop cliff faces using global positioning system (GPS) coordinates, and used to drape digital elevation models (DEM) (e.g., Deveugle et al., 2011). The accuracy of this technique however, is limited by sparse spatial coordinate data and perspective effects on the photomontages, in which measurements of sedimentary features or geobodies may be skewed by outcrop shape and orientation (Pringle et al., 2004). High-resolution, 3D digital data from outcrops, can be captured using LIght Detection And Ranging (LIDAR) -based methods (e.g., Wehr and Lohr, 1999; Bellian et al., 2005; Enge and Howell, 2010). LIDAR-based methods can define bedding with sub meter accuracy but require a wide unobstructed view of the sky, so that the models can be referenced and accurately positioned using differential GPS (DGPS) data. Surfaces have been deterministically interpolated between control points

at outcrop in both 2D models (e.g., White & Barton, 1999; White et al., 2004) and 3D models (Sech et al., 2009; Enge and Howell, 2010) of outcrop analogues. However, purely deterministic approaches to surface-based modelling are not suitable for field-scale reservoir models, primarily due to a paucity of data typically available from subsurface reservoirs relating to spatial distributions and geometries. However, even if data were available, deterministic modelling would be a vastly time-consuming task, particularly if multiple scenarios and realizations are needed to undertake uncertainty analysis for the assessment of risk.

Stochastic surface-based approaches are required to address these issues. Any object- based or pixel-based facies modelling algorithm could be used to generate geobodies or facies distributions, but surfaces that represent facies boundaries or geobody boundaries are then extracted and the initial modelling grid discarded (Fig. 1.3C) (e.g., MacDonald et al., 1998; Jackson et al., in press). Alternatively, surfaces can be generated using geostatistical approaches without recourse to an underlying cell-based grid (e.g., Hassanpour et al., 2013). However, there are relatively few documented 3D stochastic surface-based approaches that are generic and yield algorithms that can be used to incorporate surfaces in reservoir models (e.g., Xie et al., 2001; Pyrcz et al., 2005; Zhang et al., 2009). None of these studies document a single method that allows the modeller to generate and distribute surfaces using a purely deterministic or stochastic approach or that combines both elements. Furthermore, previous stochastic surface-based modelling studies focused on deepwater depositional environments (e.g., Xie et al., 2001; Pyrcz et al., 2005; Zhang et al., 2009) and there are currently no stochastic surface-based algorithms available at present to incorporate heterogeneities within shallow-marine reservoirs. Finally, of the stochastic surface-based algorithms previously

reported, none went on to demonstrate the application of their methods to build geological models suitable for fluid flow simulation or assessed which heterogeneities were key controls on fluid flow and hydrocarbon recovery.

1.5 Thesis aims and objectives

The aim of this study is to develop a stochastic surface-based modelling algorithm, characterised from outcrop datasets, which can be used to incorporate complex heterogeneity within models of shallow-marine reservoirs. The geometry and distribution of heterogeneity is to be preserved in fluid flow simulations to establish which heterogeneities are key controls on fluid flow and hydrocarbon recovery in shallow-marine reservoirs. This thesis addresses the following principal objectives:

(1) To develop an algorithm-based method to incorporate clinoform surfaces into models of shallow-marine reservoirs and ensure that it is sufficiently flexible to match clinoform geometries and distributions observed at outcrop and also to honour subsurface data;

(2) To quantify the impact of different types of heterogeneity on fluid flow and hydrocarbon recovery in fluvial-dominated deltaic reservoirs;

(3) Outline a method for collecting 3D, high resolution, digital outcrop data that is suitable for characterizing the vertical permeability of distal lower shoreface deposits in wave-dominated shallow-marine reservoirs.

1.6 Thesis structure

Within the context of shallow-marine environments, the term modelling may take on a different meaning depending on the interests of the reader. This thesis focuses on aspects of geological modelling, modelling fluid flow and hydrocarbon recovery and digital outcrop modelling. We begin by describing a simple conceptual framework to describe clinoform geometries and distributions, which allows clinoforms to be incorporated into reservoir volumes deposited in different shallow-marine environments (Chapter 2). From this, an algorithm to model multiple clinoform surfaces in shallow-marine reservoirs is developed. To demonstrate the algorithm as a practical method to model clinoforms, we use high-resolution outcrop data to build a reservoir model of a well-exposed fluvial-deltaic outcrop analogue (Cretaceous Ferron Sandstone Member, Utah, USA). Similarly, the algorithm is validated by generating a reservoir model using a sparse subsurface dataset from the deltaic Jurassic Sognefjord Formation in a sector model of the Troll Field, offshore Norway. Finally, we use the reservoir model of the Ferron Sandstone Member outcrop analogue to make preliminary observations of the impact of mudstone drapes along clinoform surfaces on fluid flow and hydrocarbon recovery under a water-flooding displacement mechanism. Similarly, we use the reservoir model of the subsurface Sognefjord Formation in the Troll Field sector to assess the potential impact of calcite cementation along clinoform surfaces on drainage patterns and hydrocarbon recovery under a gas cap expansion and aquifer influx displacement mechanism. This chapter will be submitted to the AAPG Bulletin, with my PhD supervisors as co-authors. At the time of writing, we are awaiting permission from sponsors to submit this manuscript.

In Chapter 3, we use the clinoform-modelling algorithm developed in Chapter 2 to create a suite of reservoir-scale models of a fluvial-dominated deltaic reservoir analogue that incorporate several stacked delta lobe deposits each containing multiple clinoform surfaces. The models are used to quantify the effect of permeability contrasts associated with clinoform surfaces on fluid-flow and hydrocarbon recovery in the context of: (1) uncertainties in reservoir characterization, such as the impact of bed-scale heterogeneity on vertical permeability; and (2) reservoir engineering decisions, such as oil production rate. The implications for reservoir monitoring and management are also detailed. This chapter will be submitted to the AAPG Bulletin, with my PhD supervisors as co-authors. At the time of writing, we are awaiting permission from sponsors to submit this manuscript.

In Chapter 4 a new method of digital outcrop data collection is described and validated via its application to an outcrop example of distal lower shoreface deposits in a wave-dominated shallow-marine reservoir analogue. The resulting digital outcrop model is used to make preliminary observations of the 3D geometry and spatial distribution of gutter casts. In this chapter, as well as my PhD supervisors, Gregory S. Benson (ExxonMobil) provided supervisory input on stereophotogrammetry data collection techniques.

A list of references cited can be found at the end of the thesis. In Appendix A, the algorithms that were developed over the course of the project are documented and provided on CD-ROM, including the clinoform-modelling algorithm. An example of an Eclipse 100 data input file used for the simulation experiments in Chapter 3 is included in Appendix B, while Appendix C details a workflow established for using Photomodeler Scanner® software to create digital outcrop models.

1.7 Journal articles and conference presentations

Two publications arising from this research that are ready for journal submission are as follows:

Graham, G. H., M. D. Jackson, and G. J. Hampson, in review a, Three-dimensional modeling of clinoforms within shallow-marine reservoirs: Part1. Concepts and application: submitted to AAPG Bulletin.

Graham, G. H., M. D. Jackson, and G. J. Hampson, in review b, Three-dimensional modeling of clinoforms within shallow-marine reservoirs: Part 2. Impact on fluid flow and hydrocarbon recovery in fluvial-deltaic reservoirs: submitted to AAPG Bulletin.

The two articles form Chapters 2 and 3 respectively. My PhD supervisors, G. J. Hampson and M. D. Jackson (Imperial College London), provided supervisory guidance and editorial comments which also apply throughout this thesis, while I was principal investigator and author. Although not explicitly presented, the results of this thesis also contributed with examples and figures to the following article:

Jackson, M. D., G. J. Hampson, A. El Sheikh, J. H. Saunders, **G. H. Graham**, and B. Y. G. Massart, in press, Surface-based reservoir modelling, Sediment body geometry and heterogeneity: analogue studies for modelling the subsurface, Geological Society (London) Special Publication.

Six presentations based on this research were given as talks or posters at international conferences:

Graham, G. H., M. D. Jackson, G. J. Hampson, R. P. Sech, and P. E. K. Deveugle, 2010, Three-dimensional numerical modelling of clinoforms within deltaic and shoreface reservoirs: Petroleum Geoscience Research Collaboration Showcase, November 23-25, Earl's Court, London, UK.

Graham, G. H., M. D. Jackson, G. J. Hampson, R. P. Sech, and P. E. K. Deveugle, 2011, Three-dimensional numerical modeling of clinoforms within deltaic and shoreface reservoirs: AAPG Annual Convention and Exhibition, April 10-13, Houston, Texas, USA.

Graham, G. H., M. D. Jackson, G. J. Hampson, R. P. Sech, and P. E. K. Deveugle, 2011, Three-dimensional numerical modeling of clinoforms within deltaic and shoreface reservoirs: EAGE Conference and Exhibition Workshop 10: Capturing Realistic Sedimentary Architecture in Geo-cellular Reservoir Models - State of the Art and Advances from Object and Process Modelling, to Multipoint Statistics, May 23-26, Vienna, Austria.

Graham, G. H., M. D. Jackson, G. J. Hampson, F. A. Dilib, R. P. Sech, and P. E. K. Deveugle, 2012, Three-dimensional numerical modelling of clinoforms and their impact on fluid flow and hydrocarbon recovery within deltaic and shoreface reservoirs: AAPG Annual Convention and Exhibition, April 22-25, Long Beach, California, USA.

Graham, G. H., M. D. Jackson, and G. J. Hampson, 2013, Controls on fluid flow and hydrocarbon recovery in a clinoform-bearing, fluvial-dominated deltaic reservoir analog: Ferron Sandstone, Utah: AAPG Annual Convention and Exhibition, May 19-22, Pittsburgh, Pennsylvania, USA.

Dilib, F. A., M. D. Jackson, **G. H. Graham**, and G. J. Hampson, 2013, Impact of heterogeneity on flow in shallow-marine reservoirs: Application to a thin oil

column produced via horizontal wells: AAPG Annual Convention and Exhibition, May 19-22, Pittsburgh, Pennsylvania, USA.

Chapter 2

Three-dimensional modelling of clinoforms within shallow-marine reservoirs: Part 1. Concepts and application

2.1 Summary

Clinoform surfaces control aspects of facies architecture within shallow-marine parasequences, and can also act as barriers or baffles to flow where they are lined by low-permeability lithologies such as carbonate cements or mudstones. Current reservoir modelling techniques are not well suited to capturing clinoform surfaces, particularly if they are numerous, below seismic resolution and/or difficult to correlate between wells. At present there are no modelling tools available to automate the generation of multiple three-dimensional clinoform surfaces using a small number of input parameters. Consequently, clinoforms are rarely incorporated in models of shallow-marine reservoirs, even when their potential impact on flow is recognized.

We present a numerical algorithm that generates multiple clinoform surfaces within a volume defined by two bounding surfaces, such as a delta-lobe deposit or shoreface parasequence. A geometrical approach is taken to construct the shape of a clinoform surface, combining its height relative to the bounding surfaces with a

mathematical function that describes clinoform geometry. The method is flexible, allowing the user to define the progradation direction and the parameters which control the geometry and distribution of individual clinoform surfaces. The algorithm is validated via construction of surface-based three-dimensional reservoir models of: (1) fluvial-dominated delta-lobe deposits exposed at outcrop (Cretaceous Ferron Sandstone Member, Utah, USA); and (2) a sparse subsurface dataset from a deltaic reservoir (Jurassic Sognefjord Formation, Troll Field, Norwegian North Sea). The resulting models are used to demonstrate that under certain displacement conditions clinoforms significantly impact hydrocarbon recovery when they are associated with areally extensive barriers to flow.

2.2 Introduction

Key factors influencing fluid flow and reservoir behaviour include facies architecture and heterogeneity distribution conditioned to stratal surfaces. Within shallow-marine reservoirs, clinoforms are one such type of stratal surface. Clinoforms are palaeoseaward-dipping surfaces whose geometry preserves the depositional morphology of the delta-front or shoreface slope, and whose distribution reflects the progradation history of the shoreline (Barrell, 1912; Rich, 1951; Gani and Bhattacharya, 2005; Sech et al., 2009) (Fig. 2.1). Clinoform surfaces control aspects of detailed facies architecture within parasequences and can also act as low-permeability barriers or baffles to flow (Wehr and Brasher, 1996; Ainsworth et al., 1999; Dutton et al., 2000; Howell et al., 2008a, 2008b; Jackson et al., 2009; Enge and Howell, 2010). Therefore, under certain displacement conditions it can be important to include clinoforms in

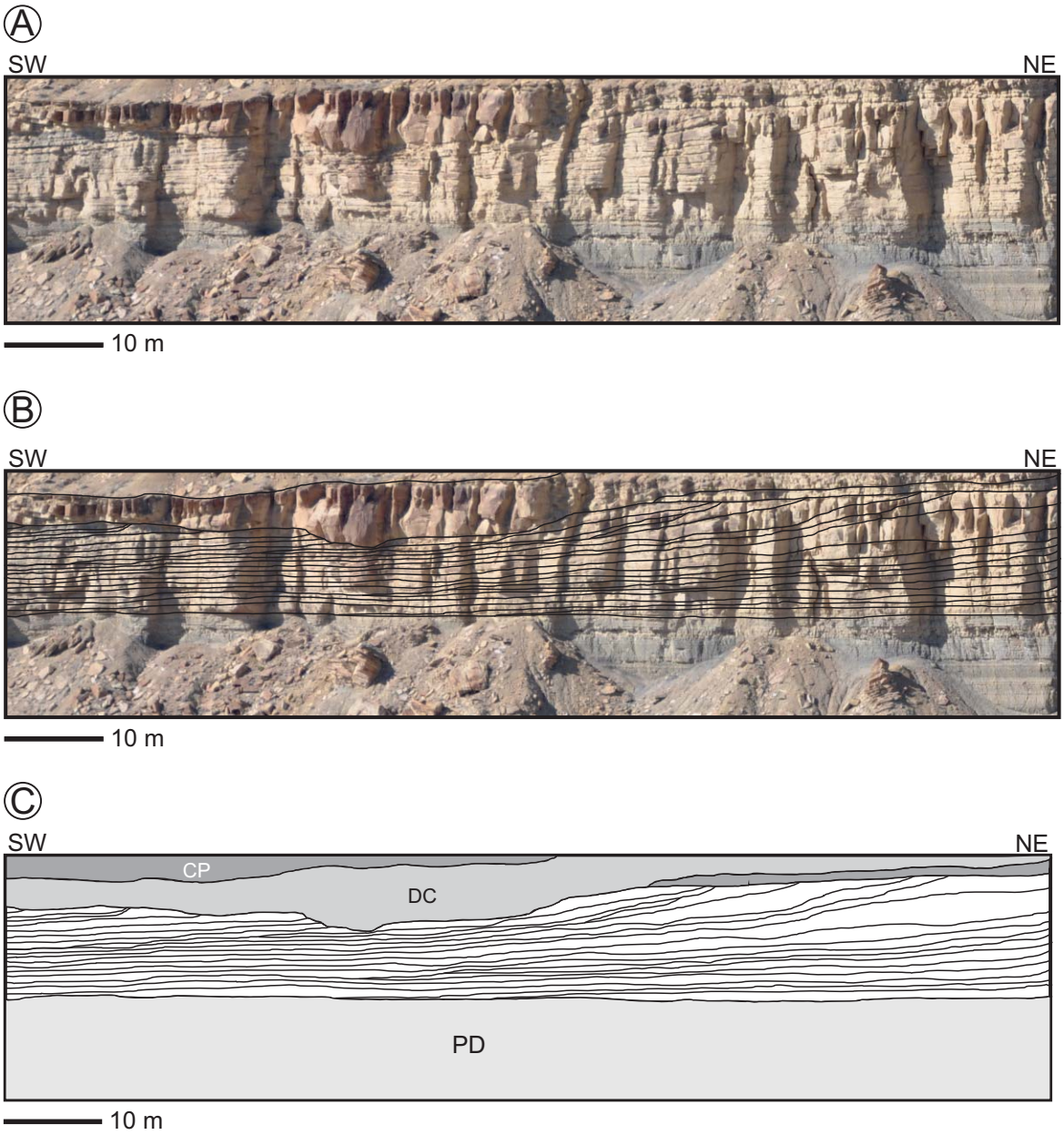


Figure 2.1. (A) Outcrop view of delta-front clinoforms in the Ferron Sandstone Member at the Ivie Creek amphitheatre, north of I-70, east-central Utah, USA (corresponding to parasequences 1.5 and 1.6 of Deveugle et al., 2011). Note the dipping nature of the delta-front sandstones and shales, and the erosional contact with an overlying distributary channel sandstone. (B) Corresponding outcrop interpretation showing clinoform surfaces within the delta-front deposits. (C) Corresponding line drawing highlighting approximately 25 clinoforms, shown as black lines on a white background. CP = Coastal plain heteroliths, DC = Distributary channel sandstone, PD = Prodelta shales. Photographs and line drawings have no vertical exaggeration.

models of shallow-marine reservoirs, in order to properly characterize facies architecture and hence volumes of hydrocarbons in place (Sech et al., 2009). Under certain

displacement conditions, if the clinoform surfaces are associated with significant barriers to flow, clinoforms must be included in dynamic simulations to accurately predict likely drainage patterns and ultimate recovery of hydrocarbons (Jackson et al., 2009).

Standard modelling techniques are not well suited to capturing clinoform surfaces, particularly if they are numerous, below seismic resolution and/or difficult to correlate between wells. A small number of studies have attempted to identify and correlate clinoforms in the subsurface (Livera and Caline, 1990; Jennette and Riley, 1996; Løseth and Ryseth, 2003; Matthews et al., 2005; Hampson et al., 2008), or built two-dimensional (2D) (Wehr and Brasher, 1996; Forster et al., 2004) or three-dimensional (3D) (Howell et al., 2008a, 2008b; Jackson et al., 2009; Sech et al., 2009; Enge and Howell, 2010) flow simulation models that incorporate clinoform surfaces. Previous studies of the Ferron Sandstone Member have incorporated simple clinoform geometries into reservoir models by using either object-based (Howell et al., 2008a) or deterministic (Howell et al., 2008b) approaches. Enge and Howell (2010) used data collected by LIght Detection And Ranging (LIDAR) equipment to precisely recreate 3D clinoform geometries from part of the Ferron Sandstone Member outcrops and the resulting flow-simulation model contained deterministically modelled clinoform surfaces, but in a volume smaller than most reservoirs (500 x 500 x 25 m). Sech et al. (2009) used a surface-based modelling approach to produce a deterministic, 3D model of a wave-dominated shoreface-shelf parasequence from a rich, high-resolution outcrop dataset (Cretaceous Kenilworth Member, Utah, USA), and Jackson et al., (2009) used this model to investigate the impact of clinoforms on flow. Jackson et al., (2009) and Enge and Howell (2010) both showed that capturing numerous clinoform surfaces in fluid-flow simulations is feasible. Deterministic clinoform modelling approaches are appropriate for modelling clinoform

surfaces that are tightly constrained by outcrop data, but are time consuming to implement; moreover, they do not allow flexibility in conditioning clinoform geometry and distribution to sparser datasets with a larger degree of uncertainty, such as those that are typically available for subsurface reservoirs. Incorporating hundreds of deterministic clinoform surfaces within a field-scale reservoir model would be a dauntingly time-consuming task, particularly if multiple scenarios and realizations that capture uncertainty in clinoform geometry and distribution are to be modelled. A stochastic, 3D, surface-based modelling approach is required to address these issues. Similar approaches have been demonstrated for other depositional environments (e.g. Xie et al., 2001; Pyrcz et al., 2005; Zhang et al., 2009), but at present, there are no tools available to automate the generation of multiple 3D clinoform surfaces in shallow-marine systems using a small number of parameters. The aim of this chapter is to develop an efficient, quick and practical method to incorporate clinoforms into models of shallow-marine reservoirs.

This chapter is structured in four parts. First, we present a simple conceptual framework to describe clinoform geometries and distributions, which allows them to be incorporated into reservoir volumes deposited in different shallow-marine environments. The framework is used to develop an algorithm-based method to represent clinoform surfaces, which is sufficiently flexible to match clinoform geometries and distributions observed in rich outcrop datasets, and also to honour sparse subsurface data. The second part of the chapter validates the clinoform-modelling algorithm via construction of a three-dimensional reservoir model using high-resolution outcrop data from fluvial-dominated delta-lobe deposits in the Cretaceous Ferron Sandstone Member of east-central Utah, USA. The model is constructed using surfaces that represent boundaries

between facies associations and surfaces that represent clinoforms. The third part of the chapter demonstrates an application of the clinoform-modelling algorithm to generate a reservoir model using a sparse subsurface dataset from the deltaic Jurassic Sognefjord Formation, in a fault-bounded sector of the Troll Field, offshore Norway. The clinoform-modelling algorithm allows flexibility in building a range of surface-based reservoir models that incorporate uncertainty in heterogeneities associated with clinoform surfaces. The resulting three-dimensional surface-based reservoir models are suitable for flow simulation without upscaling. Finally, we use the reservoir model of the Ferron Sandstone Member outcrop analogue to make preliminary observations of the impact of mudstone drapes along clinoform surfaces on fluid flow and hydrocarbon recovery under a water-flooding displacement mechanism. Similarly, we use the reservoir model of the subsurface Sognefjord Formation in the Troll Field sector to assess the potential impact of calcite cementation along clinoform surfaces on drainage patterns and hydrocarbon recovery under a gas cap expansion and aquifer influx displacement mechanism.

In Chapter 3 we apply the clinoform-modelling algorithm to build reservoir-scale models of the Ferron Sandstone Member and investigate the impact of clinoforms on fluid flow in the context of other uncertain reservoir geological parameters, such as the presence of distributary and fluvial channels, the magnitude of permeability contrasts between facies associations, and the impact of bed-scale heterogeneity on vertical permeability, as well as reservoir engineering decisions, including well locations and production rates.

2.3 Conceptual framework for clinoform modelling

Clinoforms occur at a wide range of spatial scales, from large, basinward-dipping surfaces at the shelf-slope margin, to the smaller surfaces associated with progradation of deltaic and shoreface systems across the shelf (e.g. Helland-Hansen and Hampson, 2009). This study focuses on developing a surface-based approach to represent clinoforms at any lengthscale in reservoir models, with emphasis on clinoforms produced by the progradation of deltaic and strandplain shorelines, which are typically up to a few tens of meters in height. The clinoform-modelling algorithm is simple to use, requiring the specification of only a few input parameters: (1) the upper and lower surfaces that define the rock volume within which the clinoforms are to be modelled; (2) the plan-view geometry of clinoform surfaces; (3) clinoform geometry in depositional-dip-oriented cross section; and (4) spacing and progradation direction of the clinoform surfaces. The user can also use a stochastic component of the clinoform-modelling algorithm if there is uncertainty in the parameter values to be used. The complete code developed for the clinoform-modelling algorithm can be found in Appendix A1, while the code developed for stochastically generating input parameters for the clinoform-modelling algorithm can be found in Appendix A2.

2.3.1 (1) Bounding surfaces that define rock volume

Each set of shoreline clinoforms is contained within a distinct, upward-shallowing, regressive succession, or parasequence (sensu Van Wagoner et al., 1990; Hampson et al., 2008), that is bounded at its base and top by flooding surfaces. Multiple clinoforms exist within each parasequence. As the algorithm is generic, any top and base bounding surfaces can be used; the only requirement is that the top bounding surface is entirely

above, or coincident with, the base bounding surface across the model volume (Fig. 2.1A-C). By using the flooding surfaces at the top and/or base of a parasequence as reference surfaces, the algorithm can produce clinoforms that are modified by post-depositional folding and faulting (Fig. 2.2A), truncation by overlying erosion surfaces (Fig. 2.2B), and/or progradation over irregular sea-floor topography (Fig. 2.2C).

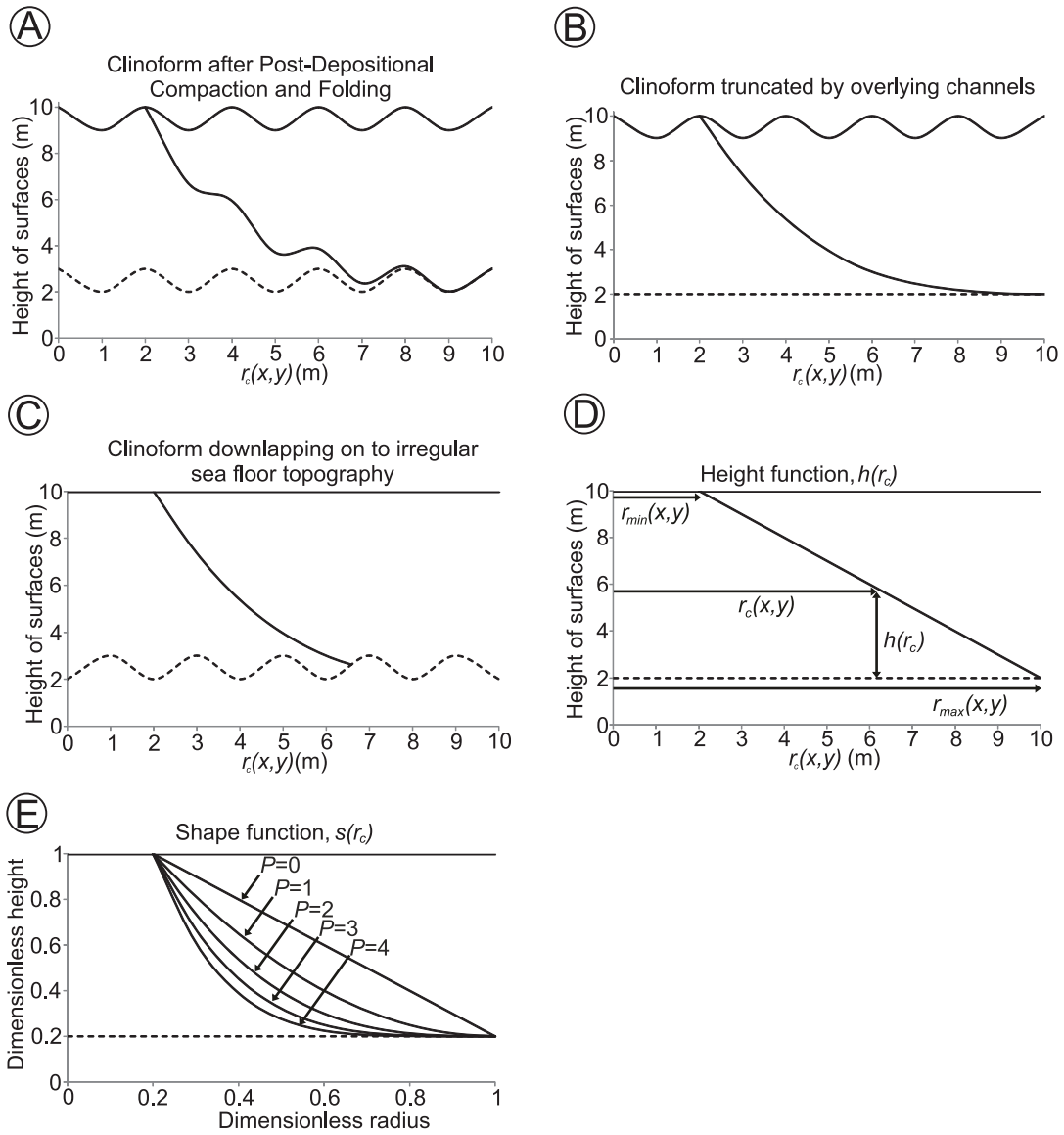


Figure 2.2. Examples of clinoforms produced by the clinoform-modeling algorithm conditioned to different bounding surfaces and clinoform geometries. (A) Bounding surfaces represent post-depositional folding of the original (depositional) geometries of the clinoform surface and the top and base bounding surfaces. (B) Bounding surfaces represent a clinoform within a volume truncated at its top, for example by a channel (Fig. 2.1). (C) Bounding surfaces represent a clinoform downlapping on to irregular sea-floor topography. (D) Height function (Eq. 2.1). (E) Shape function (Eq. 2.7) demonstrating that increasing the exponent, P (Table 2.1), increases the dip angle of clinoforms.

Table 2.1. Nomenclature for parameters used in the clinoform-modelling algorithm.

Parameter	Description	Units	Stochastic Modelling Component
b_L	length of base ellipse in depositional dip direction	M	✓
b_W	length of base ellipse in depositional strike direction	M	✓
$c(r_c)$	clinoform shape function	M	N/A
$h(r_c)$	height function, to give height of clinoform at $r_c(x,y)$	M	N/A
$h_{max}(r_c)$	maximum height of top bounding surface at $r_c(x,y)$	M	N/A
$h_{min}(r_c)$	minimum height of top bounding surface at $r_c(x,y)$	M	N/A
L	clinoform length	M	✓
P	shape function exponent	None	✓
p_O	axis of progradation relative to bounding surfaces	None	✓
$r_c(x,y)$	radius from clinoform origin to point on surface	M	N/A
$r_{max}(x,y)$	maximum radius of base ellipse	M	N/A
$r_{min}(x,y)$	minimum radius of base ellipse	M	N/A
S	clinoform spacing	M	✓
$s(r_c)$	Shape function (power law for concave-upwards geometry)	None	N/A
θ	clinoform progradation angle relative to north	°	✓
t_L	length of top ellipse in depositional dip direction	M	✓
t_W	length of top ellipse in depositional strike direction	M	✓
x	x-coordinate on surface	None	N/A
x_{origin}	x-coordinate of clinoform origin on surface	None	N/A
y	y-coordinate on surface	None	N/A
y_{origin}	y-coordinate of clinoform origin on surface	None	N/A

The parasequence-bounding flooding surfaces are first read into the clinoform-modelling algorithm, using a standard gridded format exported from a reservoir modelling software package. Clinoforms created by the algorithm adapt to the morphology of either, or both, bounding surfaces, using a height function, $h(r_c)$ (Fig. 2.2D, Table 2.1), that calculates the height of the clinoform surface relative to the length along the clinoform surface and the height difference between the top and base bounding surfaces (see Table 2.1 for nomenclature):

$$h\,(r_c) = (h_{max}(r_c) - h_{min}(r_c)) - \left[\frac{(r_c(x,y) - r_{min}(x,y))}{(r_{max}(x,y) - r_{min}(x,y))}(h_{max}(r_c) - h_{min}(r_c))\right]. \qquad (2.1)$$

This allows the clinoforms to adapt to the morphology of the bounding surfaces (Fig. 2.2A). For cases where an overlying erosional bounding surface is interpreted to truncate clinoforms (Fig. 2.2B) and/or clinoforms are interpreted to downlap on to a bounding surface that reflects irregular sea-floor topography (Fig. 2.2C), a planar and horizontal dummy surface is used either above the erosional bounding surface or below the bounding surface reflecting irregular sea-floor topography. The height function, $h(r_c)$ (Eq. 2.1), is applied to the planar dummy surfaces to insert clinoforms and, in a final step, the bounding surface geometries are used to remove the upper and/or lower portions of the clinoform surfaces, where appropriate, to match interpreted truncation (Fig. 2.2B) and/or downlap (Fig. 2.2C).

2.3.2 (2) Plan-view clinoform geometry

The depositional processes acting at the shoreline control the plan-view shape and the abundance of clinoform surfaces and their associated heterogeneity (Howell et al., 2008b). We use maps, satellite images and aerial photographs of modern systems to

make a first-order approximation of the plan-view shape of clinoforms in different depositional environments (Fig. 2.3), as there is a paucity of reliable data of this type from subsurface reservoirs and ancient analogues. This approximation assumes that the

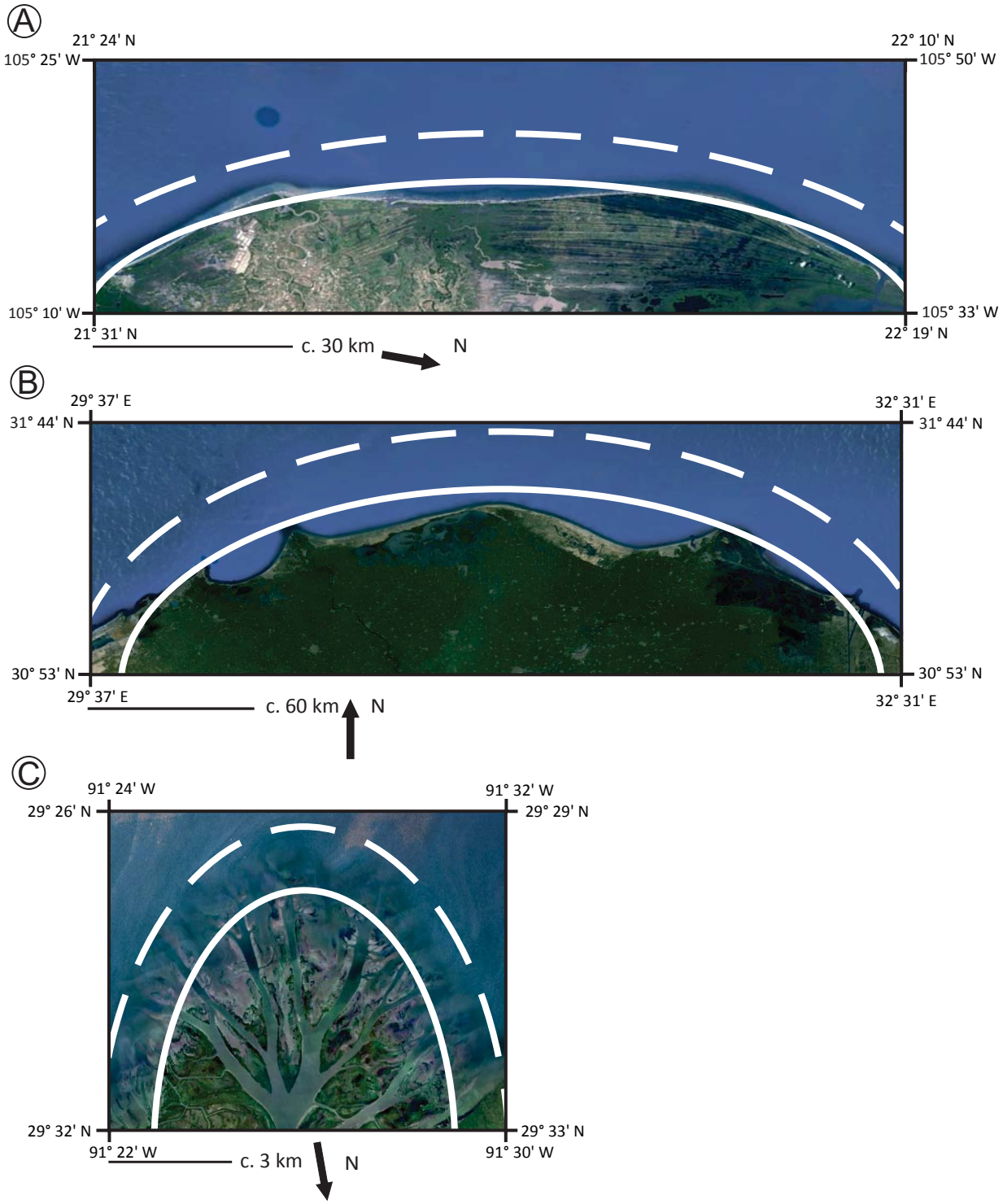


Figure 2.3. Generalized, first-order approximations of the plan-view geometry of clinoforms in different depositional environments: (A) Nayarit Coast, Mexico, representative of a wave-dominated strandplain; (B) Nile Delta, Egypt, representative of a wave-dominated delta; and (C) Wax Lake Delta, Louisiana, USA, representative of a fluvial-dominated delta. (Images modified after Google Earth, 2013).

modern-day shape of a shoreline represents a 'snap-shot' in time that mimics the geometry of clinoform surfaces and associated depositional elements preserved in the stratigraphic record (Howell et al., 2008b). Mattson and Chan (2004) assumed a simple radial geometry in plan-view for fluvial-dominated deltaic clinoforms in the Ferron Sandstone Member outcrop analogue, but this geometry is not universally applicable even as a first-order approximation. For example, wave-dominated strandplains are nearly linear in plan-view (Fig. 2.3A), wave-dominated deltas have broad arcuate forms (Fig. 2.3B), and fluvial-dominated deltaic shorelines form discrete, lobate protuberances (Fig. 2.3C) (e.g. Galloway, 1975).

As the algorithm is generic, the user can specify the shape of an ellipse that approximates the plan-view geometry of clinoforms (Fig. 2.4A). Using an ellipse, rather than a radial geometry, allows the user to specify a wide range of plan-view clinoform geometries using a simple function, depending on the interpreted environment of deposition and scale of shoreline curvature. Two ellipses are used: the top ellipse represents the shoreline at the clinoform top, and the base ellipse represents the maximum extent of the clinoform surface at its downlap termination on the underlying sea floor. The user defines the length of the top and base ellipses in depositional dip and strike directions (t_W, t_L, b_W, b_L; Fig. 2.4B, Table 2.1), relative to the origin of the clinoform. The difference between the user-defined maximum extents of the top and base ellipses yields the clinoform length. If clinoform length, L (Fig. 2.4D), is known, the maximum extent of the top and base ellipses can be obtained:

$$b_W = t_W + L\,, \tag{2.2}$$

$$b_L = t_L + L\,, \tag{2.3}$$

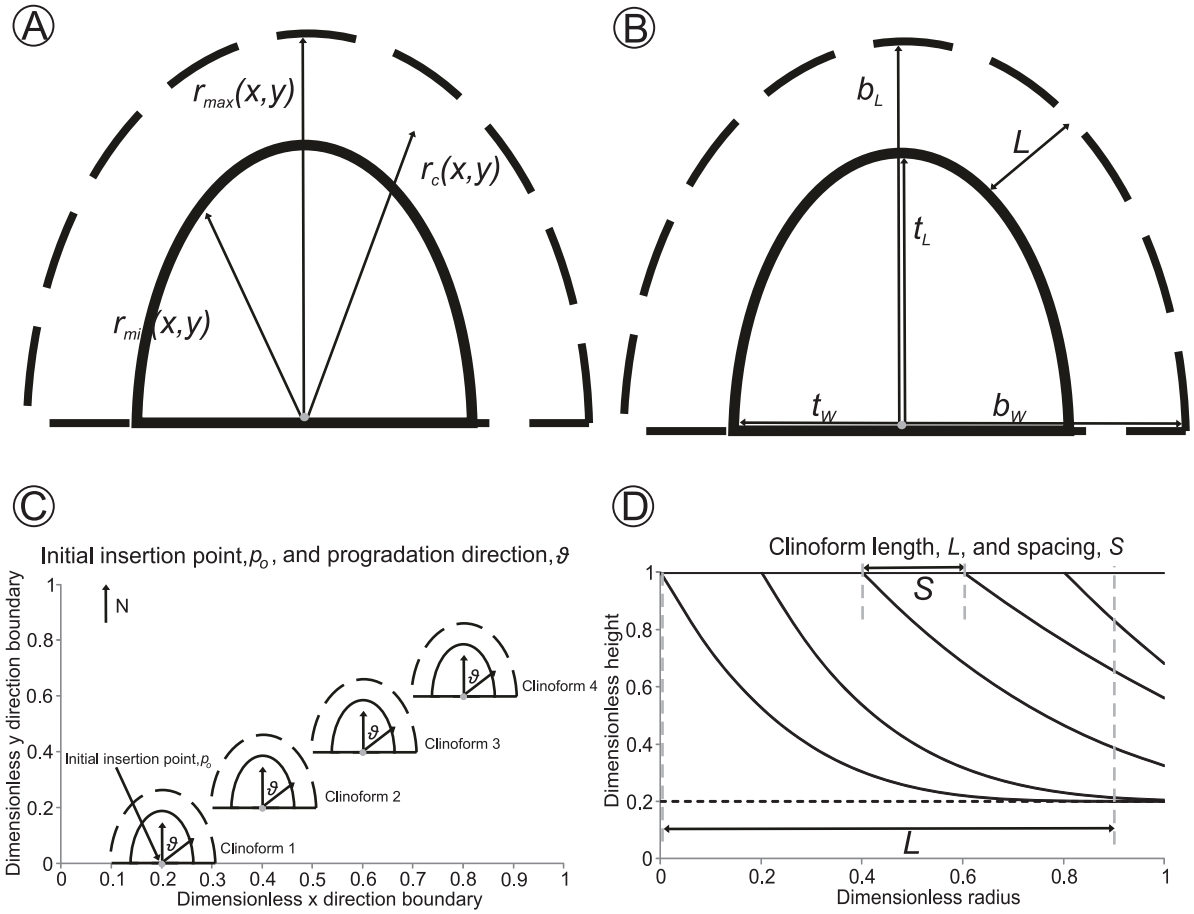


Figure 2.4. (A) A user specifies the widths and lengths of the top ellipse (solid line) and base ellipse (dashed line) relative to the clinoform origin. The clinoform surface is created in the volume between the top (solid line) and base (dashed line) ellipses. (B) At a point on the clinoform surface, we calculate the radius relative to the clinoform origin (black arrow, $r_c(x,y)$), the radius of the base ellipse (black arrow, $r_{max}(x,y)$) and the radius of the top ellipse (black arrow, $r_{min}(x,y)$). (C) Plan view of four adjacent clinoforms. The user specifies the overall progradation direction of the clinoform surfaces relative to north as well as the coordinates of the initial insertion point, p_O. (D) Conceptual depositional-dip-oriented cross-section view of clinoform surfaces. Clinoform spacing, S, is defined as the distance between the top truncation points of two adjacent clinoform surfaces. Clinoform length, L, is defined as the distance between the top and base truncations by the user-specified bounding surfaces along a single clinoform surface.

The clinoform surface is generated in the volume between the top and base ellipses (Fig. 2.4A, B). In this volume, the radius of each point on the clinoform surface, $r_c(x,y)$, is calculated relative to the clinoform origin, (x_{origin}, y_{origin}), using:

$$r_c(x,y) = \sqrt{\left(x_{origin} - x\right)^2 + \left(y_{origin} - y\right)^2}\,. \tag{2.4}$$

At each point on the clinoform surface we also calculate the maximum radius of the top ellipse relative to the clinoform origin:

$$r_{min}(x,y) = \frac{(t_W t_L)}{\sqrt{\frac{\left(t_W{}^2\left(x_{origin}-x\right)^2\right)+\left(t_L{}^2\left(y_{origin}-y\right)^2\right)}{\left(x_{origin}-x\right)^2+\left(y_{origin}-y\right)^2}}}, \quad (2.5)$$

and the maximum radius of the base ellipse:

$$r_{max}(x,y) = \frac{(b_W b_L)}{\sqrt{\frac{\left(b_W{}^2\left(x_{origin}-x\right)^2\right)+\left(b_L{}^2\left(y_{origin}-y\right)^2\right)}{\left(x_{origin}-x\right)^2+\left(y_{origin}-y\right)^2}}}. \quad (2.6)$$

To specify highly lobate plan-view clinoform geometry, characteristic of a fluvial-dominated delta (Fig. 2.3C), the user specifies a larger value for the axis of the ellipse in the depositional dip direction than for the axis of the ellipse in the strike direction. For a highly elongate or near-linear plan-view clinoform geometry, characteristic of a wave-dominated shoreline (Fig. 2.3A, B), the user specifies a much larger value for axis of the ellipse in the depositional strike direction than for the axis of the ellipse in the dip direction. Data describing ellipse extent in depositional dip and strike directions can be extracted from published data on the dimensions of ancient shorelines, or analysis of their modern counterparts (e.g. Tables 1 and 2 in Howell et al., 2008b).

2.3.3 (3) Cross-sectional clinoform geometry

The shape and dip angle of a deltaic or shoreface clinoform surface in cross section is a function of mean grain size and the depositional process regime at the shoreline. In sandy, fluvial-dominated deltas, clinoforms have simple concave-upward geometries and steep dip angles (up to 15°) (Gani and Bhattacharya, 2005) (e.g. Fig. 2.1). Similar geometries have been documented in sandy, tide-influenced deltas (dip angles up

to 5-15°) (Willis et al., 1999). Concave-upward clinoform geometry is also typical of sandy, wave-dominated deltas and strandplains, although the clinoforms have smaller dip angles (typically up to 1-2°) (Hampson and Storms, 2003; Gani and Bhattacharya, 2005). Clinoforms are consistently inclined palaeoseaward down depositional dip and, along depositional strike, exhibit bidirectional, concave-upward dips if the delta front was lobate in plan-view (e.g. Willis et al., 1999; Kolla et al., 2000), or appear horizontal if the shoreline was approximately linear (e.g. Hampson, 2000). Clinoforms are usually truncated at their tops by a variety of channelized erosion surfaces formed during shoreline advance (e.g. distributary channels, incised valleys) and by channelized and/or planar transgressive erosion surfaces (tide and wave ravinement surfaces sensu Swift, 1968) associated with the overlying flooding surface. Consequently, most sandy shoreline clinoforms lack a decrease in depositional dip ("rollover") near their tops, although this geometry is ubiquitous in larger, shelf-slope margin clinoforms (e.g. Steckler et al., 1999) and in the outer, muddy portion of "compound" deltaic clinoforms with a broad subaqueous topset that lies seaward of the shoreline (e.g. Pirmez et al., 1998).

Here, we use a geometrical approach to represent the depositional dip cross-section shape of a clinoform surface with a dimensionless shape function, $s(r_c)$ (Fig. 2.2E), such as a power law for concave-upward, sandy, shoreline clinoforms:

$$s(r_c) = \left(\frac{\left(r_{max}(x,y) - r_c(x,y)\right)^P}{\left(r_{max}(x,y) - r_{min}(x,y)\right)^P} \right). \quad (2.7)$$

However, as the algorithm is generic, the mathematical expression of the dimensionless shape function is interchangeable so that other clinoform geometries could be represented; for example, a sigmoid function could be used to represent clinoforms in a

larger, shelf-slope margin settings (e.g. Steckler et al., 1999). By combining the height function (Eq. 2.1), with the shape function (Eq. 2.7), the clinoform shape function, $c(r_c)$, is used to construct the shape of a clinoform surface:

$$c(r_c) = h_{min}(r_c) + \left(\frac{(r_{max}(x,y) - r_c(x,y))^P}{(r_{max}(x,y) - r_{min}(x,y))^P} h\,(r_c) \right). \quad (2.8)$$

By varying the exponent in the clinoform shape function, P, the user can increase or decrease the dip angle and change the shape of the clinoform surface (Fig. 2.2E). However, a similar geometry is shared by clinoform surfaces within a parasequence, because they are inferred to have formed under the influence of similar hydrodynamic and sedimentological processes. Hence, we can apply the same value of exponent in the clinoform shape function, P (Eq. 2.8), to each clinoform modelled within a parasequence.

2.3.4 (4) Spacing and progradation direction of clinoform surfaces

The clinoform-modelling algorithm allows the user to specify the main progradation direction of the clinoform surfaces, and also define the intervals along the progradation path at which clinoform surfaces are generated (i.e. the clinoform spacing). The user specifies a progradation direction relative to north, θ (Fig. 2.4C, Table 2.1), along which successive clinoform surfaces are generated, which corresponds to the progradation path of the shoreline during clinoform deposition (plan-view shoreline trajectory of Helland-Hansen and Hampson, 2009). The user also specifies the initial insertion point for the clinoforms, p_o (Fig. 2.4C). This provides flexibility in where to place the initial clinoform surface relative to the proximal model boundary. The spacing between each clinoform surface, S (Table 2.1), is also designated by the user. Clinoform

spacing is defined as the distance between the top-truncation points of two successive clinoform surfaces, and determines the origin position, (x_{origin}, y_{origin}), of successive clinoforms (Fig. 2.4D).

2.3.5 Stochastic modelling of clinoforms

Each of the input parameters described for the clinoform modelling algorithm can be applied deterministically, however, many of the parameters can be also be applied stochastically (Table 2.1). If a reservoir model is created using an outcrop dataset, it may be appropriate for the user to specify the parameter values for each clinoform surface. If a subsurface reservoir model is being created in which the parameter values are uncertain, the user can constrain a continuous probability distribution, such as a normal distribution, to assign values to each parameter. Since most intrinsic pseudo-random number generators only produce sequences that are uniformly distributed, additional sampling methods are required in order to obtain random variables with non-uniform continuous probability distributions. In this study a Box-Muller transform (Box and Muller, 1958) is applied to map the random variables from the uniform distribution to a normal distribution (Appendix A2). The user specifies the mean, standard deviation and maximum and minimum values for the normal distribution from which values are drawn to assign values to the parameters in the clinoform-modelling algorithm.

As many of the input parameters can be defined stochastically, one of the consequences of this aspect of the clinoform-modelling algorithm is that it is possible to generate more complex geometries, such as in cases where clinoforms are observed to onlap against older clinoform surfaces in the same parasequence. A combination of three factors is postulated to cause subtle changes in clinoform geometry and position,

which combine to produce onlap in depositional-dip-oriented cross sections: (1) in fluvial-dominated deltas, distributary mouth bars have complex 3D geometries that can shift along depositional strike as well as down depositional dip (e.g. Olariu et al., 2005); (2) riverine sediment supply to delta-front clinoforms exhibits temporal and spatial variability that is related, at least in part, to downstream branching and switching of distributary channels as deltas advance (e.g. Wellner et al., 2005); and (3) clinoform geometries are locally modified by basinal processes such as waves and tides (e.g. Gani and Bhattacharya, 2007) .

To produce onlap and other subtle geometric features between successive clinoforms, the user can use the stochastic component of the clinoform modelling algorithm to generate small variations in the parameter values of either or all of; progradation direction, θ (Table 2.1), clinoform spacing, S (Table 2.1), and clinoform length, L (Table 2.1) (Appendix A2). If the parameters that define a clinoform surface cause it to be present below an earlier surface, it is truncated by the earlier surface to produce onlap. We now describe how the algorithm can be applied to a rich, outcrop dataset or a sparse, subsurface dataset.

2.4 Example 1: Ferron Sandstone reservoir analogue

2.4.1 Geological setting

Construction and fluid-flow simulation of models based on outcrop analogues is an established method for investigating geological controls on subsurface reservoir performance (e.g. Ciammetti et al., 1995; White and Barton, 1999; White et al., 2004; Jackson et al., 2009; Sech et al., 2009; Enge and Howell, 2010). Here, we use the

clinoform-modelling algorithm to build a reservoir model from a high-resolution outcrop dataset from the Ferron Sandstone Member, Utah, USA, at a scale that is comparable to the interwell spacing (750 x 3000 m aerially) in a typical hydrocarbon reservoir, and captures several tens of clinoforms and their associated heterogeneities. The aim is to verify that the clinoform-modelling algorithm can produce realistic stratigraphic architectures that mimic rich outcrop datasets when conditioned to sparse input data that are typical in the subsurface. The scale of the model fills the gap between detailed, but sparse, 2D core and well-log data, and low-resolution, but extensive, 3D seismic data.

The Ferron Sandstone Member of the Mancos Shale is located in east-central Utah. The unit was deposited during the late Cretaceous (Turonian-Coniacian) on the western margin of the Western Interior Seaway and, in the study area, records the progradation of the 'Last Chance' delta system from southwest (palaeolandward) to northeast (palaeoseaward) (Cotter, 1976) (Fig. 2.5A). These deltaic deposits form a basinward-thinning wedge that passes eastward into the offshore deposits of the Mancos Shale. The wedge contains either seven (Ryer, 1991; Gardner, 1993; Barton et al., 2004) or eight sandstone tongues (Anderson and Ryer, 2004; Garrison Jr. and Van den Bergh, 2004), where one tongue is equivalent to a parasequence set of Deveugle et al. (2011) (Fig. 2.5B). We focus on a single delta-lobe deposit within the lowermost sandstone tongue (bedset Kf-1-Iv[a] of Anderson et al., 2004; parasequence 1h of Garrison Jr. and Van den Bergh, 2004; parasequence 1.6 of Deveugle et al., 2011) (Fig. 2.5C, D). The delta-lobe deposit is fluvial-dominated with low-to-moderate wave influence (Gardner, 1993; Garrison Jr. and Van den Bergh, 2004; Ryer and Anderson, 2004), and contains numerous, well-documented clinoform surfaces in the exposures of the Ivie Creek amphitheatre (Anderson et al., 2002, 2003, 2004; Forster et al., 2004; Enge and Howell, 2010)

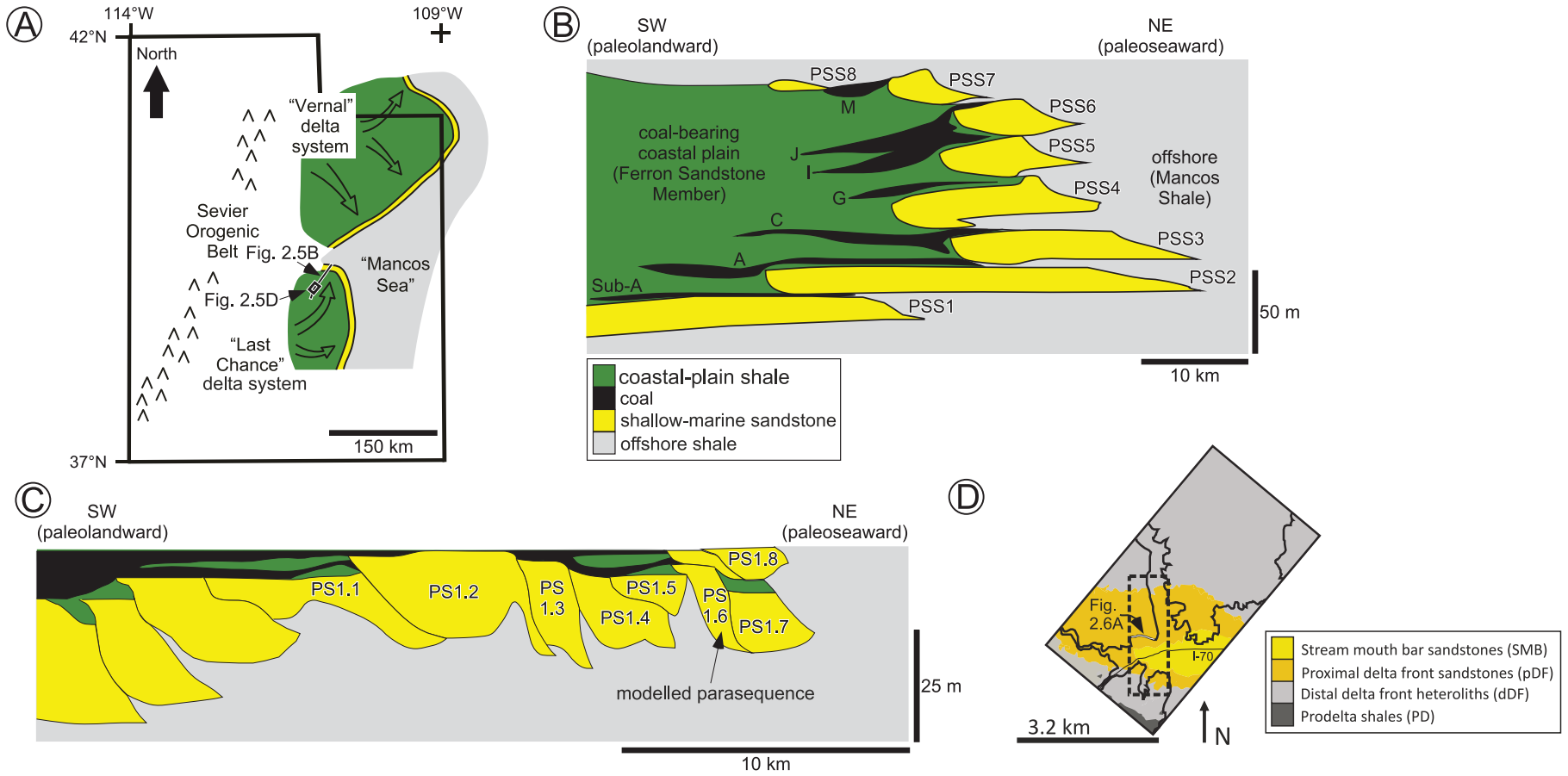


Figure 2.5. (A) Paleogeographic reconstruction of the late Cretaceous "Last Chance" and "Vernal" delta systems of the Ferron Sandstone Member of the Mancos Shale in present-day Utah (after Cotter, 1976). The location of Deveugle et al.'s (2011) model (Fig. 2.5D) and a regional cross section (Fig. 2.5B) are highlighted. (B) Schematic regional cross section through the "Last Chance" delta system of the Ferron Sandstone Member and its eight component shallow-marine tongues (numbered PSS1 to PSS8, using the nomenclature of Deveugle et al., 2011), from southwest (paleolandward) to northeast (paleoseaward) (after Anderson and Ryer, 2004). (C) Detailed cross section through the lowermost shallow-marine tongues (PSS1 in Fig. 2.5B) and associated coastal-plain strata (after Garrison Jr. and van den Bergh, 2004). The tongue is subdivided into constituent parasequences (after Deveugle et al., 2011). Parasequence 1.6 is modelled in this study. (D) Map showing distribution of facies-association belts at the top of PS 1.6, in Deveugle et al.'s (2011) model area. The area of the model constructed in this study (Figs. 2.7-2.10) lies within the dashed lines.

(Fig. 2.5D). Deveugle et al. (2011) used a high-resolution outcrop dataset to build a reservoir-scale (7200 x 3800 x 50 m), surface-based model of the lower two tongues (parasequence sets) of the Ferron Sandstone Member. Clinoform surfaces were not represented in the delta-lobe deposits (cf. parasequences) of the Deveugle et al. (2011) model, and we use their surface-based model as the context in which to apply the clinoform-modelling algorithm.

2.4.2 Model construction

We extract the top and base flooding surfaces of parasequence 1.6 from the model of Deveugle et al., (2011), and these serve as the bounding surfaces used in the clinoform algorithm (Fig. 2.2). The surfaces are cropped to cover a model area of 750 x 3000 m in the Ivie Creek amphitheatre (Fig. 2.5D). We also extract and crop additional surfaces representing the boundaries between facies associations from the model of Deveugle et al. (2011), and these define the distribution of facies associations present in each rock volume bounded by two clinoform surfaces (i.e. clinothem) (cf. Table 1 in Deveugle et al., 2011). From distal to proximal, the modelled facies associations are prodelta mudstone (PD), distal delta front heteroliths (dDF), proximal delta front sandstones (pDF), and stream mouth bar sandstones (SMB) (Fig. 2.5D). Where facies associations pinch out, the facies association boundary surfaces are adjusted to coincide throughout the remainder of the model volume with either the top or base parasequence bounding surface. This ensures that the surface is defined across the entire model volume and is suitable for gridding (Jackson et al., 2009). There are no faults within the model volume of 750 x 3000 x 6 m. In a final step, we construct an isochore map between the top and the base flooding surfaces and isochore maps

between facies association boundary surfaces and the base flooding surface. From these maps we flatten the base bounding surface, to mimic clinoform progradation over a flat, horizontal sea floor. We then use the isochore maps to modify the geometries of the top bounding surface and facies association boundary surfaces above the flat, horizontal base bounding surface. In contrast to the Troll West reservoir sector model described later, we have modified the bounding surfaces from the existing model of Deveugle et al. (2011), as the present day structure of the Ferron Sandstone is not a realistic representation of a subsurface reservoir.

The parameters used to insert clinoforms into the model volume are summarized in Table 2.2. The delta lobe in parasequence 1.6 is approximately 8.1 km wide and 12.2 km long, giving a plan-view aspect ratio of 0.7 (Deveugle et al., 2011), similar to the value of 0.9 for the Wax Lake Delta (after data in Wellner et al., 2005) (Fig. 2.3C).

Table 2.2. Clinoform modelling parameters used in the clinoform-bearing model of the Ferron Sandstone Member reservoir analogue.

Parameter	Description	Min.-Max. Values	Units
t_L	length of top ellipse in depositional dip direction	6100	M
t_W	length of top ellipse in depositional strike direction	4050	M
L	clinoform length	60-495	M
b_L	length of base ellipse in depositional dip direction (=$t_L + L$)	6160-6595	M
b_W	length of base ellipse in depositional strike direction (=$t_W + L$)	4110-4545	M
P	shape function exponent	2	None
p_O	axis of progradation relative to bounding surfaces	32%	None
θ	clinoform progradation angle relative to north	274	°
S	clinoform spacing	25	M

We infer that the values of these dimensions were smaller during the growth of the delta lobe and, arbitrarily, assume that the lobe initiated with dimensions (t_L, t_W) that were a third of those of the final preserved delta lobe. The length, L, and spacing, S, of clinoforms in depositional dip cross-section were extracted from the bedding-diagram interpretations of Forster et al. (2004) (Fig. 2.6A), clinoform length and dip statistics of

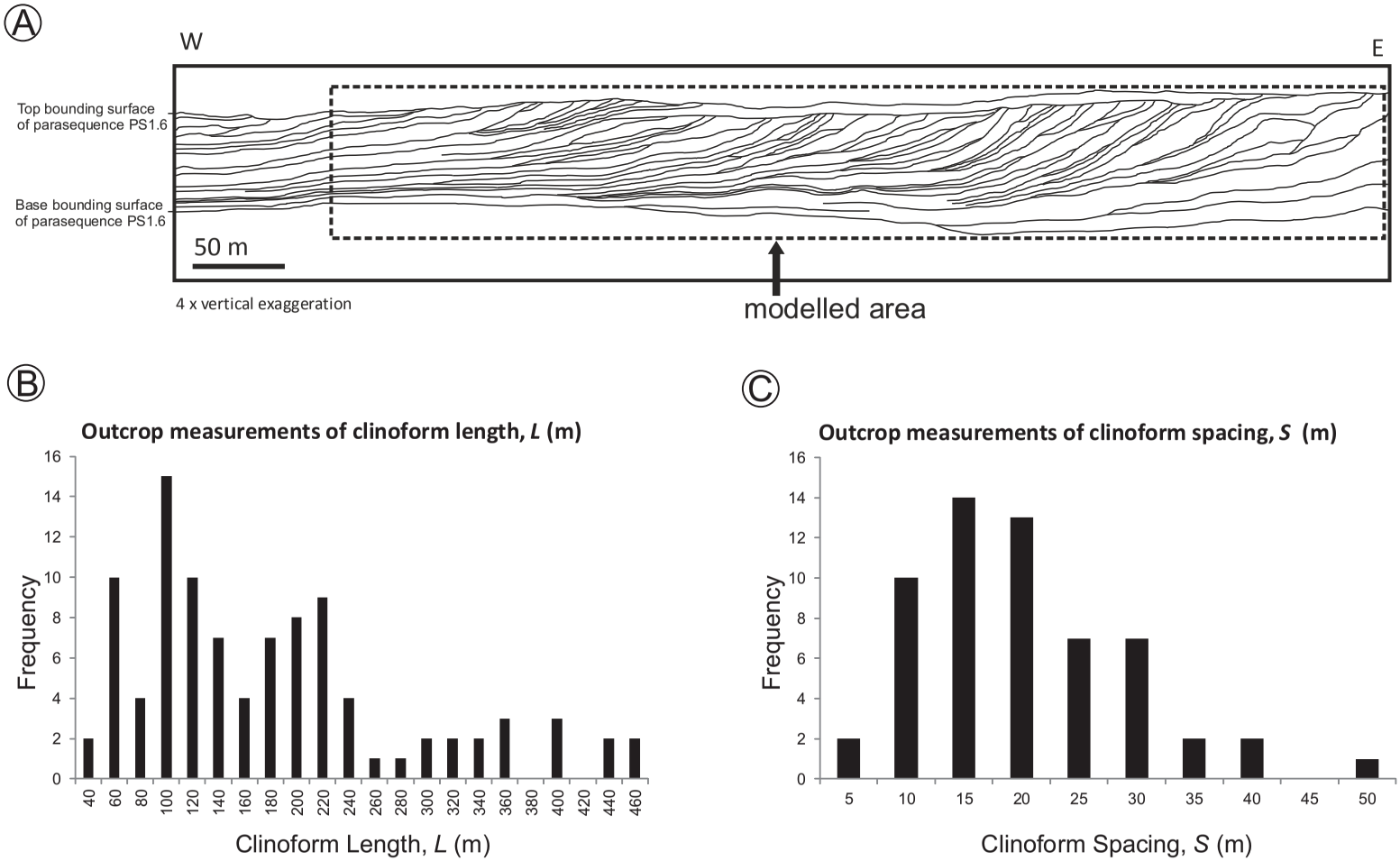


Figure 2.6. (A) Interpreted line drawing of clinoforms at the Junction Point section of Ivie Creek Amphitheatre (Fig. 2.5D) (modified after Forster et al., 2004). Data from 104 clinoforms were collected to condition the clinoform-modeling algorithm. Frequency distributions of values measured from outcrop data for (B) clinoform length (Fig. 2.4D), and (C) clinoform spacing (Fig. 2.4D) which are used as input parameters in the clinoform-modeling algorithm.

Enge et al. (2010), and the LIDAR data used to create the model of Enge and Howell (2010). A database of clinoform lengths, dips and spacings was compiled from these data sources, yielding frequency distributions from which the geometry or spatial arrangement of clinoform surfaces, or a trend in these parameters, can be extracted (Fig. 2.6B-C). We use the clinoform-modelling algorithm to build 31 clinoform surfaces in the modelled volume of parasequence 1.6 (Fig. 2.7). For simplicity, clinoform spacing is fixed at 25m, which is the average value observed at outcrop (Fig. 2.6C). A constant value of 2 was assigned to the clinoform shape function exponent, P (Fig. 2.2E), to ensure that the clinoform dip angle is always in the range extracted from the data of Enge et al. (2010). The initial clinoform insertion point, p_o (Fig. 2.4C), was qualitatively matched with a plan view map of facies association belts at the top of parasequence 1.6 (Fig. 2.5D, taken from Deveugle et al., 2011) and the overall progradation direction for the clinoforms, θ, was assigned an azimuth of 274° relative to North, which corresponds to the interpreted progradation direction of the delta lobe in parasequence PS1.6 (Deveugle at al., 2011). In a subsequent step, we use the facies association boundary surfaces extracted from the model of Deveugle et al. (2011) to create facies association zones within each clinothem. Application of the clinoform-modelling algorithm yields a surface-based model measuring 750 × 3000 × 6 m, which contains 95 surfaces: the top- and base- parasequence bounding surfaces, 31 clinoform surfaces, and 62 facies-association boundary surfaces (Fig. 2.8). We use a cornerpoint gridding scheme in which variations in facies architecture are represented by variations in grid architecture (White and Barton, 1999; Jackson et al., 2005; Sech et al., 2009). The grid has vertical pillars with a constant spacing of 20 m in x- and y-(horizontal) directions. Grid layering in the z- (vertical) direction within each facies-association zone conforms to the underlying clinoform surface, so that layers are parallel

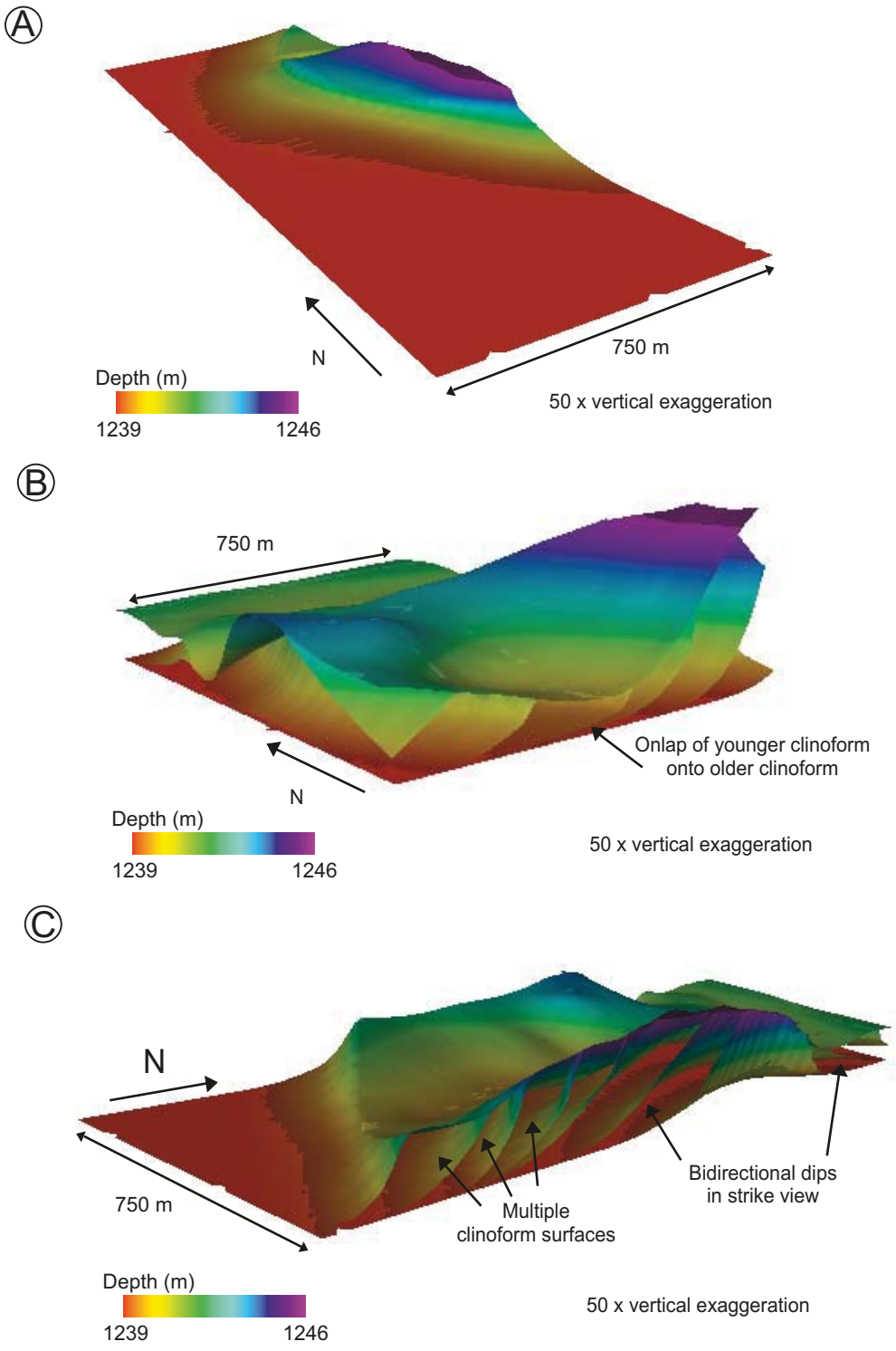


Figure 2.7. Surfaces generated by the clinoform-modeling algorithm for the model of part of parasequence PS1.6 of the Ferron Sandstone Member (Fig. 2.5C, D). (A) Single 3D clinoform surface generated by the clinoform modelling algorithm. (B) 3D dip cross section showing the concave upward geometry of the clinoform surfaces, and (C) 3D strike section of the model showing surfaces that exhibit bidirectional dips. Not all surfaces used in the model of part of Ferron Sandstone Member (Fig. 2.8) are shown.

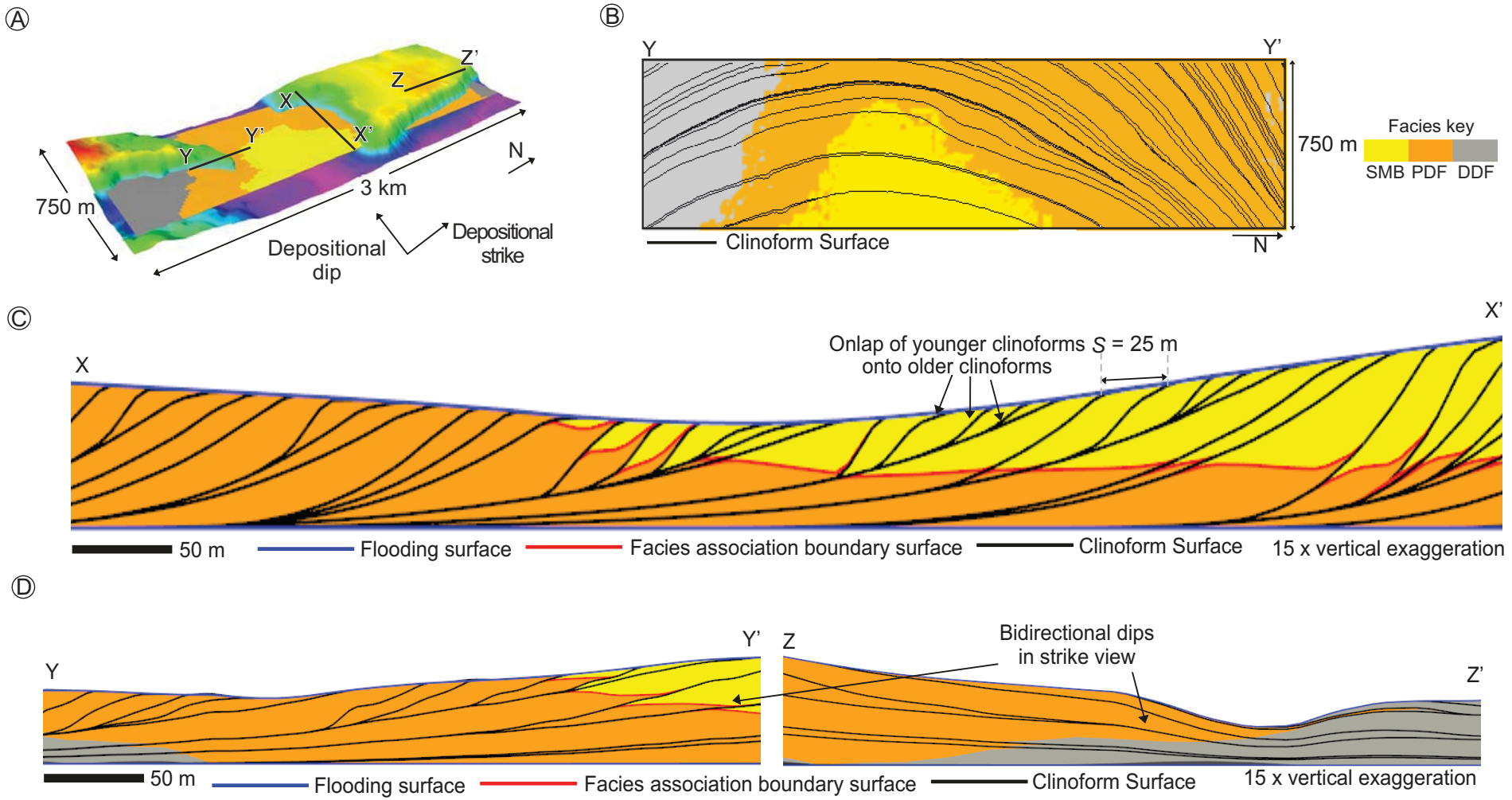


Figure 2.8. Surface-based model of part of parasequence PS1.6 of the Ferron Sandstone Member (Fig. 2.5C, D), a fluvial-dominated delta lobe. (A) 3D view of the model superimposed on a digital elevation map of the study area, with no vertical exaggeration and orientations of regional depositional dip and strike shown. (B) Plan-view section of model showing curved clinoform surfaces, consistent with the geometry of fluvial-dominated delta lobes. (C) 2D dip section and (D) 2D strike section through the model, showing details of the complex internal architecture. Red lines indicate facies boundaries and blue lines parasequence-bounding flooding surfaces. Black lines represent clinoform surfaces.

to the basal clinoform. Grid layers have a constant thickness of 0.2m; however each facies- association zone is gridded separately and the grid layers pinch out against facies-association boundaries and parasequence-bounding flooding surfaces. This gridding approach was used by Sech et al. (2009), and ensures that the grid layering conforms to the architecture of the clinoform surfaces, preserving their dip and geometry, but also captures facies association boundaries (Fig. 2.9). Where a grid layer pinches out, the grid

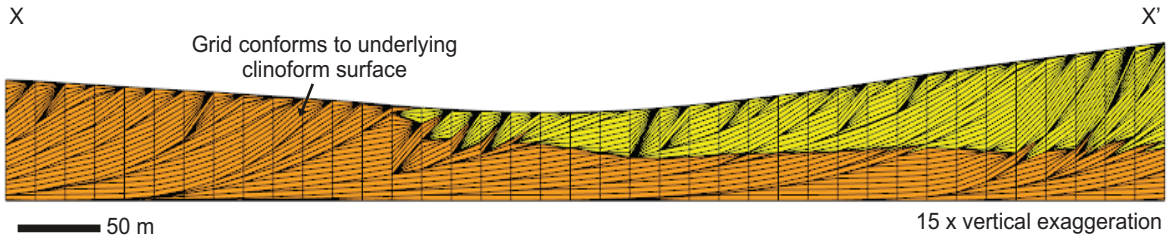


Figure 2.9. View of Figure 2.8C showing grid layering that conforms to the architecture of the clinoform surfaces, facies association boundaries and parasequence-bounding flooding surfaces.

cells have zero thickness and are set to be inactive in flow simulations. These zero-thickness cells are bridged using non- neighbour connections so that they do not act as barriers to flow. The chosen cell size of 20 × 20 × 0.2 m yields a total of approximately 5 million cells, of which 140,000 (2.6%) are active. Since the number of active grid cells is small, we can perform fluid-flow simulations on the grid without upscaling. The cornerpoint gridding approach described above does not introduce any numerical artefacts during flow simulation in comparison with traditional gridding approaches that conform only to parasequence-bounding flooding surfaces, provided that it is carefully implemented (e.g. White et al., 2004; Jackson et al., 2005; Sech et al., 2009; Janczak, 2011; Faure-Llorens, 2012). In the final step before fluid flow simulation, we populate the grid cells with petrophysical properties from a mature subsurface reservoir analogue (Table 1 of Deveugle et al., 2011). Petrophysical properties are assigned to each facies

association, which typically have order-of-magnitude contrasts in permeability between them. In a separate step, transmissibility multipliers are assigned along the base of the grid cells in the layer directly above each clinoform surface, in order to represent mudstone baffles and barriers commonly associated with clinoforms in fluvial-dominated deltaic reservoirs (Howell et al., 2008b) in a geometrically accurate and efficient way. This aspect of modelling is discussed in greater detail in Chapter 3.

2.4.3 Geological model results

We begin by investigating the ability of the clinoform-modelling algorithm to generate realistic stratal geometries from the Ferron Sandstone Member outcrops. Visual inspection of the algorithm-generated model against outcrop photopans (Fig. 2.1) and bedding diagram interpretations (Fig. 2.6A) shows a close correspondence between key geometrical aspects of the observed data and concepts reproduced in the model, as outlined below.

A single delta lobe is present in the model, and extends beyond the model volume (Figs. 2.5D, 2.8A). As a result, clinoform surfaces are larger in their depositional dip and strike extent (t_L and t_W respectively; Table 2.2) than the model area, and they form arcs in plan view in the model (Fig. 2.8B). This plan-view geometry is consistent with the approximately lobate plan-view geometries of clinoforms in fluvial-dominated deltas (Fig. 2.3C). The clinoform-modelling algorithm generates the concave upwards clinoform geometry observed at outcrop (Fig. 2.7B, 2.8C), whilst honouring the topography of the parasequence bounding surfaces. The variation in topographic elevation of the modelled parasequence (Fig. 2.7, 2.8) is attributed to post-depositional compaction. In a depositional strike cross-section of the clinoform-bearing model, the algorithm produces

bidirectional concave-upward dips (Fig. 2.7C, 2.8D) that are consistent with delta-front bodies that are lobate in plan view (e.g. Willis et al., 1999; Kolla et al., 2000). Additionally, the model contains stratal geometries observed at outcrop such as onlap and downlap of younger clinoforms onto older clinoforms (Fig. 2.7B, 2.8C). The clinoform-modelling algorithm also produces clinoforms that are consistently distributed in the same orientation as those in the observed delta-lobe deposits and its interpreted plan-view progradation direction (Figs. 2.5A, 2.8B). Facies proportions in the model are 8% stream mouth bar sandstones (SMB), 50% proximal delta front sandstones (pDF), 31% distal delta front heteroliths (dDF), and 11% prodelta mudstone (PD). Using porosity values that are characteristic of these facies associations in analogous reservoirs (Table 2.3), the volume of oil in place in the model is 7.1 MMBbl. We now use the clinoform-

Table 2.3. Reservoir, fluid and rock properties used in the model of the Ferron Sandstone Member reservoir analogue (after Farrell and Abreu, 2006; Deveugle et al., 2011).

Reservoir properties	Value	Units
Reservoir pressure (P_r)	100	Bar
OWC	1892	M
Top	1239	M
Base	1246	M
Fluid properties		
Oil viscosity (μ_o)	0.7	Cp
Oil density (ρ_o)	650	kg/m^3
Oil compressibility (c_o)	10^{-4}	1/bar
Oil formation volume factor (B_o)	1.00000009	(rm^3/sm^3)
Water viscosity (μ_w)	0.3	Cp
Water density (ρ_w)	950	kg/m^3
Water compressibility (c_w)	10^{-5}	1/bar
Water formation volume factor (B_w)	1	(rm^3/sm^3)
Rock properties		
Porosity ($\emptyset$) of prodelta mudstone (PD) facies association	0	%
Horizontal (k_h) and vertical permeability (k_v) of PD facies association	0 (k_h), 0 (k_v)	mD
Porosity ($\emptyset$) of distal delta front heteroliths (dDF) facies association	18	%
Horizontal (k_h) and vertical permeability (k_v) of dDF facies association	71 (k_h), 7 (k_v)	mD
Porosity ($\emptyset$) of proximal delta front sandstones (pDF) facies association	27	%
Horizontal (k_h) and vertical permeability (k_v) of pDF facies association	433 (k_h), 325 (k_v)	mD
Porosity ($\emptyset$) of stream mouth bar sandstones (SMB) facies association	28	%
Horizontal (k_h) and vertical permeability (k_v) of SMB facies association	1793 (k_h), 1614 (k_v)	mD
Rock compressibility for all facies associations (c_r)	10^{-12}	1/bar

bearing model to investigate the impact of heterogeneities associated with clinoforms on fluid-flow during waterflooding within this fluvial-dominated deltaic parasequence.

2.4.4 Production strategy

Waterflooding is simulated using conventional black oil simulation software, using a line drive of four vertical injector wells and six vertical producer wells (Fig. 2.10A). The producer and injector wells are spaced 750 m apart, with water being injected down local depositional dip, from east to west. Oil production and water injection are set to maintain a target production rate over 20 years of 175 S m^3/day (1100 bbl/day) for the groups of producers and injectors, and a minimum bottom hole pressure constraint of 50 bars (725 psi) for each production well and a maximum bottom hole pressure constraint of 150 bars (2175 psi) for each injection well. Further information on reservoir properties is summarized in Table 2.3. Heterogeneity along clinoforms is specified in terms of the percentage of each clinoform surface that acts as a barrier to flow. The volume of the barriers along clinoform surfaces is negligible, so they have little impact on the volume of oil in place. Two simulation runs are completed in which: (1) clinoforms are not associated with mudstone barriers to flow (0% barrier coverage along clinoforms); and (2) clinoforms are associated with significant mudstone barriers to flow (90% barrier coverage along clinoforms; Fig. 2.10B). All other parameters remain fixed between the simulations. In Chapter 3 we apply the clinoform-modelling algorithm to build a range of models to investigate the impact of a broader range of uncertainties in clinoform parameters, such as clinoform spacing and barrier coverage, on hydrocarbon recovery. The method is further extended to build reservoir-scale models of the Ferron Sandstone,

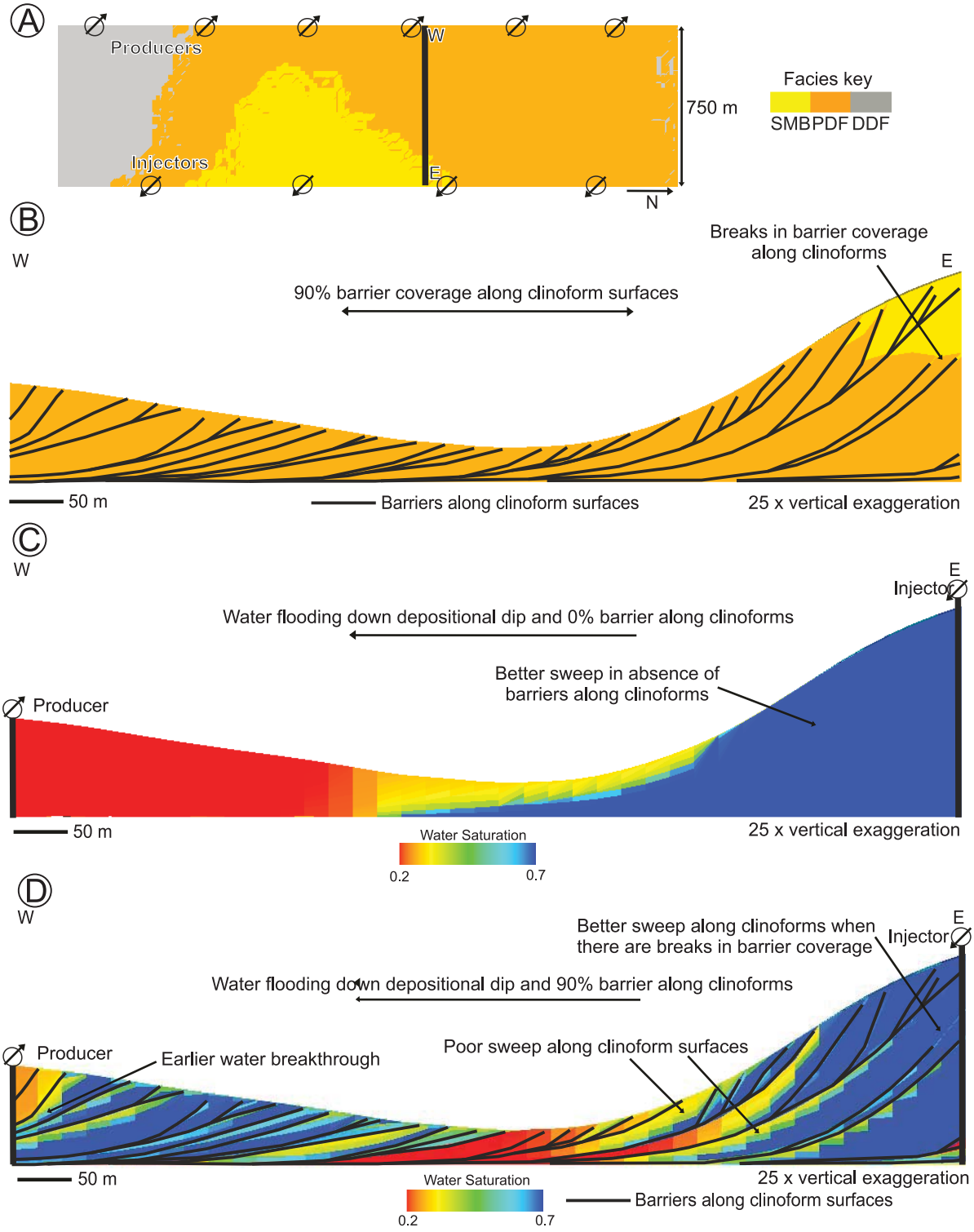


Figure 2.10. (A) Plan view facies association map of the Ferron Sandstone Member extracted from our reservoir model (Fig. 2.5D), showing location of injector and producer wells, and the cross-section illustrated in (B-D). The colour scheme is the same as in Figures 2.5D and 2.8A. (B) Depositional-dip-oriented cross-section showing the internal facies architecture of the modelled parasequence with the location of barriers along the clinoforms shown as black lines. (C, D) The same depositional-dip-oriented cross-section showing water saturation after 5 years of production where water has been injected down depositional dip, from east to west, for models with (C) 0% barrier coverage along clinoforms, and (D) 90% barrier coverage along clinoforms. Note oil is bypassed below clinoform surfaces in (D).

to investigate the impact of clinoforms on fluid flow under uncertain geological and engineering parameters.

2.4.5 Simulation results

When clinoforms are not associated with barriers to flow, they have little impact on production results (Fig. 2.10C); however, if barriers occupy 90% of the clinoform surfaces, then clinoforms can have a significant impact on recovery. We find that models that do not include barriers to flow along clinoform surfaces may overestimate recovery by up to 36% (compare Fig. 2.10C and Fig. 2.10D, Fig. 2.11A). In a similar way, previous simulation studies of the Ferron Sandstone Member by Howell et al. (2008a) and Enge and Howell (2010) found that including clinoforms with impermeable barriers along them lowered hydrocarbon recovery by several tens of percent.

Including clinoforms with mudstone barriers to flow along them in models of the Ferron Sandstone Member also considerably decreases sweep efficiency as each clinothem becomes hydraulically separated from its neighbours. Consequently, significant oil is bypassed in the reservoir, particularly beneath barriers along clinoforms and at the toe of each clinothem (Fig. 2.10D). Increased reservoir compartmentalization also means that the target oil production rate cannot be met and as a result, models that include barriers along clinoforms produce significantly lower volumes of oil per day (Fig. 2.11B). Enge and Howell (2010) also found that including barriers along clinoform surfaces in reservoir models of the Ferron Sandstone Member increased reservoir compartmentalization.

Finally, models that include barriers along clinoform surfaces have earlier water

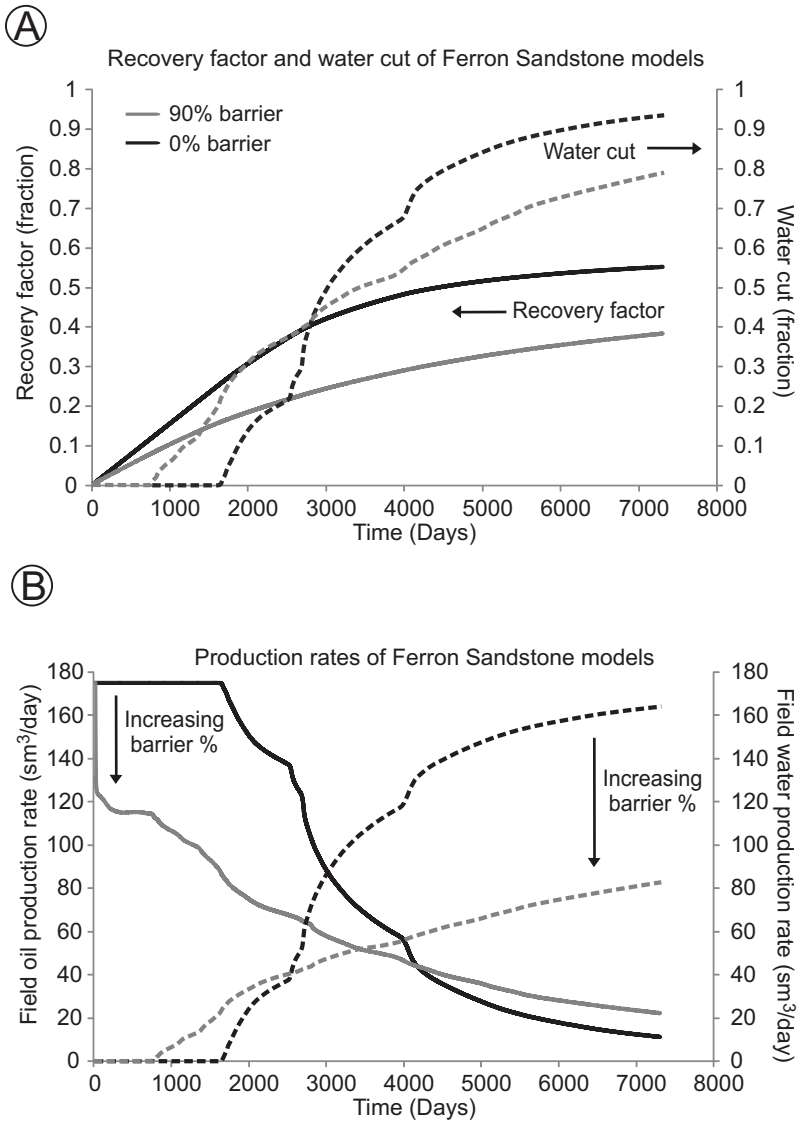


Figure 2.11. (A) Recovery factor (solid lines) and water cut (dashed lines) as function of time in the simulation model of part of parasequence 1.6 of the Ferron Sandstone Member. Curves in black denote results for the model with 0% barrier coverage along clinoforms, and curves in grey denote the model with 90% barrier coverage along clinoforms. Note the significant decrease in recovery factor for the model with 90% barrier coverage along clinoforms. (B) Oil (solid lines) and water (dashed lines) production rate as a function of time. In the models with 90% barrier coverage along clinoforms, the target production rate is not met and water breakthrough occurs earlier than in models where barriers are not present along clinoforms.

breakthrough than models that lack barriers along clinoforms (Fig. 2.11). Including barriers to flow along clinoforms increases the tortuosity of flow pathways as the fluids can only move between clinothems by exploiting the gap in the barriers at the top of each clinoform surface. However, as the number of potential flow pathways is decreased

by including barriers to flow along clinoforms, the injected water exploits the pathways between the injectors and producers faster, which leads to earlier water breakthrough. Similar results were obtained in clinoform-bearing models of a wave-dominated shoreface system (Jackson et al., 2009).

Although barriers to flow along clinoforms are thin (<20 cm), and constitute only a small proportion of the overall model volume, they significantly affect permeability architecture, sweep pattern and simulated oil recovery. Therefore, under certain displacement conditions, it is important to include barriers associated with clinoforms in simulation models of analogous shallow-marine reservoirs. The clinoform-modelling algorithm supports the results of previous studies of the Ferron Sandstone Member and demonstrates a new efficient method to incorporate multiple geometrically realistic clinoform surfaces into simulation models.

2.5 Example 2: Troll west reservoir sector model

2.5.1 Geological setting

We now apply the clinoform-modelling algorithm to construct a model of the Late Jurassic Sognefjord Formation reservoir in a fault-bounded sector of the Troll Field, offshore Norway (Fig. 2.12A, B). The Troll Field is a supergiant gas field which initially hosted about 40% of the total gas reserves on the Norwegian continental shelf, and which still contains ca. 1000 x 109 S m^3 (35 Tcf) of gas (Norwegian Petroleum Directorate, 2013). The western and eastern parts of the Troll Field accumulation occur in different structures, Troll West and Troll East. The Sognefjord Formation is interpreted to record deposition in a mixed fluvial-, tide- and wave- influenced delta system (Dreyer et al.,

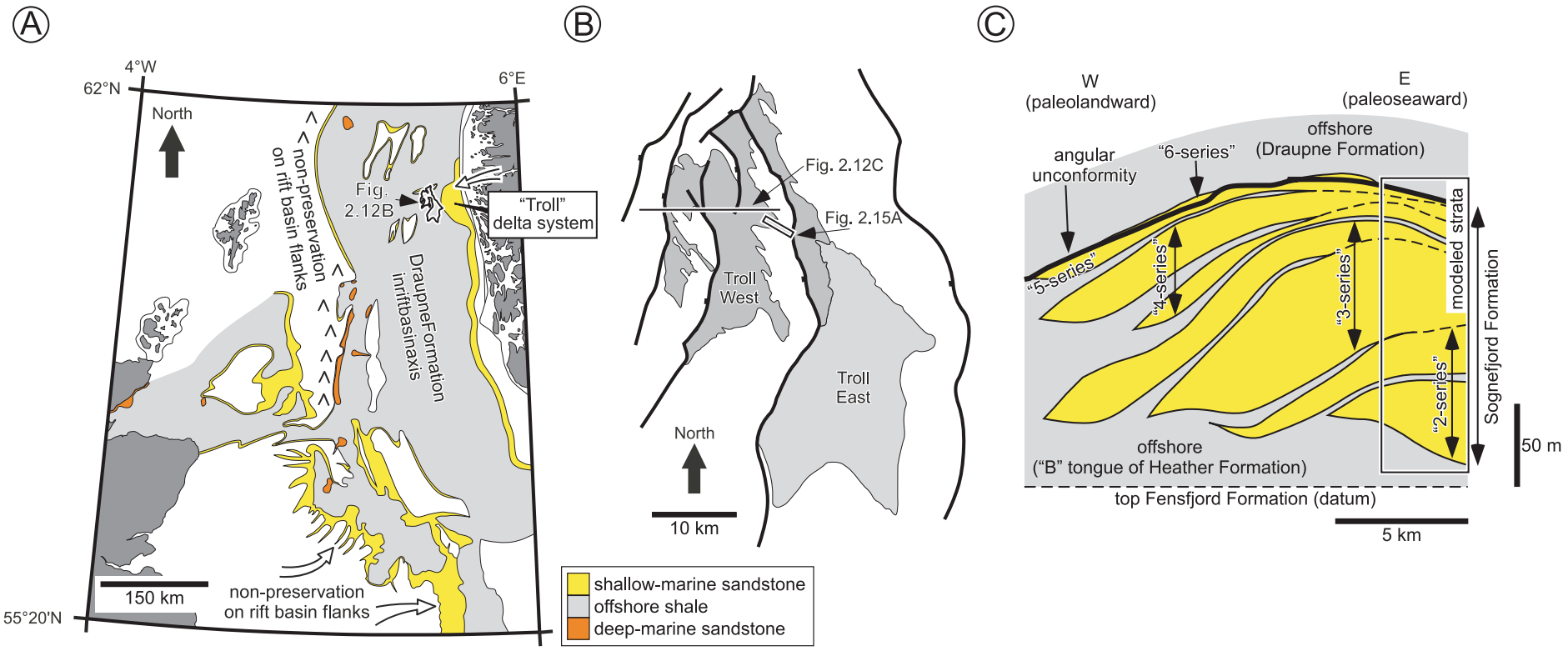


Figure 2.12. (A) Paleogeographic reconstruction of gross depositional environments in the central and northern North Sea during the early-to-mid Kimmeridgian (modified from Fraser et al., 2003), marked by retreat and drowning of the "Troll delta" system ("series-6" of the Sognefjord Formation; Dreyer et al., 2005). (B) Simplified outline of the Troll Field, highlighting major blocks bounded by normal faults that post-date deposition of the Sognefjord Formation. The location of the modelled area and a stratigraphic cross section across Troll West (Fig. 2.12C) are shown. (C) Schematic cross section through the "Troll delta" system of the Sognefjord Formation in Troll West, from west (paleoseaward) to east (paleolandward). Major shallow-marine tongues (labelled "series-1" to "series-6", using the nomenclature of Dreyer et al., 2005) and their component parasequences are shown (after Gibbons et al., 1993).

2005). The formation is up to 170 m thick in the Troll Field, and consists of five, vertically stacked regressive-transgressive successions bounded by major flooding surfaces (the 2-, 3-, 4-, 5- and 6-series; Fig. 2.12C) (Dreyer et al., 2005). Each regressive-transgressive succession exhibits internal stratigraphic variability across the lateral extent of the reservoir, such that it can be interpreted as a sequence with constituent systems tracts and parasequences (Dreyer et al., 2005). The reservoir volume to be modelled contains seven, vertically stacked parasequences. The lower parasequences were deposited by regression of wave-dominated delta fronts, whereas the upper parasequences comprise more tide-influenced delta-front deposits (Dreyer at al., 2005). Reservoir zones in the Troll West accumulation are defined by alternating layers of fine-grained, micaceous sandstone and coarse-grained sandstone (informally referred to as “m sands” and “c sands”, respectively). The coarse-grained sandstones have higher porosity and permeability (100’s – 1000’s mD) than the fine-grained, micaceous sandstones (10’s – 100’s mD) (Dreyer et al., 2005; Gibbons et al., 1993). Each couplet of fine-grained, micaceous sandstone and overlying coarse-grained sandstones corresponds to the lower and upper part of a single delta-front parasequence (Dreyer at al., 2005). 3D seismic data image laterally extensive (up to 30 km along depositional strike), near-linear, NNE-SSW-trending clinoforms that dip west-northwestwards at 1.5-4° (Dreyer et al., 2005). The structure of the Troll West reservoir is defined by two rotated fault blocks that formed after reservoir deposition, and the reservoir is further segmented by smaller post-depositional faults that trend WNW-ESE to NNW-SSE (Dreyer at al., 2005) (Fig. 2.12B).

Troll West contains a thin oil column (11-26 m) that is exploitable through the use of horizontal wells (Dreyer et al., 2005) and the productivity of these wells is likely to be sensitive to the ratio of vertical to horizontal permeability (cf. Joshi, 1987). This ratio is

predicted to be influenced by laterally extensive calcite-cemented concretionary beds which are abundant in the Sognefjord Formation reservoir along parasequence-bounding flooding surfaces (Gibbons et al., 1993) and, potentially, also along clinoform surfaces within parasequences. Furthermore, seismic cross-sections and time slices through the Sognefjord Formation show a change from low to high amplitude values across clinoform surfaces within each parasequence, which may reflect a change in lithology (Dreyer et al., 2005). Thus it appears that permeability barriers and baffles in the form of calcite-cemented concretions and lithological contrasts may occur along clinoform surfaces. Heterogeneities associated with dipping clinoform surfaces could influence drainage patterns and recovery from the thin oil zone (Gibbons et al., 1993). Dilib and Jackson (2012) used a sector model of the Sognefjord Formation (dimensions: 3200 x 750 x 150 m) to investigate production optimization using intelligent wells for a range of uncertainty in geologic parameters. We use the model of Dilib and Jackson (2012) as the context in which to apply the clinoform-modelling algorithm.

2.5.2 Model construction

The stratigraphic framework of the reservoir model is defined by flooding surfaces that bound seven parasequences. The bounding surfaces are offset by two post-depositional faults that are oriented NW-SE across the model volume. We extract the faulted parasequence-bounding flooding surfaces from the existing reservoir model (Dilib and Jackson, 2012). We use the faulted parasequence boundaries to construct the final Troll West sector model but, as a quality control step for applying the clinoform-modelling algorithm, we first take the faulted parasequence-bounded flooding surfaces and adjust them so that they are horizontal. Each parasequence also contains a laterally

continuous surface that represents the facies-association boundary between fine-grained, micaceous sandstone ("m sands") below and coarse-grained sandstone ("c sands") above; these surfaces are extracted from the model of Dilib and Jackson (2012) and also adjusted to remove the effects of faulting in the same way as the flooding surfaces. Additionally, where facies associations pinch out, the facies association boundary surfaces are adjusted to coincide throughout the remainder of the model volume with the top parasequence bounding surface. This procedure creates flooding surfaces and facies-association boundaries in the model that mimic their depositional geometries, which are used as a reference framework to validate that the clinoform geometries and distributions applied later using the faulted parasequence-bounding surfaces are consistent with geological concepts. Table 2.4 shows the parameters used in the clinoform-modelling algorithm.

Table 2.4. Clinoform modelling parameters used in the clinoform-bearing sector model of the Sognefjord Formation reservoir, Troll Field.

Parameter	Description	Min.-Max. Values	Units
t_L	length of top ellipse in depositional dip direction	3000	M
t_W	length of top ellipse in depositional strike direction	6000	M
L	clinoform length	150-900	M
b_L	length of base ellipse in depositional dip direction (=$t_L + L$)	3150-3900	M
b_W	length of base ellipse in depositional strike direction (=$t_W + L$)	6150-6900	M
P	shape function exponent	2	None
p_O	axis of progradation relative to bounding surfaces	50	None
θ	clinoform progradation angle relative to north	320	°
S	clinoform spacing	105-390	M

In order to honour the nearly linear plan-view geometry of clinoforms observed in seismic data (Figures 3 and 12 in Dreyer et al., 2005), we define a width for the top-clinoform ellipse, t_W, that is far greater than the depositional-dip extent of the bounding surfaces in the model area (3200 m), and a top-clinoform ellipse length, t_L, that is half of

t_W, to give a plan-view aspect ratio of 2 (c.f. wave-dominated shoreface systems in Howell at al., 2008b). Seismically resolved clinoform dip values of 1.5-4° (Dreyer et al., 2005) were used in conjunction with the estimated parasequence thickness to calculate clinoform length, L, using simple trigonometry. As there are only a small number of seismically resolved clinoforms in a few palaeogeographic locations and within a few stratigraphic levels to extract clinoform length, we generate a normal distribution based on the extracted data (Fig. 2.13A), and then draw values at random from this distribution

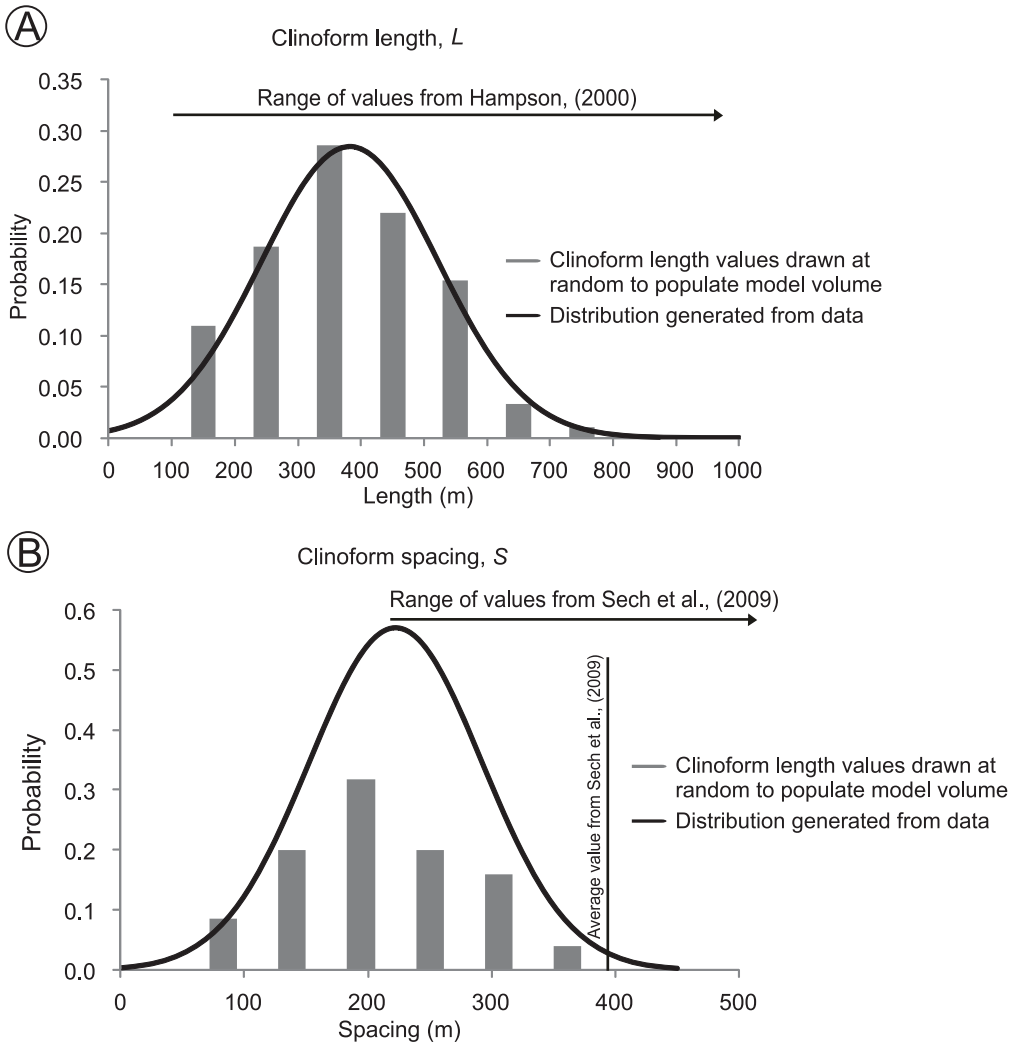


Figure 2.13. Normal distributions, shown as black lines, for (A) clinoform ength (Fig. 2.4D), and (B) clinoform spacing (Fig. 2.4D) generated from published seismic data from the Sognefjord Formation (Figures 3 and 12 in Dreyer et al., 2005). Columns in grey represent the values for clinoform length and spacing drawn at random from the normal distribution and used to populate the Troll sector model.

to populate the model volume (Fig. 2.13A). Finally, the pre-modelling lengths were compared to the seismically resolved clinoforms (Dreyer et al., 2005), to validate that the algorithm-generated lengths are reasonable. Similarly, the horizontal spacing of seismically resolved clinoform surfaces (Figures 3 and 12 in Dreyer et al. 2005) is used to generate a normal distribution of values for clinoform spacing, *S* (Fig. 2.13B), and values are drawn at random from this distribution to populate the model volume (Fig. 2.13B). The resulting values of clinoform spacing are consistent with those observed at outcrop for other wave-dominated shorelines (e.g. Hampson, 2000; Sech et al, 2009) (Fig. 2.13B). We assume that the clinoform shape function is the same as the Ferron Sandstone Member example (defined by P =2 in Eq. 2.8), as this gives a good match to the seismically resolved clinoform surfaces and, furthermore, we assume that a similar geometry is shared by clinoform surfaces in all parasequences in all locations throughout the model volume. As a first step, the insertion point of the first clinoform surface, p_o, is arbitrarily selected in the centre of the proximal model boundary, and consistent west-northwest progradation of clinoforms (Figure 3 in Dreyer et al., 2005) is used to define a progradation direction, θ, of 320˚ relative to north. We then use the facies-association boundary surfaces extracted from the model of Dilib and Jackson (2012) to create zones of m- and c-sands within each clinothem. The application of the clinoform-modelling algorithm yields a model containing 100 clinoform surfaces. We perform a visual quality control check to ensure that the clinoforms produced by the algorithm are consistent with the geological concepts of the model (e.g. clinoform spacing, dip, length) in the absence of post-depositional faults.

After this validation, we use the same parameters as previously (Table 2.4), but apply the clinoform–modelling algorithm using the faulted parasequence-bounding

flooding surfaces and the faulted facies-association boundary surfaces. This approach generates clinoform geometries and distributions in the model volume that reflect present-day reservoir structure. The resulting surface-based model measures approximately 3200 x 750 x 150 m, and contains 215 surfaces: the 8 top and base parasequence bounding surfaces, 100 clinoform surfaces and 107 facies-association-boundary surfaces. A hybrid gridding method is used, because previous work shows that this approach better captures the movement of gas and water in the vicinity of a horizontal production well located in a thin oil-rim (Vinje et al., 2011). The areal grid resolution of the model is fixed (50 × 25 m), but the vertical resolution varies. In the gas cap and aquifer, the vertical layering is stratigraphic, conforming to the flooding surfaces that bound the parasequences and with a single grid layer representing each facies association zone. In an interval of the reservoir that contains the oil column, from 3 m above the gas-oil contact (GOC) and to 3 m below the oil-water contact (OWC), the grid is horizontal and regular, with finer layering (0.25 -2 m) parallel to the initial GOC and OWC (Dilib and Jackson, 2012). Very fine grid resolution is required to capture the geometry of clinoform surfaces in this regular, orthogonal part of the grid. For the model to be suitable for flow simulation, it is not possible to have this level of grid resolution everywhere in the model. Petrophysical properties were assigned by facies association in a similar manner to the model of the Ferron Sandstone Member reservoir analogue. Calcite-cementation that may be associated with clinoforms is incorporated in flow-simulation models by using transmissibility multipliers along clinoform surfaces. We use a different approach to modelling the clinoform controlled heterogeneity than used in the Ferron Sandstone Member model, because part of the grid is horizontal and regular. Transmissibility multipliers representing the heterogeneity along clinoforms are placed in

the cells adjacent to the clinoform surface in the orthogonal part of grid around the oil rim. As the orthogonal grid is very fine, we can use this approach and still honour the geometry of the clinoform surfaces. We use a trend to enforce greater continuity and extent of heterogeneity in the m-sands that lie above the lower part of each clinoform.

2.5.3 Geological model results

We find that clinoform surfaces incorporated into the Troll sector model show similar geometries and spacing to those that are seismically resolved in the Sognefjord formation (Figures 3 and 12 in Dreyer et al. 2005). The clinoforms are linear in plan view (Fig. 2.14B), consistent with interpreted plan view geometries of wave-dominated shoreface systems (Fig. 2.3A) (Howell et al., 2008b), consistently prograde west-northwestwards (progradation direction, θ, of 320˚ relative to north), as established through 3D seismic data (Dreyer et al., 2005), and have the concave-upwards geometry observed in seismic dip sections through the Sognefjord formation (Figures 3 and 12 in Dreyer et al., 2005) (Fig. 2.14A, Fig. 2.15B). In depositional strike cross-section, the algorithm produces near-horizontal clinoform geometries, consistent with seismically resolved clinoforms (Figure 3 in Dreyer et al., 2005) (Fig. 2.15C). The stochastic component of the clinoform-modelling algorithm distributes clinoforms with cross-sectional geometries and spacings (Fig. 2.14A, 2.15B) that are consistent with outcrop studies of wave-dominated deltas (Hampson, 2000; Sech et al., 2009) (Fig. 2.13) and honour the sparse subsurface data. In contrast to the Ferron Sandstone Member example, the Troll West sector model does not contain subtle clinoform geometries such as onlap and downlap of younger clinoforms on to older clinoforms (Fig. 2.14A, 2.15B). This can be attributed to these features being below the resolution of the seismic data

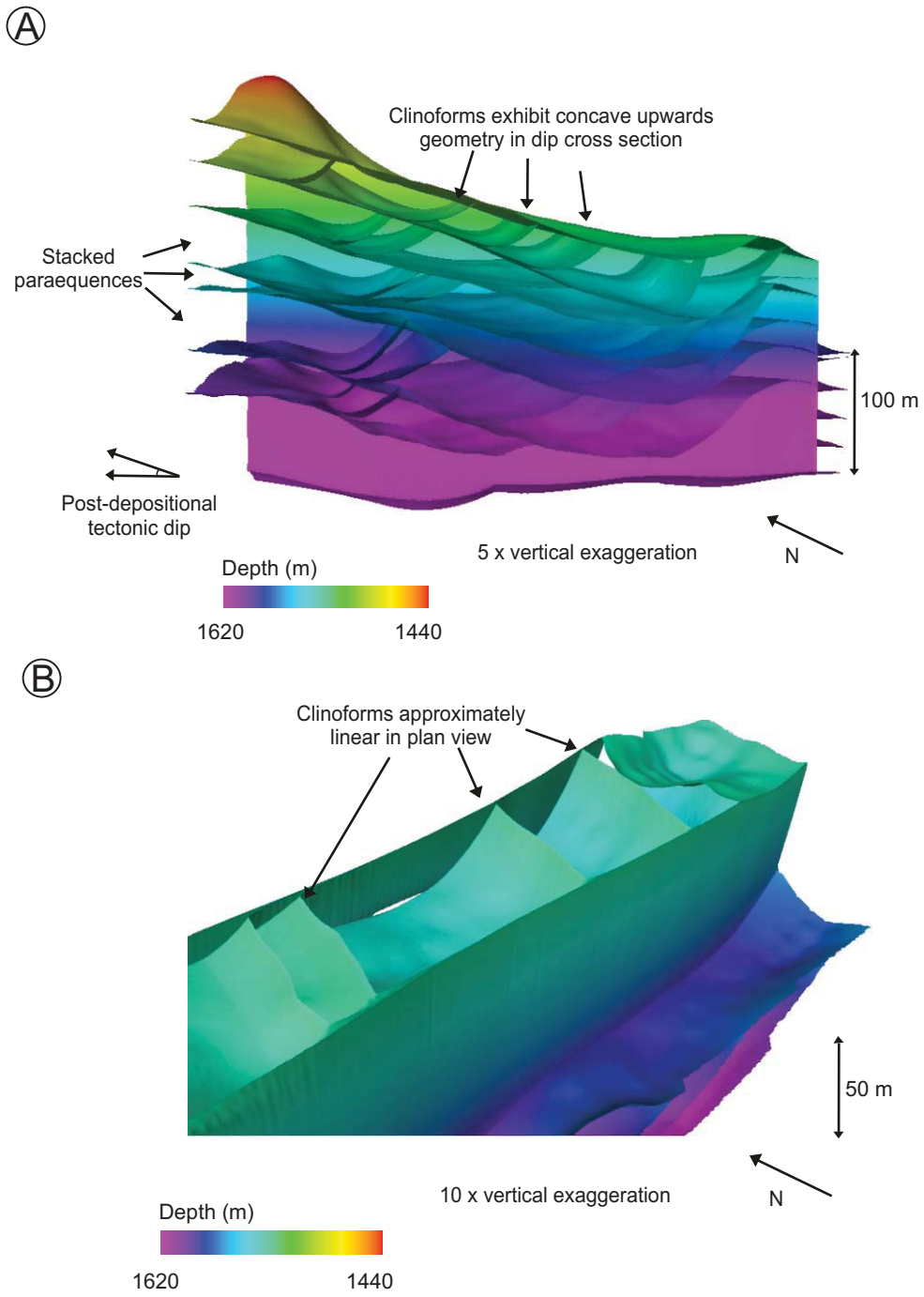


Figure 2.14. Surfaces generated by the clinoform-modeling algorithm for the Troll sector model. (A) 3D dip cross-section of clinoform surfaces in the model demonstrating their concave upwards geometry, and (B) 3D view of clinoform surfaces in the model showing close to linear clinoforms in plan-view within fault-bounded compartment. Not all surfaces used in the Troll sector model (Fig. 2.15) are shown.

used to extract the parameters that were used in the algorithm, decreasing their likelihood of being observed. The clinoform surfaces are also faulted in the same way as the parasequence-bounding flooding surfaces (cf. Fig. 2.2A) (Fig. 2.15C).

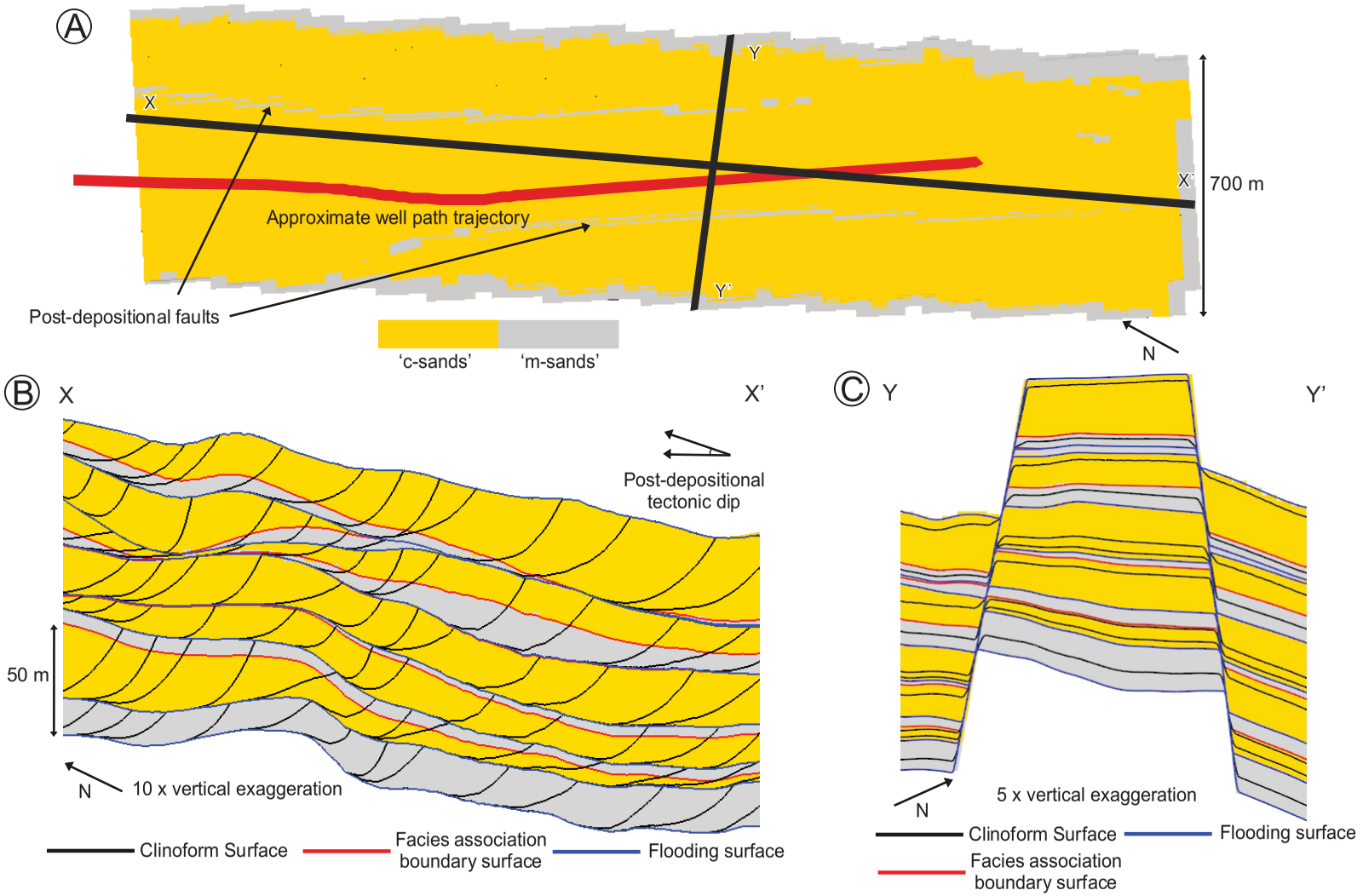


Figure 2.15. (A) Plan view facies association map of the Sognefjord Formation in our Troll West sector model, showing the location of compartmentalizing faults and a horizontal well. Cross sections along (B) depositional dip and (C) depositional strike, showing bounding flooding surfaces (blue), surfaces representing facies-association boundaries (red), and clinoforms generated by the modelling algorithm (black) for all parasequences in the model volume.

2.5.4 Production strategy

We now use the clinoform-bearing Troll West sector model to simulate production through gas expansion and aquifer influx using a 2600 m long horizontal well, placed 2 m above the initial OWC (Figs. 2.15A, 2.16A). The well is controlled by maximum gas production rate, minimum oil production rate, and minimum bottom-hole-pressure constraints. Reservoir, rock and fluid properties are summarized in Table 2.5. The

Table 2.5. Reservoir, fluid and rock properties used in the sector model of the Sognefjord Formation reservoir, Troll Field.

Reservoir properties	Value	Units
Reservoir pressure (P_r)	158	Bar
OWC	1559	m
Top	1705	m
Base	1481	m
Fluid properties		
Oil viscosity (μ_o)	1.83	cp
Oil density (ρ_o)	890	kg/m^3
Oil compressibility (c_o)	2×10^{-6}	1/bar
Oil formation volume factor (B_o)	1.18	(rm^3/sm^3)
Water viscosity (μ_w)	0.45	cp
Water density (ρ_w)	1045	kg/m^3
Water compressibility (c_w)	3×10^{-6}	1/bar
Water formation volume factor (B_w)	1	(rm^3/sm^3)
Rock properties		
Rock porosity ($\emptyset$) (average)	30	%
Horizontal (k_h) and vertical permeability (k_v) of m-sands	25 (k_h), 2.5 (k_v)	mD
Horizontal (k_h) and vertical permeability (k_v) of c-sands	4500 (k_h), 2250 (k_v)	mD
Rock compressibility for all facies associations (c_r)	4.35×10^{-5}	1/bar

presence of permeability barriers along clinoforms is modelled using transmissibility modifiers, and specified in terms of the percentage of each clinoform surface that acts as a barrier to flow. Similar to the Ferron Sandstone Member example, two simulations of the Troll Field sector model are conducted in which: (1) clinoforms are not associated with calcite-cemented barriers to flow (0% barrier coverage along clinoforms); and (2) clinoforms are associated with significant calcite-cemented barriers to flow (90% barrier

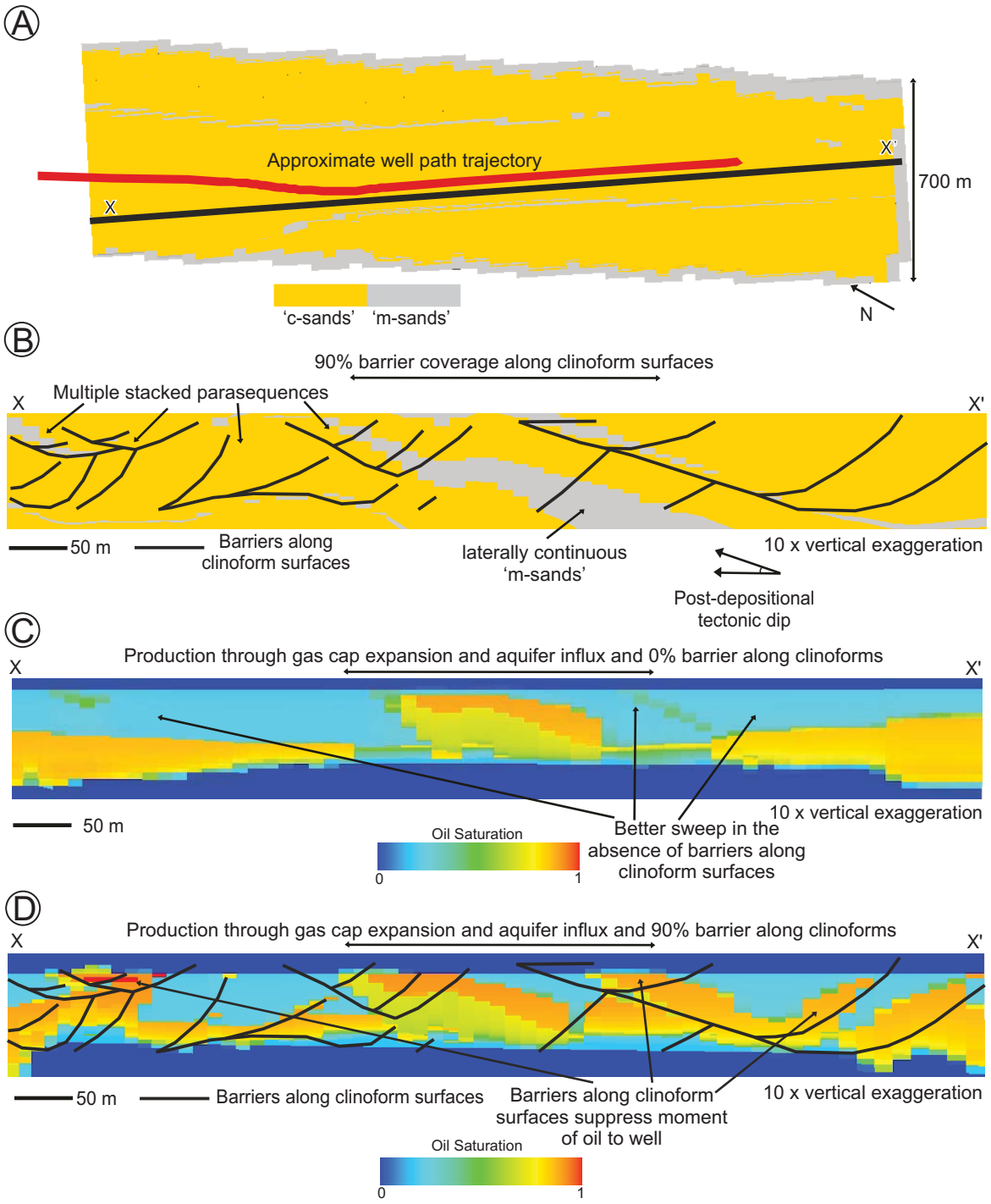


Figure 2.16. (A) Plan view facies association map of the Sognefjord Formation extracted from our Troll West sector model, showing the location of the horizontal well and the cross-section shown in (B-D). (B) Depositional-dip-oriented cross-section showing the internal facies architecture of the modeled parasequences with the location of barriers along the clinoforms shown as black lines. (C, D) The same depositional-dip-oriented cross-section showing water saturation after 1000 days of production, for models with (C) 0% barrier coverage along clinoforms, and (D) 90% barrier coverage along clinoforms.

coverage along clinoforms, Fig. 2.16B). All other parameters remain fixed between the simulations.

2.5.5 Simulation results

The presence of barriers along 90% of the area of each clinoform surface significantly alters the movement of fluids in the reservoir, by increasing the tortuosity of flow pathways. As a result, gas breakthrough is later when calcite-cemented barriers are present along clinoforms (30 vs. 15 days, Fig. 2.17C), and oil production remains at plateau for longer (30 vs. 15 days, Fig. 2.17A). However, after gas breakthrough, the rate of oil production rapidly falls below that for the case lacking calcite-cemented barriers (Fig. 2.17A). Water cut is significantly lower for the model containing calcite-cemented barriers throughout production (Fig. 2.17B). The calcite-cemented barriers along clinoform surfaces prevent lateral movement of oil and the upward movement of water from the aquifer to the well (Fig. 2.16D), but have a less significant effect on the downward movement of more mobile gas. As a result, the gas-oil ratio (GOR) increases for production in the model containing calcite-cemented barriers along clinoform surfaces. Most importantly, the recovery of oil could be overestimated by up to 14% if calcite cements present in the reservoir were omitted from the reservoir model (Fig. 2.17D; also compare Fig. 2.16C, D), which is consistent with the results of Jackson et al., (2009) which showed that omitting clinoforms from wave-dominated shoreface systems could lead to overprediction of hydrocarbon recovery. In models that omit clinoforms, these results could be attributed to discontinuous horizontal calcite-cemented barriers that subdivide the oil zone (e.g. Kantorowicz et al., 1987; Gibbons et al., 1993). However, Jackson and Muggeridge (2000) have shown that isolated horizontal barriers are likely to

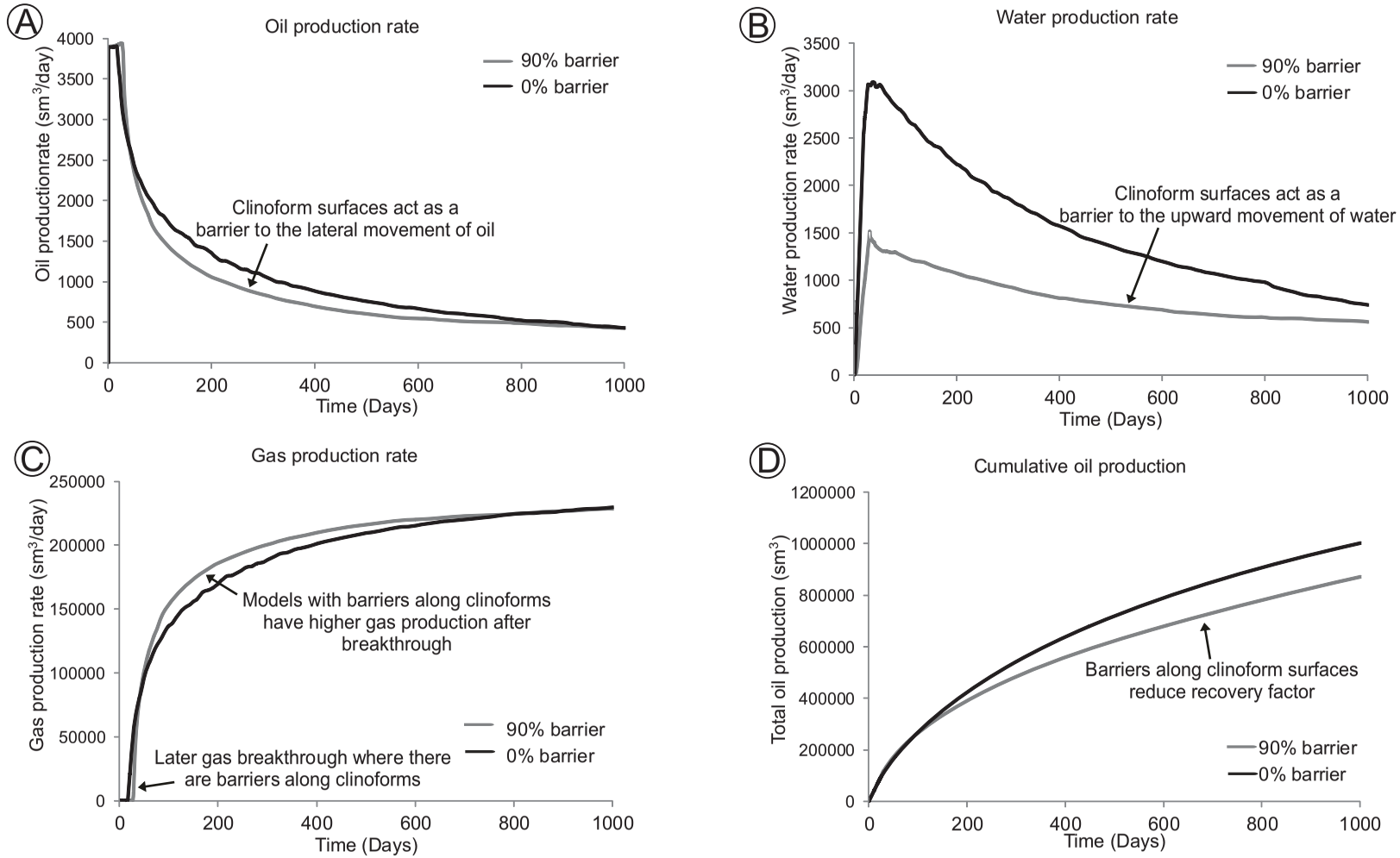


Figure 2.17. (A) Oil, (B) water, and (C) gas production rates, and (D) cumulative oil production as a function of time in the simulation model of the Sognefjord Formation in a fault-bounded sector of the Troll Field (Fig. 2.12B), for production from a single horizontal well through gas cap expansion and aquifer influx (Fig. 2.16). In the models with 90% barrier coverage along clinoforms, free gas breakthrough is delayed (Fig. 2.17C) and liquid production is decreased (Fig. 2.17A, B, D) relative to the models lacking barriers along clinoforms.

have a negligible effect on recovery unless they are steeply inclined to flow and are continuous over large areas, such as barriers to flow associated with clinoform surfaces. This also has implications for history matching; if the underlying geological model has omitted clinoform surfaces and is not representative of the reservoir, future production is unlikely to be accurately forecasted. Further discussion on the effects of heterogeneity on simulated production in the Sognefjord Formation reservoir sector model is presented in Dilib and Jackson (2012).

2.6 Discussion

We have described the conceptual and mathematical basis of a modelling algorithm to generate surface-based reservoir models that include clinoforms, and demonstrated its application using: (1) a deterministic approach where a rich, high resolution dataset is available (Ferron Sandstone Member outcrop analogue); and (2) a stochastic element where the data are sparse (Sognefjord Formation, Troll Field sector).

Several previous studies of the Ferron Sandstone Member have incorporated clinoform surfaces in flow simulation models using a combination of object-based methods to place barriers along clinoforms (Howell et al., 2008a), or deterministic methods to map clinoform surfaces (Enge and Howell, 2010; Howell et al., 2008b). While these studies have demonstrated that, under certain displacement conditions, it is important to include clinoform surfaces in models of shallow-marine reservoirs, it is not clear how these models could be applied in the subsurface or at full-field scale. Other studies have indicated that surfaces should be used to incorporate clinoforms into reservoir models, as surfaces are much less computationally expensive to generate and

manipulate than large 3D geocellular grids (Jackson et al., 2009; Sech et al., 2009; Enge and Howell, 2010; Jackson et al., in press). These deterministic approaches to modelling clinoforms are appropriate for modelling clinoform surfaces that are tightly constrained by outcrop data, but do not allow flexibility in conditioning clinoform geometry and distribution to sparser datasets with a large degree of uncertainty.

Our results support previous work in demonstrating that it can be important to include clinoform surfaces in models of shallow-marine reservoirs in order to accurately predict fluid-flow patterns and hydrocarbon recovery. However, the work presented here differs from previous modelling investigations in providing a generic method of incorporating clinoforms with geologically realistic geometries and spacing into models of shallow-marine reservoirs. The algorithm can be also be applied at a variety of lengthscales as demonstrated in Chapter 3, where a reservoir scale model that comprises multiple stacked parasequences is used to investigate the impact of clinoforms under geological uncertainty and reservoir engineering decisions.

We recognize that the algorithm does not explicitly incorporate every clinoform surface that may be present; nor does it represent their detailed geometry, as may be possible using process-based forward numerical models (e.g. Edmonds and Slingerland, 2010; Geleynse et al., 2011). However, there are uncertainties in the values of input parameters to use in process-based models. There are also no simple relationships between the input parameters for process-based models and the geometries of clinoforms produced. Process-based models are also difficult to condition to available data and require large computational times, which makes them less feasible for modelling a range of realizations. The clinoform-modelling algorithm provides a flexible

and efficient method for incorporating multiple clinoform surfaces with realistic geometries into models of shallow-marine reservoirs.

The impact of clinoforms on flow also has implications for history matching reservoir models to production data. If the underlying geological model has omitted clinoform surfaces, history matching will fail to produce reliable models for forecasting future production. The clinoform-modelling algorithm allows multiple surface-based, clinoform-bearing models to be generated rapidly in order to investigate uncertainty in reservoir characterization, and to develop production strategies to mitigate this uncertainty. The algorithm can thus be used in conjunction with other modelling tools and techniques as a basis to inform fast decision making in reservoir management.

2.7 Conclusions

A surface-based clinoform-modelling algorithm has been developed as a tool for rapidly incorporating clinoform surfaces into models of shallow-marine reservoirs. The algorithm is flexible and can be used in different shallow-marine environments through the user specifying a small number of input parameters.

We have used the clinoform-modelling algorithm with a rich, high-resolution outcrop dataset from a fluvial-deltaic reservoir analogue (Cretaceous Ferron Sandstone Member, Utah, USA) to deterministically model clinoform surfaces. We have also applied the clinoform-modelling algorithm to incorporate clinoforms in a sector model of a subsurface reservoir (Jurassic Sognefjord Formation, Troll Field, Norwegian North Sea) using a sparse subsurface dataset to stochastically model clinoform surfaces. In both applications geometrically realistic clinoforms are incorporated into reservoir models.

Finally, the clinoform-modelling algorithm allows clinoform geometry to be retained efficiently for fluid flow simulation. We find that when using water-flooding or gas cap expansion and aquifer influx displacement mechanisms, omission of barriers to flow along clinoform surfaces can lead to poor prediction of fluid movement and hydrocarbon recovery.

Chapter 3

Three-dimensional modelling of clinoforms within shallow-marine reservoirs: Part 2. Impact on fluid flow and hydrocarbon recovery in fluvial-dominated deltaic reservoirs

3.1 Summary

Permeability contrasts associated with clinoforms have been previously identified as an important control on fluid flow and hydrocarbon recovery in fluvial-dominated deltaic parasequences. However, they are typically neglected in subsurface reservoir models or considered in isolation in reservoir simulation experiments, because clinoforms are difficult to capture using current modelling tools. We use a suite of three-dimensional reservoir models constructed with a novel, stochastic, surface-based clinoform-modelling algorithm and outcrop-analogue data (Upper Cretaceous Ferron Sandstone Member, Utah, USA) to quantify the impact of clinoforms on fluid flow in the

context of: (1) other uncertainties in reservoir characterization, such as the presence of channelized fluvial sandbodies and the impact of bed-scale heterogeneity on vertical permeability; and (2) reservoir engineering decisions, including oil production rate.

The proportion and distribution of barriers to flow along clinoforms exert the greatest influence on hydrocarbon recovery; equivalent models that neglect these barriers overpredict recovery by up to 35%. Continuity of channelized sandbodies that cut across clinoform tops, and vertical permeability within distal delta-front facies, influence sweep within clinothems bounded by barriers. Sweep efficiency is reduced when producing at higher rates over shorter periods, because oil is bypassed at the toe of each clinothem. Clinoforms are difficult to detect using production data, but our results indicate that they can have a significant influence on hydrocarbon recovery and their impact may be larger than that of other geological heterogeneities and of reservoir engineering decisions. Clinoforms should be included models of fluvial-dominated deltaic reservoirs under certain displacement conditions in order to accurately predict hydrocarbon recovery and drainage patterns.

3.2 Introduction

Fluvial-dominated deltaic reservoirs often exhibit pressure compartmentalization, poor sweep efficiency, early water breakthrough, and lower than expected ultimate recovery of hydrocarbons (e.g., Begg et al., 1992; Tye et al., 1999). These reservoirs consist of multiple stacked delta lobes, juxtaposed with coastal-plain and channel-fill deposits. Within individual delta lobes, heterogeneity along inclined clinoform surfaces in delta-front deposits can create tortuous flow pathways and variable sandbody

connectivity (Ainsworth et al., 1999), and may contribute to these production characteristics. Clinoform surfaces are formed by the progradation of delta or shoreface systems (Barell, 1912; Rich, 1951; Gani and Bhattacharya, 2005), are typically below seismic resolution, and can be difficult to correlate between wells (e.g. Ainsworth et al., 1999; Hampson, 2000). This can make their characterization in both static (geological) and dynamic (fluid-flow simulation) reservoir models difficult, such that clinoforms are typically omitted in models of shallow-marine reservoirs (Howell et al., 2008b).

A number of studies have indicated that it is important to include barriers to flow associated with clinoforms in reservoir models, in order to accurately predict hydrocarbon recovery and drainage patterns in fluvial-dominated deltaic reservoirs. However, these studies investigated the effects of heterogeneity along clinoform surfaces using either two-dimensional (2D) models (e.g., White and Barton, 1999), which may overestimate the impact of permeability contrasts along clinoforms because they are assumed to be continuous in the third dimension (Jackson and Muggeridge, 2000), or three-dimensional (3D) models of volumes much smaller than most reservoirs (e.g., Forster et al., 2004; Mattson and Chan, 2004; Howell et al., 2008a; Enge and Howell, 2010). Deveugle et al. (2011) created a reservoir-scale, 3D model of multiple stacked delta-lobe deposits in an outcrop analogue, and found that sweep efficiency in stacked delta-lobe deposits is controlled by the orientation, continuity and permeability of channelized sandbodies, and by the vertical permeability of laterally extensive heterolithic distal delta-front deposits that form the lower part of each lobe. However, their models did not include clinoform surfaces. Only one 3D reservoir-scale model that incorporates clinoforms in fluvial-dominated deltaic strata has been reported (Howell at al., 2008b), but this contained a limited number of deterministically modelled clinoforms

with a simplified planar geometry. Consequently, the impact of clinoforms and their effect on fluid-flow and hydrocarbon recovery in reservoir-scale models of fluvial-dominated deltaic reservoirs is still poorly understood, as no models have yet been developed that incorporate several stacked delta-lobe deposits, of which each contains multiple clinoform surfaces.

The aim of this chapter is to quantify the impact of uncertainty in clinoform distribution and clinoform-related heterogeneity on fluid flow during hydrocarbon recovery from multiple, stacked, fluvial-dominated delta-lobe deposits in the context of: (1) other uncertainties in reservoir characterization, including the impact of bed-scale heterogeneity on vertical permeability, and the orientation and continuity of stacked delta-front parasequences and associated channelized sandbodies; and (2) reservoir engineering decisions, including oil production rate. We use the clinoform-modelling algorithm described in Chapter 2 to incorporate multiple clinoform surfaces into a suite of reservoir-scale, surface-based 3D geological models containing several stacked delta lobes of varying azimuthal orientation, based on data and an existing, high-resolution outcrop model from an outcrop analogue, the Ferron Sandstone Member, central Utah, USA (Deveugle et al., 2011).

In order to address this aim, we focus on the impact of five key parameters: (1) continuity of channelized fluvial sandbodies; (2) bed-scale heterogeneity in distal delta-front facies; (3) distribution of laterally extensive mudstone barriers or baffles to flow along clinoforms; (4) permeability of channelized fluvial sandbodies; and (5) oil production rate. Model results are compared using dynamic measures of sweep through the reservoir volume (e.g. recovery factor, water breakthrough), and pressure and saturation measurements in the modelled production wells, as a proxy for reservoir-

monitoring techniques that are widely applied to diagnose heterogeneity during production.

3.3 Geological heterogeneity in fluvial-dominated deltaic reservoirs

We begin by presenting a hierarchy of stratigraphic and sedimentological heterogeneity in fluvial-dominated deltaic reservoirs (modified after the more generic scheme for shallow-marine reservoirs of Kjønsvik et al., 1994), which provides a framework to identify, organize and model the heterogeneities observed. The hierarchy classifies six lengthscales of heterogeneity, from field scale (c. 10 km) to pore scale (c. 1 mm) (Van de Graaf and Ealey, 1989).

The largest lengthscale is represented by a basinward-thinning wedge of strata that records the overall advance and retreat of a delta system ("genetic sequence" *sensu* Galloway, 1989) (Fig. 3.1A). The wedge can be subdivided into a number of vertically stacked, shallow-marine tongues that interfinger with coeval offshore shales in a palaeoseaward direction, and with coeval coastal-plain deposits in a palaeolandward direction. The stacking of successive shallow-marine tongues defines progradation followed by aggradation and then retrogradation. The top of each shallow-marine tongue and their associated coastal-plain deposits are locally eroded by channelized sandbodies of different types (e.g. deltaic distributary channel fills, fluvial channel fills, incised valley fills). Wedges are most likely formed by changes in tectonic subsidence (e.g. Galloway, 1989; Van Wagoner et al., 1990), although long-term autogenic processes internal to the source-to-sink delta system cannot be discounted ("autoretreat" *sensu* Muto and Steel,

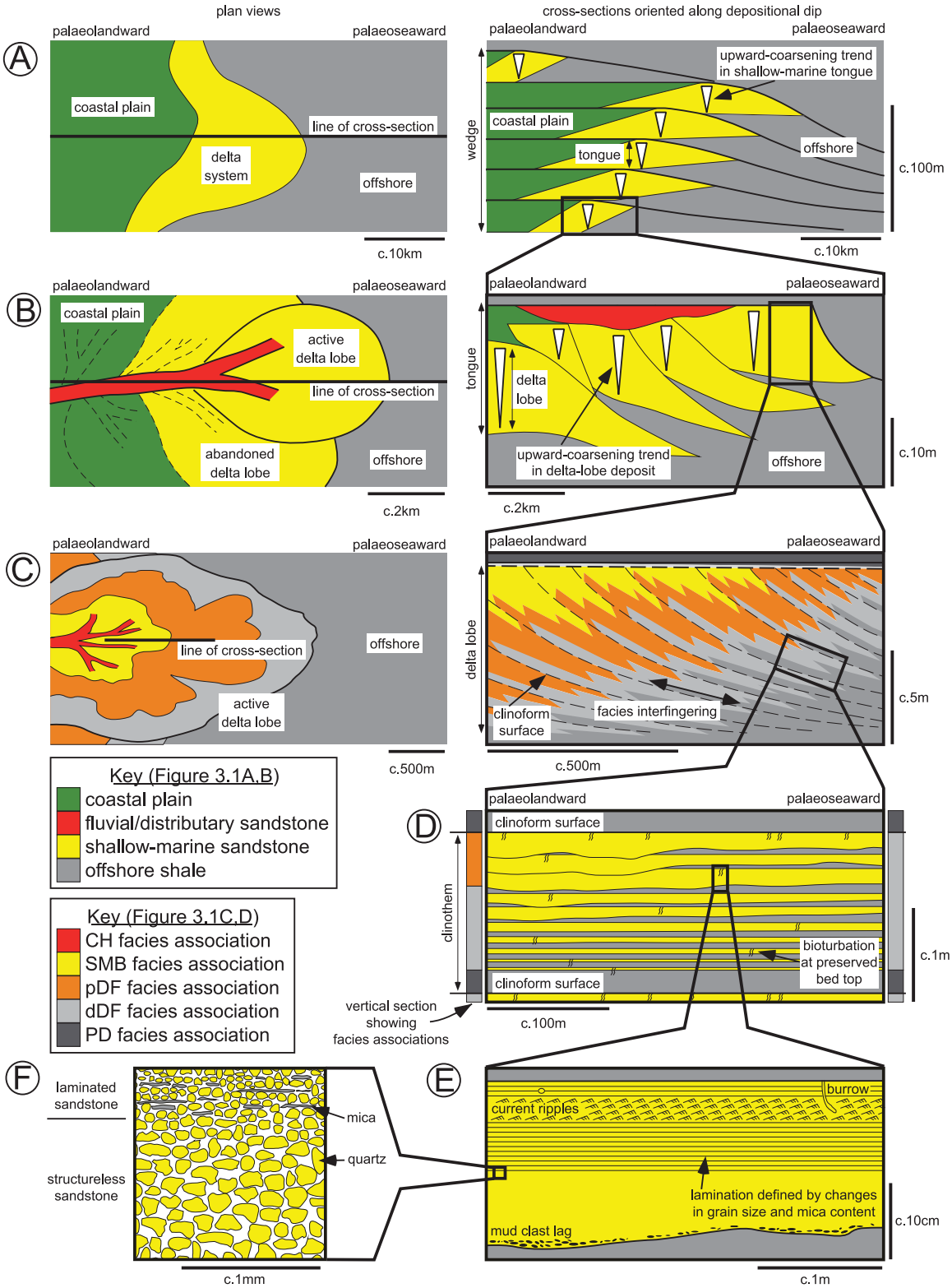


Figure 3.1. Generic hierarchy of heterogeneities within fluvial-dominated deltaic reservoirs across a range of lengthscales. Plan view maps with corresponding cross-sections oriented along depositional dip are shown for three orders of stratigraphic cycle: (A) vertically stacked shallow-marine tongues within a basinward-thinning wedge; (B) an individual shallow-marine tongue comprising compensationally stacked delta-lobe deposits; and (C) an individual delta-lobe deposit. Sedimentological heterogeneity at smaller lengthscales is shown for: (D) an upward-coarsening clinothem succession consisting of gravity-flow sandstone beds bounded by clinoform surfaces within the distal delta front (dDF) facies-association belt; (E) internal structure of an individual gravity-flow sandstone bed; and (F) microscopic lamination.

1992; Muto et al., 2007). The development and stacking of shallow-marine tongues within a deltaic wedge is generally attributed to a combination of relative sea-level, sediment supply and compactional subsidence (e.g. Galloway, 1989; Van Wagoner et al., 1990).

Shallow-marine tongues can be further subdivided into multiple, smaller stratigraphic units that are broadly equivalent to delta lobes (Fig. 3.1B). Each delta-lobe deposit was fed by a trunk deltaic distributary channel that branched downstream. Nodal avulsion of the trunk distributary channel controls the lateral switching of lobes, which are stacked in a compensational pattern within each shallow-marine tongue (each tongue thus constitutes a "delta complex" *sensu* Frazier, 1967) (Fig. 3.1B). This stacking is at least partly autogenic, and reflects internal geomorphic thresholds and morphodynamic responses within the delta system (Frazier, 1967; Coleman, 1988; Hoyal and Sheets, 2009). The application of sequence stratigraphic terminology to shallow-marine tongues and their constituent delta-lobe deposits has been ambiguous in the Ferron Sandstone Member and likely in other deltaic strata also. Shallow-marine tongues have been interpreted as either parasequences (e.g., Anderson and Ryer, 2004) or as parasequence sets in which their constituent delta-lobe deposits represent parasequences (e.g. Garrison and van den Bergh, 2004; Deveugle et al., 2011). Here we follow the latter nomenclature, with each shallow-marine tongue assigned to a parasequence set and each delta-lobe deposit to a parasequence.

Within a single delta-lobe deposit, there is a proximal-to-distal trend in facies associations from a trunk distributary channel sandstone (CH), which branches downstream into terminal distributaries that are contiguous with assemblages of stream mouth bar sandstones (SMB) (Olariu and Bhattacharya, 2006) that in turn pass

successively down dip into proximal delta front sandstones (pDF), distal delta front heteroliths (dDF), and prodelta mudstones (PD) (e.g. Van Wagoner in Wellner et al., 2005) (Fig. 3.1C). Clinoform surfaces control aspects of detailed facies architecture at this lengthscale, such as interfingering of facies-association belts (Ainsworth et al., 1999; Dutton et al., 2000; Howell et al., 2008a, 2008b; Enge and Howell, 2010). Each facies-association belt exhibits variations in bed geometry, thickness and stacking. For example, the dDF facies-association belt consists of sharp or erosionally based sandstone beds alternating with mudstones (Fig. 3.1D). Sandstone-beds are arranged into upward-coarsening successions that are bounded by clinoform surfaces; these successions constitute clinothems (*sensu* Rich, 1951) or bedsets (e.g., Howell et al., 2008a; Enge and Howell, 2010). Each bed contains a vertical succession that records deposition from a waning, unidirectional gravity flow, such as a turbidity current or hyperpycnal flow (e.g., Newman and Chan, 1991; Mulder et al., 2003; Olariu et al., 2010). Sandstone beds generally form sheets that thin gradually in a palaeoseaward direction, but they may be amalgamated as a result of localized erosion at their bases (e.g., Ryer and Anderson, 2004; Olariu et al., 2010). Interfingering of facies-association belts and the variable bed-scale successions within the belts reflect a variety of controls, including spatial and temporal (seasonal-to-millennial) variations in sediment and water discharge via the distributary channels (e.g., Olariu et al., 2010), and interaction of the delta front with basinal processes such as waves, storms and tides (e.g., Gani and Bhattacharya, 2007). Smaller-scale heterogeneities include sedimentary structures and the degree and type of bioturbation present within beds (Fig. 3.1E), and grain size and sorting characteristics, which control pore geometries at the microscopic scale (Fig. 3.1F).

3.4 Geological heterogeneity investigated in this study

We use the hierarchy described for fluvial-dominated deltaic reservoirs (Fig. 3.1) as a framework to select the heterogeneities we investigate in flow simulation experiments. We are particularly interested in capturing heterogeneity at the lengthscales within individual delta-lobe deposits (i.e. intra-parasequence scale) in models that comprise multiple, stacked, delta lobe deposits (Fig. 3.1B-C). Consequently, the models explicitly capture multiple clinoform surfaces and associated barriers, facies association boundaries within delta-lobe parasequences, and the geometry and distribution of channelized sandbodies that truncate the top of delta-lobe parasequences. The parameters used to describe these heterogeneities, and the range of values assigned to these parameters, are taken largely from a well-documented outcrop analogue, the Ferron Sandstone Member of east-central Utah (Fig. 3.2). Four key parameters are investigated, whose character is likely to be uncertain in the subsurface (summarized in Table 3.1).

3.4.1 (1) Presence of channelized fluvial sandbodies

There is uncertainty in the interpretation that channelized fluvial sandbodies (FC facies association) are present in the model area (Fig. 3.3E) and cut into genetically unrelated, stacked delta-lobe deposits from a higher stratigraphic interval (Fig. 3.3A-D). The presence of channelized fluvial sandbodies is inferred from regional mapping outside the study area, where the basal contact of the coastal plain interval is interpreted as a sequence boundary marked by channelized sandbodies (Deveugle et al., 2011). The presence of channelized fluvial sandbodies in subsurface fluvial-dominated deltaic

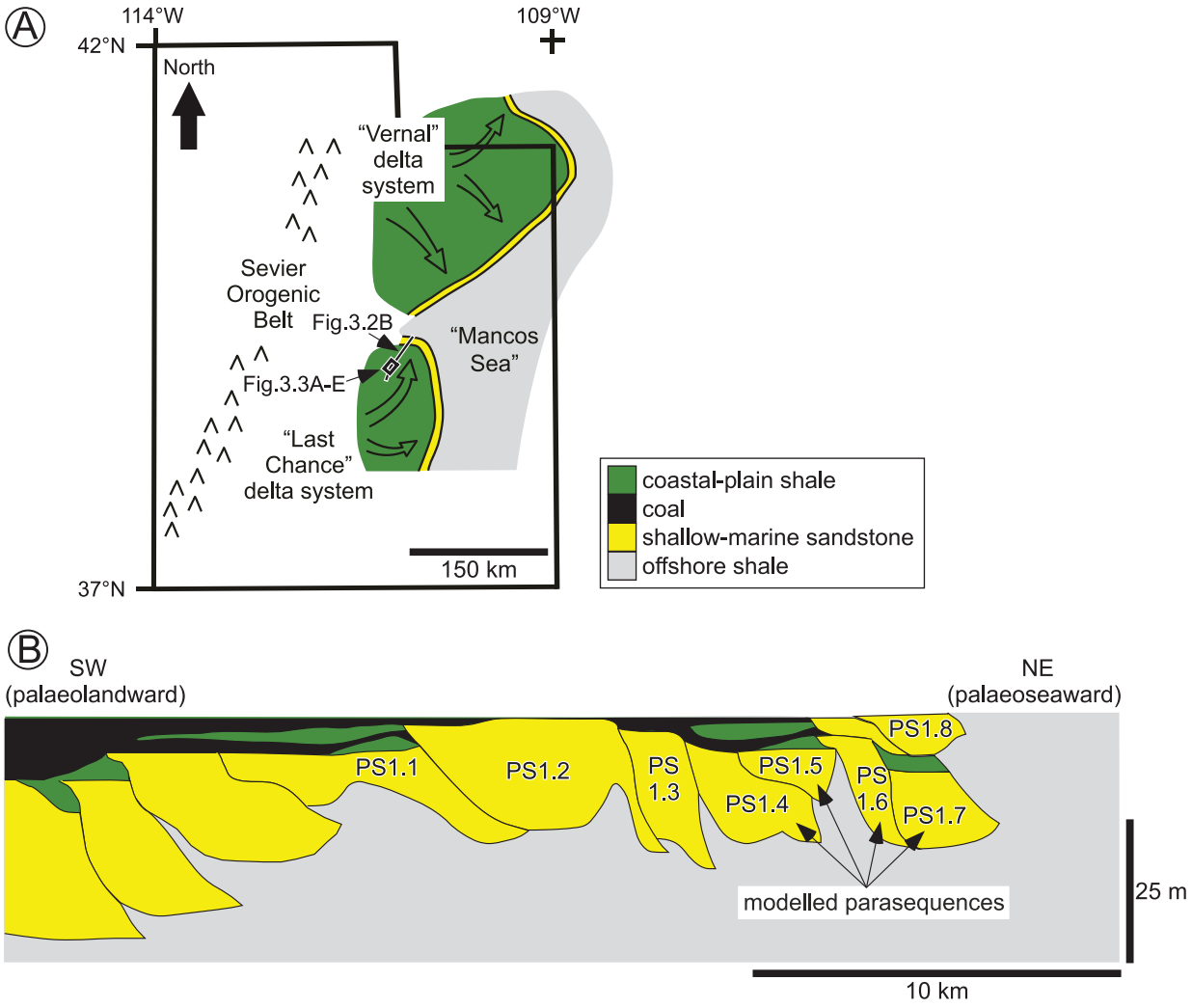


Figure 3.2. (A) Palaeogeographic reconstruction of the late Cretaceous "Last Chance" and "Vernal" delta systems of the Ferron Sandstone Member of the Mancos Shale in present-day Utah (after Cotter, 1976). The location of a regional cross section shown in (B) is highlighted, as well as the location of the plan view facies-association maps in Fig. 3.3A-E. (B) Detailed regional cross section through the lowermost shallow-marine tongue of the "Last Chance" delta system of the Ferron Sandstone Member (parasequence set 1 of Deveugle et al., 2011) (after Garrison Jr. and van den Bergh, 2004). Four delta-lobe deposits (parasequences 1.4, 1.5, 1.6, and 1.7 of Deveugle et al., 2011) are modelled in this study.

reservoirs is subject to similar uncertainties in interpretation (e.g. Tye, 2004).

However, even if channels are interpreted to be present in the model area there is still considerable uncertainty in how the channelized fluvial sandbodies are represented in reservoir models. The channelized fluvial sandbodies were populated in the model of Deveugle et al. (2011) using a single, stochastic, object-based modelling realization constrained by published data on sandbody dimensions (Reynolds, 1999; Tye,

Table 3.1. Factors investigated in simulation experiments. Four factors investigate uncertain parameters in reservoir characterization which correspond to three lengthscales of heterogeneity in the hierarchy described for fluvial-dominated deltaic reservoirs (Fig. 3.1B-D). One further factor investigates engineering decisions. The right hand column shows the values of factors varied (grey boxes) and held constant (white boxes) in each set of simulation experiments.

	Reservoir characterization uncertainty or engineering decision	Setting		Simulation experiment	
		Low	High	Set:1	Set:2
Reservoir characterization	1. Channelized fluvial sandbodies (Fig. 3.1B,C)	**not** present in model	**present** in model	Set 1: channelized fluvial sandbodies may be present or absent	channelized fluvial sandbodies present
	2. Vertical permeability of distal delta-front (dDF) facies association (Fig. 3.1D)	k_v/k_h = 0	k_v/k_h = 0.1		Set 2: channelized fluvial sandbodies are always present
	3. Barrier along clinoform surfaces (Fig. 3.1C)	0%	90%		
	4. Channelized fluvial sandbody permeability	1793mD	8965mD	N/A	
Reservoir Engineering	5. Oil production rate	175 S m^3/day (1100 bbl/day) over 20 years	350 S m^3/day (2200bbl/day) over 10 years		

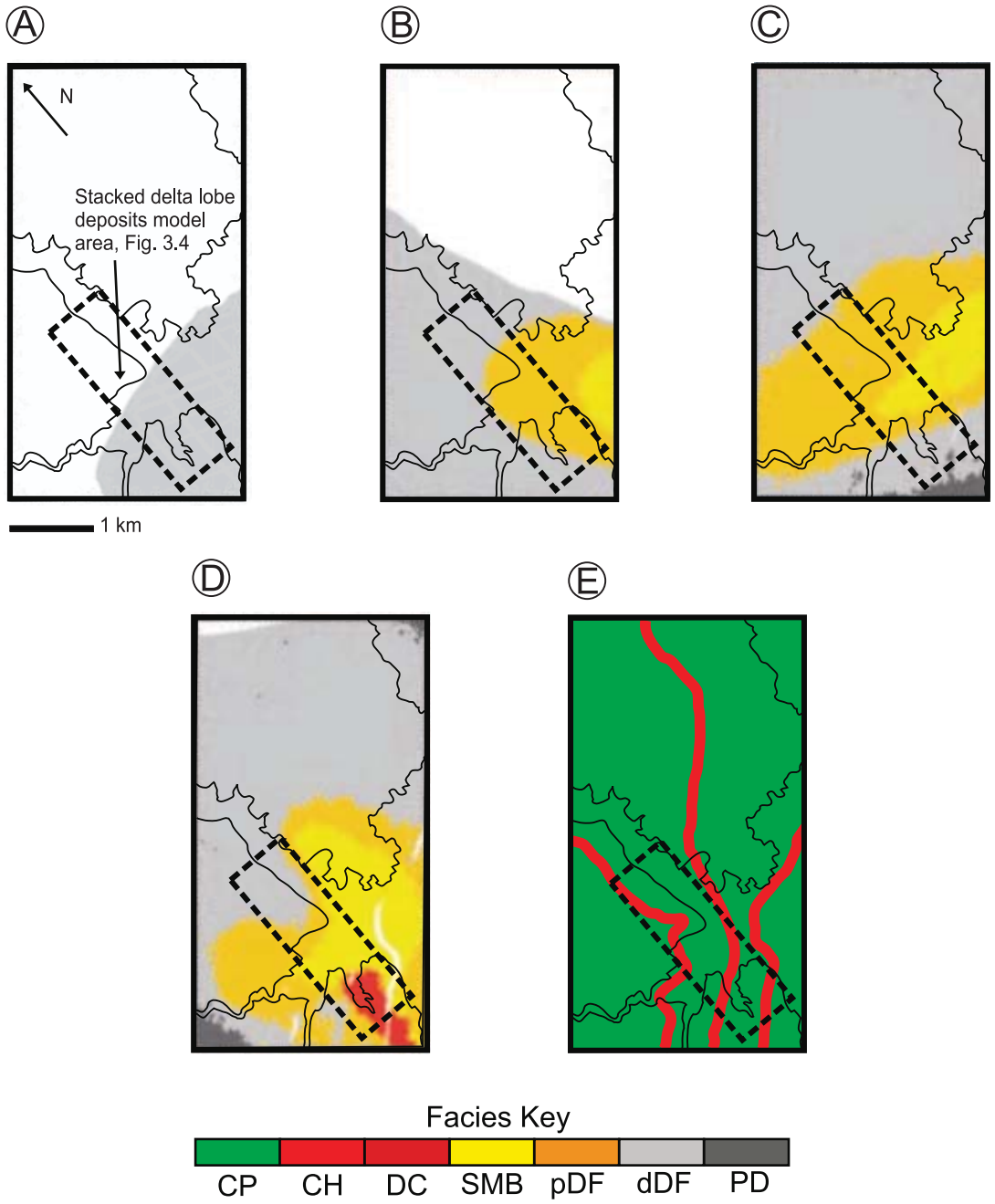


Figure 3.3. (A-E) Maps showing the distribution of facies-association belts at the top of parasequences 1.4, 1.5, 1.6, and 1.7 and in the overlying coastal-plain interval (after Deveugle et al. 2011), with the area of the models described in this paper shown by dashed lines. The regional palaeogeographic and stratigraphic context of the maps is illustrated in Figure 3.2.

2004). However, if further stochastic realizations of the model were generated, the position, geometry and orientation of the channelized sandbodies would change with each realization, such that channelized fluvial sandbodies may not be present in the study area (Fig. 3.3E). Modelling such sandbodies in subsurface fluvial-dominated deltaic

reservoirs is also subject to similar uncertainty. We consider uncertainties in interpretation and modelling strategies by considering two settings in the models presented herein, with channelized fluvial sandbodies either present (i.e. taken from the model of Deveugle et al., 2011) or absent (Fig. 3.4) (Table 3.1).

3.4.2 (2) Permeability anisotropy in distal delta-front heteroliths

Distal delta-front heteroliths consist of sharp or erosionally based sandstone beds alternating with mudstones (Fig. 3.1D). Sandstone beds generally form sheets that thin gradually in a palaeoseaward direction, but they may be amalgamated as a result of localized erosion at their bases (e.g., Ryer and Anderson, 2004; Olariu et al., 2010). Where mudstone beds are laterally extensive, effective vertical permeability approaches zero. The spatial distribution of erosion at the base of sandstone beds is poorly understood, but where present increases connectivity between sandstone beds that are otherwise isolated, thus increasing the effective vertical permeability (Haldorsen and Lake, 1984; Begg and Chang, 1985; Begg and King, 1985). We consider both scenarios by applying k_v/k_h ratios of 0 and 0.1 to distal delta-front deposits in our simulation experiments (Table 3.1).

3.4.3 (3) Barrier coverage along clinoform surfaces

Heterogeneity along clinoform surfaces is subject to considerable uncertainty in characterization using both outcrop and subsurface datasets, such that the proportion of each clinoform surface that acts as a barrier to flow is poorly documented, even in well-studied outcrop analogues (Howell et al., 2008b; Enge and Howell, 2010). In models of stacked delta-lobe parasequences, we investigate end-member scenarios in which

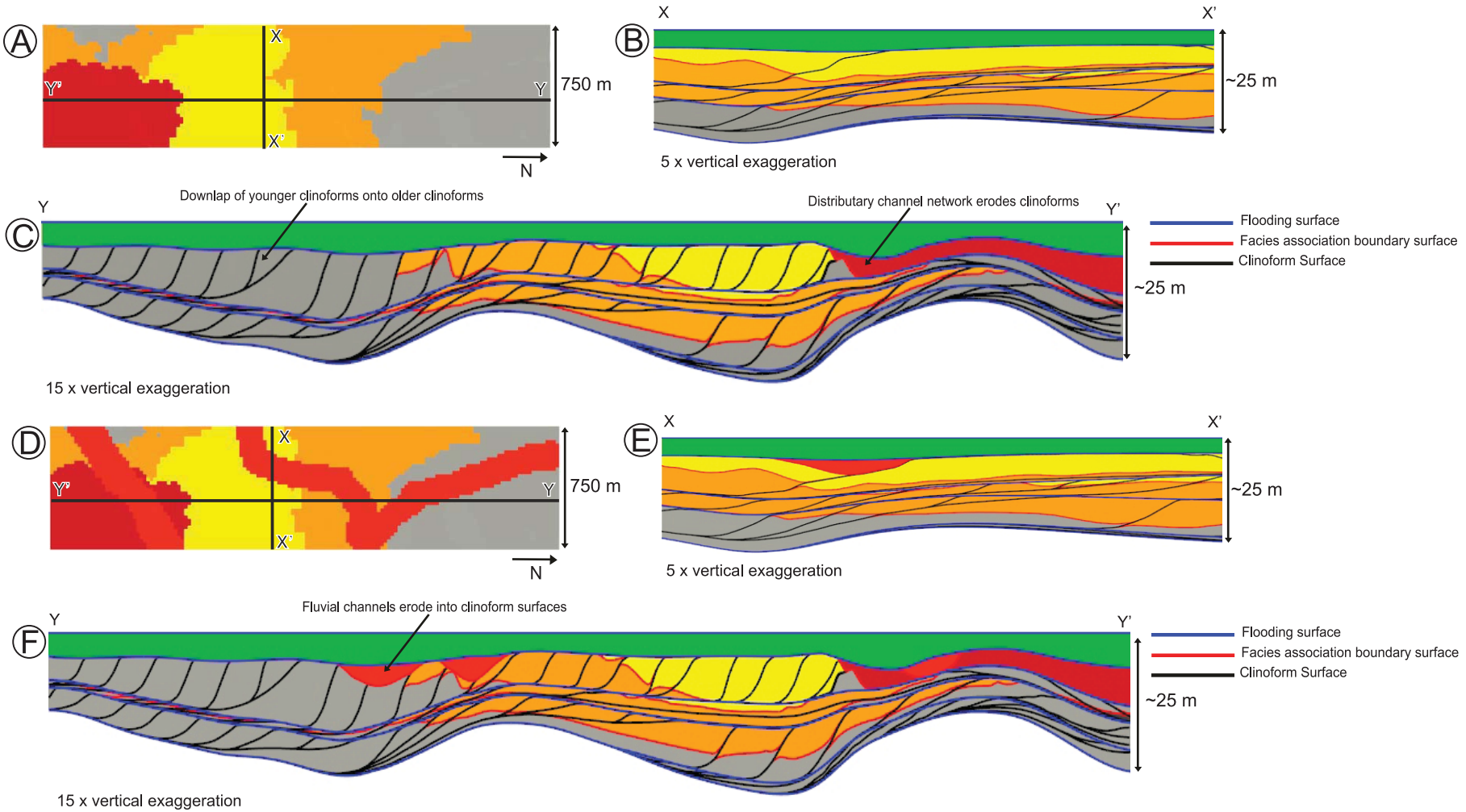


Figure 3.4. (A, D) Maps showing the distribution of facies-association belts at the top of shallow-marine deposits in models of stacked delta-lobe parasequences, and associated model cross-sections illustrating facies architecture along (B, E) regional depositional dip and (C, F) regional depositional strike. Two models are shown, either (A-C) lacking or (D-F) containing channelized fluvial sandbodies that truncate the underlying delta-lobe parasequences.

mudstone barriers along clinoform surfaces are either absent (0% barrier coverage along clinoform surfaces) or extensive (90% barrier coverage along clinoform surfaces) (Table 3.1).

3.4.4 (4) Permeability of channelized sandbodies

Deveugle et al. (2011) noted that distributary channel-fill sandstones (DC facies association) are genetically related to the delta-lobe deposits at their down-dip terminations, and hence inferred that they share similar sediment-textural characteristics and petrophysical properties with the stream-mouth bar (SMB) facies association in the proximal parts of delta lobes (Fig. 3.1C). In contrast, fluvial channel-fill sandstones (FC facies association) (Fig. 3.3E) are genetically unrelated to underlying delta-lobe deposits, and may have markedly differing sediment-textural characteristics and petrophysical properties. We follow the approach of Deveugle et al. (2011) by investigating the impact of sediment-textural characteristics such as grain size on flow (Fig. 3.1E), by assigning higher permeability values to channelized fluvial sandbodies. We investigate two scenarios, in which permeabilities in channelized fluvial sandbodies remain the same as distributary channel-fill (DC) and stream-mouth bar (SMB) sandstones, or are five times larger (Table 3.1).

3.5 Production strategy

Production is simulated using a line-drive waterflood development, using conventional black oil simulation software, with four vertical injection wells and six vertical production wells spaced 750 m apart (Fig. 3.5). An example data input file used

with the simulation software can be found in Appendix B1. All wells are completed over the whole reservoir interval in each model. Two scenarios are used to investigate the impact of production rate on sweep efficiency, with oil production and water injection for the groups of production and injection wells set to maintain a target production rate over 10 years of 350 S m^3/day (2200 bbl/day), and over 20 years of 175 S m^3/day (1100 bbl/day) (Table 3.1). Similar rates were used in fluid flow simulations of clinoform-bearing models of the Ferron Sandstone Member in Enge and Howell (2010). In both production scenarios, there is a minimum bottom hole pressure (BHP) constraint of 50 bars (725 psi) for each production well and a maximum BHP constraint of 150 bars (2175 psi) for each injection well.

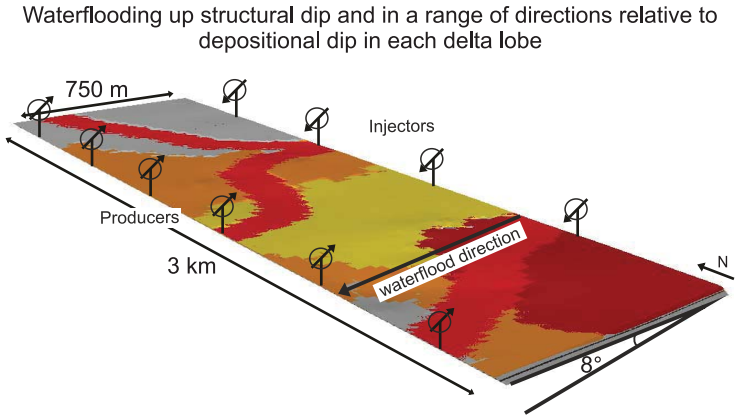


Figure 3.5. 3D perspective view showing the simulated production scheme used in the models of several stacked delta-lobe deposits (parasequences 1.4-1.7 and overlying coastal-plain deposits of Deveugle et al., 2011; Fig. 3.3A-E) illustrated using maps of facies-association belts at the top of the model volumes. A structural dip of 8° is applied to all models, which results in simulated waterflooding in a range of directions relative to the local depositional dip (i.e. azimuthal orientation) of each delta-lobe parasequence (Fig. 3.3A-E). In all models, production is simulated using a line drive of four injection wells located down structural dip of six production wells.

3.6 Design of simulation experiments

We use an experimental design approach and analysis of variance, which allows the relative effects of different variables to be quantified whilst minimizing the number

of simulation experiments (Box and Draper 1987; Willis and White, 2000). Two sets of simulation experiments were carried out using the reservoir-scale models of several, stacked delta-lobe deposits, in order to quantify the impact of four geological heterogeneities (numbered 1-4 in Table 3.1) and one engineering decision (numbered 5 in Table 3.1) on recovery. In the first set of simulation experiments, channelized fluvial sandbodies may be present or absent (Table 3.1), while in the second set, channelized fluvial sandbodies of varying permeability are always present (Table 3.1). A two-level fractional-factorial design was used in both sets of simulation experiments, with each of the studied factors varied between two end-member settings (Table 3.1).

3.7 Model construction

We follow a surface-based approach to model construction (Sech et al., 2009; Jackson et al., in press), in which surfaces are used to represent both key stratigraphic surfaces and facies boundaries. Surfaces are modelled before the grid is defined, so that model resolution is not limited by grid resolution (Jackson et al., 2009). The geometry of the grid is driven by the geometry of the modelled surfaces and we simulate fluid-flow directly on these grids without upscaling, thus allowing the complex spatial geometries in the model to be preserved during flow simulation.

3.7.1 Geological framework for clinoform-bearing models of the Ferron Sandstone outcrop analogue

We focus on four delta-lobe deposits within the lowermost sandstone tongue of the Ferron Sandstone Member (parasequences 1.4, 1.5, 1.6 and 1.7 of Deveugle et al.,

2011) and thin (< 10 m) overlying coastal-plain deposits in the Ivie Creek study area (Figs. 3.3A-E, 3.4). Each delta-lobe deposit exhibits a subtle change in plan-view aspect ratio (width/length) and azimuthal orientation (Fig. 3.3A-D) (Figure 11 in Deveugle et al., 2011). Surfaces representing parasequence-bounding flooding surfaces and facies-association boundaries are extracted from the model of Deveugle et al. (2011) over a model area of 750 x 3000 m (Fig. 3.3). There are no geological faults within the model volume. In the model of stacked delta-lobe deposits (Fig. 3.4), we adjust the surface representing the top of the coastal-plain deposits (approximating the sub-A coal seam; Anderson and Ryer, 2004) so that it is horizontal over the model area, and use it as a reference surface from which the vertical positions of all other flooding surfaces and facies-association boundaries are reconstructed via isochores. This reference horizon is chosen because it is underlain by the sub-A coal seam, implying that it was essentially palaeohorizontal (Deveugle et al., 2011). The parasequence-bounding flooding surfaces at the top and base of each delta lobe deposit define the rock volume within which clinoform surfaces are to be modelled, and are used as an input for the clinoform-modelling algorithm described in Chapter 2. In a subsequent step, described in a later section, we apply a uniform structural dip to the model.

3.7.2 Modelling the geometry and distribution of clinoform surfaces

The clinoform-modelling algorithm (Chapter 2) allows the user to specify the plan-view and cross-sectional geometries, distribution and progradation direction of clinoform surfaces within a delta-lobe deposit. Its application to modelling clinoforms in multiple, stacked delta lobe deposits is outlined briefly below (for a fuller description of its

application, see Chapter 2). The plan-view aspect ratio and azimuthal orientation of each delta-lobe deposit was taken from Deveugle et al. (2011; their Figure 11).

Geometrical data describing the distribution, cross-sectional shape and length of clinoforms in depositional dip cross-section were extracted from bedding-diagram interpretations of Forster et al. (2004), clinoform length and dip statistics of Enge et al. (2010), and the LIDAR data used to create the model of Enge and Howell (2010) (Table 3.2). For delta-lobe deposits in which only one or two distal facies associations are present in the model volume (parasequences 1.4 and 1.5, Fig. 3.3A-B), we extract data describing clinoform geometry for each facies-association type in the area where outcrop data are available and use these values as inputs for applying the clinoform-modelling algorithm (Table 3.2). We use the clinoform-modelling algorithm to deterministically model clinoform surfaces in the area where outcrop data are available, and to stochastically populate clinoform surfaces elsewhere in the model volume. Clinoforms are distributed in each delta-lobe deposit with a uniform spacing of 100 m (e.g. Fig. 3.4), where clinoform spacing is defined as the horizontal distance between the top-truncation points of two successive clinoform surfaces (see Chapter 2). Each delta-lobe deposit is interpreted to contain a dense, downstream-branching network of distributary channels (e.g. Wellner et al., 2005; Olariu and Bhattacharya, 2006; cf. Fig. 3.1B), which is represented as an erosionally based, downstream-thinning and downstream-widening zone lacking clinoforms in the innermost part of each modelled delta-lobe deposit (e.g. Fig. 3.4). The uppermost delta-lobe parasequence (parasequence 1.7) is locally truncated by channelized fluvial sandbodies in some models (Fig. 3.4D-F). We then use facies-association boundary surfaces extracted from the model of Deveugle et al., (2011), in combination with the clinoform surfaces and parasequence-bounding flooding surfaces,

Table 3.2. Values of parameters used in the clinoform-modelling algorithm described in Chapter 2, for models of the Ferron Sandstone Member reservoir analogue.

Parasequence	Parameter	Description	Min.-Max. Values	Units
1.4	t_L	length of top ellipse in depositional dip direction	3700	m
	t_W	length of top ellipse in depositional strike direction	2400	m
	L	clinoform length	160-980	m
	b_L	length of base ellipse in depositional dip direction	3860-4680	m
	b_W	length of base ellipse in depositional strike direction	2560-3380	m
	P	clinoform shape function exponent	2	none
	p_O	axis of progradation relative to bounding surfaces	50%	none
	θ	clinoform progradation angle relative to north	000	°
	S	clinoform spacing	100	m
1.5	t_L	length of top ellipse in depositional dip direction	3700	m
	t_W	length of top ellipse in depositional strike direction	2400	m
	L	clinoform length	60-1200	m
	b_L	length of base ellipse in depositional dip direction	3760-4900	m
	b_W	length of base ellipse in depositional strike direction	2460-3600	m
	P	clinoform shape function exponent	2	none
	p_O	axis of progradation relative to bounding surfaces	60%	none
	θ	clinoform progradation angle relative to north	314	°
	S	clinoform spacing	100	m
1.6	t_L	length of top ellipse in depositional dip direction	3700	m
	t_W	length of top ellipse in depositional strike direction	2400	m
	L	clinoform length	50-625	m
	b_L	length of base ellipse in depositional dip direction	3750-4325	m
	b_W	length of base ellipse in depositional strike direction	2450-3025	m
	P	clinoform shape function exponent	2	none
	p_O	axis of progradation relative to bounding surfaces	32%	none
	θ	clinoform progradation angle relative to north	274	°
	S	clinoform spacing	25, 50 or 100	m
1.7	t_L	length of top ellipse in depositional dip direction	3700	m
	t_W	length of top ellipse in depositional strike direction	2400	m
	L	clinoform length	40-490	m
	b_L	length of base ellipse in depositional dip direction	3740-4190	m
	b_W	length of base ellipse in depositional strike direction	2440-2890	m
	P	clinoform shape function exponent	2	none
	p_O	axis of progradation relative to bounding surfaces	50%	none
	θ	clinoform progradation angle relative to north	005	°
	S	clinoform spacing	100	m

to create facies-association zones within each clinothem (i.e. between each pair of clinoform surfaces). Each facies-association zone is gridded separately, such that the grid conforms to the architecture of the flooding surfaces, clinoform surfaces, and facies-association boundaries. The resulting surface-based models contain up to 211 surfaces (5 flooding surfaces, 100 clinoform surfaces, and 106 facies-association boundaries) and capture the complex facies architectures and clinoform distributions within the parasequence set (Fig. 3.4).

3.7.3 Modelling heterogeneity along clinoform surfaces

We represent discontinuous, impermeable mudstone or concretionary cemented barriers along clinoform surfaces in the models using bodies that are elliptical in plan view (after the methodology of Jackson et al., 2009). There are few outcrop datasets that quantify the extent or geometry of such barriers along clinoform surfaces (e.g., White and Willis, 2000; Hampson et al., in review). Sensitivity tests indicate that ellipses are suitable objects to represent these barriers for modelling and flow simulation purposes, because they can be described using simple mathematical functions, and their abundance and overlap control barrier coverage along clinoforms provided that ellipse dimensions are small relative to the area of the clinoform surface (Jackson et al., 2009). In this case, small ellipses (<150 m diameter) are stochastically placed along each clinoform surface using a frequency function that decreases the probability of ellipses being placed along the upper part of the clinoform (Fig. 3.6B) (Appendix A1):

$$f(x) = \frac{a}{\left[1+e^{(bx+c)}\right]}, \tag{3.1}$$

where a, b and c are dimensionless constants (a = 1. 00, b = 9.65, c = -4.32) and x is the normalized distance from the down-dip termination of the clinoform, given by:

$$x = 1 - \frac{[(b_L R) - t_L]}{[b_L - t_L]}, \tag{3.2}$$

where b_L and t_L are the respective lengths of ellipses representing the base and top of a clinoform in plan view (Table 2.1), and R is a uniformly generated random number.

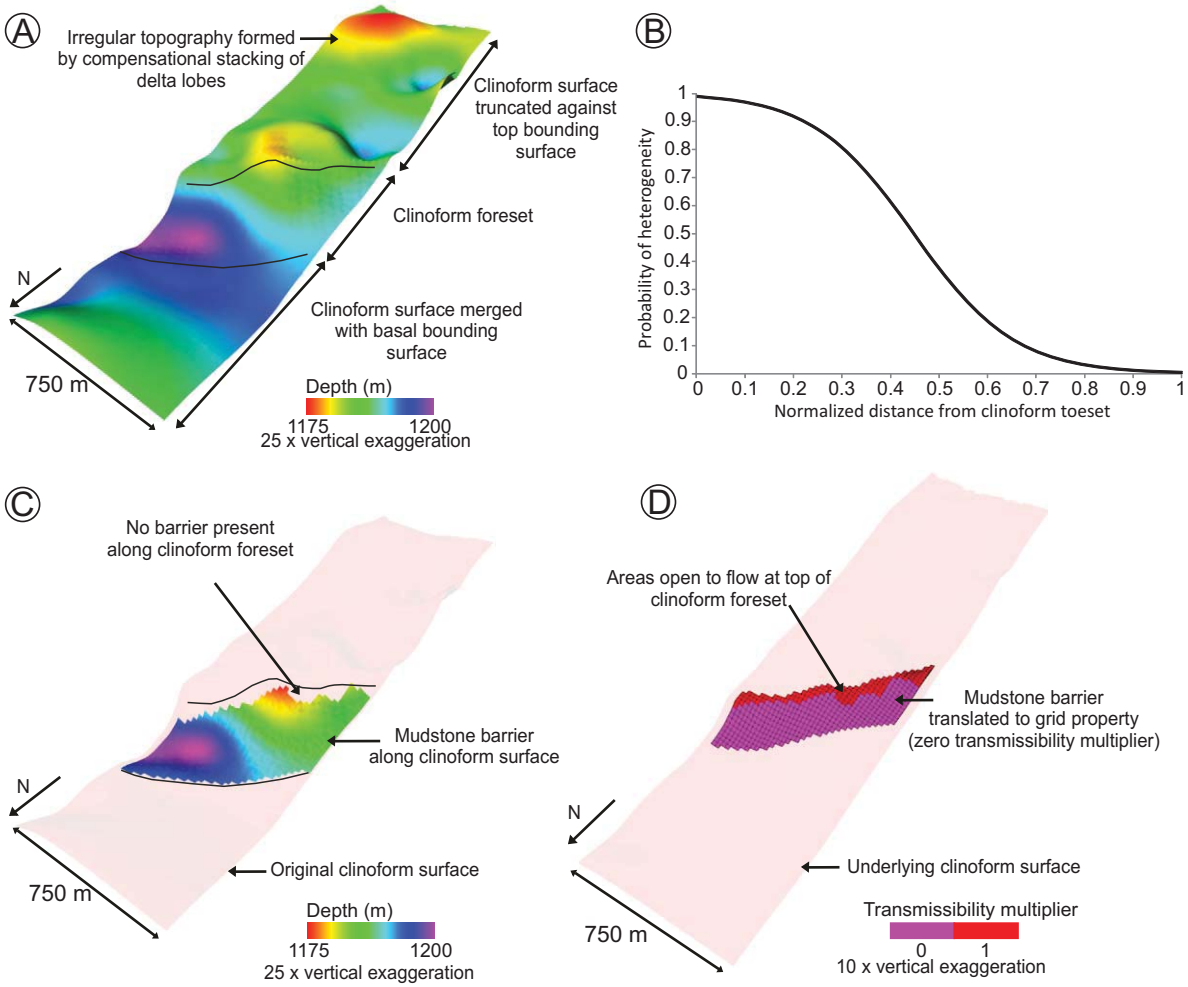


Figure 3.6. (A) 3D clinoform surface from parasequence 1.5 in the reservoir-scale model of the Ferron Sandstone (Figs. 3.2B, 3.3B), generated using the clinoform modelling algorithm described in Chapter 2. (B) The frequency function (Eq. 3.1) used to place elliptical barriers along each clinoform surface. (C) Extent of overlapping elliptical barriers along 3D clinoform surface in part A. The barriers cover 80% of the clinoform surface. (D) The barrier-covered clinoform surface in part C is translated into a transmissibility multiplier grid property in x, y, and/or z directions, depending on the orientation of the clinoform. The transmissibility multiplier is modified for cells in the grid layer above the clinoform surface. Grid cells in red are assigned a transmissibility multiplier of 1 and are open to flow, whereas grid cells in purple are assigned a transmissibility multiplier of 0 and act as a barrier to flow.

In the absence of quantitative data, the constants in Eq. 3.1 are obtained through qualitative comparison of the function with previous studies of the Ferron Sandstone Member outcrops (Garrison Jr. and Van den Bergh, 2004; Howell et al., 2008a; Enge and Howell, 2010). This method defines the spatial distribution of barriers along a clinoform surface for a value of barrier coverage that is specified by the user (Fig. 3.6C). In a final step, we translate barrier coverage along the clinoform surface into a grid property. The transmissibility of the cells in the grid layer above the clinoform surface is set to zero where a barrier is present, and remains one where barriers are absent (Fig. 3.6D). We use this process to create models in which barrier coverage along the clinoform surfaces ranges from 0 to 90%.

3.7.4 Modelling reservoir structure

The structural configuration of the reservoir influences well placement, so that water is injected up structural dip to production wells, and the density contrast between oil and water helps to stabilize the displacement front. The relationship between structural dip and waterflood direction can also strongly modify the effect of depositional clinoform dip on sweep (Wehr and Brasher, 1996; Howell et al., 2008a; Jackson et al., 2009). We apply the methodology of Jackson et al., (2009) to adjust the vertical coordinates of the grid cells in every grid layer to impose a uniform structural dip of 8° that is representative of fluvial-dominated deltaic reservoirs in the Prudhoe Bay field (e.g. Begg et al., 1992), and shallow-marine reservoirs within tilted fault blocks in the North Sea (e.g. Tollas and McKinney, 1991; Wehr and Brasher, 1996; Husmo et al., 2003). For the model of stacked delta-lobe deposits, waterflooding is simulated up structural dip (Fig. 3.5), but each of the delta-lobe deposits in the model has a different azimuthal

orientation relative to the waterflood direction, such that some are aligned along depositional dip and others along depositional strike (Fig. 3.3A-D).

3.7.5 Rock and fluid properties

In the final step before fluid flow simulation, petrophysical properties are assigned to each facies-association type using values from an analogous subsurface reservoir (Table 1 of Deveugle et al., 2011). In all models, a single value of porosity and permeability is assigned to each facies association (Table 3.3). We use this approach

Table 3.3. Reservoir, rock and fluid properties used in models of the Ferron Sandstone Member reservoir analogue.

Reservoir properties	Value	Units
Reservoir pressure (P_r)	100	bar
Top (single parasequence model)	1130	m
Base (single parasequence model)	1246	m
Top (stacked parasequence model)	1078	m
Base (stacked parasequence model)	1198	m
Fluid properties		
Oil viscosity (μ_o)	0.7	cp
Oil density (ρ_o)	650	kg/m^3
Oil compressibility (c_o)	10^{-4}	1/bar
Oil formation volume factor (B_o)	1.00000009	(rm^3/sm^3)
Water viscosity (μ_w)	0.3	cp
Water density (ρ_w)	950	kg/m^3
Water compressibility (c_w)	10^{-5}	1/bar
Water formation volume factor (B_w)	1	(rm^3/sm^3)
Rock properties		
Porosity ($\emptyset$) of prodelta mudstone (PD) facies association	0	%
Horizontal (k_h) and vertical permeability (k_v) of PD facies association	0 (k_h), 0 (k_v)	mD
Porosity ($\emptyset$) of distal delta front heteroliths (dDF) facies association	18	%
Horizontal (k_h) and vertical permeability (k_v) of dDF facies association	71 (k_h), 7 (k_v)	mD
Porosity ($\emptyset$) of proximal delta front sandstones (pDF) facies association	27	%
Horizontal (k_h) and vertical permeability (k_v) of pDF facies association	433 (k_h), 325 (k_v)	mD
Porosity ($\emptyset$) of stream mouth bar sandstones (SMB) facies association	28	%
Horizontal (k_h) and vertical permeability (k_v) of SMB facies association	1793 (k_h), 1614 (k_v)	mD
Porosity ($\emptyset$) of distributary channel-fill sandstones (DC) facies association	28	%
Horizontal (k_h) and vertical permeability (k_v) of DC facies association	1793 (k_h), 1614 (k_v)	mD
Porosity ($\emptyset$) of fluvial channel-fill sandstones (FC) facies association	28	%
Horizontal (k_h) and vertical permeability (k_v) of FC facies association	1793 (k_h), 1614 (k_v)	mD
Rock compressibility for all facies associations (c_r)	10^{-12}	1/bar

because the boundaries between facies associations are typically marked by order-of-magnitude contrasts in permeability that control sweep patterns. Although we recognize that petrophysical properties vary within facies-association types, we do not explicitly include these heterogeneities because they occur over lengthscales smaller than a single grid block in the models (Fig. 3.1D-F). We apply the same relative permeability data, which are typical of water-wet reservoirs in the North Sea (e.g. Anderson, 1987; Stiles and Hutfilz, 1992), to each facies association. Capillary pressure curves are dependent on the facies-association type. These data, as well as oil and water properties, are similar to those documented in many North Sea Brent Group reservoirs and have been widely used in previous modelling studies of shallow-marine reservoirs (e.g. Kjønsvik et al. 1994; Matthews et al., 2008; Jackson et al., 2009).

3.8 Results

We begin by considering the first set of simulation experiments where models of stacked delta-lobe deposits either contain or lack channelized fluvial sandbodies (Table 3.1). We quantify the impact of geological heterogeneities and/or engineering decisions on recovery factor and total water produced, by calculating the average change in response from the mean when a factor is changed from setting one to setting two (Table 3.1). We then go on to consider models of stacked delta-lobe deposits that always contain channelized fluvial sandbodies in the second set of simulation experiments (Table 3.1). We use this approach in order to quantify the effect on recovery factor and total water produced of varying the rock properties of the channelized fluvial sandbody (FC)

facies association, in the context of other reservoir characterization and engineering parameters.

3.8.1 Stacked delta-lobe deposits with channelized fluvial sandbodies either present or absent

Simulated oil recovery after 10 or 20 years of production at the target production rates (Table 3.1) ranges from 19 to 24 % of the original oil-in-place. Recovery is dominated by production from stream mouth-bar sandstone (SMB) and proximal delta-front sandstone (pDF) facies associations, and the variation in recovery is principally controlled by the presence or absence of laterally extensive barriers to flow along clinoforms (Fig. 3.7A). Modelling clinoforms with a 90% barrier to flow along them decreases oil recovery by c. 5% (green bar in Fig. 3.7A) and increases the total water produced in the models by c. 55% (blue bar in Fig. 3.7A), which suggests that characterizing clinoforms in field-scale models of fluvial-dominated deltaic reservoirs is important to accurately predict water breakthrough and hydrocarbon recovery.

When k_v/k_h = 0.1 in the distal delta-front heteroliths (dDF) facies association, oil recovery is increased by c. 2% and total water produced is decreased by c. 44% (Fig. 3.7A). If there is a barrier along 90% of each clinoform surface and k_v/k_h = 0.1 in the dDF facies association, oil recovery is increased by c. 2%, but total water produced is increased by c. 34% (Fig. 3.7A). This suggests that a greater volume of oil is displaced in the dDF facies association when vertical permeability is increased, but it does not have the same impact on sweep efficiency in the reservoir as the presence of channelized fluvial sandbodies.

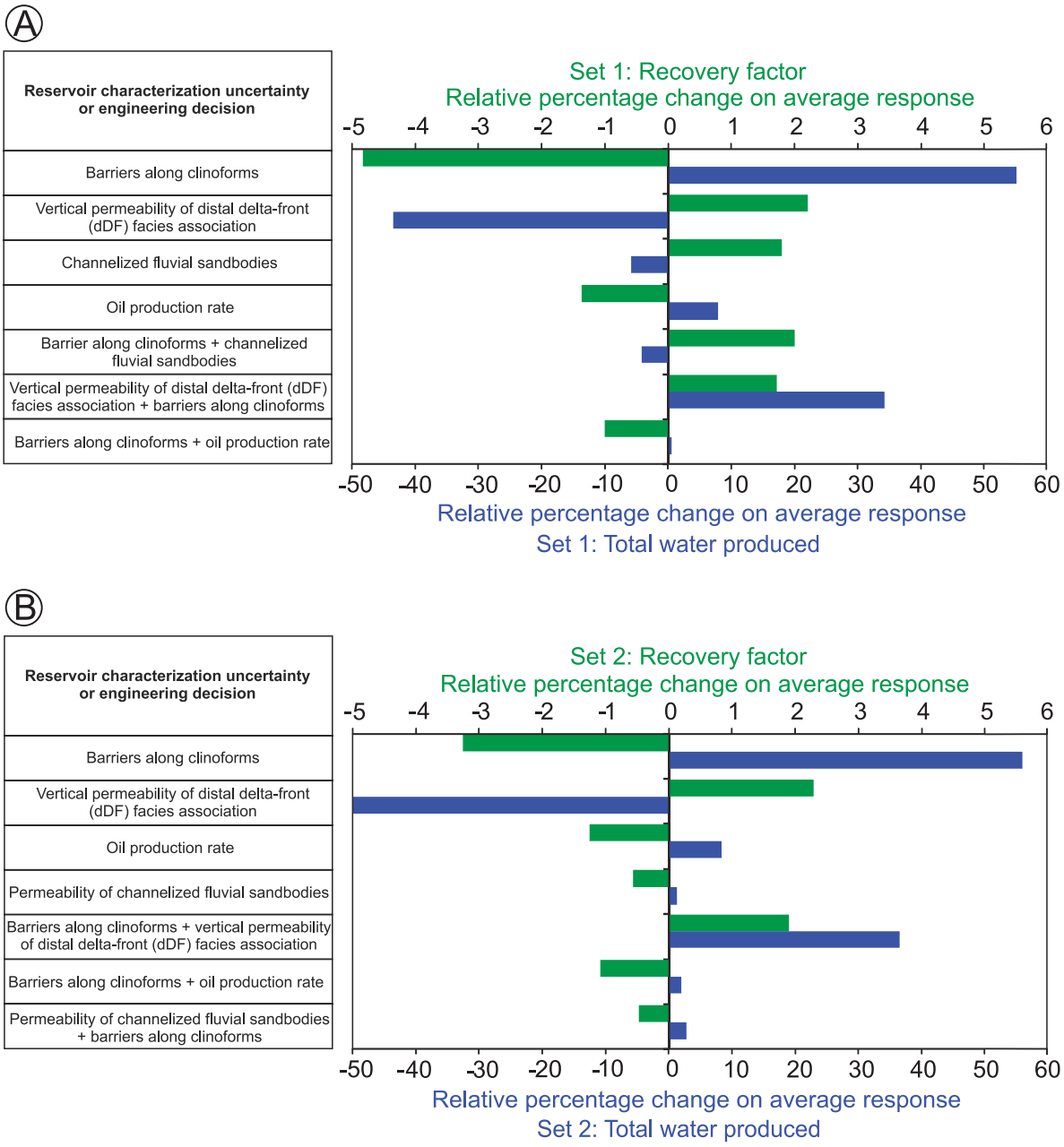


Figure 3.7. Average percentage change in oil recovery (green bars) and total volume of water produced (blue bars) in models of stacked delta-lobe deposits, observed when each factor in the experimental design is varied from setting 1 to setting 2 (Table 3.1), for: (A) models that either contain or lack channelized fluvial sandbodies (i.e. set 1 of simulation experiments in Table 3.1); and (B) models that contain channelized fluvial sandbodies of varying permeability (i.e. set 2 of simulation experiments in Table 3.1). If the bars lie to the right then the change is positive and more oil is recovered or more water is produced. For example, if the models contain a 90% barrier to flow along clinoforms (setting 2), oil recovery decreases by c. 5% and increases the total water produced in the models by c. 55% compared with models containing clinoforms with 0% barrier coverage (setting 1). The effects of individual factors and combinations of factors are displayed, where these are considered significant (i.e. >0.5% change in recovery factor, >1% change in total water produced).

The presence of laterally continuous, channelized fluvial sandbodies alone increases oil recovery by c. 2 % and reduces the total water produced by c. 6% (Fig. 3.7A). Furthermore, if clinoforms are present with a 90% barrier along them, the presence of channelized fluvial sandbodies can increase recovery by c. 2% and decrease total water production by c. 4% (Fig. 3.7A), suggesting that their presence improves sweep efficiency in the reservoir.

Engineering parameters have much less impact on oil recovery, with the average effect of increasing the oil production rate being below that for variations in geological heterogeneity (c. 1% decrease; Fig. 3.7A). Increasing oil production rate increases total water production by c. 7%, (Fig. 3.7A).

3.8.2 Stacked delta-lobe deposits with channelized fluvial sandbodies always present

In these experiments simulated oil recovery after 10 or 20 years of production at the target production rate (Table 3.1) ranges from 20 to 24 % of the original oil-in-place. The presence or absence of laterally extensive barriers along clinoforms also has the most significant impact on oil recovery (Fig. 3.7B). When clinoforms are covered along 90% of their area by a barrier to flow, the average effect across the models is that oil recovery is reduced by c. 3% (green bar in Fig. 3.7B) and total water produced is increased by c. 50% (blue bar in Fig. 3.7B). Both of these values are less than the equivalent response in the first set of experiments when channelized fluvial sandbodies are absent (Fig. 3.7A).

As in the first set of simulation experiments, increasing the vertical permeability of the distal delta-front (dDF) facies association has the most significant positive impact on oil recovery. When k_v/k_h = 0.1, oil recovery is increased by c. 2% and total water

produced is reduced by c. 50% (Fig. 3.7B). When the effect of increasing vertical permeability is combined with that of including laterally extensive barriers to flow along clinoforms, the average response of oil recovery also increases by c.2% (Fig. 3.7B). Oil production rate has a more significant impact on oil recovery than in the first set of simulation experiments. Increasing oil production rate (from setting one to setting two; Table 3.1) decreases oil production by c. 1% on average and increases total water produced by c. 8% (Fig. 3.7B).

The permeability of the channelized fluvial sandbodies does not have a significant impact in the simulation experiments if the modelled permeability is increased by a factor of five. Oil recovery is reduced by <1% and total water production is increased by c. 1% (Fig. 3.7B). Similarly, there is not a significant impact on either oil recovery or total water production when the effect of increased permeability of channelized fluvial sandbodies is combined with that of including laterally extensive barriers to flow along clinoforms (Fig. 3.7B).

3.9 Discussion

Our results indicate that modelling barriers to flow along clinoforms has the most significant effect on hydrocarbon recovery and total water produced in models of multiple, stacked fluvial-dominated delta-lobe deposits (Fig. 3.7). We also find that modelling channelized fluvial sandbodies and non-zero vertical permeability in the distal delta-front (dDF) facies association can have a significant positive effect on hydrocarbon recovery when clinoforms are present with a 90% barrier to flow along them. The

reasons for these results are discussed below, along with the implications for reservoir monitoring schemes and reservoir management strategies.

3.9.1 Impact of clinoform-surface character, distribution and associated uncertainty

Mudstone barriers along clinoform surfaces control the tortuosity of flow paths between injection and production wells, and hence sweep efficiency in the models. When there is no barrier coverage along clinoforms, pressure communication between injection and production wells is maintained, which leads to high sweep efficiency and oil recovery (Fig. 3.8C). Injected water moves first through the SMB facies-association belt. The density contrast between water in the SMB facies-association belt and oil in the underlying pDF facies-association belt then causes gravity-driven downward movement of water to displace oil from the pDF deposits. The dDF facies-association belt remains largely unswept if there is no vertical permeability to allow similar gravity-driven displacement to occur (Fig. 3.8C). When there is 90% barrier coverage along clinoforms, sweep efficiency is reduced (Fig. 3.8D) and hence oil recovery decreases. The number of potential flow pathways between injection and production wells decreases, such that injected water is forced to exploit complex and tortuous flow pathways through the upper part of each clinothem, which reduces pressure communication between wells. This causes an increase in pressure drawdown at the production wells in order to maintain the target oil production rate, increasing the contribution of viscous forces relative to gravity, further suppressing the downward movement of water. The injected water exploits the shortest high permeability pathways through the SMB facies-associated belt, which leads to earlier water breakthrough (Fig. 3.8D). As viscous forces increasingly dominate in the reservoir, the efficiency of gravity-driven downward flow

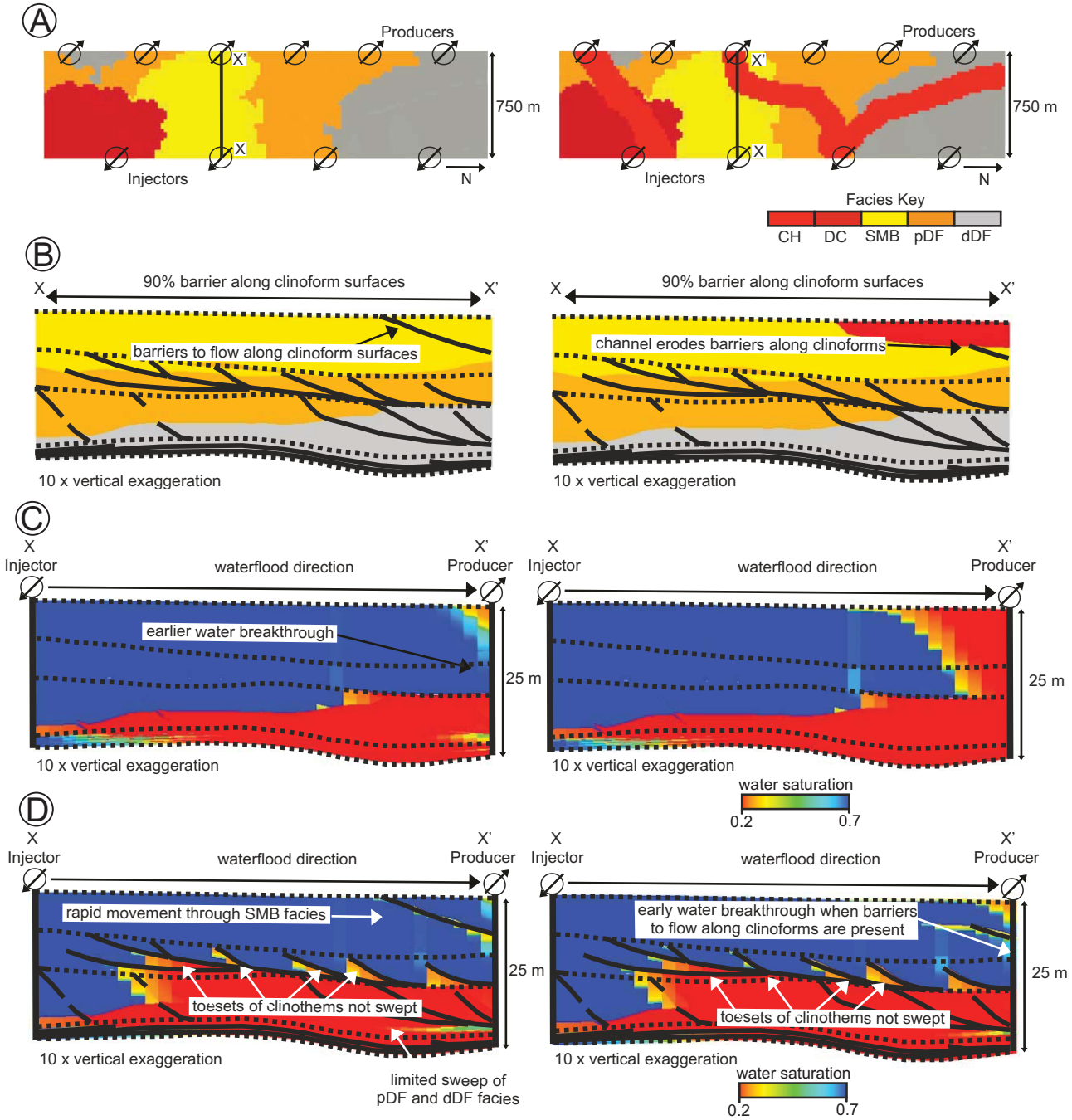


Figure 3.8. Maps and cross-sections illustrating models of stacked delta-lobe deposits that either (left column) lack or (right column) contain channelized fluvial sandbodies which erode down from overlying coastal-plain deposits. (A) Maps of facies-association belts near the top of the models (parasequence 1.7, Fig. 3.3D, with overlying coastal-plain deposits, Fig. 3.3E, removed) showing location of injection and production wells, and the cross-sections illustrated in parts B-E. (B) Depositional-dip-oriented cross-sections showing the internal facies architecture of the modelled parasequences, with barriers covering 90% of each clinoform surface shown as black lines and the location of parasequence-bounding flooding surfaces shown as dashed black lines. (C) Depositional-dip-oriented cross-sections showing water saturation after 10 years of production for models that lack barriers to flow along clinoforms with a target oil production rate over 10 years of 350 S m^3/day (2200 bbl/day). Earlier water breakthrough occurs locally in the model lacking channelized fluvial sandbodies (left). (D) Corresponding cross-sections showing water saturation after 10 years of production with a target oil production rate over 10 years of 350 S m^3/day (2200 bbl/day) for models that have a 90% barrier to flow along clinoforms. Early water breakthrough occurs in both models locally when a 90% barrier to flow along clinoforms is present.

into underlying pDF deposits within each clinothem is reduced. Therefore as barrier coverage along clinoforms increases, less oil is displaced in the pDF facies-associated belt and oil recovery is reduced accordingly (Fig. 3.8D).

Although seismic reflection data may in some cases allow the position of clinoforms to be mapped in the subsurface (e.g. Dreyer et al. 2005), clinoform distribution is at best only partially resolved. To gain an understanding of the impact of varying clinoform distribution, we analyze the sensitivity of oil recovery in models with spacing between clinoforms of either 25 m, 50 m or 100m in models of a single delta-lobe deposit (parasequence 1.6, Fig. 3.3C), to reflect uncertainty arising from the limited resolution of seismic data and associated uncertainty in interpretation. Similarly, we analyze the impact of varying barrier coverage in models of a single delta-lobe deposit (parasequence 1.6, Fig. 3.3C), and follow the approach of previous studies by varying barrier coverage along clinoforms in 10% increments between the end-member settings of 0 and 90% (Table 3.1) (Howell et al., 2008b; Enge and Howell, 2010; Jackson et al, 2009). Increasing the spacing between clinoform surfaces decreases the tortuosity of flow paths between injectors and producers, such that the effects of gravity become more pronounced. When clinoform spacing is large, there is greater pressure communication between injection and production wells, and the pressure drawdown at the production wells is relatively modest. Injected water moves rapidly through the SMB facies-association belt, and the density contrast with oil in the underlying pDF deposits causes gravity-driven downward movement of water along the clinoform surface to sweep the underlying pDF facies-association belt (Fig. 3.9C). This effect is increasingly suppressed as the clinoforms become more closely spaced (Fig. 3.9D, E). Therefore,

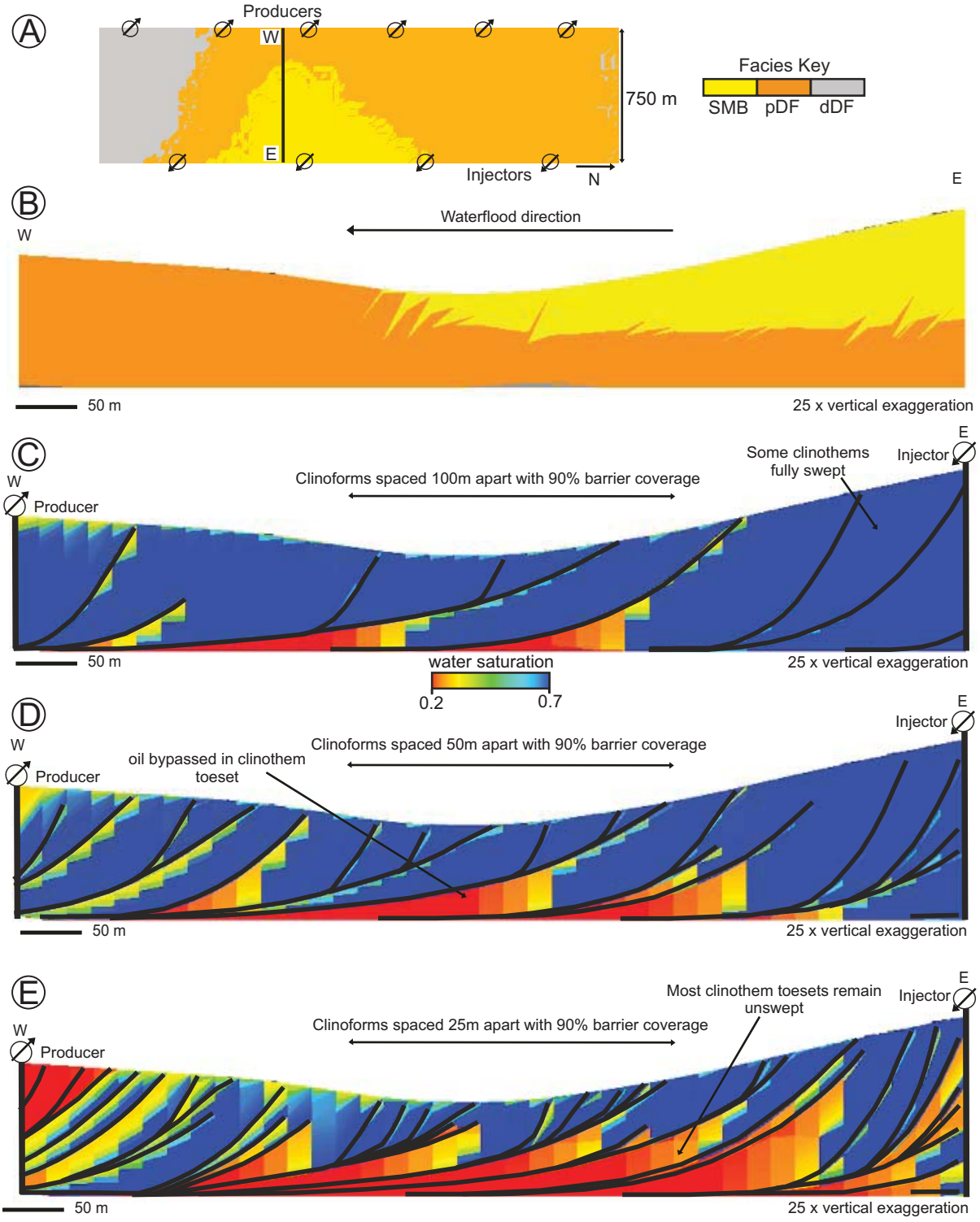


Figure 3.9. (A) Map of facies-association belts at the top of a single delta-lobe deposit extracted from our reservoir model (parasequence 1.6 in Figs. 3.3C, 3.4), showing location of injection and production wells, and the cross-sections illustrated in parts B-E. (B) Depositional-dip-oriented cross-section showing the internal facies architecture of the modelled parasequence; barriers along clinoforms are not shown. Depositional-dip-oriented cross-sections showing water saturation after 15 years of production where water has been injected via waterflooding down depositional dip with a target oil production rate over 20 years of 175 S m^3/day (1100 bbl/day), from east to west, with 90% barrier coverage along clinoform surfaces, for models with clinoform spacing of: (C) 100 m, (D) 50 m, and (E) 25 m.

increasing the spacing between clinoforms decreases the impact of barriers to flow along clinoform surfaces (Fig. 3.10A).

We observe a direct relationship between increasing barrier coverage and decreasing oil recovery (Fig. 3.10A). However, local variations in the positioning of

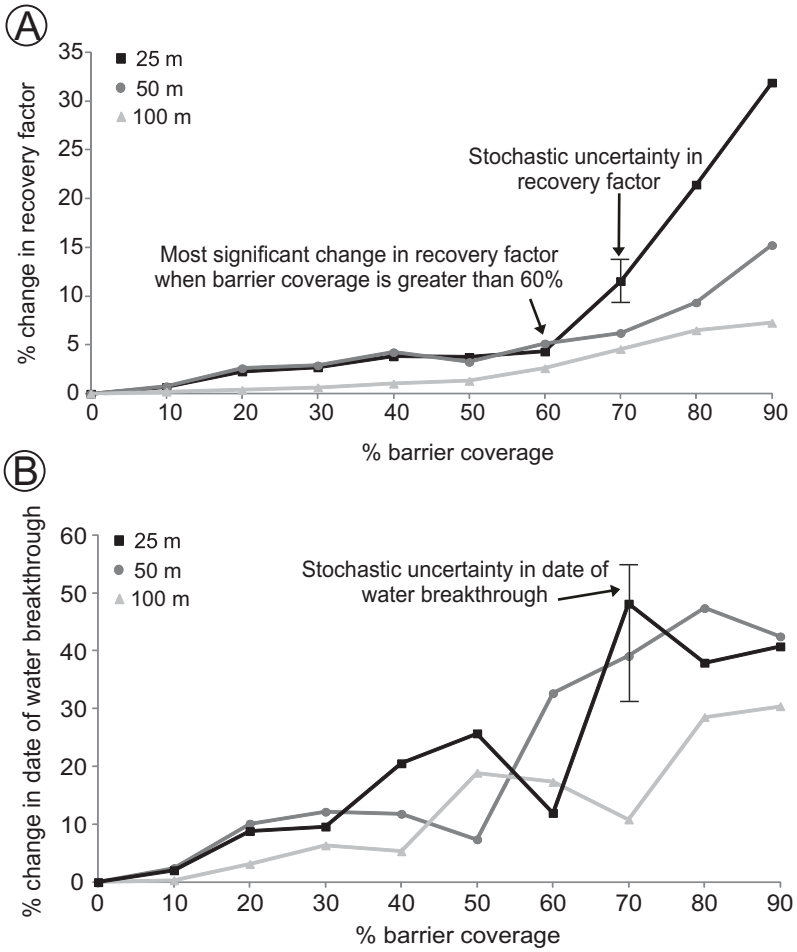


Figure 3.10. Change in (A) recovery factor and (B) time of water breakthrough with increasing barrier coverage for models of a single delta-lobe deposit (parasequence 1.6 in Figs. 3.3C, 3.4, 3.10) with different spacings of clinoform surfaces. Waterflooding is up structural dip and down depositional dip, with a target oil production rate over 20 years of 175 S m^3/day (1100 bbl/day). For 70% barrier coverage a range of values is given for recovery factor and date of water breakthrough. While the trend used to place barriers along clinoforms and the overall percentage of the surface that acts as a barrier to flow is honoured, the local position of barriers along clinoforms changes with each stochastic realization.

barriers along clinoforms determine the location of the shortest flow pathways between injection and production wells through the SMB facies-association belt and can influence

oil recovery (Fig. 3.10A). The distribution of barriers along clinoforms is generated stochastically so although the trend used to place barriers along clinoforms, and the overall percentage of the surface that acts as a barrier to flow is honoured, the local position of barriers along clinoforms changes with each realization. This causes small changes in the final predicted oil recovery demonstrated by the error bar in Figure 3.10. Stochastically generated barriers along clinoforms have greater influence on the exact time of water breakthrough (Fig. 3.10B). This reflects the detailed barrier distribution along clinoforms, relative to the location of the high-permeability SMB facies-association belt and of the injection and production wells, as well as the proportion of barrier coverage along clinoforms.

Flow-simulation results for models of stacked delta-lobe parasequences indicate that omitting widely spaced (100 m) clinoforms associated with extensive barriers (90% coverage) can lead to overprediction of oil recovery by up to 5% (Fig. 3.7), which shows close correspondence with results of equivalent models of a single delta lobe deposit (Fig. 3.10A). Further flow-simulation results for models of a single delta-lobe parasequence indicate that models lacking clinoforms may overpredict recovery by up to 35% for clinoforms of similar character and closer spacing (c. 25 m; Fig. 3.10A). Our results indicate that, of the studied geological heterogeneities and reservoir engineering parameters, clinoform surfaces have the greatest impact on oil recovery in fluvial-deltaic reservoirs (Figs. 3.7, 3.8, 3.9, 3.10).

3.9.2 Impact of channelized sandbodies

Models that contain channelized fluvial sandbodies have a higher oil recovery factor than equivalent models that lack such sandbodies, especially models in which

there are laterally extensive barriers to flow along clinoforms (Fig. 3.7A). Channelized fluvial sandbodies (FC facies association) erode into the clinoforms from a higher stratigraphic level (Figs. 3.4C, E, F, 3.11E, F), and can improve sweep efficiency by

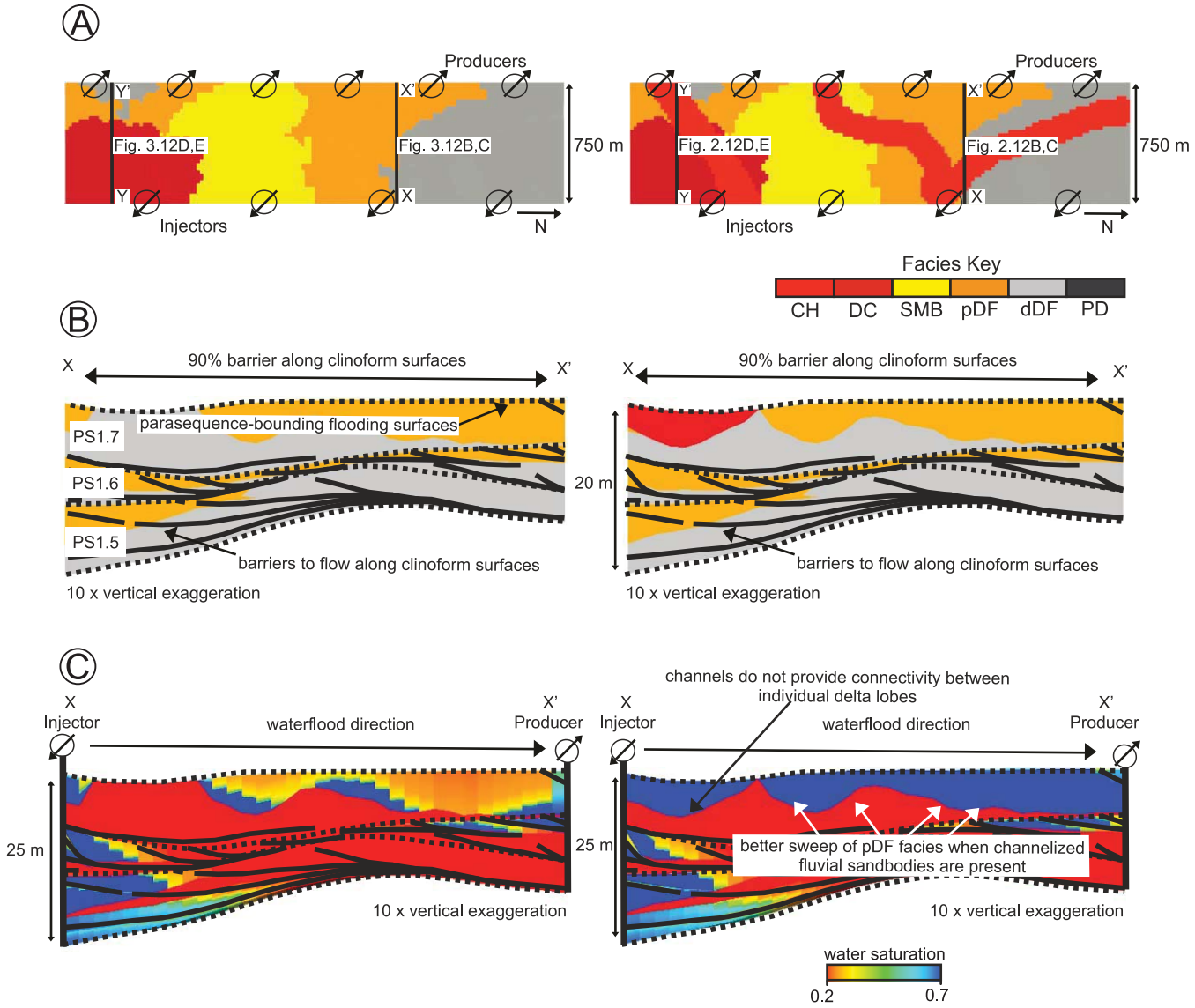


Figure 3.11A. Maps and cross-sections illustrating models of stacked delta-lobe deposits that either (left column) lack or (right column) contain channelized fluvial sandbodies that erode down from overlying coastal-plain deposits. (A) Maps of facies-association belts near the top of the models (parasequence 1.7, Fig. 3.3D, with overlying coastal-plain deposits, Fig. 3.3E, removed) showing locati n of injection and production wells, and the cross-sections illustrated in parts B-E. (B) Depositional-dip-oriented cross-sections showing the internal facies architecture of the modelled parasequences with barriers covering 90% of each clinoform surface shown as black lines and parasequence-bounding flooding surfaces as dashed lines. (C) Corresponding cross-section showing water saturation after 10 years of production with a target oil production rate over 10 years of 350 S m^3/day (2200 bbl/day). Sweep is improved locally in the model containing channelized fluvial sandbodies (right). (D-E) shown on next page.

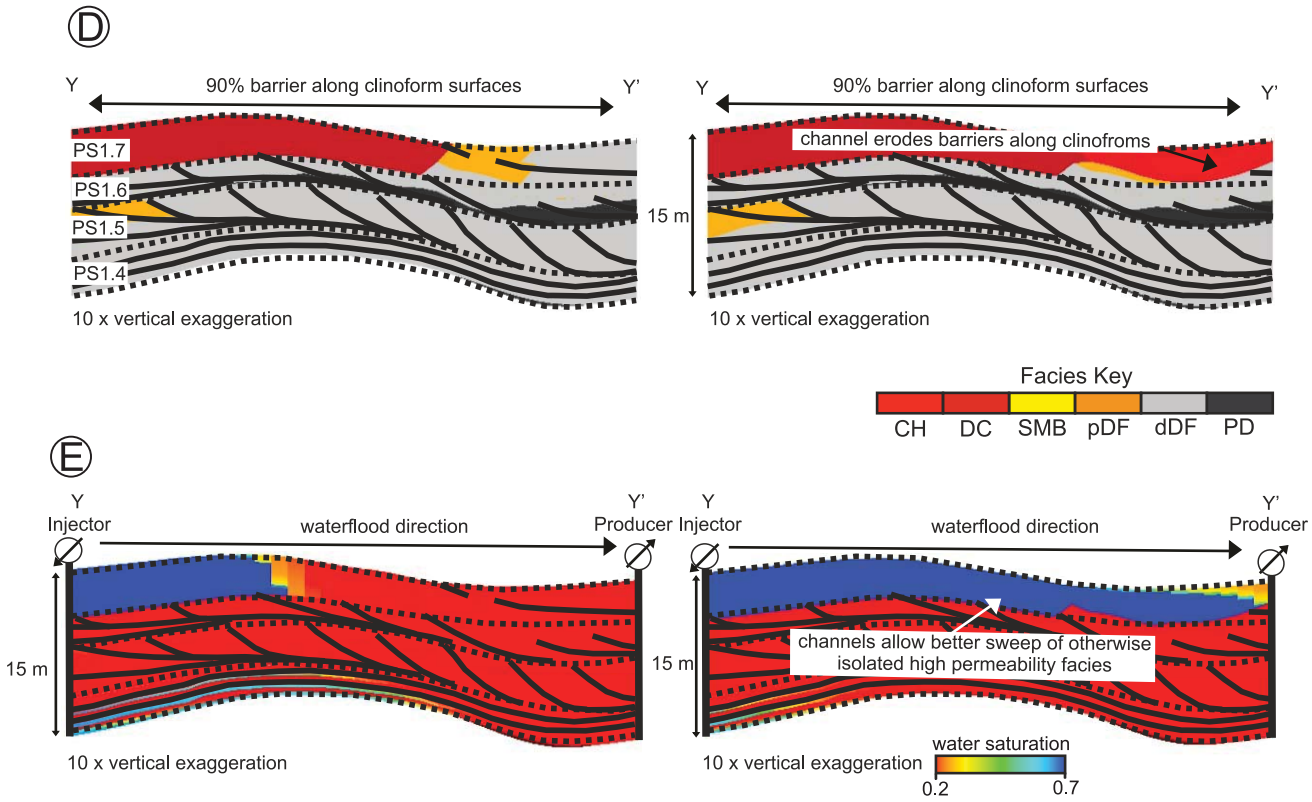


Figure 3.11B. Cross-sections illustrating models of stacked delta-lobe deposits that either (left column) lack or (right column) contain channelized fluvial sandbodies that erode down from overlying coastal-plain deposits (location maps shown in part (A) on previous page). (D) Depositional-dip-oriented cross-sections showing the internal facies architecture of the modelled parasequences with barriers covering 90% of each clinoform surface shown as black lines and parasequence-bounding flooding surfaces showed as dashed lines. Note that barriers near the top of the clinoforms (left) have been replaced by channelized fluvial sandbodies (right). (E) Corresponding cross-section showing water saturation after 10 years of production. Sweep is improved, and earlier water breakthrough occurs locally in the model containing channelized fluvial sandbodies (right).

creating additional flow paths between clinothems that may otherwise be locally isolated by laterally extensive barriers or low-permeability dDF and PD deposits along their bounding clinoforms. Gravity-driven downward movement of injected water from the channelized fluvial sandbodies into high-to-moderate-permeability SMB and pDF deposits in the underlying clinothems may also enhance sweep. In models that lack channelized fluvial sandbodies, the shortest direct flow path between injection and production wells is through SMB sandstones, which may have similar petrophysical properties to the channelized fluvial sandbodies. Channelized fluvial sandbodies draw the

injected water away from the shortest flow paths in SMB deposits, thus delaying water breakthrough and improving sweep (e.g. Fig. 3.8C). Channelized fluvial sandbodies also create additional direct flow conduits between injectors and producers that allow otherwise isolated high-to-moderate permeability facies associations to be swept (Fig. 3.11C, E). In models that do not contain channelized fluvial sandbodies, high permeability distributary channel-fill deposits become isolated from producers by lower permeability proximal and distal delta front (pDF and dDF) deposits and remain largely unswept (Fig. 3.11E). These results indicate that the geometry, continuity and local positioning of channelized fluvial sandbodies are important controls on the drainage patterns, sweep efficiency, and hydrocarbon recovery of clinoform-bearing models.

When the difference in permeability between channelized fluvial sandbodies and SMB and DC sandstones is high, recovery factor decreases (Fig. 3.7B), because water movement through channelized fluvial sandbodies that directly link injection and production wells is more rapid (Fig. 3.12). Sweep efficiency is lowered, as gravity-driven downward flow of water from the very-high-permeability FC sandbodies into high-permeability SMB and DC sandstones of the underlying clinothems is reduced, leaving bypassed oil in the latter (Fig. 3.12D, in comparison to Fig. 3.12B-C). However, this effect is less pronounced than reported in Deveugle et al. (2011), where very-high-permeability channelized fluvial sandbodies acted as thief zones. The difference in the interpretation of the importance of channelized fluvial sandbody permeability can be attributed to the streamline-based tracer simulations used in Deveugle et al. (2011), which do not include gravity effects. However, we have shown gravity drainage to be an important mechanism for sweeping oil from some of the high-to-moderate permeability DC, SMB and pDF sandstones of the underlying clinothems.

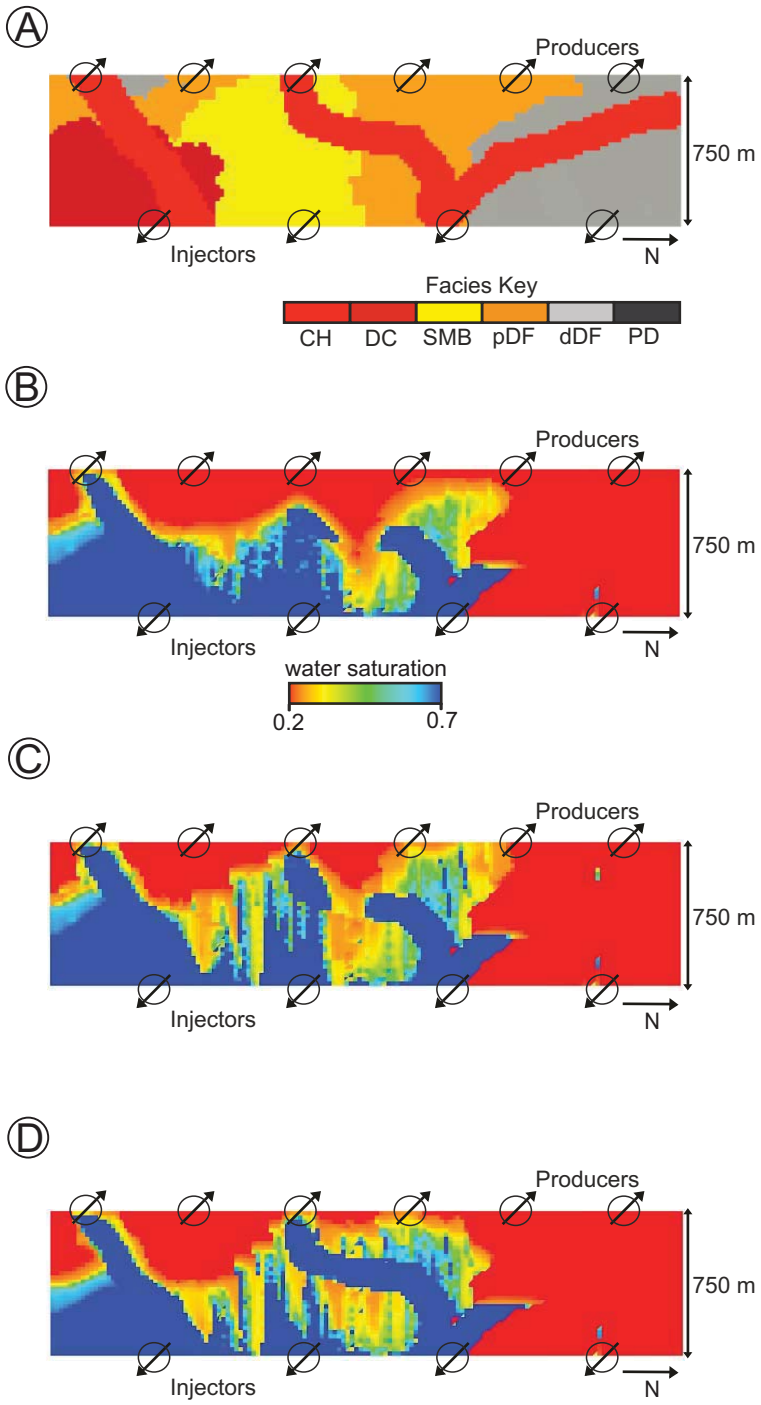


Figure 3.12. (A) Map of facies-association belts near the top of the model of stacked delta-lobe deposits containing channelized fluvial sandstones (with coastal-plain deposits, Fig. 3.3E, removed), showing the location of injection and production wells. Maps of water saturation after 10 years of production, with a target oil production rate over 10 years of 350 S m^3/day (2200 bbl/day) for: (B) model containing 0% barrier coverage along clinoform surfaces and channelized fluvial sandbody permeability (k_h) of 1 × (1793) mD, and (C-D) models containing 90% barrier coverage along clinoform surfaces with channelized fluvial sandbody permeability (k_h) of (C) 1 × (1793) mD, and (D) 5 × (1793) mD. Sweep efficiency is reduced when the permeability of channelized fluvial sandbodies is 5 × (1793) mD.

3.9.3 Impact of bed-scale heterogeneity in distal delta-front heteroliths

When the interbedded sandstones and shales of the dDF facies association are assigned zero vertical permeability, oil is only displaced from these rocks by horizontal movement of water in regions close to the injection wells (e.g. Figs. 3.8C, 3.11C). Consequently, large volumes of oil are bypassed, as the dDF facies association comprises up to 55% of the model volume and holds a significant volume of oil that can be potentially recovered (Fig. 3.13A, C). When the vertical permeability of the dDF facies association is increased, oil recovery increases and total water produced decreases (Fig. 3.7), because water in the overlying, swept channelized fluvial sandbodies or pDF facies association moves downward under gravity to displace oil in the dDF facies association (Fig. 3.13D).

Oil recovery and sweep of dDF deposits increases even when each clinoform is covered over 90% of its area by a barrier to flow and the dDF facies association is assigned a non-zero vertical permeability (Figs. 3.7, 3.13D). However, oil recovery is lower than equivalent models containing clinoforms with 0% barrier coverage (Fig. 3.7). This comparison suggests that the sweep efficiency of the lower part of each delta-lobe deposit is dependent on the preserved coverage of barriers along clinoform surfaces. An increase in hydrocarbon recovery when the dDF facies association is assigned a non-zero vertical permeability supports the results of Deveugle et al. (2011), who found that increasing the k_v/k_h ratio of dDF deposits increased sweep efficiency. However, we find less communication between delta-lobe deposits than Deveugle et al. (2011), due to the occurrence of laterally extensive barriers along the toes of clinoforms (Fig. 3.13D) and to the inclusion in our models of relative-permeability effects that reduce displacement efficiency in the swept part of the reservoir. The streamline-based tracer simulations

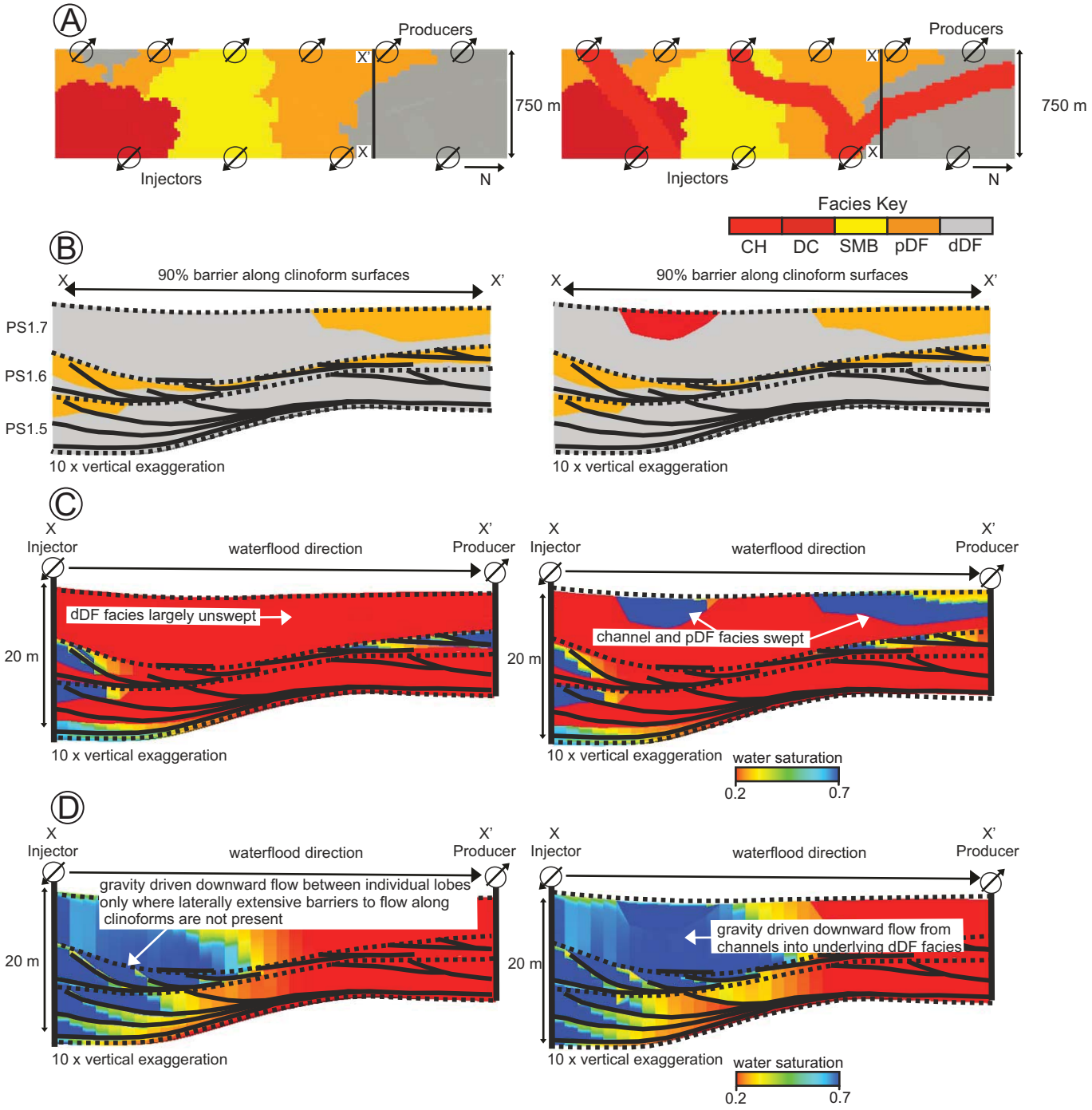


Figure 3.13. Maps and cross-sections illustrating models of stacked delta-lobe deposits that either have zero vertical permeability or non-zero vertical permeability in distal delta-front facies in the presence of a 90% barrier to flow along clinoforms, in models that either (left column) lack or (right column) contain channelized fluvial sandbodies. (A) Maps of facies-association belts near the top of the models (parasequence 1.7, Fig. 3.3D, with overlying coastal-plain deposits, Fig. 3.3E, removed) showing location of injection and production wells, and the cross-sections illustrated in parts in B-D. (B) Depositional-dip-oriented cross-section showing the internal facies architecture of the modelled parasequences with barriers covering 90% of each clinoform surface shown as black lines and parasequence-bounding flooding surfaces showed as dashed lines. (C, D) Depositional-dip-oriented cross-section showing water saturation after 20 years of production, with a target oil production rate over 20 years of 175 S m^3/day (2200 bbl/day), where there is (C) zero vertical permeability in dDF deposits, and (D) non-zero vertical permeability (k_v of 7 mD) in dDF deposits. Sweep is improved locally in the models containing low vertical permeability (k_v of 7 mD) in dDF deposits.

used in Deveugle et al. (2011) did not include relative-permeability effects.

3.9.4 Impact of reservoir engineering decisions

Higher production rates decrease oil recovery and result in early water breakthrough (Fig. 3.7). Increased pressure drawdown at the production wells, which is required to maintain the higher rate of oil production, causes more rapid water movement through the shortest flow paths in high-permeability FC, DC and SMB sandstones near the tops of the delta-lobe parasequences (Fig. 3.14B). Viscous forces associated with pressure drawdown are dominant, which results in less gravity-driven downward movement of water to displace oil in underlying, moderate-permeability pDF and low-permeability dDF sandstones near the lower part of the delta-lobe parasequences (Fig. 3.14D). The effect is most pronounced when 90% barriers to flow

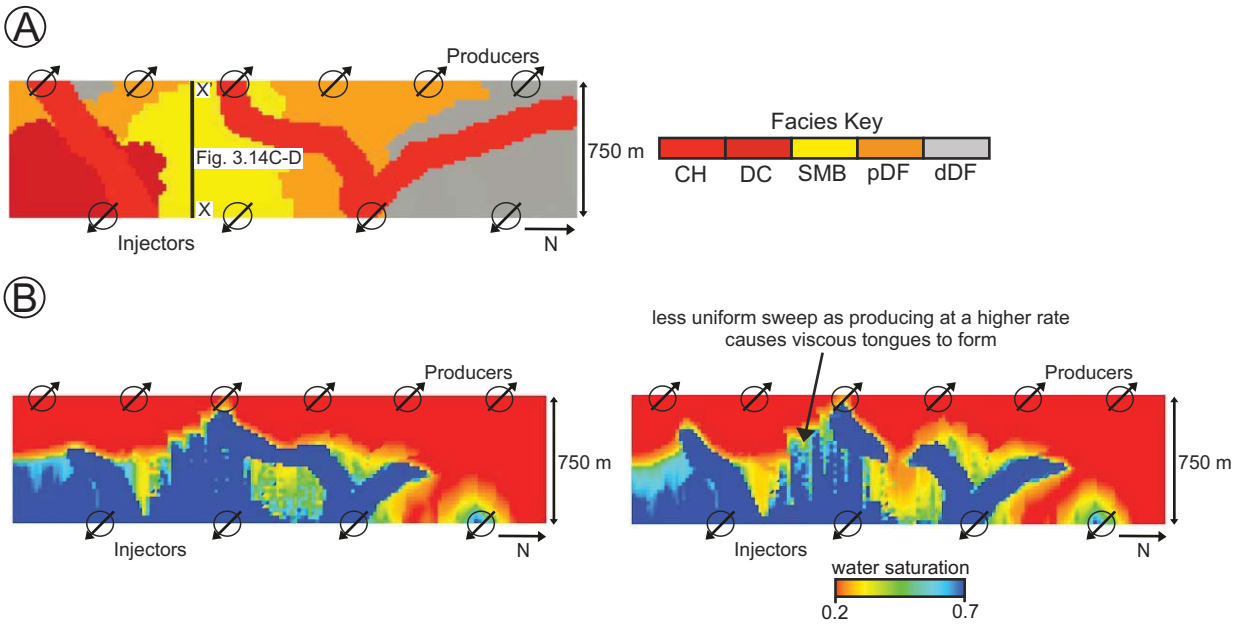


Figure 3.14A. (A) Map of facies-association belts near the top of the model of stacked delta-lobe deposits containing channelized fluvial sandstones (with coastal-plain deposits, Fig. 3.3E, removed), showing the location of injection and production wells. (B) Maps of water saturation for models containing 90% barrier coverage along clinoform surfaces and non-zero vertical permeability (k_v of 7 mD) in dDF deposits, with a low target oil production rate over 20 years of 175 S m^3/day (1100 bbl/day) (left column) and a higher target oil production rate over 10 years of 350 S m^3/day (2200 bbl/day) (right column). (C-D) shown on next page.

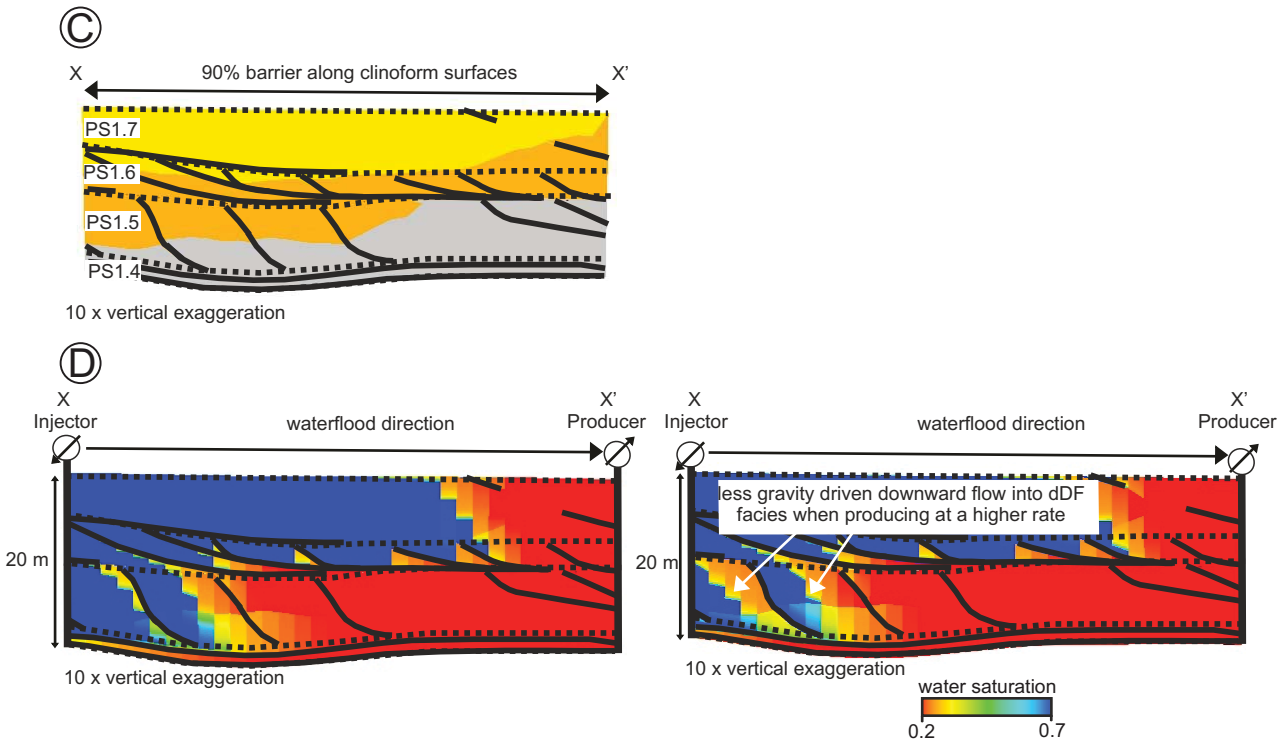


Figure 3.14B. (C) Depositional-dip-oriented cross-section showing the internal facies architecture of the modelled parasequences with barriers covering 90% of each clinoform surface shown as black lines and parasequence-bounding flooding surfaces showed as dashed lines (facies key and location map shown in part (A) on previous page). (D) Depositional-dip-oriented cross-sections showing water saturation at the end of production using the low target oil production rate (left column) and the higher target oil production rate (right column). Sweep efficiency is reduced when producing at the higher oil production rate.

along clinoforms are present, oriented perpendicular to the principal flow direction within an individual delta lobe deposit (Fig. 3.14D).

3.9.5 Implications for reservoir monitoring and management

The presence and extent of barriers to flow along clinoform surfaces is difficult to characterize in the subsurface. Seismic data may, in some cases, identify a change in lithology at, or across clinoform surfaces (e.g. Dreyer et al. 2005) but such changes are not consistently or clearly imaged. Similarly, core and wireline-log data may allow the identification of clinoform surfaces at a limited number of locations within the reservoir, but the extent of barrier coverage away from well locations is difficult to evaluate. Here,

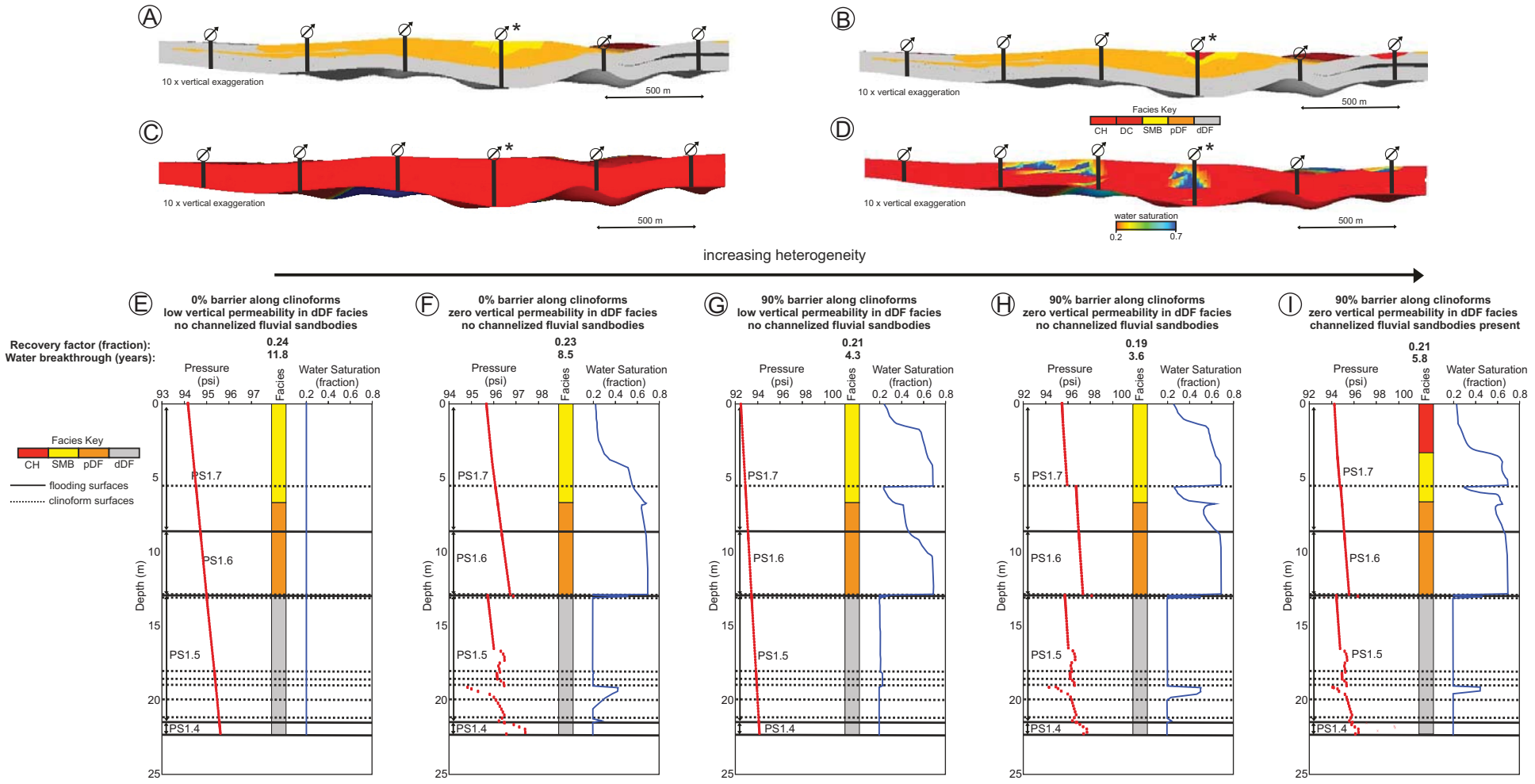


Figure 3.15. (A, B) Cross-sections of facies-association belts along the structural crest of two models containing multiple, stacked delta-lobe deposits (with coastal-plain deposits, Fig. 3.3E, removed), showing the location of production wells: (A) 0% barrier to flow along clinoforms, non-zero vertical permeability (k_v of 7 mD) in dDF deposits, and no channelized fluvial sandbodies; and (B) 90% barrier to flow along clinoforms, zero vertical permeability in dDF deposits, and channelized fluvial sandbodies present. Pressure and water-saturation profiles along the labelled well in both models are shown in parts E-I. (C, D) Corresponding cross-sections showing water saturation after 10 years of production with a target oil production rate over 10 years of 350 S m^3/day (2200 bbl/day). (E-I) Facies-association successions, stratigraphic surfaces and pressure and water-saturation profiles after 10 years of production along production well (labelled in parts A-D), with dashed lines denoting clinoform surfaces and black lines representing parasequence bounding flooding surfaces. Well data extracted from five models are shown, with increasing heterogeneity from left to right: (E) 0% barrier to flow along clinoforms, non-zero vertical permeability (k_v of 7 mD) in dDF deposits, and no channelized fluvial sandbodies; (F) 0% barrier to flow along clinoforms, non-zero vertical permeability (k_v of 7 mD) in dDF deposits, and no channelized fluvial sandbodies; (G) 90% barrier to flow along clinoforms, zero vertical permeability (k_v of 7 mD) in dDF deposits, and no channelized fluvial sandbodies; (H) 90% barrier to flow along clinoforms, non-zero vertical permeability (k_v of 7 mD) in dDF deposits, and no channelized fluvial sandbodies; and (I) 90% barrier to flow along clinoforms, zero vertical permeability in dDF deposits, and channelized fluvial sandbodies present.

we use pressure and water saturation profiles along wells to monitor the development of breaks across clinoform surfaces during production in the models of stacked delta-lobe deposits (Fig. 3.15).

When clinoform surfaces are not associated with significant barriers to flow, no breaks in pressure occur along them (Fig. 3.15E), and pressure breaks only result from a significant contrast in petrophysical properties between pDF and dDF facies associations in models where there is zero vertical permeability in dDF facies (Fig. 3.15F). Even clinoforms with 90% barrier coverage along them are associated with only small breaks in pressure (Fig. 3.15H-I), making it difficult to detect their presence using downhole pressure monitoring techniques. This is because the lateral extent of the heterogeneity associated with clinoforms surfaces is limited away from production wells, such that diagnostic breaks in pressure do not build up across them. However, clinoforms with significant barriers to flow along them are associated with prominent breaks in water saturation (Fig. 3.15G-I), indicating that sweep becomes stratigraphically compartmentalized. Gravity-driven downward flow of water caused by the density contrast between water and oil stops at barriers along clinoforms, in models that both contain and lack channelized fluvial sandbodies. Similar breaks in water saturation across clinoforms were observed in models of an outcrop analogue of a wave-dominated shoreface-shelf parasequences (Jackson et al., 2009), in the wave-dominated Rannoch and Etive formations of the Brent Group reservoir, Brent Field, UK North Sea (Hampson et al., 2008), and in the storm-dominated Jurassic Bridport Sandstone Formation reservoir, Wytch Farm Field, southern UK (Hampson et al., in review). The complex sweep patterns observed in our models have implications for history matching: if

clinoforms have been omitted the wrong properties may be adjusted in models to match observed data, yielding erroneous predictions for future production behaviour.

3.9.6 Closing summary

We have defined a hierarchy of geological heterogeneity in fluvial-deltaic reservoirs, and used it in combination with a novel, stochastic, surface-based, clinoform-modelling algorithm and data from an outcrop analogue (Cretaceous Ferron Sandstone Member, Utah, USA), to construct three-dimensional models of multiple, stacked fluvial-dominated delta-lobe deposits, each of which contains numerous clinoform surfaces. The models were then used to quantify the impact on oil recovery of geological heterogeneity and reservoir engineering decisions. The investigated geological heterogeneities include the distribution and character of clinoforms, occurrence and character of fluvial channelized sandbodies, and the vertical permeability of interbedded sandstones and shales in distal delta-front deposits.

We have demonstrated that under certain displacement conditions clinoforms can have a significant impact on fluid flow and hydrocarbon recovery and that their impact can be larger than that of other geological heterogeneities and reservoir engineering decisions. The results presented in this chapter can be applied to existing reservoir models, or those in development, to constrain uncertainty in the subsurface. Firstly, the clinoform-modelling algorithm described in Chapter 2 can be applied to incorporate multiple clinoform surfaces into field-scale models of shallow-marine reservoirs. We have demonstrated its application to developing models of a fluvial-dominated deltaic reservoir analogue but the algorithm can also be used in the context of existing reservoir zonation and modelling schemes, with appropriate analogue and

subsurface datasets data, to capture clinoform geometry and distribution within existing reservoir models. Secondly, to mitigate uncertainty arising from sparse subsurface data requires multiple realizations of a reservoir model so that the impact of varying clinoform orientation, spacing and barrier coverage on fluid flow can be quantified or used to match historical production data within existing reservoirs. Finally, in order to capture quantitative data on the complex sweep patterns that we have observed, detailed downhole monitoring of water saturation in subsurface reservoirs is required to diagnose the presence of clinoform surfaces.

3.10 Conclusions

We find that the proportion and distribution of barriers to flow along clinoforms exert the greatest influence on recovery; equivalent models that neglect these barriers overpredict recovery by up to 35%. Furthermore, the impact of clinoforms may be larger than that of other geological heterogeneities and reservoir engineering decisions.

The vertical permeability of the distal delta-front (dDF) facies association has the most significant positive impact on oil recovery; when vertical permeability is non-zero oil recovery is increased by up to 2% in comparison to models with zero vertical permeability in the dDF facies association. Oil recovery increases, because water in the overlying, swept channelized fluvial sandbodies or pDF facies association moves downward under gravity to displace oil in the dDF facies association.

The models provide insights into the data types required to appropriately characterize, monitor and manage fluvial-dominated deltaic reservoirs containing clinoforms. Although they can exert a significant impact on sweep and recovery,

clinoforms are only rarely associated with large breaks in pressure in production wells. However, clinoforms associated with significant barriers to flow are marked by prominent breaks in water saturation that may be detected and monitored in production wells, in order to characterize clinoform-related sweep patterns during production. Our results also suggest that history matching of observed sweep patterns and pressure data would lead to erroneous predictions of future production behaviour in models lacking clinoforms. Therefore clinoforms should be included routinely in models of fluvial-dominated deltaic reservoirs under certain displacement conditions, in order to accurately predict hydrocarbon recovery and drainage patterns.

Chapter 4

Three-dimensional digital outcrop modelling using stereophotogrammetry: Application to improved characterization of sandbody connectivity in thinly bedded intervals of wave-dominated shallow-marine reservoirs

4.1 Summary

Previous studies have shown that it is important to characterize vertical permeability in thinly-bedded reservoir intervals, because if hydrocarbons contained within the beds can be produced, they may constitute significant additional reserves in shallow-marine reservoirs. However, it is difficult to characterize thinly-bedded intervals as they cannot be detected using conventional seismic and wireline-log data techniques. Gutter casts are sand-filled scour structures formed by storm-generated flows in distal parts of wave-dominated shallow-marine reservoirs, and may increase connectivity between tabular sandstone beds that are otherwise isolated by shales, thus creating

effective vertical permeability. At present there is limited information on the three-dimensional (3D) geometry and spatial distribution of gutter casts.

We present a digital outcrop modelling method and apply it to capture distal lower shoreface deposits exposed at outcrop (G2 parasequence, Grassy Member, Blackhawk Formation, Utah, USA). The method offers several advantages over other digital outcrop modelling techniques such as LIDAR, including that it is at least an order of magnitude less expensive, yet provides comparable results. We use the digital outcrop model to make preliminary observations of 3D gutter cast geometry. In contrast with previous published data, we observe a wider range of gutter cast geometries, implying gutter casts occur either as sinuous channels with marked variations in along-axis scour, or as down-flow shallowing and widening scours reminiscent of flute-cast geometries. The digital outcrop model and proposed 3D gutter cast profile can be captured in reservoir models and used to quantify sandbody connectivity and effective flow properties.

4.2 Introduction

Hydrocarbon production from shallow-marine reservoirs that contain intervals of thinly-bedded sandstone and shale (also termed low resistivity and/or low contrast pay) (e.g., Atkinson et al., 1986; Begg et al., 1992) is challenging, because it is difficult to characterise fluid flow behaviour of these intervals before and during production (Baillie and James-Romano, 2010). Seismic and conventional wireline-log data cannot detect the presence of thinly-bedded intervals (Worthington, 2000), but if thinly-bedded intervals can be resolved using well data (e.g. core, high-resolution image logs), no information is

provided on sandstone bed connectivity, dimensions or geometry away from the well (e.g., Coll et al., 1996; Passey et al., 2006; Henderson et al., 2010). Furthermore, it is not clear how thinly-bedded intervals should be represented in subsurface reservoir models; previous studies have either used stochastic object-based modelling of elliptical bodies to represent sandstone connectivity (e.g. Sylvester et al., 2005) or used upscaled effective permeabilities derived from core scale experiments (Fløl o et al., 2000). However, it can be important to characterize the vertical permeability of thinly-bedded intervals, because if the hydrocarbons contained within the sandstone beds can be produced, they may constitute significant additional reserves in shallow-marine reservoirs as demonstrated in Chapter 3 (Figs. 3.7, 3.14) (see also Ainsworth et al., 1999; Deveugle et al., 2011).

Key controls influencing vertical permeability of thinly-bedded intervals in shallow-marine reservoirs include the lateral extent of mudstone beds and the magnitude and spatial distribution of erosion at the base of sandstone beds. Within shallow-marine reservoirs, distal lower shoreface deposits are one example of a thinly-bedded reservoir type that comprises sharp or erosionally based sandstone beds alternating with mudstones (Figs. 3.1D, 4.1). Where mudstone beds are laterally



Figure 4.1. Outcrop view of distal lower shoreface deposits in the G2 parasequence of the Grassy Member, Blackhawk Formation, north of Green River, east-central Utah, USA (Figs. 4.4, 4.5). Note the irregular geometries of the sandstone beds. Photograph has no vertical exaggeration.

extensive, effective vertical permeability approaches zero. However, sandstone bed geometries are often highly variable (Fig. 4.1), reflecting localised erosion by storm-generated flows that form steep-sided, sand-filled scours termed gutter casts (Whitaker, 1973). Gutter casts may increase connectivity between sandstone beds that are otherwise isolated, thus creating effective vertical permeability (Haldorsen and Lake, 1984; Begg and Chang, 1985; Begg and King, 1985; King 1990). The geometry of gutter casts in ancient shallow-marine deposits has been documented from a limited number of two-dimensional (2D) outcrop examples (Myrow, 1992; Guilpain, 2006), but there is limited information at present on their three-dimensional (3D) geometry and spatial distribution. Examples of reservoirs that may contain gutter casts include Miocene reservoirs of Brunei (e.g., Atkinson et al., 1986) and Pliocene reservoirs of the Columbus Basin, Trinidad (e.g., Sydow et al., 2003), where uncertainty in reservoir connectivity in thinly-bedded reservoir intervals resulted in greater than expected recovery of hydrocarbons (e.g., Sylvester et al., 2005).

Outcrop data are commonly used to provide quantitative data on dimensions, distributions and architecture of geological bodies to bridge the resolution gap between seismic and well data (e.g., Alexander, 1993; Reynolds, 1999; Bryant et al., 2000; Visser and Chessa, 2000; White and Willis, 2000; Amour et al., 2012). Digital outcrop modelling studies (DOM) have been used as a method to capture geological data from reservoir analogues from a variety of depositional environments and over a range of lengthscales; from a few kilometres (e.g., Adams et al., 2005) down to the interwell scale (e.g., Kjønsvik et al, 1994). The distal lower shoreface deposits of the Upper Cretaceous Blackhawk Formation of east-central Utah, offer narrow branching canyon systems and excellent exposure allowing 3D digital outcrop data to be captured. We can use the digital outcrop

data to analyse the detailed 3D geometry and architecture of sandstone beds including many containing gutter casts, across the narrow canyons (<15 m). However, existing methods for capturing high-resolution, 3D digital data from outcrops, such as LIght Detection And Ranging (LIDAR) (e.g., Wehr and Lohr, 1999; Bellian et al., 2005; Enge and Howell, 2010) and Differential Global Positioning System (DGPS) mapping (e.g., Amour et al, 2012) can define bedding with sub meter accuracy, but may require significant capital expenditure in order to obtain the equipment used to capture the outcrop dataset (see Pringle et al., 2006 for typical costs) which can render studies economically unviable. Alternatively, 2D photomontages of well exposed 2D outcrop cliff faces that have been spatially referenced using Global Positioning System (GPS) coordinates, have been used to drape digital elevation models (DEM) (e.g., Deveugle et al., 2011) at lower expense (see Pringle et al., 2006). The accuracy of this technique however, is limited by sparse spatial coordinate data and perspective effects on the photomontages, in which measurements of sedimentary features or geobodies may be skewed by outcrop shape and orientation (Pringle et al., 2004). The aim of this chapter is to describe a fast method for creating 3D, high-resolution, digital outcrop models based on digital photogrammetry (e.g., Sgavetti, 1992; Xu et al., 2000; 2001; McCaffrey et al., 2005), that can approach the accuracy of LIDAR, but can be applied at less cost.

The chapter is structured in three parts. First, we outline a method for collecting a 3D, high resolution, digital outcrop dataset that is suitable for characterizing the geometry and architecture of sandstone beds in distal lower shoreface deposits when it is not economically viable to use other digital outcrop data collection techniques such as LIDAR. The method is generic and can be applied to other outcrop locations. The second part of the chapter validates the digital outcrop data collection method via its application

to an outcrop example of distal lower shoreface deposits in a wave-dominated delta (G2 parasequence, Grassy Member, Blackhawk Formation exposed in Book Cliffs, Utah, USA). The digital outcrop model has to have sufficient resolution and accuracy that it can be used to characterise the 3D architecture of gutter casts and related beds. Finally, we use the digital outcrop model to make preliminary observations of the 3D geometry and spatial distribution of gutter casts in the digital outcrop model.

4.3 Storm event beds and gutter casts

Distal lower shoreface deposits are situated between mean fairweather wave base (MFWWB) and mean storm wave base (MSWB) (Fig. 4.2), and reflect deposition from storm and fairweather wave processes. Episodic storms, typically affecting water depths of 20-50 m, erode sand from the upper shoreface and transport it seawards, where it is deposited as sandstone beds on the lower shoreface and inner shelf. Storm-event beds typically range in thickness from millimetres to a few decimetres, and gradually thin from proximal to distal locations (Aigner, 1985). These beds can be divided into two categories based on their geometry: (1) sandstones infilling and confined to erosional scours; and (2) sheet sandstones resulting from unconfined deposition (Goldring and Bridges, 1973). Gutter casts were first described in the Upper Silurian Ringerike Group, South Norway (Whitaker, 1973) and are documented as downward bulging scours formed by erosional incision into a cohesive muddy substrate (Myrow, 1992).

Most gutter casts are considered to be storm-generated features. During storms, sea level is raised at the coast by onshore-directed winds (i.e. storm surge), causing

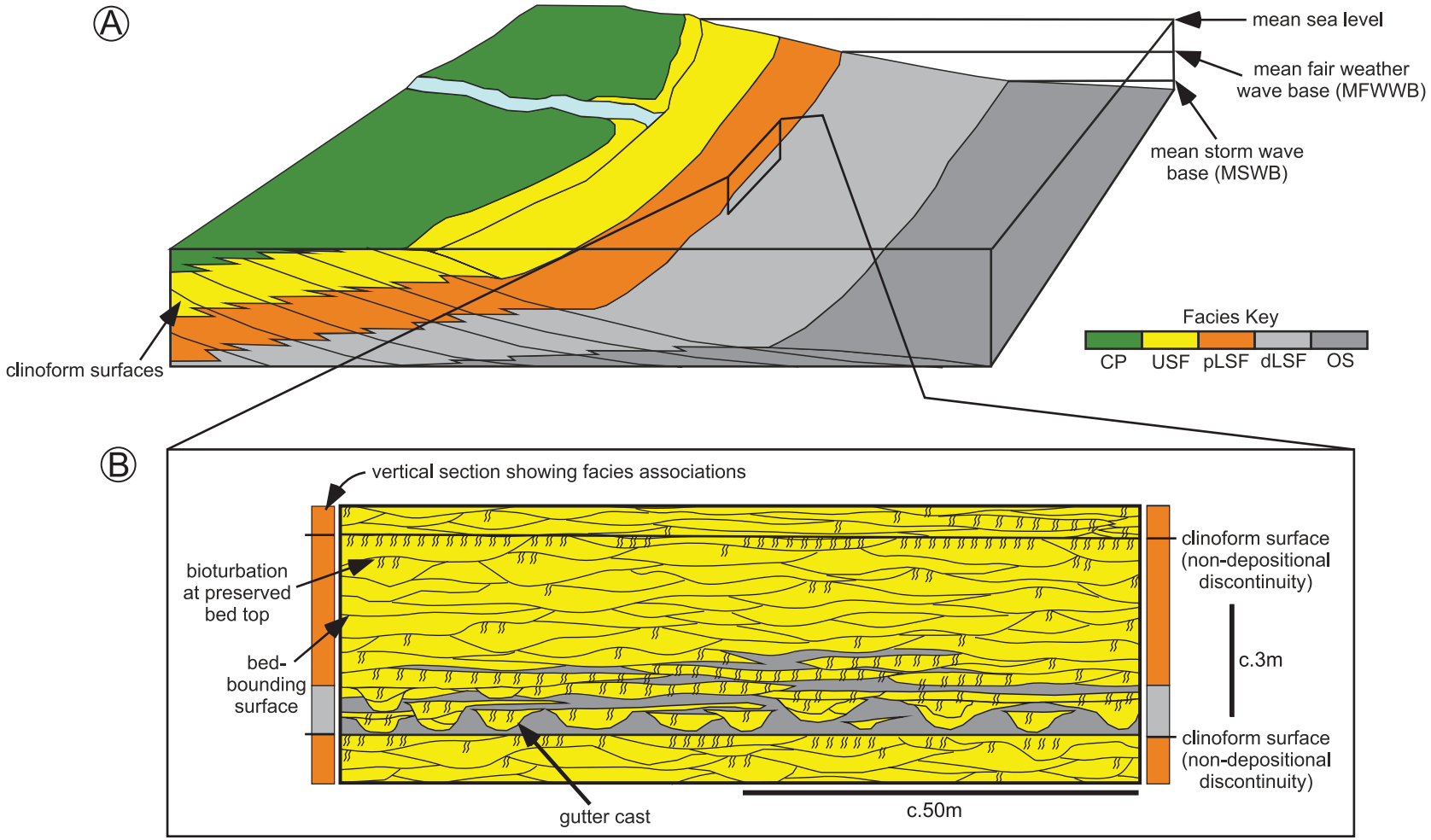


Figure 4.2. (A) Generalised depositional model of a shoreface fronting a wave-dominated delta, highlighting the position of distal lower shoreface deposits relative to the mean fair weather wave base and mean storm wave base (modified after Howell et al., 2008a). (B) Schematic cross-section oriented along depositional strike illustrating heterogeneity within an upward-coarsening succession (bedset) of distal lower shoreface deposits bounded by clinoform surfaces (modified after Sech et al., 2009). Note the presence of gutter casts within the distal lower shoreface.

considerable erosion of the upper shoreface (Ball et al., 1967; Reineck and Singh, 1972; Goldring and Bridges, 1973). Eroded sediment is transported seaward by gravity-driven high-velocity, sediment-laden currents flowing along the sea bed (return flows). These currents can also erode finer grained material on the lower shoreface and inner shelf. However, the nature of the eroding currents that shape gutter casts is a subject of debate. Erosion is hypothesised to result from strong near-bottom offshore-directed unidirectional flows during the initial phase of a storm event, to form linear scours with axes oriented perpendicular to the shoreline (Myrow, 1992; Chakraborty, 1995; Bhattacharya et al., 2004). Spiralling patterns on the sole of gutter casts are interpreted to have been formed by helical flow at the base of unidirectional currents moving parallel to the long axis of gutter casts (Myrow, 1992). However, other studies document a wide range of sole mark orientations that are inferred to have resulted from multi-directional currents (Aigner, 1985). Infilling of gutter casts is the result of oscillatory flow during the waning phase of a storm event, consistent with outcrop observations of hummocky cross-stratification (HCS) and swaley cross-stratification (SCS) within gutter casts (Dott and Bourgeois, 1982; Duke, 1985; Dumas et al., 2005). Sediment transport to gutter casts is postulated to result from either turbidity currents initiated by storm surge erosion in coastal areas, which flow perpendicular to the shoreline (Leckie & Krystinik, 1989), or seaward returning geostrophic (wind-driven) flows that flow mainly parallel or oblique to bathymetric contours (Swift et al., 1986; Duke, 1990).

Gutter casts are observed across a variety of lengthscales in 2D cross-sections (Fig. 4.3). Isolated and amalgamated gutter casts have been documented over centimetre- to metre-scales (Myrow, 1992; Guilpain, 2006), most thoroughly in the Cambrian Chapel Island Formation, Newfoundland, Canada (Myrow, 1992). Their cross-

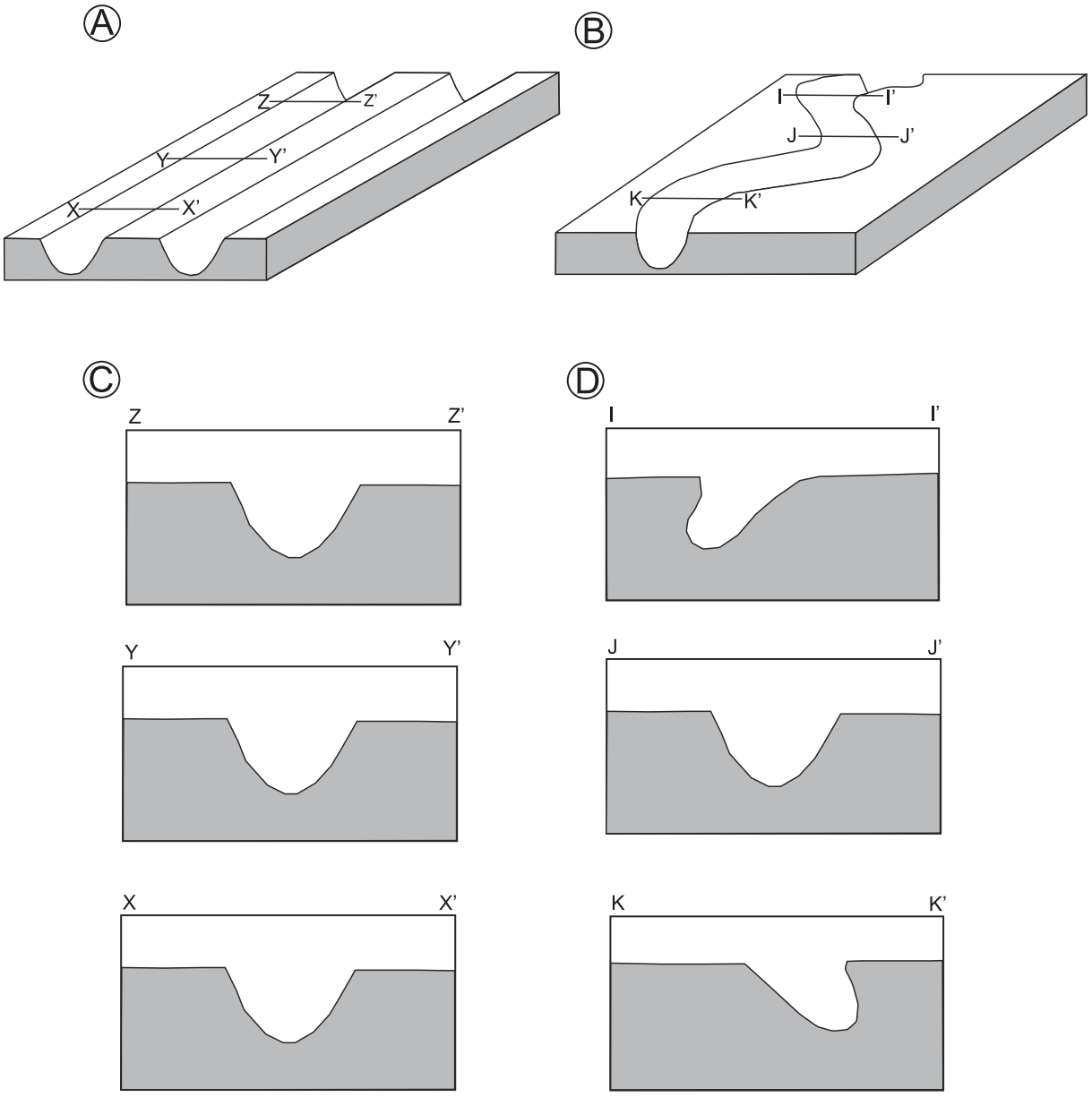


Figure 4.3. Previous interpretations of gutter cast geometry in (A-B) plan view, and (C-D) cross-section (modified after Myrow, 1992). Gutter casts are interpreted to be straight (left) or sinuous (right) channelized scours that are continuous along their axes.

sectional geometries range from symmetrical to strongly asymmetrical U- or V-shaped profiles with steep sided (40-90°) walls (Fig. 4.3C, D). In plan view, gutter casts are hypothesized to exhibit moderately sinuous to straight channelized geometries that extend over several tens of times greater than their thickness (Fig. 4.3A, B), which reflect a pattern of helical vortices with a horizontal axis parallel to the flow direction (Myrow,

1992). Narrow, sinuous gutter casts are postulated to form from slow helical vortices and wider, straighter gutter casts forming from faster vortices (Myrow, 1992). However, gutter cast geometry and spatial distribution has been evaluated in too few datasets for their along-axis geometry to be known with certainty. The outcrop dataset described in this chapter provides some 3D control on the dimensions, geometry and spatial distribution of gutter casts, as well as their internal architecture, so that these parameters can be later quantified from a 3D high-resolution digital outcrop model.

4.4 Geological setting and study area

The Upper Cretaceous Blackhawk Formation and overlying Castlegate Sandstone form a clastic wedge that represents the overall progradation of a wave-dominated shoreline and associated coastal plain into the offshore deposits of the Mancos Shale along the western margin of the Western Interior Seaway and (inset map in Fig. 4.4A) (Kauffman and Caldwell, 1993; Hampson and Howell, 2005). Deposits along this western shoreline are generally wave-dominated, although tidal and fluvial processes were locally dominant (McGookey et al., 1972; Hampson and Howell, 2005). The Blackhawk Formation is exposed in the Book Cliffs, which form a prominent west-east trending escarpment that runs for approximately 250 km through east-central Utah and west-central Colorado (Fig. 4.4A). The first detailed facies analysis of the succession was undertaken by Balsley (1980), but more recent work has concentrated on applying high-resolution sequence stratigraphy to individual members of the Blackhawk Formation and the overlying Castlegate Sandstone (e.g., O'Bryne and Flint, 1995) and on constructing a high-resolution (parasequence scale) sequence stratigraphic framework for the

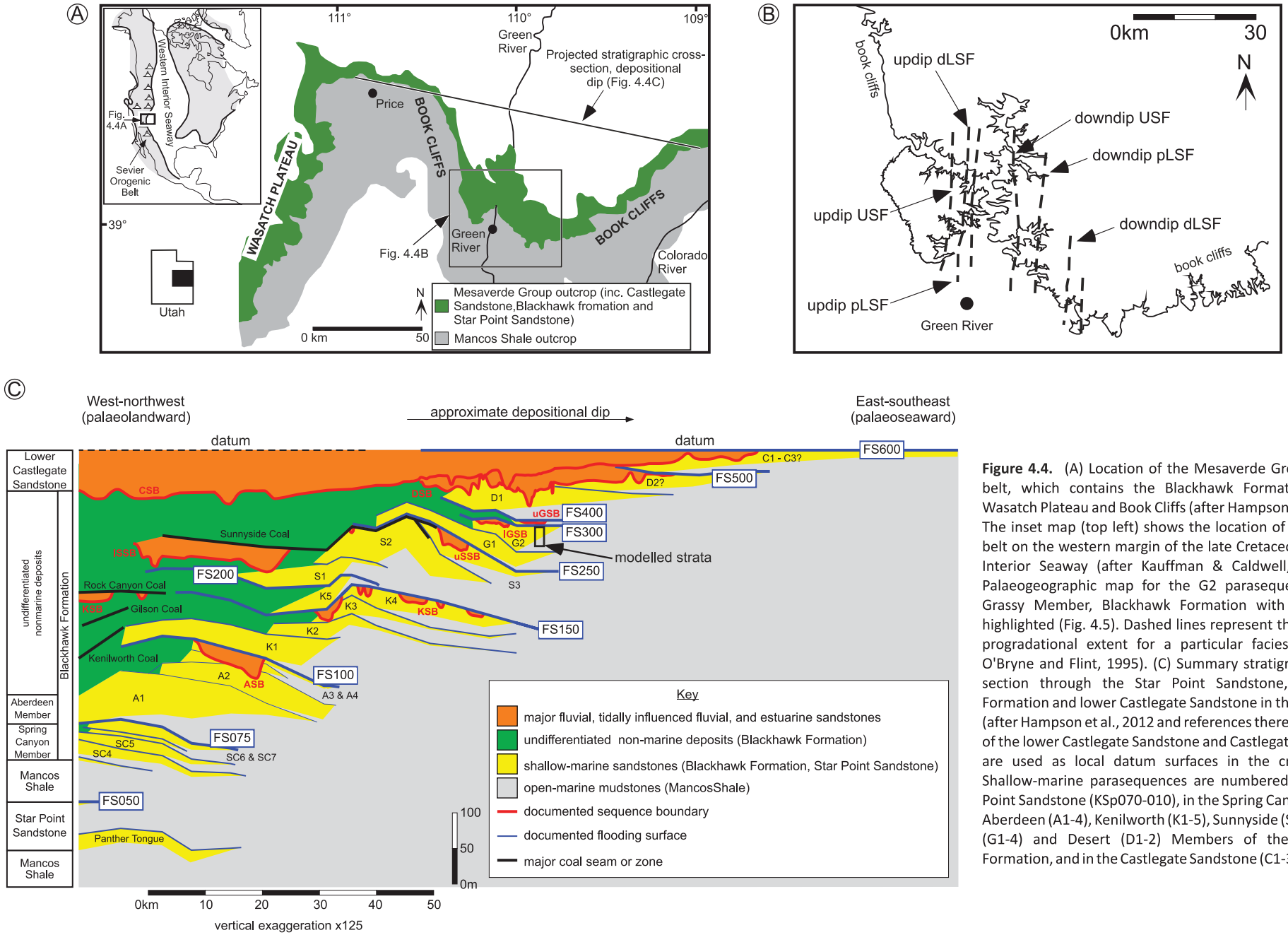


Figure 4.4. (A) Location of the Mesaverde Group outcrop belt, which contains the Blackhawk Formation, in the Wasatch Plateau and Book Cliffs (after Hampson et al. 2012). The inset map (top left) shows the location of the outcrop belt on the western margin of the late Cretaceous Western Interior Seaway (after Kauffman & Caldwell, 1993). (B) Palaeogeographic map for the G2 parasequence of the Grassy Member, Blackhawk Formation with study area highlighted (Fig. 4.5). Dashed lines represent the maximum progradational extent for a particular facies belt (after O'Bryne and Flint, 1995). (C) Summary stratigraphic cross-section through the Star Point Sandstone, Blackhawk Formation and lower Castlegate Sandstone in the Book Cliffs (after Hampson et al., 2012 and references therein). The tops of the lower Castlegate Sandstone and Castlegate Sandstone are used as local datum surfaces in the cross-section. Shallow-marine parasequences are numbered in the Star Point Sandstone (KSp070-010), in the Spring Canyon (SC4-7), Aberdeen (A1-4), Kenilworth (K1-5), Sunnyside (S1-3), Grassy (G1-4) and Desert (D1-2) Members of the Blackhawk Formation, and in the Castlegate Sandstone (C1-3).

formation (Fig. 4.4C) (e.g. Hampson and Howell, 2005).

O'Bryne and Flint (1995) documented the high-resolution sequence stratigraphic architecture of the Grassy Member, which contains the interval of interest for this study. We focus on the distal exposures of the upper part of the G2 parasequence of the Grassy Member, which is interpreted to comprise the deposits of a symmetrical wave-dominated delta (Hampson and Howell, 2005) with a north-south-trending, near-linear shoreline (Fig. 4.4B; O'Byrne and Flint, 1995) (Figs. 4.4B, C). The studied strata are exposed in Tusher Canyon, in an area of c. 260 m x 250 m that corresponds approximately to the location of log TC8 of O'Byrne and Flint (1995). The studied interval is c. 25 m thick, and consists of four vertically stacked, coarsening-upward successions (bedsets in O'Byrne and Flint, 1995) of distal lower shoreface facies in the upper part of the parasequence (O'Byrne and Flint, 1995). Each succession consists of hummocky-cross stratified sandstone beds interbedded with shales that decrease upwards in thickness, such that the sandstone beds become more amalgamated in the upper part of the succession. The studied strata are exposed in near-continuous cliff faces along the walls of Tusher Canyon, which trends west-east, and a narrow side canyon, which trends north-south (Fig. 4.5). These branching canyon walls provide an appropriate context for detailed analysis of 3D architecture at the scale of individual beds.

4.5 Data collection

Data for digital outcrop models can be collected using several different techniques, which may be combined, including; digital photogrammetry (e.g., Sgavetti, 1992; Xu et al., 2000; 2001; McCaffrey et al., 2005); terrestrial or airborne LIDAR (e.g.,

Bellian et al., 2005; Enge and Howell, 2007, Buckley et al., 2008; Van Lanen et al., 2009; Enge and Howell, 2010); kinematic DGPS (e.g., Adams et al., 2005; Amour et al., 2012), Ground Penetrating Radar (GPR) (e.g., Corbeanu et al., 2001; Pringle et al., 2004), and orthorectified aerial or satellite photographs draped over digital elevation models (e.g., Wilson et al. 2009). The technique that is utilized to create digital outcrop models is dependent on a number of factors, such as cost constraints, detail and precision required, duration of study, location (e.g. accessibility; see Fig. 4.5) and the nature of the

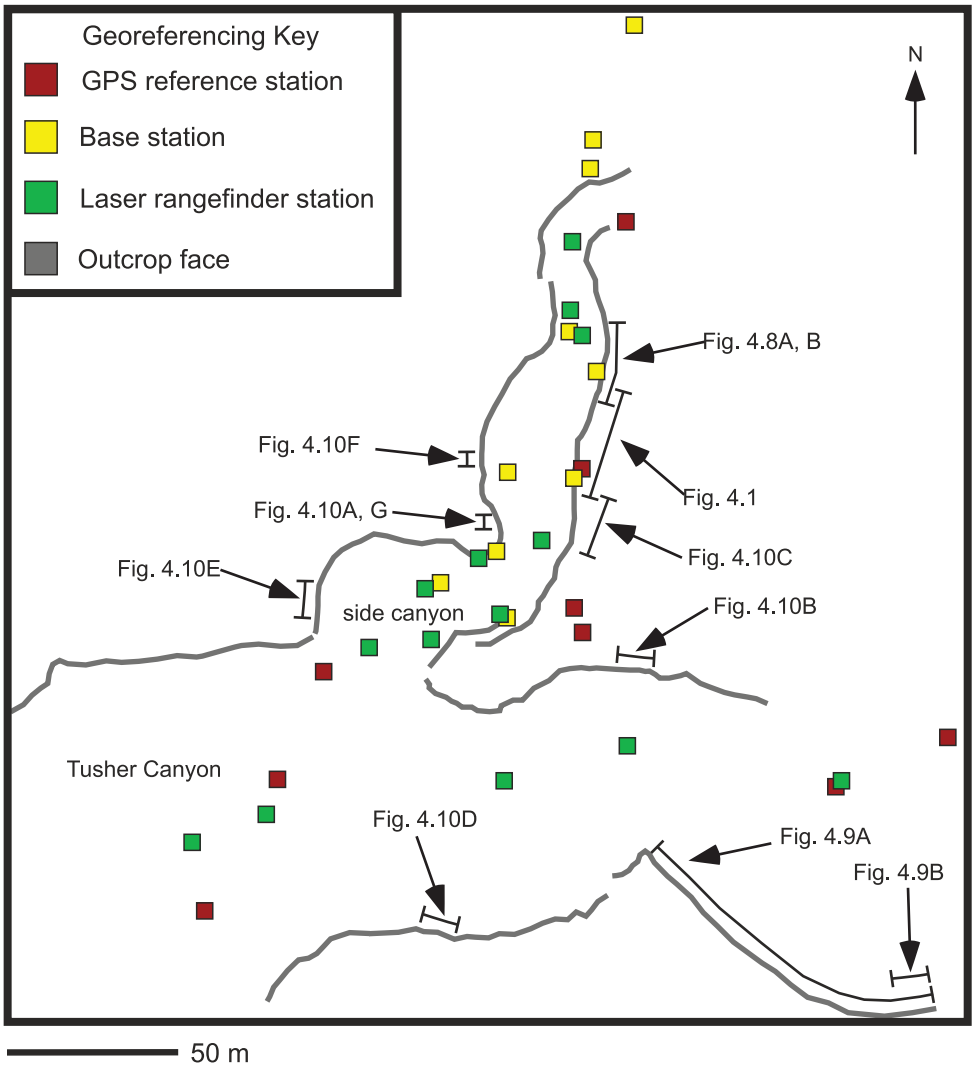


Figure 4.5. Basemap of the study area, highlighting the sub-vertical cliff face walls in which the G2 parasequence of the Grassy Member is exposed. The georeferencing stations used to capture and spatially position outcrop data using the stereophotogrammetric technique are shown.

outcrop itself (e.g. exposure and quality) (Jones et al. 2008; Van Lanen et al., 2009). We describe a method that uses digital stereophotogrammetry combined with GPS data to create 3D, high-resolution, digital outcrop models that can approach the accuracy of LIDAR (Fig. 4.6). The method builds on the previous work of Xu et al. (2000; 2001) and is a quick, practical and cost effective alternative to LIDAR.

4.5.1 Georeferencing

A common method of georeferencing geological data is using DGPS. This method uses two receivers working simultaneously; one takes measurement of data points at outcrop, while the other receiver stays at a fixed location taking second-by-second satellite data corrections relative to a known location. The latter receiver is used to post-process the data points acquired by the receiver taking outcrop measurements (Amour et al., 2012). However, as the cost of DGPS equipment can be significant (see Pringle et al., 2006), it may render this approach unviable.

Alternatively, at the outcrop we can position several GPS reference stations at suitably open locations, for example, at the top of the walls of the narrow canyon that is being modelled, using GPS units that are orders of magnitude less expensive than DGPS equipment (Pringle et al., 2006). These GPS units must be able to be seen from inside the narrow canyon and positioned so that they have a wide unobstructed view of the sky. The GPS units are set to perform long-term averaging to record their coordinates at regular, frequent intervals and post-processed to remove all points that are beyond a user-specified tolerance from the centroid. Secondary stations, termed base stations, are then located in positions within the narrow canyon that have clear lines of sight to GPS reference stations. A laser rangefinder is used to measure the azimuth, inclination

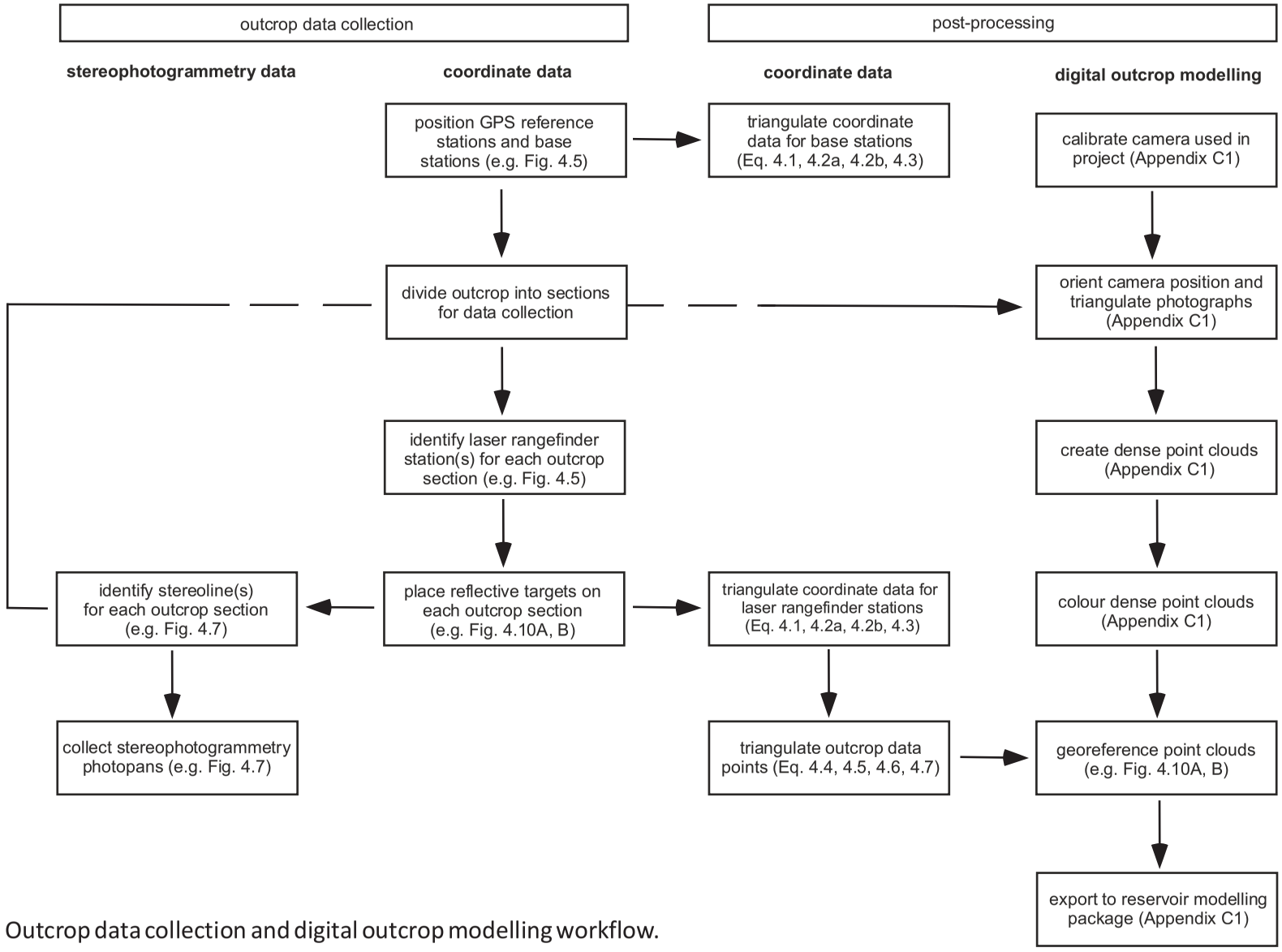


Figure 4.6. Outcrop data collection and digital outcrop modelling workflow.

and distance from base stations to GPS reference stations. Each base station must have line of sight within a range of 250 m to at least three GPS reference stations, but these GPS reference stations must not all lie in a straight line as we use the measurements to triangulate the position of the base station. We triangulate the coordinates of the base stations, honouring the distances and inclinations measured with the laser rangefinder and the coordinates of the GPS reference stations (Gregory S. Benson, ExxonMobil, personal communication, April, 2012). Firstly, a trial distance, D_t (Table 4.1), is calculated in 3D:

$$D_t = \sqrt{(i_2 - i_1)^2 + (j_2 - j_1)^2 + (k_2 - k_1)^2}, \quad (4.1)$$

as well as the corresponding trial inclination, I_t (Table 4.1), calculated in 3D, for all measurements between GPS reference stations and base stations:

If I > 90° then;

$$I_t = 90 + \left[\left(\text{atan}\left[\frac{((k_2+H_t)-k_1)}{\sqrt{(i_2-i_1)^2+(j_2-j_1)^2}}\right]\right)\left(\frac{180}{\pi}\right)\right], \quad (4.2a)$$

If I < 90° then;

$$I_t = 90 - \left[\left(\text{atan}\left[\frac{((k_2+H_t)-k_1)}{\sqrt{(i_2-i_1)^2+(j_2-j_1)^2}}\right]\right)\left(\frac{180}{\pi}\right)\right]. \quad (4.2b)$$

We then calculate an objective function, T_e (Table 4.1), which is the sum of all the differences between trial values (derived from Eq. 4.1, 4.2a, 4.2b) and measured values:

$$\sum_{i=1}^{n} T_e = [(D - D_T) + (I - I_T)]. \quad (4.3)$$

The coordinates of the GPS reference stations are allowed to remain fixed, while the coordinates of the base stations are allowed to change to minimise the objective function

(Eq. 4.3) using a solver iteration function. From this we establish a network of known locations from which we can begin to create a point cloud to represent the coordinates of the outcrop in narrow canyons. We then go on to place reflective targets on the outcrop, and establish locations for laser rangefinder stations.

Table 4.1. Nomenclature for parameters used in georeferencing digital outcrop models.

Parameter	Description	Units
D	measured horizontal distance	m
D_T	calculated trial distance	m
δ	magnetic declination	°
H_T	tripod height	m
i_1	x-coordinate of base station or laser rangefinder station to be triangulated	n/a
i_2	x-coordinate of GPS reference station or base station that has previously been established	n/a
I	summation variable	none
I	measured inclination	°
I_T	calculated trial inclination	°
j_1	y-coordinate of base station or laser rangefinder station to be triangulated	n/a
j_2	y-coordinate of GPS reference station or base station that has previously been established	n/a
k_1	z-coordinate of base station or laser rangefinder station to be triangulated	n/a
k_2	z-coordinate of GPS reference station or base station that has previously been established	n/a
n	total number of measurements made between GPS reference stations, base stations and laser rangefinder stations	none
T_e	Sum of the difference between trial and measured distances and inclinations	none
θ_{OUT}	measured azimuth	°
θ_{QC}	measured azimuth after correction for magnetic declination	°
x_{OUT}	x-coordinate of outcrop target	n/a
x_{LSR}	x-coordinate of laser rangefinder station	n/a
y_{OUT}	y-coordinate of outcrop target	n/a
y_{LSR}	y-coordinate of laser rangefinder station	n/a
z_{OUT}	z-coordinate of outcrop target	n/a
z_{LSR}	2-coordinate of laser rangefinder station	n/a

Laser rangefinder stations must be within range of the outcrop targets and have line-of-sight to at least one GPS reference station and two or more base stations, within a range of 250 m, but these base stations must not lie in a straight line relative to the laser

rangefinder station. We measure the distance, azimuth and inclination from the laser rangefinder stations to the GPS reference station(s) and base station(s). We then follow a similar approach to that used to locate the GPS reference stations, and calculate trial distances, D_t (Eq. 4.1), trial inclinations, I_t (Eq. 4.2a, 4.2b) and an objective function, T_e, (Eq. 4.3) for the laser rangefinder stations. However, this time the coordinates of the GPS reference stations and base stations are allowed to remain fixed, while the coordinates of the laser rangefinder stations are allowed to change to minimise the objective function (Eq. 4.3) using a solver iteration function.

In a final step, we use the distance, azimuth and inclination measurements from the laser rangefinder stations to triangulate the positions of the outcrop targets, where the x-coordinate, x_{OUT} (Table 4.1), is given by:

$$x_{OUT} = x_{LSR} + Dsin\left(\frac{\pi}{180}I\right) sin\left(\frac{\pi}{180}\theta_{QC}\right), \tag{4.4}$$

where θ_{QC} (Table 4.1), is given by:

$$\theta_{QC} = \theta_{OUT} + \delta\,, \tag{4.5}$$

the y-coordinate, y_{OUT} (Table 4.1), by:

$$y_{OUT} = y_{LSR} + Dsin\left(\frac{\pi}{180}I\right) cos\left(\frac{\pi}{180}\theta_{QC}\right), \tag{4.6}$$

and the z-coordinate, z_{OUT} (Table 4.1), by:

$$z_{OUT} = z_{LSR} + Dcos\left(\frac{\pi}{180}\theta_{QC}\right). \tag{4.7}$$

From these positions, a point cloud that represents the XYZ coordinates of the outcrop cliff faces in narrow canyons can be created, with the user controlling the density of

spatial data collected. The XYZ coordinate data is used to georeference a dense point cloud created using stereophotogrammetry.

4.5.2 Stereophotogrammetry

Stereophotogrammetry is the process of reconstructing the 3D coordinates of a point from two or more 2D photographs taken from different positions. Individual points (e.g. pixels) on a photo are identified, from which lines of sight are reconstructed to the position of the camera when the photograph was taken. The 3D coordinates of a point are determined from lines of sight from different camera positions that intersect for a common point. We can use this triangulation technique to create 3D point clouds from multiple, overlapping 2D photographs of outcrops.

The quality of the photographs is the key parameter that controls the quality of the final digital outcrop model. For outcrop cliff faces, photographs should be taken from positions that are close to each other, and with low angle separation between photographs (Fig. 4.7). The orientation of the camera should not be allowed to vary greatly between photographs in a stereoline (Fig. 4.7), as low angle separation between photographs ensures that features look similar in successive photographs and can thus be reliably triangulated. Photographs for each outcrop section should be taken at the same time of day; triangulation becomes difficult if the orientation of the light source changes markedly between photographs. Similarly, if there is a stark contrast between light exposure on the outcrop (e.g. large shadows and bright light on the same image) the quality of the resulting point cloud decreases. All important points on the outcrop should be present on at least three adjacent photographs (Fig. 4.7), with as much overlap between photographs as possible to reduce potential holes in the point cloud. Having

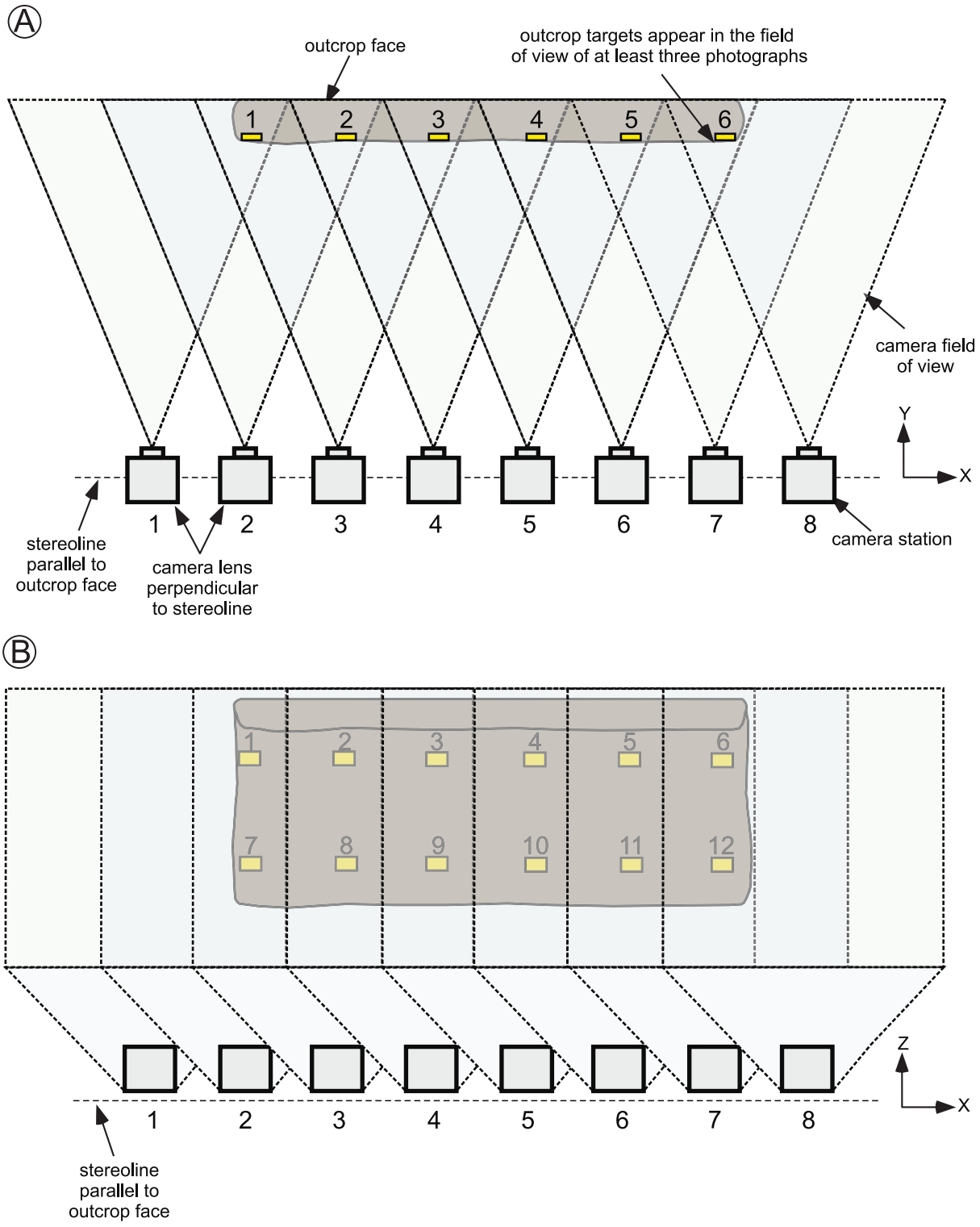


Figure 4.7. (A) Example of stereophotogrammetry outcrop data collection technique in plan-view and (B) oriented in front of the outcrop face. Camera stations one and eight are positioned first and cross-checked to ensure that the stereoline is parallel to the outcrop face and that the camera lens in each position are oriented perpendicular to the stereoline. Each outcrop target should appear in at least three photographs. Camera position one and eight only capture the outcrop target and a small proportion of the outcrop face, but ensure that the targets at the edge of the outcrop appear in sufficient images that these parts of the outcrop can be triangulated.

outcrop targets in the photographs is also useful for identifying the coordinate positions of the outcrop on the dense point cloud. The software used to create the dense point cloud triangulates points in the photographs (e.g. pixels) in 3D and corrects for the distortion of the photo frames, thus limiting perspective effects. A detailed workflow on using the software to create dense point clouds can be found in Appendix C1. The camera used to capture the outcrop must however be calibrated in a separate procedure prior to creating a dense point cloud. Calibrating the camera prior to modelling is described in greater detail in Appendix C1. The density of the point cloud generated using this technique is determined by the user; points can be spaced as close as 1 mm apart and approach the resolution of textured surfaces created with LIDAR datasets. Data from photographs can be used to add red, green and blue (RGB) values to each of the points in the dense point cloud generated using stereophotogrammetry. We follow this approach rather than generating textured surfaces (e.g., Bellian et al., 2005; Enge et al., 2007), as point clouds can be directly imported into conventional reservoir modelling software. In a final step, the dense point cloud is registered to georeferenced outcrop coordinates, so that each point in the dense point cloud has a value of XYZ in "real world" coordinates. The resulting digital outcrop models can be interpreted directly to identify geological surfaces and units for use in geological models.

4.6 Digital outcrop model construction

We now describe the application of this digital outcrop modelling technique to capture the 3D architecture of gutter casts in the G2 parasequence of the Grassy Member, Blackhawk Formation in Tusher Canyon and its side canyon (Fig. 4.5). The side

canyon measures c. 150 m in length and is less than 15 m in width in places, while Tusher canyon measures c. 260 m in length and 100 m in width in the study area (Fig. 4.5).

The first step in creating the digital outcrop model was to georeference the outcrop (Fig. 4.6). Nine GPS reference stations were placed in either high topographic locations in the side canyon that allowed an unobstructed view of the sky and could be viewed from the floor of the side canyon, or in prominent locations in Tusher Canyon, where the canyon is sufficiently wide to allow an unobstructed view of the sky (Figs. 4.5, 4.6). Ten further base stations were placed within the side canyon to create a network of stations (Fig. 4.5) and their coordinates triangulated (using Eq. 4.1, 4.2a, 4.2b, 4.3). The outcrop was then divided into 22 sections to organize data collection. The sections were divided according to the outcrop topography, such that sections end either where the outcrop pinches out or at corners and protrusions. An appropriate laser rangefinder station was identified for each section. In some cases, two laser rangefinder stations were necessary to characterize a given outcrop section. This is because while one stereoline may be have been sufficient to capture minor irregularities in outcrop topography (e.g. protrusions from the cliff face), it was not possible to capture all outcrop targets for the section from one laser rangefinder location and simultaneously position the laser rangefinder station so that it was suitable for triangulation. Where possible, laser rangefinder stations were placed directly over base stations, which minimized the error in the coordinates of the corresponding outcrop targets. In total 28 laser rangefinder stations were used and triangulated relative to the GPS reference station and base station network (using Eq. 4.1, 4.2a, 4.2b, 4.3).

For each outcrop section, reflective targets were placed on the outcrop, spaced approximately 1 m apart, so that both lower and upper parts of the cliff faces had

outcrop targets in view. Measurements of azimuth, distance and inclination were recorded for each outcrop target at a given laser rangefinder station and repeated for each outcrop section. Where outcrop sections were adjacent to one another, measurements of the last three outcrop targets taken from the previous laser rangefinder station position were measured from the new laser rangefinder station position. This allowed overlap between successive outcrop sections between laser rangefinder stations and minimized the potential mismatch of coordinates between the adjacent outcrop sections. Over 2000 targets were measured and triangulated in total (Eq. 4.4, 4.5, 4.6, 4.7) over a two week period. Outcrop coordinate data were then imported into a reservoir modelling package. In a final step, if there was a mismatch in the coordinate data between overlapping parts of two outcrop sections, the outcrop points were rotated around the fixed coordinates of the laser rangefinder station from which the measurements were taken, until the overlap is matched. This step allows the potential error between different coordinate datasets to be minimized.

Photographs were taken at each outcrop section (Fig. 4.6). To ensure that photographs were suitable for stereophotogrammetry, we identified stereolines for each outcrop section. A stereoline was defined by an initial photograph location and an end photograph location for each outcrop section. Intermediate photograph locations along the stereoline were identified with the criteria that each prominent topographic feature was in at least three successive photographs between the two fixed stereoline endpoints. Care was taken to ensure that the camera was positioned parallel to the outcrop face along a given stereoline (Fig. 4.7). More than one stereoline was required for certain outcrop sections characterised by irregular outcrop topography (e.g. protrusions from the cliff face). Approximately 600 photographs were recorded over a one week period to

characterize the outcrop. For the final step in the process, we used the photographs for each outcrop section to create and texture dense point clouds (Fig. 4.6). Each point cloud was individually georeferenced using the triangulated coordinate data and exported into a reservoir model for interpretation. We find that registering the point cloud to as many georeferenced outcrop targets as possible minimises the error in the resulting dense point cloud, which in turn reduces the potential mismatch between adjacent point clouds.

4.7. Digital outcrop model results

Thirty point clouds were created in total to characterize the outcrop. We begin by investigating the ability of the digital outcrop modelling methodology to generate dense 3D point clouds that approach the quality of high-resolution 2D photopans. Visual inspection of the digital outcrop model against outcrop photopans (Fig. 4.8) show a close correspondence in resolution. The stereophotogrammetry-based method results approach the quality of LIDAR-based methods, as each dense cloud can have less than 2 mm between each point, and contain 1-8 million points (Fig. 4.9). This results in high-resolution 3D point clouds that can be directly interpreted using conventional reservoir modelling software (Fig. 4.9). Analysing a 3D dataset in this way removes any errors in estimating geobody dimensions from 2D photopans (Pringle et al., 2004).

We calculate the error in the initial base station and laser rangefinder station triangulation as the average error between trial calculations and actual measurements over all the individual measurements made. We find the average error in distance measurements is 50 cm and the average error in inclination is 0.13° for the base stations.

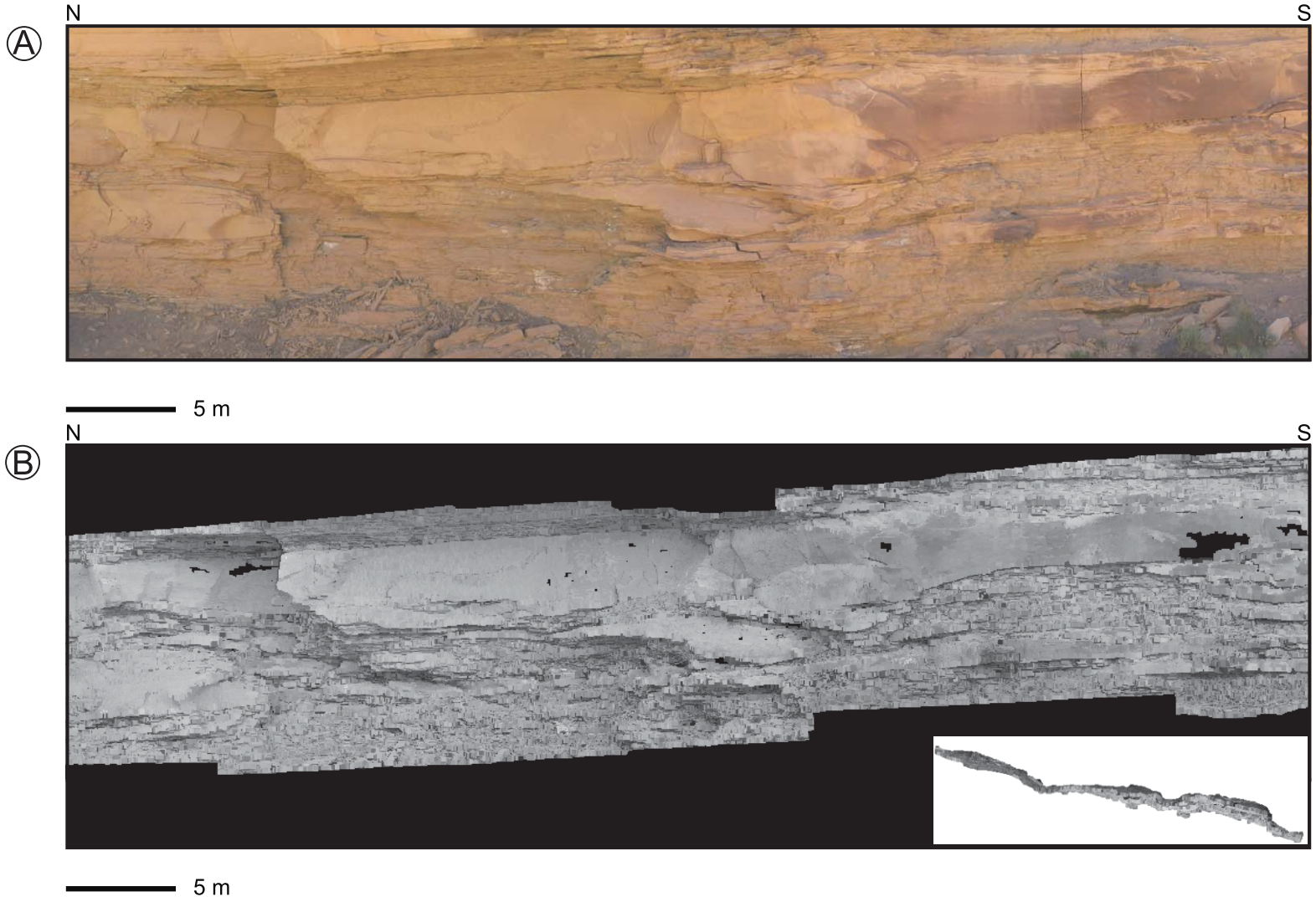


Figure 4.8. (A) Photograph of distal lower shoreface deposits in one of the studied cliff faces (located in Fig. 4.5). (B) Corresponding part of digital outcrop model point cloud with inset map view highlighting the 3D aspect of the point cloud. There is no vertical exaggeration in either image.

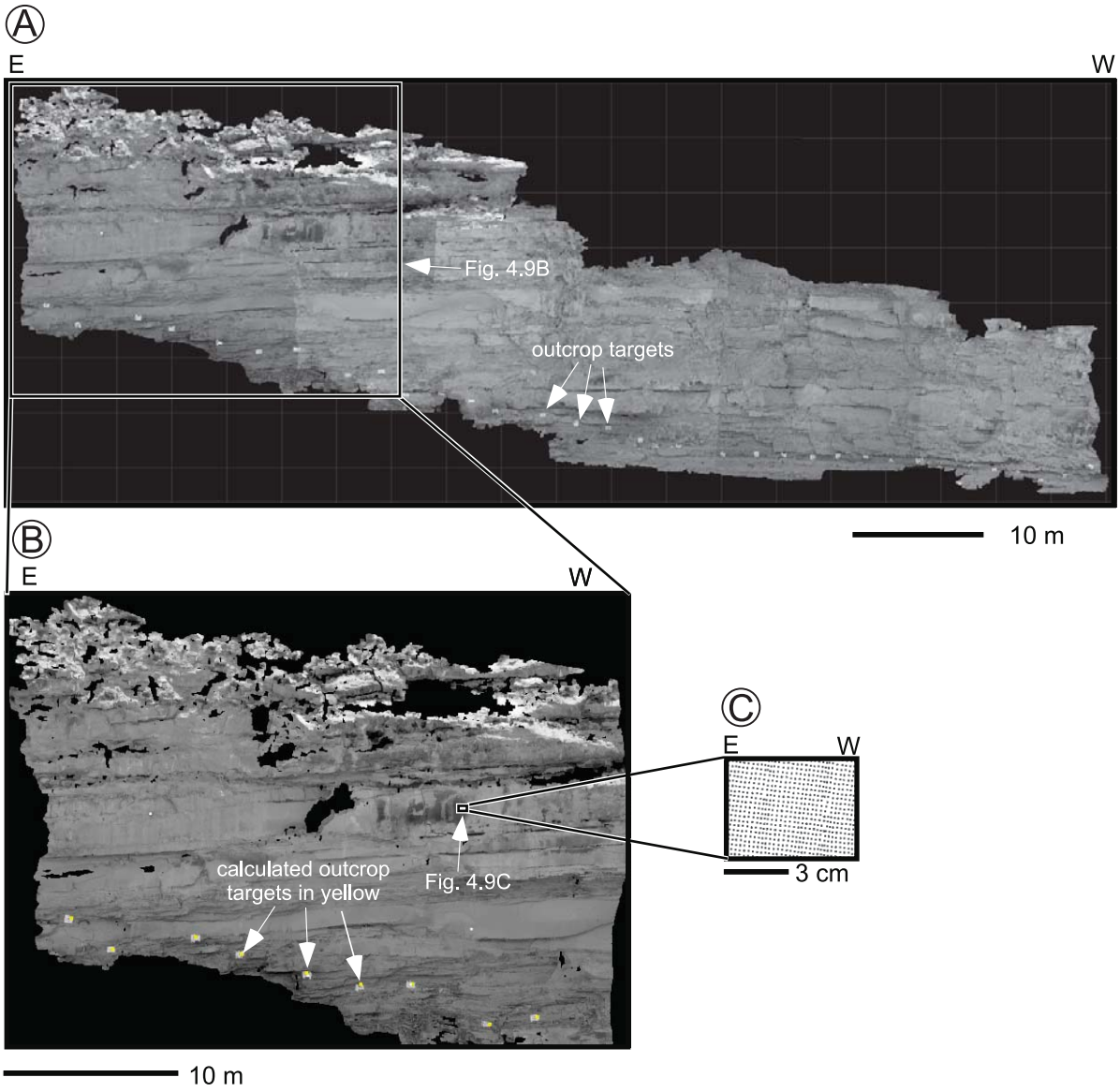


Figure 4.9. (A) Part of the digital outcrop model comprising 12 point clouds. Note the white rectangles at the base of the digital outcrop model, which house the reflective targets at their centre (located in Fig. 4.5). (B) One point cloud extracted from Figure 4.9A is made up of 761636 individual points. Note yellow points at the base of the point cloud, which are the calculated positions of the outcrop targets (Eq. 4.4, 4.5, 4.6, 4.7), which show close correspondence with the original positions on the outcrop face (white rectangles) (located in Fig. 4.5). (C) Closer view of individual point cloud in Figure 4.9B, highlighting the dense point cloud created with less than 2 mm spacing between points. Point clouds are shown with no vertical exaggeration.

The equivalent errors in distance and inclination measurements are typically less than 1 m and less than 0.3°, respectively, for the laser rangefinder stations. The error is typically larger for laser rangefinder stations as measurements are taken over larger distances than for the base stations. Typically, laser rangefinder stations have <50 cm error in

distance measurements with GPS reference stations and base stations that are <50 m in separation, and larger errors occur when the stations are >50 m in separation. After post-processing the outcrop coordinate dataset in conventional reservoir modelling software (Fig. 4.6), the discrepancy between the resulting dense point cloud and the initial triangulated coordinates used for georeferencing is typically less than 50 cm and is consistent with previously reported photogrammetry-based methods (Pringle et al., 2006).

4.8 Preliminary analysis of gutter cast geometry and spatial distribution

4.8.1 Description

Gutter casts are distributed at multiple stratigraphic levels in the studied outcrop (Fig. 4.10). Gutter casts are observed close to the upper boundary of distal lower shoreface deposits (Fig. 4.10D), which is used as a horizontal datum in the digital outcrop model, but also towards the base of these deposits (Fig. 4.10C). Similarly, gutter casts are observed in multiple geographical positions at outcrop (Fig. 4.10A-F). We observe gutter casts that are adjoined to overlying sheet sandstones (Fig. 4.10B) and gutter casts encased in shale (Fig. 4.10A, C). It is not yet clear from these initial observations if these two types of gutter casts occur preferentially at particular stratigraphic horizons or geographical locations.

We also observe gutter casts that exhibit significant variability in scale and cross-sectional geometry (Fig. 4.10). The thickness of gutter casts ranges from c. 0.5 m (Fig. 4.10A) to c. 3 m (Fig. 4.10B) and width ranges from c. 1 m (Fig. 4.10F) to c. 15 m (Fig.

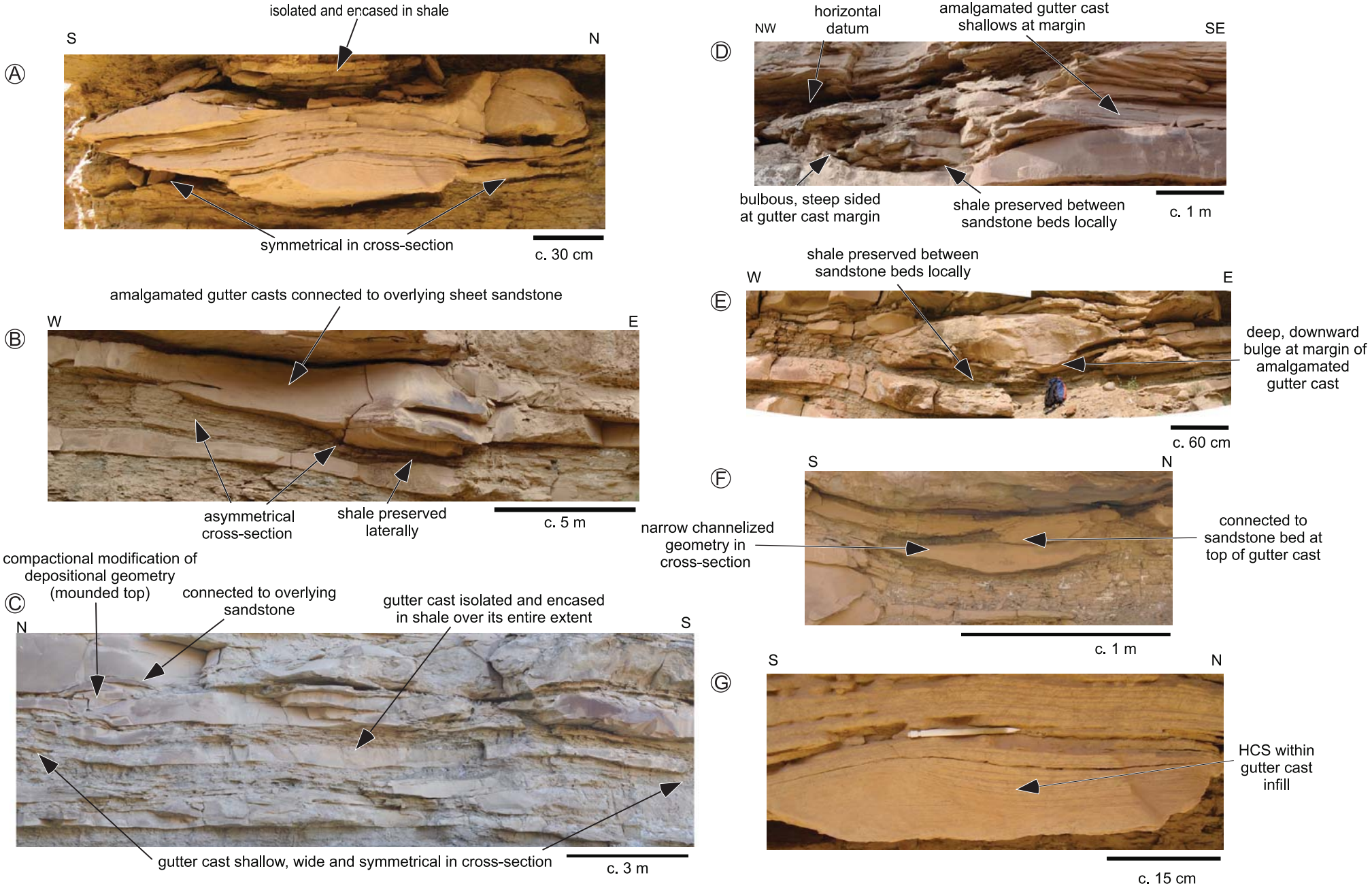


Figure 4.10. (A-G) 2D cross-sections of gutter casts from selected photopans (located in Fig. 4.5), illustrating the range of distributions, geometries, and internal structure of gutter casts in the study area.

4.10C). Gutter casts appear either as symmetrical lenses, which typically have steeply dipping, concave-upward bases and gently dipping, mounded tops (e.g. Fig. 4.10A, C, F), or as asymmetrical lenses, with steeper dips at one margin and shallower dips at the other margin (Fig. 4.10B, D, E). Gutter casts with both types of cross-sectional geometry are observed in cliff faces with a range of local orientations, implying that their axes were oriented from N-S (e.g. Fig. 4.10C) to W-E (e.g., Fig. 4.10B). From our preliminary observations, shallow (c. 0.5 m) gutter casts tend to appear as isolated, narrow or wide symmetrical lenses (e.g., Fig. 4.10C, F), while asymmetrical gutter casts often appear as an amalgamated complex of multiple individual gutter casts that are connected to an overlying sheet sandstone (e.g., Fig. 4.10B, E). Asymmetrical gutter casts are observed to erode into shale beds (e.g., Fig. 4.10B, E) with a thin laterally continuous shale bed preserved locally, or erode into an older sandstone bed, where sandstone beds become connected locally and the lateral continuity of intervening shale beds is not preserved (e.g., Fig. 4.10C, D). It is not clear from these initial observations if one cross-sectional gutter cast geometry or orientation is more abundant. We observe gutter casts that are predominantly filled with very-fine to fine-grained sandstone containing HCS (e.g. Fig. 4.10G). Individual units of HCS are 20 – 90 cm in thickness and exhibit angles of cross-stratification of 8 - 25°. Although rare, gutter casts are observed to contain discontinuous layers of siltstone of thickness less than 10 cm (e.g. Fig. 4.10D).

4.8.2 Interpretation

The occurrence of gutter casts at multiple stratigraphic levels and in all geographical locations within the study area indicates that their process of formation was inherent to all storm events during deposition of the G2 parasequence in the Tusher

Canyon area. Interpretations of their scale and geometry must therefore be applicable to all storm events affecting a particular region of the lower shoreface and shelf during shoreline progradation.

The gutter casts in the study area are significantly larger (up to several metres in depth and several metres to tens of metres in apparent width) than most that have been documented previously (e.g. centimetres in depth and width; Myrow, 1992). Gutter casts of similar size have only previously been described from a Miocene shelf-edge succession in Brunei (Guilpain, 2006). There are two reasons why larger gutter casts, representing deeper and more pronounced storm scour into a cohesive muddy substrate, may have formed. First, the G2 parasequence extends further into the basin than the down-dip pinchouts of several stacked, underlying parasequences (K5, S1-3, G1 parasequences in Fig. 4.4). This large-scale stratigraphic architecture suggests that the G2 shoreface was fronted by relatively deep water (c. 100 m) (Fig. 4.4C), in the context of the Blackhawk Formation depositional systems, such that there was little attenuation of storm waves by friction as they travelled across the Mancos Shale shelf at this time. In this scenario, the G2 shoreface is placed in a physiographic setting similar to a shelf edge that was exposed to large storm waves. Secondly, lowering of storm wave base may have exposed more of the lower shoreface to inner shelf to erosion by storm-generated currents. Such lowering may reflect a change to a more energetic storm-wave regime with no attendant reduction in water depth (cf. “erosional discontinuities” of Hampson, 2000), or a relative fall in sea level (e.g. Hadley and Elliott, 1993). The latter is consistent with the occurrence of an incised valley at the top of the G2 parasequence (O’Byrne and Flint, 1995).

The occurrence of both symmetrical and asymmetrical cross-sectional (2D) geometries for gutter casts, and the difficulty in correlating gutter casts between closely

spaced canyon walls indicates that the 3D geometries and/or orientations of gutter casts differ from previously proposed models (e.g. Myrow, 1992). The range of observed cross-sectional geometries can be accounted for by a sinuous channel geometry (Fig. 4.3B), but not by a linear channel geometry (Fig. 4.3A). The apparent lack of correlation between closely spaced canyon walls implies that gutter casts may have limited continuity along their axes, and/or that they are oriented in a range of directions. One 3D geometrical template which is consistent with the observed 2D cross-sections through gutter casts and their inferred lack of along-axis continuity is that of a flute cast, which is symmetrical in flow-perpendicular cross-section and asymmetrical in flow-parallel cross-section. Flute casts have bulbous, steep-sided noses that face up-flow, and become progressively shallower and wider down-flow (Fig. 4.11) (Allen, 1982). Gutter casts are generally interpreted to be oriented perpendicular to the palaeoshoreline (Myrow, 1992; Chakraborty, 1995; Bhattacharya et al., 2004). In the study area, gutter casts would then be expected to be aligned consistently from west (up-flow) to east (down-flow), relative to the shoreline trend shown in Figure 4.4B. However, this is not consistent with observations of a large range of gutter cast widths, which imply a range of orientations that are perpendicular and oblique to the palaeoshoreline. Although the predominant direction of palaeo-flow may have been perpendicular to the palaeoshoreline, there were pronounced local variations in its orientation.

Evidence of HCS implies that the sandstone beds within gutter casts (e.g. Fig. 4.10G) were deposited under the influence of oscillatory flow during the waning phase of storms (e.g., Dott and Bourgeois, 1982; Duke, 1985; Dumas et al., 2005) and is consistent with previous observations of gutter casts (e.g., Myrow, 1992). However, the occurrence of siltstone lenses (e.g. Fig. 4.10D) suggests that during the latter phases of storm events

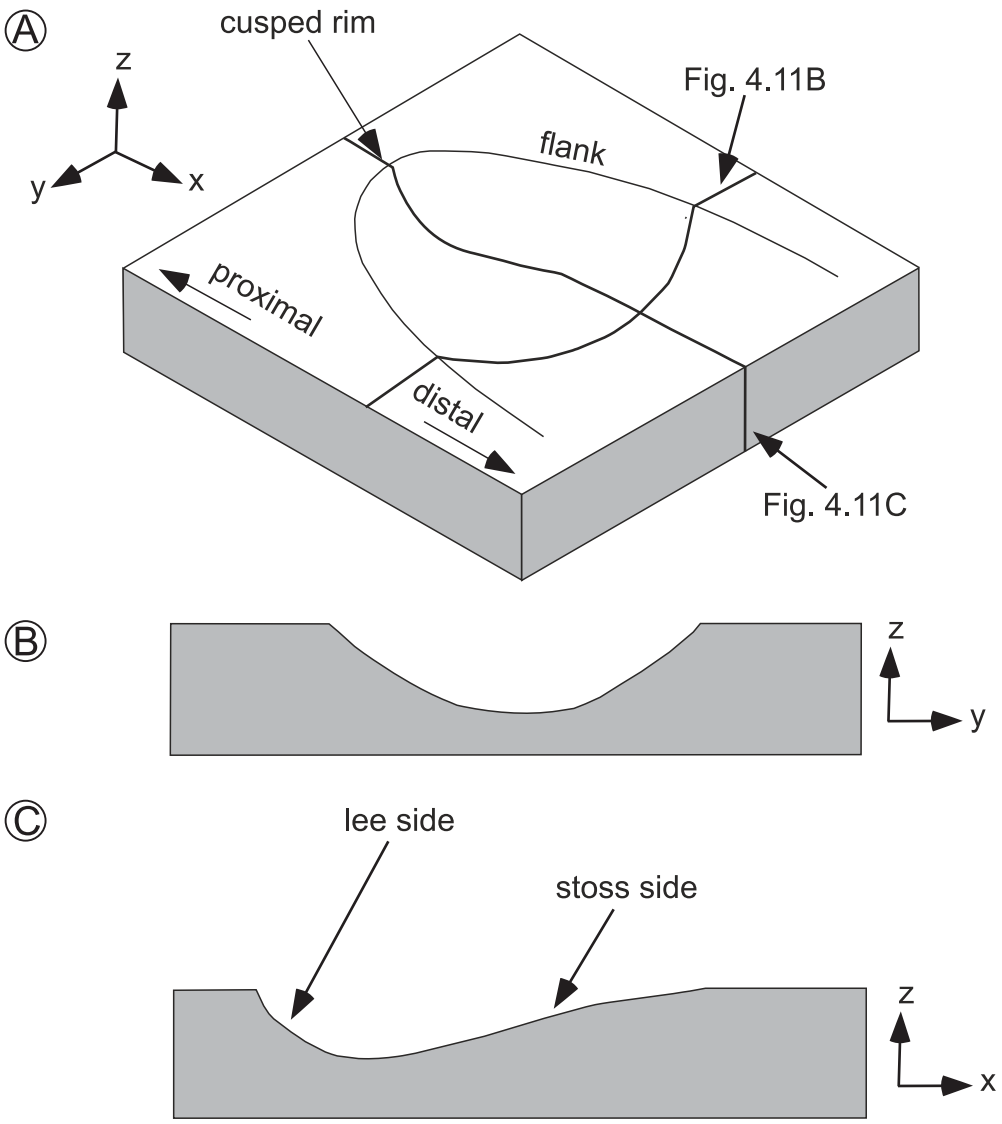


Figure 4.11. Flute cast geometry in (A) plan view, (B) flow-perpendicular cross-section, and (C) flow-parallel cross-section (modified after Allen, 1982). This 3D geometry can account for many of 2D cross-sections through gutter casts observed in the study area.

some gutter casts may have remained unfilled, such that subsequent silt deposition occurred under suspension when fair weather conditions returned.

4.9 Reservoir implications and future applications

We can use the digital outcrop model and interpretation of 3D gutter cast geometry to guide the construction of small-scale reservoir models. These models of the

approximate size of a typical simulation grid block, could then be used to obtain representative values of effective vertical permeability that can then be assigned to distal lower shoreface deposits in full-field reservoir models. Similarly, we can use small-scale models to ascertain if there is an overall sandstone net-to-gross threshold that determines a transition between reservoir and non-reservoir in distal lower shoreface deposits, based on likely sandbody connectivity. Sandstone net-to-gross is a parameter that could be obtained from core- and log-derived measurements in subsurface reservoirs, and may be a useful proxy for sandbody connectivity.

There are several methodologies that can be used to capture the geometry of sandstone bodies in small-scale reservoir models, and that incorporate both stochastic and deterministic components. The most commonly used methodology involves using geostatistical algorithms, such as the Truncated Gaussian Simulation algorithm (TGSim) (White et al., 2003), Sequential Indicator Simulation algorithm (SISim) (Kjønsvik et al., 1994) or Indicator Kriging algorithm (IK) (Falivene et al., 2007), to stochastically populate bodies within the framework of user defined grid. This method has the advantage that numerous realisations can be rapidly generated, but has the considerable disadvantage that grid based methods typically fail to honour complex geometries unless a very fine grid resolution is used. If a very fine grid resolution is used, then this increases fluid-flow simulation times and reduces the number of realisations that can be tested within a reasonable timeframe. Gutter cast geometry and spatial distribution however, may be key parameters that influence sandbody connectivity in distal lower shoreface deposits, and the overall shape of the connected sandstone volume is an important factor in determining effective vertical permeability (King, 1990). Instead, a surface-based modelling approach as demonstrated in Chapter 2 (see also Sech et al., 2009; Enge and

Howell, 2010) should be used to represent the geometry of gutter casts in reservoir models. While a reservoir model constrained by the digital outcrop model presented in this chapter would be largely deterministic, a surfaced-based approach to describing gutter cast geometry and distribution would yield a method in which gutter casts could be reproduced in other reservoir models using a stochastic approach. The resulting models could then be used to capture Representative Elementary Volumes (REV) of distal lower shoreface deposits, for analysis of the overall sandbody connectivity and conductivity and to quantify effective flow properties.

4.10 Discussion

To gain an understanding of the effectiveness of the digital outcrop modelling technique described in this chapter (Fig. 4.6), we evaluate its the strengths and weaknesses relative to LIDAR-based methods that are commonly used to construct digital outcrop models (e.g., Bellian et al., 2005; Enge and Howell, 2007, Buckley et al., 2008; Van Lanen et al., 2009; Enge and Howell, 2010).

We recognise three advantages of the stereophotogrammetry-based method (Table 4.2). (1) The digital outcrop modelling technique we have outlined is a much more cost efficient approach, which represents a considerable advantage over LIDAR-based methods (Pringle et al., 2006). Using stereophotogrammetry is at least an order of magnitude less expensive than LIDAR (e.g., Amour et al., 2012), yet provides comparable point clouds (Figs. 4.8, 4.9). The cost efficiency lies in the lower initial cost of the stereophotogrammetry equipment and software. (2) A further advantage is the speed at which georeferenced dense point clouds can be captured and post-processed. Collection

Table 4.2. Summary of the strengths and weaknesses of the stereophotogrammetry-based method of digital outcrop model construction relative to LIDAR-based methods.

Parameter	Stereophotogrammetry – based methods	LIDAR – based methods
Cost	**Low** Lower cost of equipment and software yet provides comparable results (Figs. 4.8, 4.9).	**High** At least an order of magnitude more expensive than stereophotogrammetry - based methods (Pringle et al., 2006).
Accuracy	**Lower** Limited by quality of photographs and effects of using a combination of different GPS data sets collected at different times	**Higher** DGPS data and scans conducted simultaneously allow for greater accuracy, while software controls both scanner and camera
Time	**Shorter** Requires less post-processing to produce georeferenced digital outcrop models (days)	**Longer** Requires significant post-processing times for triangulation and creation of mesh (days-weeks, e.g. Enge et al., 2007)
Output	**Simple** Point clouds can be interpreted directly in conventional reservoir modelling software (e.g., Figs. 4.8, 4.9)	**Complex** May require additional manipulation and software before data can be used in conventional reservoir modelling software

and post-processing of an equivalent LIDAR survey would take at least twice as long to achieve comparable results (e.g., Pringle et al., 2006; Enge et al., 2007; Amour et al., 2012). (3) The dense point cloud created using the method outlined in this chapter can be manipulated directly using conventional reservoir modelling software. Textured meshes are a common output of LIDAR surveys (e.g., Enge et al., 2007, Bellian et al., 2005), and construction of the resulting digital outcrop models require software that is not specifically designed for geological interpretation. Key stratigraphic surfaces and geobodies are represented using points and exported to conventional reservoir modelling software; however the digital outcrop model is not then present for cross-comparison for quality control in the reservoir modelling package. In house software has been developed by several research groups for the purpose of geological interpretation of textured meshes (e.g. LIDAR Interpretation and Manipulation Environment, LIME,

developed by Simon Buckley at the Centre for Integrated Petroleum Research, Bergen, Norway), but the digital outcrop models still cannot be interpreted, and used to drive reservoir zonation, gridding, and/or facies modelling in one software package. This adds to the complexity of the workflow and reduces efficiency in comparison with the method outlined in this chapter.

However, our stereophotogrammetry-based method has two weaknesses relative to a LIDAR-based workflow (Table 4.2). (1) We find some larger errors in georeferencing the outcrop when using laser rangefinders stations as we typically make measurements to other reference stations over large distances. The scope on the laser rangefinder is the only tool available to aim the laser, and it can be difficult to determine the exact point on the target with which the laser makes contact. While we use reflective targets to increase accuracy of the contact point (e.g. Fig. 4.9A, B), this is not possible for every target (e.g. on high, vertical cliff faces or beneath overhanging ledges). (2) Furthermore, using a combination of different GPS data sets, collected at different times, can result in vertical and/or horizontal offsets between one data set and another (Verwer et al., 2007; Tomás et al., 2010; Amour et al., 2012). These discrepancies can increase processing times of the coordinate data needed to fit dense point clouds together accurately. We find that the limit of producing the dense point cloud occurs at the scale of individual beds. For example, in the head of the side canyon considered in our case study (Fig. 4.5), just the top of the studied stratigraphic interval is exposed, such that in places only an individual bed is captured in each photo frame. It is therefore difficult to obtain a good spread of outcrop GPS coordinate data points, because all points appear at a similar horizon within the photo frame. When registering the point cloud to "real world" coordinates, the small spread of data points cannot provide a sufficient range of depth

data to adequately constrain vertical topography. One further weakness that is shared by both the stereophotogrammetry-based method and LIDAR-based methods is that using point clouds to construct a high-resolution digital outcrop model requires a large number of points (Table 4.2). This can make the point clouds difficult to manipulate easily in conventional reservoir modelling software, and similarly makes it challenging to view multiple dense point clouds simultaneously. A common approach is to decimate the point clouds with removal of a certain proportion of the points (e.g., Enge et al., 2007). However with the stereophotogrammetry-based approach, this results in a compromise between digital outcrop model resolution and visualization efficiency.

4.11 Conclusions

A generic method of capturing 3D, high resolution, digital outcrop datasets has been developed as a tool for creating digital outcrop models when is it is not practicable to use other digital outcrop data collection techniques such as LIDAR. The method is based on stereophotogrammetry and spatial referencing of GPS datasets.

We apply the digital outcrop data collection method to capture the architecture of interbedded sandstone and shale beds in exposures of distal lower shoreface deposits that contain abundant gutter casts. The method provides comparable results to other digital outcrop modelling techniques, such as those based on LIDAR, but has several advantages over these techniques, including the lower cost of data acquisition. Limitations of the technique include the lower accuracy of GPS data measured over large (> 50m) distances, which increases post-processing times.

The resulting digital outcrop model is used to make a preliminary interpretation of 3D gutter cast geometry and spatial distribution in a rock volume of c. 260 x 250 x 25 m, comparable in scale to an inter-well volume in a thinly bedded, shallow-marine reservoir. The digital outcrop model and stereo photogrammetric dataset enable a wider range of gutter cast geometries to be documented than in previous case studies, implying that gutter casts occur either as sinuous channels with marked variations in along-axis scour, or as down-flow shallowing and widening scours similar to flute casts. For either geometrical template, gutter casts are not parallel to each other, but instead exhibit a relatively wide range of orientations. The gutter casts occur at multiple stratigraphic levels and do not appear to occur preferentially in a particular geographic area, implying that they are an integral component of every storm-event bed in the studied succession. The digital outcrop models and the proposed 3D gutter cast geometries and distributions can be readily captured in reservoir models and used to quantify sandbody connectivity and effective flow properties.

Chapter 5

Discussion and Conclusions

5.1 Discussion

5.1.1 Surface-based modelling of heterogeneity in shallow-marine reservoirs

Permeability contrasts associated with clinoform surfaces have been previously identified as a key control on fluid flow and hydrocarbon recovery within shallow-marine reservoirs (e.g., Wehr and Brasher, 1996; Ainsworth et al., 1999; Dutton et al., 2000; Howell et al., 2008a, 2008b; Jackson et al., 2009; Enge and Howell, 2010). This thesis has described a stochastic, surface-based algorithm that can be used as a tool for rapidly incorporating multiple three-dimensional clinoform surfaces and their associated heterogeneity into models of shallow-marine reservoirs (e.g. Figs. 2.7, 2.14). The application of clinoform-modelling algorithm has been demonstrated using: (1) a deterministic approach where a rich, high resolution dataset is available (Ferron Sandstone Member outcrop analogue) (Fig. 2.8); and (2) a stochastic element where the data are sparse (Sognefjord Formation, Troll Field sector) (Fig. 2.15).

As the algorithm is generic it can be applied to generate clinoforms within reservoir models of different shallow-marine systems. However with modification, the clinoform-modelling algorithm (Appendix A1) could be adapted to represent the geometries of other heterogeneities present over a range of lengthscales within shallow-marine systems. Specifically, the dimensionless shape function (Eq. 2.7, Chapter 2, Section 2.3.3) could be replaced with another mathematical function to

describe other observed geometries. One particular application would be to replace the dimensionless shape function (Eq. 2.7) with a sigmoid function that could be used to represent compound deltaic clinoforms (e.g. Pirmez et al., 1998). Furthermore, the clinoform-modelling algorithm could be adapted and applied in other depositional systems, for example, to represent heterogeneities in inclined heterolithic strata within fluvial point bar systems (e.g. Hassanpour et al., 2013) or clinoforms within carbonate platforms (e.g. Adams et al., 2011). Thus, the clinoform-modelling algorithm provides a platform on which to develop a suite of generic surface-based algorithms that describe key geometries that impact on fluid-flow and hydrocarbon recovery across a range of depositional systems.

5.1.2 Quantifying the impact of heterogeneity on fluid flow and hydrocarbon recovery in fluvial-dominated deltaic reservoirs

In contrast with previous stochastic surface-based modelling approaches (e.g., Xie et al., 2001; Pyrcz et al., 2005; Zhang et al., 2009), the clinoform-modelling algorithm yielded a suite of geological models suitable for fluid flow simulation (e.g. Figs. 2.8, 2.15, 3.4). Furthermore, the geometry and distribution of heterogeneity associated with clinoform surfaces was retained in fluid flow simulations. The resulting models were used to quantify the impact on oil recovery of geological heterogeneity and reservoir engineering decisions in fluvial-dominated deltaic shallow-marine reservoirs (Fig. 3.7).

Although the impact of heterogeneity associated with clinoforms is typically larger than that of other geological heterogeneities and of reservoir engineering decisions, clinoforms are difficult to detect using conventional reservoir-monitoring

techniques (e.g. Fig. 3.15) and are often omitted from shallow-marine reservoir models. However, we have demonstrated that clinoforms associated with significant barriers to flow are marked by prominent breaks in water saturation that may be detected and monitored in production wells, in order to characterize clinoform-related sweep patterns during production (Fig. 3.15). Similar breaks in water saturation have been recorded across clinoform surfaces in other shallow-marine systems (e.g. Hampson et al., 2008; Hampson et al., in review). Subsurface datasets can be combined with the clinoform-modelling algorithm described in Chapter 2, to develop production strategies to mitigate the impact of heterogeneities associated with clinoforms on fluid flow and hydrocarbon recovery in shallow-marine reservoirs. Specifically, if data from clinoform-bearing shallow-marine reservoirs were available, a future application of this work would be to develop the clinoform-modelling algorithm so that it can be conditioned to subsurface datasets. This process could be automated to produce multiple realisations of clinoform-bearing reservoir models that honour subsurface data to assist history-matching processes.

5.1.3 Three-dimensional digital outcrop modelling using stereophotogrammetry

We have identified that the vertical permeability of thinly-bedded reservoir intervals has a significant impact on sweep efficiency and hydrocarbon recovery within shallow-marine reservoirs (Fig. 3.7). This thesis has described a stereophotogrammetry-based digital outcrop data collection method (Fig. 4.6) and demonstrated its application to capture exposures of distal lower shoreface deposits that contain abundant gutter casts in order to better characterize vertical permeability in thinly-bedded reservoir intervals (Figs. 4.8, 4.9).

Conventional approaches to capture the spatial distribution of petrophysical properties within facies types are typically limited by grid resolution rather than underlying geology, and often fail to represent the true geometries of the heterogeneity present (Jackson et al., 2013). Future work should focus on developing a stochastic surface-based modelling approach as demonstrated in Chapter 2 (See also Sech et al., 2009; Enge and Howell, 2010) to capture the geometry and spatial distribution of gutter casts. This approach would yield a method that could be reproduced in other shallow-marine reservoir models. The resulting surface-based models can be used to explicitly model surfaces that capture the architecture of interbedded sandstone and shale beds in small-scale models. Petrophysical properties can be derived at the Representative Elementary Volume (e.g. Jackson et al., 2003), in which case they represent effective properties that can be assigned to discrete volumes bounded by surfaces in larger-scale models of shallow-marine reservoirs regardless of volume (Jackson et al., in press). The stereophotogrammetry-based workflow could be extended further to identify and capture key smaller-scale heterogeneities within shallow-marine reservoirs at a lower cost of data acquisition and processing, and at greater speed than other digital outcrop modelling techniques including LIDAR-based methods.

5.1.4 Surface-based modelling for flow simulation: future directions

We have described an application of surface-based modelling that allows multiple clinoform surfaces to be captured in models of shallow-marine reservoirs. Clinoform geometry is retained efficiently for flow simulation as surfaces can be used to model clinoforms prior to gridding, so that fewer grid cells are required to capture

their geometry in flow simulation, in comparison with conventional reservoir modelling approaches (see sections 1.3 and 1.4 in Chapter 1 for review). However, in this thesis we have described heterogeneity within shallow-marine reservoirs over multiple lengthscales (e.g. Fig. 3.1C and Fig. 4.2B) and at present it is not possible to explicitly capture and integrate both lengthscales of heterogeneity in a single reservoir model for flow simulation. Even using a surface-based reservoir modelling approach would yield models with grids containing too large a number of cells for direct flow simulation to be computationally feasible.

We suggest that such integrated models that represent the spatial distribution and geometry of heterogeneity over multiple lengthscales using surfaces, may be possible in the long term. As described in Chapter 1, surfaces are used to define closed volumes or zones (e.g. channel bodies Fig. 5.1B), which are each gridded separately. In conventional reservoir simulation experiments such as those presented in Chapters 2 and 3, grid resolution is fixed for a given reservoir zone bounded by surfaces. More recently, methods have been developed that allow volumes or zones bounded by surfaces to be gridded using unstructured, adaptive, tetrahedral meshes (e.g. Fig. 5.1C) (e.g. Jackson et al., 2013; Jackson et al., in press). Unstructured, adaptive meshes for simulation of flow through porous media actively refine and coarsen during the simulation (Fig. 5.2). This offers a considerable advantage as in many production scenarios, high grid resolution is only required in specific regions of the model where pressure or saturation gradients are large, thus computational effort is focused on regions of the model where it is most required (Jackson et al., in press). For example, in the waterflooding simulation experiments presented in Chapters 2 and 3 (e.g. Fig. 2.10 and Fig. 3.8), high resolution of the grid would only be required

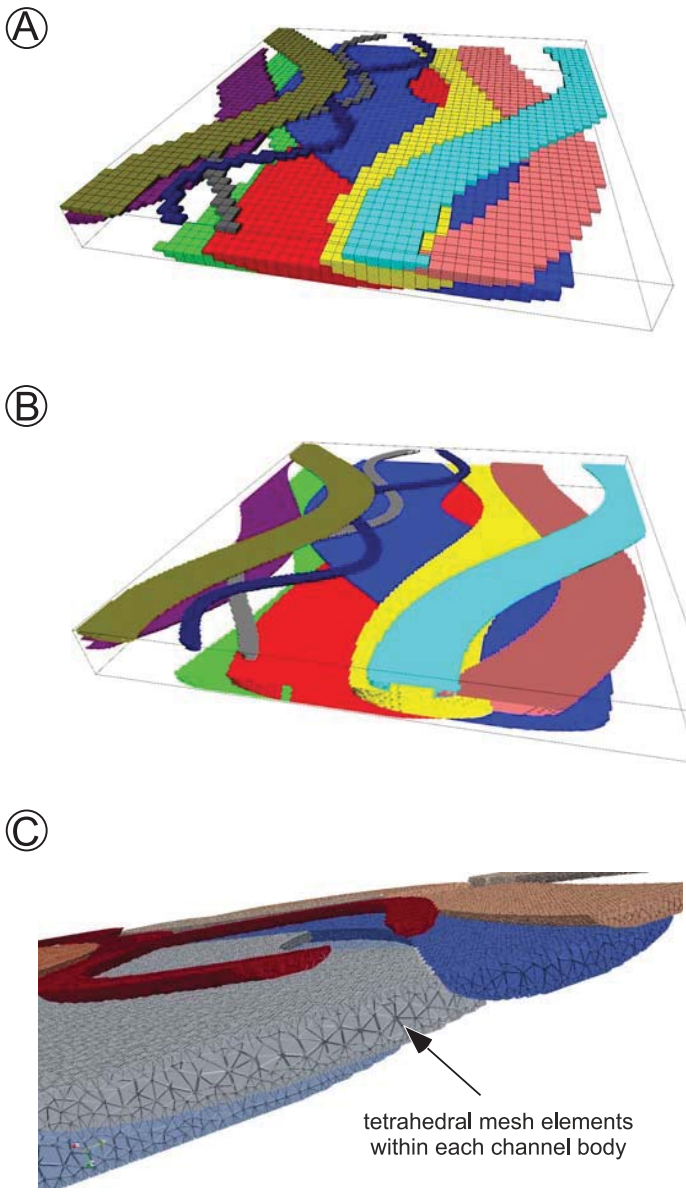


Figure 5.1. (A) Object-based modelling approach to capture channelized sandbodies in a non-reservoir (mudstone) background on a fine-scale cell-based grid. Channelized sandbodies have a 'stair-step' geometry limited by grid resolution. Channelized sandbodies are shown in colour while the non-reservoir background and associated grid-cells are not shown. (B) Surface-based model to capture channelized sandbodies in a non-reservoir (mudstone) background; each channelized sandbody is defined by an upper and lower surface. (C) Close up view of part of the surface-based model shown in (B), meshed with tetrahedral elements. The element shape and size is adapted to capture the varying size of the channelized sandbodies; the non-reservoir background is not meshed as it does not contribute to flow. The complex sandbody architecture is well preserved with efficient use of mesh elements (compare Fig. 5.1A and Fig. 5.1C) (modified after Jackson et al., in press).

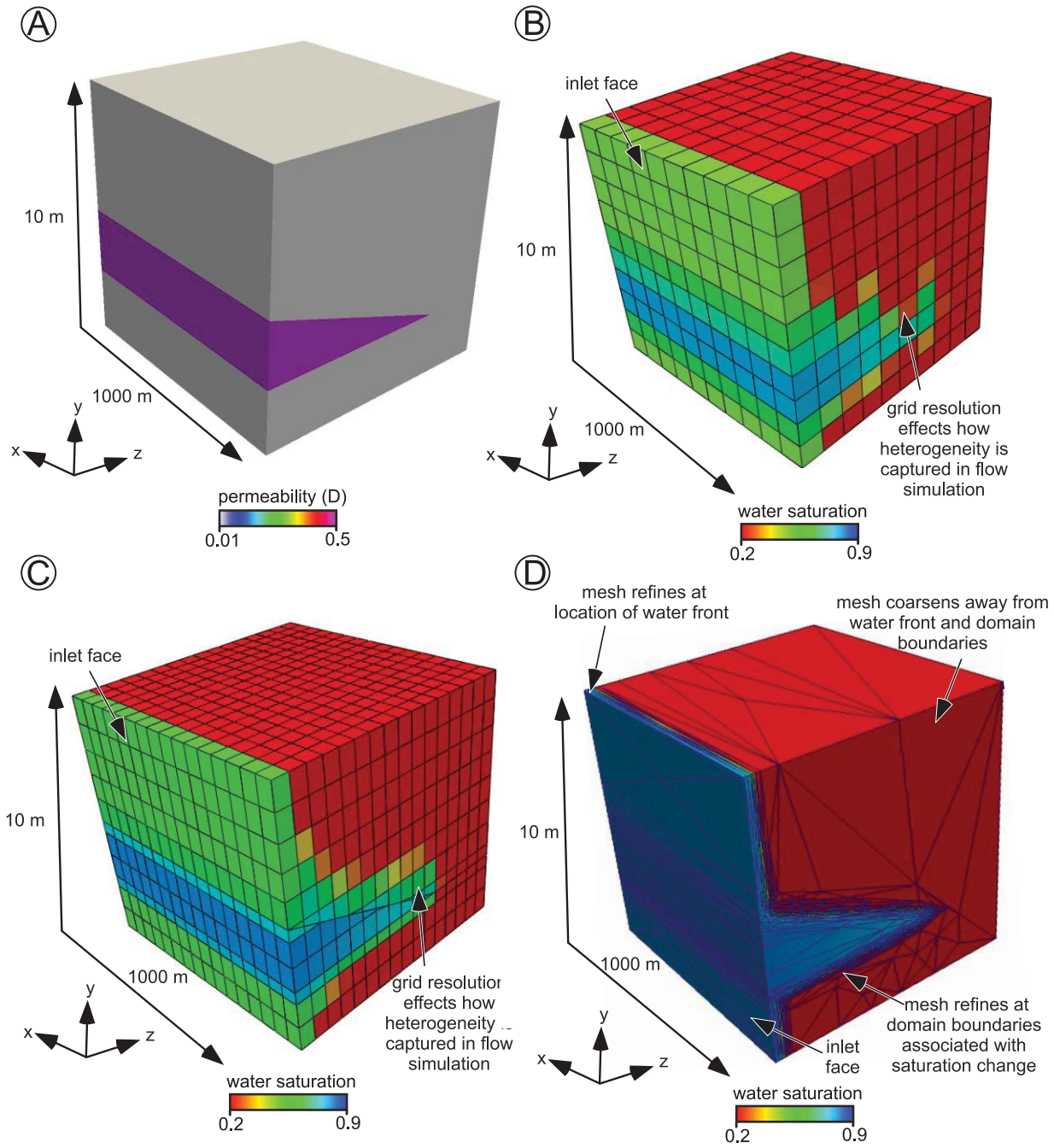


Figure 5.2. Comparison of numerical solutions obtained using an adaptive mesh in a heterogeneous model, with those obtained using conventional methods. (A) View highlighting the distribution of heterogeneity in models (C) and (D). Purple denotes high permeability while grey denotes low permeability. Permeability for cartesian model in (B) not shown. Water saturation at a snapshot in time (0.2 pore-volumes injected (PVI) in (B) cartesian grid, (C) cornerpoint grid and (D) adaptive, unstructured mesh. Note the variation in water saturation profiles between models (B) and (C) with model (D), arising from numerical dispersion affecting the movement of water which significantly alters the time to water breakthrough and oil recovery at breakthrough (modified after Jackson et al., 2013).

close to the water front where the saturation gradient is large, but behind the front the saturation changes gradually and high resolution is not required (Jackson et al., in press). As well as offering computational efficiency for fluid flow simulation experiments, unstructured adaptive meshes have demonstrated a further key advantage over conventional gridding approaches. As shown in Figure 5.2B and C, grid resolution affects how heterogeneity is captured in flow simulation, and numerical dispersion effects may cause discrepancies between predicted and observed time to water breakthrough and oil recovery (Jackson et al., 2013). Thus, a surface-based approach to reservoir modelling coupled with the next generation of unstructured, adaptive mesh simulators, may facilitate a step-change in reservoir modelling capabilities. The surface-based models described in this thesis (e.g. Figs. 2.8, 2.15) would be compatible with unstructured, adaptive, tetrahedral meshes, but at present unstructured adaptive meshes, for flow through porous media have only been demonstrated for simple heterogeneous models (e.g. Fig. 5.2A, D). When unstructured, adaptive, tetrahedral meshes can be used with more complex heterogeneous shallow-marine reservoir models such as those presented in this thesis, a future aspect of this PhD work would be to integrate the surface-based clinoform-bearing models with the meshes for flow simulation.

5.2 Recommendations for future work

The research conducted in this thesis could be extended in the following areas:

(1) Expand the clinoform-modelling algorithm so that it can be conditioned to subsurface datasets.

(2) Results from the fluid-flow simulations of the clinoform-bearing Troll West sector model should be compared with actual production data to demonstrate the potential benefits of modelling heterogeneities associated with clinoforms.

(3) Develop a suite of generic surface-based algorithms that describe key geometries that impact on fluid-flow and hydrocarbon recovery across a range of depositional systems.

(4) Use the digital outcrop model and interpretation of 3D gutter cast geometry to guide the construction of 3D, stochastic, surface-based, small-scale reservoir models.

(5) Obtain representative values of effective vertical permeability that can be assigned to distal lower shoreface deposits in full-field reservoir models.

(6) Use percolation theory to ascertain if there is an overall sandstone net-to-gross threshold that determines a transition between reservoir and non-reservoir in distal lower shoreface deposits, based on likely sandbody connectivity.

(7) Integrate the surface-based clinoform-bearing models described in this thesis with unstructured, adaptive, tetrahedral meshes for flow simulation, when this approach becomes feasible.

5.3 Conclusions

The research conducted for this thesis leads to the following conclusions:

(1) A clinoform-modelling algorithm has been developed that allows efficient incorporation of clinoforms into field-scale reservoir models using deterministic or stochastic components.

(2) The algorithm can match clinoform geometries and distributions observed at outcrop as well as honouring subsurface data.

(3) Under certain displacement conditions the impact of clinoforms can be larger than that of other uncertainties in reservoir characterization or reservoir engineering decisions.

(4) The proportion and distribution of barriers to flow along clinoforms exert the greatest influence on hydrocarbon recovery in models of fluvial-dominated deltaic reservoirs; equivalent models that neglect these barriers over-predict recovery by up to 35%.

(5) The vertical permeability of the distal delta-front (dDF) facies association has the most significant positive impact on oil recovery in models of fluvial-dominated deltaic reservoirs; when vertical permeability is non-zero oil recovery is increased.

(6) Clinoforms can have a significant impact on sweep and hydrocarbon recovery but are not associated with breaks in pressure. This makes the presence of clinoforms difficult to diagnose.

(7) Clinoforms should be routinely included in models of fluvial-dominated deltaic reservoirs, in order to better estimate hydrocarbon recovery and uncertainty in drainage patterns.

(8) A generic method of capturing 3D, high resolution, digital outcrop datasets has been developed as a tool for creating digital outcrop models when is it is not practicable to use other digital outcrop data collection techniques such as LIDAR.

(9) The method provides comparable results to other digital outcrop modelling techniques, such as those based on LIDAR, but has several advantages over these techniques, including the lower cost of data acquisition and processing, and greater speed with which georeferenced dense point clouds can be captured.

(10) Limitations of the technique include the lower accuracy of GPS data measured over large (> 50m) distances, which increases post-processing times.

(11) The digital outcrop model and stereo photogrammetric dataset enable a wider range of gutter cast geometries to be documented than in previous case studies, implying that gutter casts occur either as sinuous channels with marked variations in along-axis scour, or as down-flow shallowing and widening scours similar to flute casts.

(12) The proposed 3D gutter cast geometries and distributions can be readily captured in reservoir models and used to quantify sandbody connectivity and effective flow properties.

Bibliography

Adams, E. W., J. P. Grotzinger, W. A. Watters, S. Schröder, D. S. McCormick, and H. A. Al-Siyabi, 2005, Digital characterization of thrombolite-stromatolite reef distribution in a carbonate ramp system (terminal Proterozoic, Nama Group, Namibia): AAPG Bulletin, v. 89, p. 1293-1318.

Adams, E. W., C. Grélaud, M. Pal, A. É. Csoma, O. S. Al Ja'aidi, and R. Al Hinai, 2011, Improving reservoir models of Cretaceous carbonates with digital outcrop modelling: (Jabal Madmar, Oman): static modelling and simulating clinoforms: Petroleum Geoscience, v. 17, p. 309-332.

Aigner, T., 1985, Storm depositional systems: dynamic stratigraphy in modern and ancient shallow-marine systems: Berlin, Springer-Verlag, 174 p.

Ainsworth, B. R., M. Sanlung, and S. T. C. Duivenvoorden, 1999, Correlation techniques, perforation strategies, and recovery factors: an integrated 3-D reservoir modelling study, Sirikit field,Thailand: AAPG Bulletin, v. 83, p. 1535-1551.

Ainsworth, R. B., B. K. Vakarelov, and R. A. Nanson, 2011, Dynamic spatial and temporal prediction of changes in depositional processes on clastic shorelines: Toward improved subsurface uncertainty reduction and management: AAPG Bulletin, v. 95, p. 267–297.

Alexander, J., 1993, A discussion on the use of analogues for reservoir geology: Advances in reservoir geology, Volume 69: London, United Kingdom, Geological Society of London, p. 177-194.

Allen, J. R. L., 1982, Sedimentary structures, their character and physical basis, v. 1: Elsevier, Amsterdam, 593 p.

Amour, F., M. Mutti, N. Christ, A. Immenhauser, S. M. Agar, G. S. Benson, S. Tomás, R. Always, and L. Kabiri, 2012, Capturing and modelling metre-scale spatial facies heterogeneity in a Jurassic ramp setting (central High Atlas, Morocco): Sedimentology, v. 59, p. 1158-1189.

Anderson, P. B., T. C. Chidsey Jr, K. McClure, A. Mattson, and S. H. Snelgrove, 2002, Ferron Sandstone stratigraphic cross-sections, Ivie Creek area, Emery County, Utah: Utah Geological Survey, Open File Report 390 (CD).

Anderson, P. B., K. McClure, T. C. Chidsey Jr, T. A. Ryer, T. H. Morris, J. A. Dewey Jr., and R. D. Adams, 2003, Interpreted regional photomosaics and cross sections, Cretaceous Ferron Sandstone, east-central Utah: Utah Geological Survey, Open File Report 412 (CD).

Anderson, P. B., T. C. Chidsey Jr., T. A. Ryer, R. D. Adams, and K. McClure, 2004, Geological framework, facies paleogeography, and reservoir analogs of the Ferron Sandstone in the Ivie Creek area, east-central Utah, *in*: T. C. Chidsey Jr, R.D. Adams, and T. H. Morris, eds., Regional to wellbore analogue for fluvial-deltaic reservoir modelling: The Ferron Sandstone of Utah: AAPG Studies in Geology 50, p. 331-356.

Anderson, P. B., and T. A. Ryer, 2004, Regional stratigraphy of the Ferron Sandstone, *in*: T. C. Chidsey Jr., R. D. Adams, and T. H. Morris, eds., Regional to wellbore analog for fluvial-deltaic reservoir modelling: the Ferron Sandstone of Utah: AAPG Studies in Geology 50, p. 211-224.

Anderson, W. G., 1987, Wettability literature survey-part 5: The effects of wettability on relative permeability: Journal of Petroleum Technology, v. 39, p. 1454-1468.

Atkinson, C. D., M. J. B. G. Goesten, A. Speksnijder, and W. Van der Vlught, 1986, Storm-generated sandstone in the Miocene Miri Formation, Seria Field, Brunei (N.W. Borneo), *in*: R. J. Knight and J. R. McLean, eds., Shelf sands and sandstones: Canadian Society of Petroleum Geologists, Memoir II, p. 213-240.

Baillie, K., and J. James-Romano, 2010, Identifying and quantifying thin bedded pay (Part B): The use of dynamic data to evaluate productivity potential in gas reservoirs: Society of Petroleum Engineers Paper 133535.

Ball, M. M., E. A. Shinn, and K. W. Stockman, 1967, The geologic effects of Hurricane Donna in south Florida: Journal of Geology, v. 75, p. 583-597.

Balsley, J. K., 1980, Cretaceous wave-dominated delta systems, Book Cliffs, east-central Utah: AAPG Continuing Education Course Field Guide, 163 p.

Barrell, J., 1912, Criteria for the recognition of ancient delta deposits: Geological Society of America Bulletin, v. 23, p. 377-446.

Barton, M. D., E. S. Angle, and N. Tyler, 2004, Stratigraphic architecture of fluvial-deltaic sandstones from the Ferron Sandstone outcrop, east-central Utah, *in*: T. C. Chidsey Jr, R. D. Adams, and T. H. Morris, eds., Regional to wellbore analogue for fluvial-deltaic reservoir modelling: the Ferron Sandstone of Utah: AAPG Studies in Geology 50, p. 193-210.

Batycky, R. P., M. R. Blunt, and M. Thiele, 1997, A 3D field-scale streamline-based reservoir simulator: Society of Petroleum Engineers Reservoir Engineering, v. 12, p. 246-254.

Begg, S. H., and D. M. Chang, 1985, A simple statistical method for calculating the effective vertical permeability of a reservoir containing discontinuous shales: Society of Petroleum Engineers Paper No. 14271, 15 p.

Begg, S. H., and P. R. King, 1985, Modeling the effects of shales on reservoir performance: calculation of effective vertical permeability: Society of Petroleum Engineers Paper No. 13529, 15 p.

Begg, S. H., E. R. Gustason, and M. W. Deacon, 1992, Characterization of a fluvial-dominated delta: Zone 1 of the Prudhoe Bay field: Society of Petroleum Engineers Paper No. 24698, 14 p.

Bellian, J. A., C. Kerans, and D. C. Jennette, 2005, Digital outcrop models: Applications of terrestrial scanning LIDAR technology in stratigraphic modeling: Journal of Sedimentary Research, v. 75, p. 166-176.

Bhattacharya, H. N., B. Bhattacharya, I. Chakraborty, and A. Chakraborty, 2004, Sole marks in storm event beds in the Permo-Carbiniferous Talchir Formation, Raniganj Basin, India: Sedimentary Geology, v. 166, p. 209-222.

Bjørkum, P. A., and O. Walderhaug, 1990, Geometrical arrangement of calcite cementation within shallow-marine sandstones: Earth Science Reviews, v. 29, p. 145-161.

Box, G. E. P., and M. E. Muller, 1958, A note on the generation of random normal deviates: The Annals of Mathematical Statistics, v. 29, p. 610-611.

Box, G. E. P., and N. R. Draper, 1987, Empirical model building and response surfaces: New York, Wiley, 669 p.

Boyd, R., R. W. Dalrymple, and B. A. Zaitlin, 1992, Classification of clastic coastal depositional environments: Sedimentary Geology, v. 80, p. 139–150.

Bryant, I. D., J. D. Kantorowicz, J.D., and C. F. Love, 1988, The origin and recognition of laterally continuous carbonate-cemented horizons in the Upper Lias Sands of southern England: Marine and Petroleum Geology, v. 5, p. 108- 133.

Bryant, I. D., D. Carr, P. Cirilli, N. Drinkwater, D. McCormick, P. Tilke, and J. Thurmond, 2000, Use of 3D digital analogs as templates in reservoir modeling: Petroleum Geoscience, v. 6, p. 195-201.

Buckley, S. J., J. A. Howell, H. D. Enge, and T. H. Kurz, 2008, Terrestrial laser scanning in geology: Data acquisition, processing and accuracy considerations: Journal of the Geological Society (London), v. 165, p. 625-638.

Chakraborty, C., 1995, Gutter casts from the Proterozoic Bijaygarh Shale Formation, India: their implication for storm-induced circulation in shelf settings: Geological Journal, v.30, p. 69-78.

Ciammetti, G., P. S. Ringrose, T. R. Good, J. M. L. Lewis, and K. S. Sorbie, 1995, Waterflood recovery and fluid flow upscaling in a shallow marine and fluvial sandstone sequence: Society of Petroleum Engineers Paper 79669.

Coleman, J. M., 1988, Dynamic changes and processes in the Mississippi River Delta: Geological Society of America Bulletin, v. 100, p. 999-1015.

Coll, C., B. Cortiula, G. Gonzalez, E. Meza, L. Rondon, 1996, Effect of vertical heterogeneities in a petrophysical evaluation of low resistivity pay zones, B sands, Upper Eocene, Block III, Lake Maracaibo: AAPG Bulletin, v. 80, 1282.

Colombera, L., F. Felletti, N. P. Mountney, and W. D. McCaffrey, 2012, A database approach for constraining stochastic simulations of the sedimentary heterogeneity of fluvial reservoirs: AAPG Bulletin, v. 96, p. 2143–2166.

Corbeanu, R. M., K. Soegaard, R. B. Szerbiak, J. B. Thurmond, G. A. McMechan, D. Wang, S. Snelgrove, G. B. Forster, and A. Menitove, 2001, Detailed internal architecture of a fluvial channel sandstone determined from outcrop, cores, and 3-D ground-

penetrating radar: example from the middle Cretaceous Ferron Sandstone, east-central Utah: AAPG Bulletin, v. 85, p. 1583–1608.

Cotter, E. 1976. The role of deltas in the evolution of the Ferron Sandstone and its coals. Brigham Young University Studies in Geology, v. 22, p. 15-41.

Deutsch, C., and L. Wang, 1996, Hierarchical object-based stochastic modeling of fluvial reservoirs: Mathematical Geology, v. 28, p. 857-880.

Deutsch, C. V., Y. Xie, and A. S. Cullick, 2001, Surface geometry and trend modeling for integration of stratigraphic data in reservoir models: Society of Petroleum Engineers Paper 68817.

Deutsch, C. V., 2002, Geostatistical reservoir modeling: New York, Oxford University Press, 376 p.

Deveugle, P. E. K., M. D. Jackson, G. J. Hampson, M. E. Farrell, A. R. Sprague, J. Stewart, and C. S. Calvert, 2011, Characterization of stratigraphic architecture and its impact on fluid flow in a fluvial-dominated deltaic reservoir analog: Upper Cretaceous Ferron Sandstone Member, Utah: AAPG Bulletin, v. 95, p. 693-727.

Dilib, F. A., and M. D. Jackson, 2012, Closed-loop feedback control in intelligent wells: Application to a heterogeneous, thin oil-rim reservoir in the North Sea: Society of Petroleum Engineers Paper 159550.

Dott, R. H., and J. Bourgeois, 1983, Hummocky cross-stratification: Significance of its variable bedding sequences: Geological Society of America Bulletin, v. 93, p. 663-680.

Dreyer, T., M. Whitaker, J. Dexter, H. Flesche, and E. Larsen, 2005, From spit system to tide-dominated delta: integrated reservoir model of the Upper Jurassic Sognefjord Formation on the Troll West Field, *in:* Doré, A. G., and Vining, B. A.,

eds., Petroleum Geology: North-West Europe and Global Perspectives - Proceedings of the 6th Petroleum Geology Conference, p. 423-448.

Duke, W. L., 1985, Hummocky cross-stratification, tropical hurricanes, and intense winter storms: Sedimentology, v. 32, p. 167-194.

Duke, W. L., 1990, Geostrophic circulation or shallow marine turbidity currents? The dilemma of paleoflow patterns in storm-influenced prograding shoreline systems: Journal of Sedimentary Petrology, v. 60, p. 870-883.

Dumas, S., R. W. C. Arnott, and J. B. Southard, 2005, Experiments on oscillatory-flow combined-flow bedforms; implications for interpreting parts of the shallow marine sedimentary record: Journal of Sedimentary Research, v. 75, p. 501-513.

Dutton, S. P., B. J. Willis, C. D. White, and J. P. Bhattacharya, 2000, Outcrop characterization of reservoir quality and interwell-scale cement distribution in a tide-influenced delta, Frontier Formation, Wyoming USA : Clay Minerals, v. 35, p. 95-105.

Edmonds, D. A., and R. L. Slingerland, 2010, Significant effect of sediment cohesion on delta morphology: Nature Geoscience, v. 3, p. 105-109.

Enge, H. D., S. J. Buckley, A. Rotevatn, J. A. Howell, 2007, From outcrop to reservoir simulation model: workflow and procedures: Geosphere, v. 3, p. 469–490.

Enge, H. D., and J. A. Howell, 2010, Impact of deltaic clinothems on reservoir performance: Dynamic studies of reservoir analogs from the Ferron Sandstone Member and Panther Tongue, Utah: AAPG Bulletin, v. 94, p. 139-161.

Enge, H. D., J. A. Howell, and S. Buckley, 2010, The geometry and internal architecture of stream mouth bars in the Panther Tongue and the Ferron Sandstone Members, Utah, U.S.A: Journal of Sedimentary Research, v. 80 p. 1018-1031.

Falivene, O., L. Cabrera, J. A. Munõz, P. Arbués, O. Fernández, and A. Sáez, 2007, Statistical grid-based facies reconstruction and modeling for sedimentary bodies. Alluvial-palustrine and turbiditic examples: Geological Acta, v. 5, p. 199–230.

Farrell, M. E., and V. Abreu, 2006, Reservoir connectivity in fluvial-deltaic depositional environments: South Timbalier 26 field study (abs.): AAPG International Conference and Exhibition, November 5-8, Perth, Australia, <http://www.searchanddiscovery.com/abstracts/pdf/2006/intl_perth/abstracts/ndx_farrell.pdf> Accessed January 14, 2013.

Faure-Llorens, C., 2012, Understanding fluid flow in complex, fluvial-deltaic reservoirs: Imperial College London, MSc thesis, 41p.

Fløl0, L. H., J. M. Kjærefjord, D. M. Arnesen, W. P. Menard, and K. W. Weissenburger, 2000, Revealing the petrophysical properties of a thin-bedded rock in a Norwegian sea reservoir with logs, core and miniperm data: Society of Petroleum Engineers Reservoir Evaluation and Engineering, v. 3, p. 249-255.

Forster, C. B., S. H. Snelgrove, and J. V. Koebbe, 2004, Modelling permeability structure and simulating fluid flow in a reservoir analog: Ferron Sandstone, Ivie Creek area, East-Central Utah, *in*: Chidsey Jr, T. C., Adams, R. D., and Morris, T. H., eds., Regional to wellbore analog for fluvial-deltaic reservoir modelling: the Ferron Sandstone of Utah: AAPG Studies in Geology 50, p. 359-382.

Fraser, S. I., A. M. Robinson, H. D. Johnson, J. R. Underhill, D. G. A. Kadolsky, R. Connell, P. Johanessen, and R. Ravnås, 2003, Upper Jurassic *in*: D. Evans, C. Graham, A. Armour, and P. Bathurst, eds., The Millennium Atlas: petroleum geology of the Central and Northern North Sea: London, The Geological Society, p. 158-189.

Frazier, D. E., 1967, Recent deltaic deposits of the Mississippi River: their development and chronology: Transactions of the Gulf Coast Association of Geological Societies, v. 17, p. 287-315.

Fürsich, 1982. Rhythmic bedding and shell bed formation in the Upper Jurassic of east Greenland, *in*: G. Einsele, and A. Seilacher, eds., Cyclic and Event Stratification: Berlin, Springer, p. 208-222.

Galloway, W. E., 1975, Process framework for describing the morphological and stratigraphic evolution of deltaic depositional systems, *in*: M. L. Broussard, ed., Deltas, models for exploration: Houston, Texas, Houston Geological Society, p. 87-98.

Galloway, W. E., 1989, Genetic stratigraphic sequences in basin analysis I: architecture and genesis of flooding-surface bounded depositional units: AAPG Bulletin, v. 73, p. 125-142.

Gani, M. R., and J. P. Bhattacharya, 2005, Lithostratigraphy versus chronostratigraphy in facies correlations of Quaternary deltas: Application of bedding correlation, *in*: Giosan, L., and Bhattacharya, J. P., eds., River deltas - Concepts, models and examples, SEPM Special Publication 83, p. 31-47.

Gani, M. R., and J. P. Bhattacharya, 2007, Basic building blocks and process variability of a Cretaceous delta: Internal facies architecture reveals a more dynamic interaction of river, wave, and tidal processes than is indicated by external shape: Journal of Sedimentary Research, v. 77, p. 284-302.

Gardner, M. H., 1993, Sequence stratigraphy and facies architecture of the Upper Cretaceous Ferron Sandstone Member of the Mancos Shale, east-central Utah: Ph.D. dissertation, Colorado School of Mines, Golden, Colorado, 528 p.

Garrison Jr., J. R., and T. C. V. Van den Bergh, 2004, High resolution depositional sequence stratigraphy of the Upper Ferron Sandstone Last Chance Delta: An application of coal-zone stratigraphy, *in*: Chidsey Jr, T. C., Adams, R. D., and Morris, T. H., eds., Regional to wellbore analog for fluvial-deltaic reservoir modelling: the Ferron Sandstone of Utah: AAPG studies in Geology 50, p. 125-192.

Geleynse, N. L., J. E. A. Storms, D. J. R. Walstra, H. R. A. Jagers, Z. B. Wang, and M. J. F. Sive, 2011, Controls on river delta formation; insights from numerical modelling: Earth and Planetary Science Letters, v. 302, p. 217-226.

Gibbons, K., T. Hellem, A. Kjemperud, S. D. Nio, and K. Vebenstad, 1993, Sequence architecture, facies development and carbonate-cemented horizons in the Troll Field reservoir, offshore Norway, *in*: M. Ashton, ed., Advances in Reservoir Geology, Geological Society (London) Special Publication 69, p. 1-31.

Goldring, R., and P. Bridges, 1973, Sublittoral sheet sandstones: Journal of Sedimentary Petrology, v. 43, p. 736-747.

Google Earth, 2013, <http://www.google.co.uk/intl/en_uk/earth/index.html> Accessed January 14, 2013.

Guilpain, P., 2006, Improved characterisation and modelling of low permeability lower shoreface facies, with application to deltaic reservoirs in the Baram Delta Province (Brunei Darussalam) and Tusher Canyon (Book Cliffs, Utah, USA): MSc dissertation, Imperial College London, London, 66 p.

Hadley, D. F., and T. Elliott, 1993, The sequence stratigraphic significance of erosive-based shorefaces in the Cretaceous Mesaverde Group of northwestern Colorado, *in*: H. W. Posamentier, C. P. Summerhayes, B. U. Haq, and G. P. Allen,

eds., Sequence Stratigraphy and Facies Associations: International Association of Sedimentologists, Special Publication 18, p. 521–535.

Haldorsen, H. H., and L. W. Lake, 1984, A new approach to shale management in field-scale models: Society of Petroleum Engineers Journal, v.24, p. 447-457.

Haldorsen, H. H., and E. Damsleth, 1990, Stochastic modeling: Journal of Petroleum Technology, v. 42, p. 404-412.

Hampson, G. J., 2000, Discontinuity surfaces, clinoforms and facies architecture in a wave-dominated, shoreface-shelf parasequence: Journal of Sedimentary Research, v. 70, p. 325-340.

Hampson, G. J., and J. E. A. Storms, 2003, Geomorphological and sequence stratigraphic variability in wave-dominated shoreface-shelf parasequences: Sedimentology, v. 50, p. 667-701.

Hampson, G. J., and J. A. Howell, 2005, Sedimentologic and geomorphic characterization of ancient wave-dominated deltaic shorelines; Upper Cretaceous Blackhawk Formation, Book Cliffs, Utah, USA, *in*: L. Giosan and J. P. Bhattacharya, eds., River deltas - concepts, models and examples: Society for Economic Paleontologists and Mineralogists Special Publication, v. 83, p. 133–154.

Hampson, G. J., A. B. Rodriguez, J. E. A. Storms, H. D. Johnson, and C. T. Meyer, 2008, Geomorphology and high-resolution stratigraphy of progradational wave-dominated shoreline deposits: impact on reservoir-scale facies architecture, *in*: G. J Hampson, R. J. Steel, P. M. Burgess, and R. W. Dalrymple, eds., Recent advances in models of siliciclastic shallow-marine stratigraphy: SEPM Special Publication 90, 117-142.

Hampson, G. J., M. R. Gani, H. Sahoo, A. Rittersbacher, A. Irfan, A. Ranson, T. O. Jewell, N. D. S. Gani, J. A. Howell, S. J. Buckley, and B. Bracken, 2012, Controls on large-scale patterns of fluvial sandbody distribution in alluvial-to-coastal plain strata: Upper Cretaceous Blackhawk Formation, Wasatch Plateau, central Utah, USA: Sedimentology, v. 59, p. 2226-2258.

Hampson, G. J., J. E. Morris, and H. D. Johnson, *in review*, Impact of time-stratigraphic relationships on hydrocarbon reservoir distribution and performance, Bridport Sand Formation, Wessex Basin, UK, *submitted to*: Bailey, R. J., and Smith, D. G., eds., Strata and Time: Geological Society of London Special Publication.

Helland-Hansen, W., and G. J. Hampson, 2009, Trajectory analysis: concepts and applications: Basin Research, v. 21, p. 454-483.

Henderson, K., H. Rose, R. Winter, 2010, Identifying and quantifying thin-bedded pay (Part A): Log characteristics and reservoir quality: Society of Petroleum Engineers Paper 133534.

Hassanpour, M. M., M. J. Pyrcz, and C. V. Deutsch, 2013, Improved geostatistical models of inclined heterolithic strata for McMurray Formation, Alberta, Canada: AAPG Bulletin, v. 97, p. 1209-1224.

Hodgetts, D., J. Imber, C. Childs, S. Flint, J. Howell, J. Kavanagh, P. Nell, and J. Walsh, 2001, Sequence stratigraphic responses to shoreline-perpendicular growth faulting in shallow marine reservoirs of the Champion field, offshore Brunei Darussalam, South China Sea: AAPG Bulletin, v. 85, p.433-457.

Howell, J. A., Å. Vassel, and T. Aune, 2008a, Modelling of dipping clinoform barriers within deltaic outcrop analogues from the Cretaceous Western Interior Basin, U.S.A., *in*: A. Robinson, P. Griffiths, S. Price, J. Hegre, and A. H. Muggeridge, eds.,

The future of geologic modelling in hydrocarbon development: Geological Society (London) Special Publication 309, p. 99-121.

Howell, J. A., A. Skorstad, A. MacDonald, A. Fordham, S. Flint, B. Fjellvoll, and T. Manzocchi, 2008b, Sedimentological parameterization of shallow-marine reservoirs: Petroleum Geoscience, v. 14, p. 17-34.

Hoyal, D. C. J. D., and B. A. Sheets, 2009, Morphodynamic evolution of experimental cohesive deltas: Journal of Geophysical Research: Earth Surface, v. 114, F02009, 18 p.

Hudson, J. D., W. J. Andrews, 1987, The diagenesis of the Great Eustarine Group, Middle Jurassic, Inner Hebrides, Scotland, *in*: J. D. Marshall, ed., Diagenesis of Sedimentary Sequences: Geological Society (London) Special Publication 36, p. 259-276.

Husmo, T., G .P. Hamar, O. Høiland, J. P. Johannessen, A. Rømuld, A. M. Spencer, and R. Titterton, 2003, Lower and Middle Jurassic, *in*: D. Evans, C. Graham, A. Armour, and P. Bathurst, eds., The millenium atlas: Petroleum geology of the central and northern North Sea: London, Geological Society, p. 129-156.

Jackson, M. D., and A. H. Muggeridge, 2000, The effect of discontinuous shales on reservoir performance during immiscible flow: SPE Journal, v. 5, p. 446-454.

Jackson, M. D., A. H. Muggeridge, S. Yoshida, and H. D. Johnson, 2003, Upscaling permeability measurements within complex heterolithic tidal sandstones: Mathematical Geology, v. 35, p. 499-520.

Jackson, M. D., S. Yoshida, A. H. Muggeridge, and H. D. Johnson, 2005, Three-dimensional reservoir characterisation and flow simulation of heterolithic tidal sandstones: AAPG Bulletin, v. 89, p. 507-528.

Jackson, M. D., G. J. Hampson, and R. P. Sech, 2009, Three-dimensional modelling of a shoreface-shelf parasequence reservoir analog: Part 2. Geological controls on fluid flow and hydrocarbon production: AAPG Bulletin, v. 93, p. 1183-1208.

Jackson, M. D, J. L. M. A. Gomes, P. Mostaghimi, J. R. Percival, B. S. Tollit, D. Pavlidis, C. C. Pain, A. H. El-Sheikh, A. H. Muggeridge, and M. J. Blunt, 2013, Reservoir modeling for flow simulation using surfaces, adaptive unstructured meshes and control-volume-finite-element methods: Society of Petroleum Engineers Paper 163633.

Jackson, M. D., G. J. Hampson, A. El Sheikh, J. H. Saunders, G. H. Graham, and B. Y. G. Massart, *in press*, Surface-based reservoir modelling, Sediment body geometry and heterogeneity: analogue studies for modelling the subsurface, Geological Society (London) Special Publication.

Janczak, A., 2011, Impact of heterogeneity on hydrocarbon recovery in fluvial dominated shallow-marine reservoirs: Imperial College London, MSc thesis, 38p.

Jennette, D. C., and C. O. Riley, 1996, Influence of relative sea level on facies and reservoir geometry of the Middle Jurassic Lower Brent Group, UK North Viking Graben, *in*: J. A. Howell, and J. F. Aitken, eds., High-resolution sequence stratigraphy: Innovations and applications: Geological Society (London) Special Publication 104, p. 87-113.

Jones, R. R., K. J. W. McCaffrey, J. Imber, R. Wightman, S. A. F. Smith, R. E. Holdsworth, P. Glegg, N. De Paola, D. Healy, R. W. Wilson, 2008, Calibration and validation of reservoir models: the importance of high resolution, quantitative outcrop analogues, *in*: A. Robinson, P. Griffiths, S. Price, J. Hegre, A. Muggeridge, eds.,

The future of geological modelling in hydrocarbon development: The Geological Society, London, Special Publications, v. 309, p. 87–98.

Joshi, S. D., 1987, Review of horizontal well and drain hole technology: Society of Petroleum Engineers Paper 16868.

Journel, A. G., J. Gomez-Hernandez, and J. Jaime, 1993, Stochastic imaging of the Wilmington clastic sequence: Society of Petroleum Engineers Formation Evaluation, v. 8, p. 33–40.

Kantorowicz, J. D., I. D. Bryant, and J. M. Dawans, 1987, Controls on the geometry and distribution of carbonate cements in Jurassic sandstones: Bridport Sands, southern England and Viking Group, Troll Field, Norway, *in*: J. D. Marshall, ed., Diagenesis of sedimentary sequences, Geological Society (London) Special Publication 36, p. 103-118.

Kauffman, E. G., and Caldwell, W. G. E., 1993, The Western Interior Basin in space and time, *in*: W. G. E Caldwell, and E. G. Kauffman, eds., Evolution of the Western Interior Basin: Geological Association of Canada Special Paper, v. 39, p. 1-30.

King, P. R., 1990, Connectivity and conductivity of overlapping sand bodies, *in*: A. T. Buller, E. Berg, and O. Hjelmeland, eds., North Sea oil and gas reservoirs: II: London, Graham and Trotman, p. 354-362.

Kjønsvik, D., J. Doyle, T. Jacobsen, and A. Jones, 1994, The Effects of Sedimentary Heterogeneities on Production From a Shallow Marine Reservoir - What Really Matters?: Society of Petroleum Engineers Paper No. 28445, 14 p.

Kolla, V., P. Biondi, B. Long, and R. Fillon, 2000, Sequence stratigraphy and architecture of the late Pleistocene Lagniappe delta complex, northeast Gulf of Mexico, *in*: D.

Hunt, and R. L. Gawthorpe, eds., Sedimentary responses to forced regressions, Geological Society (London) Special Publication 172, p. 291-327.

Larue, D. K., and H. Legarre, 2004, Flow units, connectivity, and reservoir characterization in a wave-dominated deltaic reservoir: Meren reservoir, Nigeria: AAPG Bulletin, v. 88, p. 303–324.

Leekie, D. A., and L. F. Krystinick, 1989, Is there evidence for geostrophic currents preserved in the sedimentary record of inner to middle-shelf deposits?: Journal of Sedimentary Petrology, v. 51, p. 823-848.

Livera, S. E., and B. Caline, 1990, The sedimentology of the Brent Group in the Cormorant Block IV oil field: Journal of Petroleum Geology, v. 13, p. 367-396.

Løseth, T. M., and A. Ryseth, 2003, A depositional model and sequence stratigraphic model for the Rannoch and Etive formations, Oseberg field, northern North Sea: Norwegian Journal of Geology, v. 83, p. 87-106.

MacDonald, A. C., Fält, L. -M. and Hektoen, A. -L., 1998, Stochastic modeling of incised valley geometries: AAPG Bulletin, v. 82, p.1156-1172.

Matheron, G., H. Beucher, C. de Fouquet, and A. Galli, 1987, Conditional simulation of the geometry of fluvio-deltaic reservoirs: Society of Petroleum Engineers Paper 16753.

Matthews, S., A. D. Thurlow, F. J. Aitken, S. Gowland, P. D. Jones, G. J. Colville, C. I. Robinson, and A. M. Taylor, 2005, A late life opportunity: Using a multidisciplinary approach to unlock reserves in the Rannoch Formation, Ninian Field, *in*: A. G. Doré, and B. A. Vining, eds., Petroleum Geology: Northwest Europe and global perspective: Proceedings of the 6th Conference of the Geological Society (London), p. 496-510.

Matthews, S., J. C. Carter, K. D. Stephen, R. W. Zimmerman, A. Skorstad, T. Manzocchi, and J. A. Howell, 2008, Assessing the effect of geological uncertainty on recovery estimates in shallow-marine reservoirs: The application of reservoir engineering to the SAIGUP project: Petroleum Geoscience, v. 14, p. 45-54.

Mattson, A., and M. A. Chan, 2004, Facies and permeability relationships for wave-modified and fluvial-dominated deposits of the Cretaceous Ferron Sandstone, Central Utah, *in*: T. C. Chidsey Jr., R. D. Adams, and T. H. Morris, eds., Regional to wellbore analog for fluvial-deltaic reservoir modelling: the Ferron Sandstone of Utah: AAPG Studies in Geology 50, p. 251-275.

McCaffrey, K. J. W., R. R. Jones, R. E. Holdsworth, R. W. Wilson, P. Clegg, J. Imber, N. Holliman, and I. Trinks, 2005, Unlocking the spatial dimension: Digital technologies and the future of geoscience fieldwork: Journal of the Geological Society (London), v. 162, p. 927-938.

McGookey, D. P., J. P. Haun, L. A. Heele, H. G. Goodell, D. G. McCubbin, R. J. Wiemer, and G. R. Wulf, 1972, Cretaceous system, *in*: W. W. Mallory, ed., Geologic map of the Rocky Mountain Region: Rocky Mountain Association of Geologists, p. 190–233.

Morris, J. E., G. J. Hampson, and H. D. Johnson, 2006, A sequence stratigraphic model for an intensely bioturbated shallow-marine sandstone: The Bridport Sand Formation, Wessex Basin, UK: Sedimentology, v. 53, p. 1229-1263.

Mulder, T., J. P. M. Syvitski, S. Migeon, J. -C. Faugéres, and B. Savoye, 2003, Marine hyperpycnal flows: Initiation, behaviour and related deposits: A review: Marine and Petroleum Geology, v. 20, p. 861-882.

Myrow, P. M., 1992, Pot and gutter casts from the Chapel-Island Formation, Southeast Newfoundland: Journal of Sedimentary Petrology, v. 62, p. 992-1007.

Muto, T., and R. J. Steel, 1992, Retreat of the front in a prograding delta: Geology, v. 20, p. 967–970.

Muto, T., R. J. Steel., and J. B. Swenson, 2007, Autostratigraphy: a framework norm for genetic stratigraphy: Journal of Sedimentary Research, v. 77, p. 2–12.

Newman, K. F., and M. A. Chan, 1991, Depositional facies and sequences in the Upper Cretaceous Panther Tongue Member of the Star Point Formation, Wasatch Plateau, Utah, *in*: Chidsey Jr, T. C., ed., Geology of east-central Utah: Utah Geological Association Publication 19, p.65-75.

North, C. P., and D. J. Prosser, 1993, Characterization of fluvial and aeolian reservoirs: problems and approaches, *in*: C. P. North and D. J. Prosser, eds., Characterization of Fluvial of Aeolian Reservoirs: Geological Society, London, Special Publication 73 p. 1–6.

Norwegian Petroleum Directorate, 2013, Positive resource accounts for the Norwegian shelf in 2011, <http://www.npd.no/en/Topics/Resource-accounts-and--analysis/Temaartikler/Resource-accounts/2011/> Accessed January 14, 2013.

O'Byrne, C. J. and S. S. Flint, 1995, Sequence, parasequence and intra-parasequence architecture of the Grassy Member, Blackhawk Formation, Book Cliffs, Utah, USA, *in*: J. C. Van Wagoner and G. T. Bertram, eds., Sequence stratigraphy of foreland basin deposits: outcrop and subsurface examples from the Cretaceous of North America, AAPG Memoirs, v. 64, p. 225–255.

Olariu, C., J. P. Bhattacharya, X. Xu, C. L. Aiken, X. Zeng, and G. A. McMechan, 2005, Integrated study of ancient delta-front deposits, using outcrop ground-penetrating radar, and three-dimensional photorealistic data: Cretaceous Panther Tongue Sandstone, Utah, U.S.A., *in*: L. Giosan, and J. P. Bhattacharya,

eds., River deltas - Concepts, models and examples: Tulsa, Oklahoma, SEPM Special Publication 83, p. 155-177.

Olariu, C., and J. P. Bhattacharya, 2006, Terminal distribuary channels and delta front architecture of river-dominated delta systems: Journal of Sedimentary Research, v. 76, p. 212-233.

Olariu, C., R. J. Steel, and A. L. Petter, 2010, Delta-front hyperpycnal bed geometry and implications for reservoir modelling: Cretaceous Panther Tongue delta, Book Cliffs, Utah: AAPG Bulletin, v. 94, p. 819-845.

Passey, Q. R., K. E. Dahlberg, K. B. Sullivan, H. Yin, R. A. Brackett, Y. H. Xiao and A. G. Guzman-Garcia, 2006, Characterizing thinly-bedded reservoirs with core data, *in*: K. E. Dahlberg, ed., Petrophysical evaluation of hydrocarbon pore-thickness in thinly-bedded clastic reservoirs, AAPG Archie Series 1, p. 73-88.

Pirmez, C., L. F. Pratson, and M. S. Steckler, 1998, Clinoform development by advection-diffusion of suspended sediment; modelling and comparison to natural systems: Journal of Geophysical Research, B, Solid Earth and Planets, v. 103, p. 24,141-24,157.

Pringle, J. K., A. R. Westerman, J. D. Clark, N. J. Drinkwater, and A. R. Gardiner, 2004, 3D high-resolution digital models of outcrop analog study sites to constrain reservoir model uncertainty: An example from Alport Castles, Derbyshire, UK: Petroleum Geoscience, v. 10, p. 343-352.

Pringle, J. K., J. A. Howell, D. Hodgetts, A. R. Westerman, and D. M. Hodgson, 2006, Virtual outcrop models of petroleum reservoir analogues: A review of the current state-of-the-art: First Break, v. 24, p. 33-42.

Pyrcz, M. J., O. Catuneanu, and C. V. Deutsch, 2005, Stochastic surface-based modelling of turbidite lobes: AAPG Bulletin, v. 89, p. 177-191.

Reineck, H. E. and I. B. Singh, 1972, Genesis of laminated sand and graded rhythmites in storm-sand layers of shelf mud: Sedimentology, v. 18, p. 123-128.

Reynolds, A. D., 1999, Dimensions of paralic sandstone bodies: AAPG Bulletin, v. 83, p. 211-238.

Rich, J. L., 1951, Three critical environments of deposition, and citeria for recognition of rocks deposited in each of them: Geological Society of America Bulletin, v. 62, p. 1-20.

Ryer, T. A., 1991, Stratigraphy, facies and depositional history of the Ferron Sandstone in the Canyon of Muddy Creek, east-central Utah, *in*: T. C. Chidsey Jr, ed., Geology of east-central Utah: Utah Geological Association Publication 19, p. 45-54.

Ryer, T. A., and P. B. Anderson, 2004, Facies of the Ferron Sandstone, East-Central Utah, *in*: Chidsey Jr, T. C., Adams, R. D., and Morris, T. H., eds., Regional to wellbore analog for fluvial-deltaic reservoir modelling: the Ferron Sandstone of Utah: AAPG Studies in Geology 50, p. 59-78.

Saigal, G . C., and K. Bjørlykke, K., 1987, Carbonate cements in clastic reservoir rocks from offshore mid Norway - relationship between isotopic composition, textural development and burial depth, *in*: J. D. Marshall, ed., Diagenesis of Sedimentary Sequences: Geological Society (London) Special Publication 36, p. 313-324.

Sech, R. P., M. D. Jackson, and G. J. Hampson, 2009, Three-dimensional modelling of a shoreface-shelf parasequence reservoir analog: Part 1. Surface-based modelling to capture high resolution facies architecture: AAPG Bulletin, v. 93, p. 1155-1181.

Sgavetti, M., 1992, Criteria for stratigraphic correlation using aerial photographs: Examples from the south-central Pyrenees: AAPG Bulletin, v. 76, p. 708-730.

Steckler, M. S., G. S. Mountain, K. G. Miller, and N. Christie-Blick, 1999, Reconstruction of tertiary progradation and clinoform development on the New Jersey passive margin by 2D backstripping: Marine Geology, v. 154, p. 399-420.

Stiles, J. H., and J. M. Hutfilz, 1992, The use of routine and special core analysis in characterizing Brent Group reservoirs, UK North Sea: Journal of Petroleum Technology, v. 44, p. 704-713.

Strebelle, S., 2002, Conditional simulation of complex geological structures using multiple-point statistics: Mathematical Geology, v. 34, p. 1-21.

Swift, D. J., 1968, Coastal erosion and transgressive stratigraphy: Journal of Geology, v. 76, p. 444-456.

Swift, D. P. J., G. Han, and C. E. Vincent, 1986, Fluid process and sea-floor response on a modern storm-dominated shelf: middle Atlantic shelf of North America. Part 1. The storm current regime, *in*: R. J. Knight and J. R. McLean, eds., Shelf sands and sandstones: Canadian Society of Petroleum Geologists, Memoir II, p. 99-121.

Sydow, J. C., J. Finneran, and A. P. Bowman, 2003, Stacked shelfedge reservoirs of the Columbus Basin, Trinidad, West Indies, *in*: H. H. Roberts, N. C. Rosen, R. H. Fillon, and J. B. Anderson, eds., Shelf margin deltas and linked down slope petroleum systems: Global significance and future exploration potential: Gulf Coast Section SEPM 23rd Annual Research Conference, p. 411–465.

Sylvester, I. F., R. Cook, R. Swift, T. Pritchard, and J. McKeever, 2005, Integrated reservoir modeling enhances the understanding of reservoir performance of the Dolphin Gas Field, Trinidad and Tobago, Society of Petroleum Engineers Paper 94343.

Tollas, J. M., and A. McKinney, 1991, Brent field 3D reservoir simulation: Journal of Petroleum Technology, v. 43, p. 589-595.

Tomás, S., M. Zitzmann, M. Homann, M. Rumpf, F. Amour, M. Benisek, G. Marcano, M. Mutti, and C. Betzler, 2010, From ramp to platform: building a 3D model of depositional geometries and facies architectures in transitional carbonates in the Miocene, northern Sardinia: Facies, v. 56, p. 195–210.

Tye, R. S., J. P. Bhattacharya, J. A. Lorsong, S. T. Sindelar, D. G. Knock, D. D. Puls, and R. A. Levinson, 1999, Geology and stratigraphy of fluvio-deltaic deposits in the Ivishak formation: Applications for development of Prudhoe Bay field Alaska: AAPG Bulletin, v. 83, p. 1588-1623.

Tye, R. S., 2004, Geomorphology: An approach to determining subsurface reservoir dimensions: AAPG Bulletin, v. 88, p. 1123-1147.

Tyler, N., and R. J. Finley, 1991, Architectural controls on the recovery of hydrocarbons from sandstone reservoirs, *in*: A.D. Miall, A.D. and N. Tyler, eds., The three-dimensional facies architecture of terrigenous clastic sediments and its implications for hydrocarbon discovery and recovery: Concepts in Sedimentology and Paleontology, Society for Sedimentary Geology, Tulsa, p. 1–5.

Vakarelov, B. K., and R. B. Ainsworth, 2013, A hierarchical approach to architectural classification in marginal-marine systems: Bridging the gap between sedimentology and sequence stratigraphy: AAPG Bulletin, v. 97, p. 1121-1161.

Van de Graaf, W., and P. Ealey, 1989, Geologic modelling for simulation studies: AAPG Bulletin, v. 73, p. 1436-1444.

Van Lanen, X. M. T., D. Hodgetts, J. Redfern, and I. Fabuel-Perez, 2009, Applications of digital outcrop models: two fluvial case studies from the Triassic Wolfville Fm., Canada and Oukaimeden Sandstone Fm., Morocco: Geological Journal, v. 44, p. 742-760.

Van Wagoner, J. C., R. M. Mitchum, K. M. Campion, and V. D. Rahmanian, 1990, Siliclastic sequence stratigraphy in well logs, cores and outcrops: Concepts for high-resolution correlation of time and facies: AAPG Methods in Exploration, v. 7, 63p.

Verwer, K., E. W. Adams, and J. A. M. Kenter, 2007, Digital outcrop models: technology and applications: First Break, v. 79, p. 57–63.

Vinje, J., R. Nybø, and G. Grinestaff, 2011, A new simulation grid type is demonstrated for the giant Troll oil and gas field: Society of Petroleum Engineers Paper 148023.

Visser, C. A., and A. G. Chessa, 2000, Estimation of length distributions from outcrop datasets - application to the Upper Permian Cutler Formation, Utah: Petroleum Geoscience, v. 6, p. 29-36.

Walderhaug, O., and P. A. Bjørkum, 1998, Calcite cement in shallow-marine sandstones: Growth mechanisms and geometry, *in*: S. Morad, ed., Carbonate cementation in sandstones: distribution patterns and geochemical evolution: International Association of Sedimentologists Special Publication 26, p. 179-192.

Weber, K. J., 1986., How heterogeneity affects oil recovery, *in*: L. W. Lake, and H. B. Carroll Jr., eds., Reservoir characterization: Academic Press, New York, p. 487-544.

Weber, K. J., and L. C. Van Guens, 1990, Framework for constructing clastic reservoir simulation models: Journal of Petroleum Technology, v. 43, p. 1248-1253.

Wehr, F. L., and L. D. Brasher, 1996, Impact of sequence-based correlation style on reservoir model behavior, lower Brent Group, North Cormorant field, UK North Sea Graben, *in:* Howell, J. A., and Aitken, J. F., eds., High resolution sequence stratigraphy: Innovations and applications: Geological Society (London) Special Publication 104, p. 115-128.

Wehr, A., and U. Lohr, 1999, Airborne Laser Scanning - An introduction and overview: ISPRS Journal of Photogrammetry and Remote Sensing, v. 54, p. 68-82.

Wellner, R., R. Beaubouef, J. C. Van Wagoner, H. H. Roberts, and T. Sun, 2005, Jet-plume depositional bodies - The primary building blocks of Wax Lake Delta: Transactions of the Gulf Coast Association of Geological Societies, v. 55, p. 867-909.

Whitaker, J. H. M., 1973, "Gutter Casts", a new name for scour- and fill- structures, with examples from the Llandoverian of Ringerike and Malmoya, Southern Norway: Norsk Geologisk Tidsskrift, v. 53, p. 403-417.

White, C. D. and M. D. Barton, 1999, Translating Outcrop Data to Flow Models, with Applications to the Ferron Sandstone. SPE Reservoir Evaluation and Engineering, v. 2, p. 341-350.

White, C. D., and B. J. Willis, 2000, A method to estimate length distributions from outcrop data: Mathematical Geology, v. 32, p. 389-419.

White, C. D., D. Novakovic, S. P. Dutton, and B. J. Willis, 2003, A geostatistical model for calcite concretions in sandstone: Mathematical Geology, v. 35, p. 549–575.

White, C. D., B. J. Willis, S. P. Dutton, J. P. Bhattacharya, and K. Narayanan, 2004, Sedimentology, statistics, and flow behaviour for a tide-influenced deltaic sandstone, Frontier Formation, Wyoming, United States, *in*: G. M. Grammer, P.

M. Harris, and G. P. Eberli, eds., Integration of outcrop and modern analogs in reservoir modelling: AAPG memoir 80, p. 129-152.

Willis, B. J., J. P. Bhattacharya, S. L. Gabel, and C. D. White, 1999, Architecture of a tide-influenced river delta in the Frontier Formation of Central Wyoming, USA: Sedimentology, v. 46, p. 667-688.

Willis, B. J., C. D. White, 2000, Quantitative outcrop data for flow simulation: Journal of Sedimentary Research, v. 70, p. 788-802.

Wilson, P., D. Hodgetts, F. Rarity, R. L. Gawthorpe, I. R. Sharp, 2009, Structural geology and 4D evolution of a half-graben: new digital outcrop modelling techniques applied to the Nukhul half-graben, Suez rift, Egypt: Journal of Structural Geology, v. 31, p. 328–345.

Worthington, P. F., 2000, Recognition and evaluation of low-resistivity pay: Petroleum Geoscience, v. 6, p. 77-92.

Xie, Y., A. S. Cullick, and C. V. Deutsch, 2001, Surface geometry and trend modelling for integration of stratigraphic data in reservoir models: Society of Petroleum Engineers Paper No. 66817.

Xu, X., C. L. Aiken, J. P. Bhattacharya, R. M. Corbeanu, K. C. Nielsen, G. A. McMechan, and M. G. Abdelsala, 2000, Creating virtual 3D outcrop: The leading edge, Society of Exploration Geophysicists, v. 19, p. 197-202.

Xu, X., J. P. Bhattacharaya, R. K. Davies, and C. L. Aiken, 2001, Digital geological mapping of the Ferron Sandstone, Muddy Creek, Utah, with GPS and reflectorless laser rangefinder: GPS Solutions, v. 5, p. 15-23.

Zhang, X., M. J. Pyrcz, and C. V. Deutsch, 2009, Stochastic surface modelling of deepwater depositional systems for improved reservoir models: Journal of Petroleum Science and Engineering, v. 68, p. 118-134.

Appendix A

A1 Clinoform-modelling algorithm

This section of the appendix contains the subroutines developed for generating multiple three-dimensional clinoform surfaces as demonstrated in Figures 2.7 and 2.14 and surfaces that represent the heterogeneity along clinoforms (Fig. 3.6C). A flowchart demonstrating the full workflow within the clinoform-modelling algorithm is shown in Figure A1.1, with the subroutines contained in this Appendix highlighted in red. We have not included pre- and post-processing functions within the clinoform modelling algorithm (black boxes in Fig. A1.1). The subroutines have been annotated to provide the reader with a brief description and to highlight the equations described in Chapters 2 and 3. The clinoform-modelling algorithm can also be found on a CD-ROM provided with this thesis.

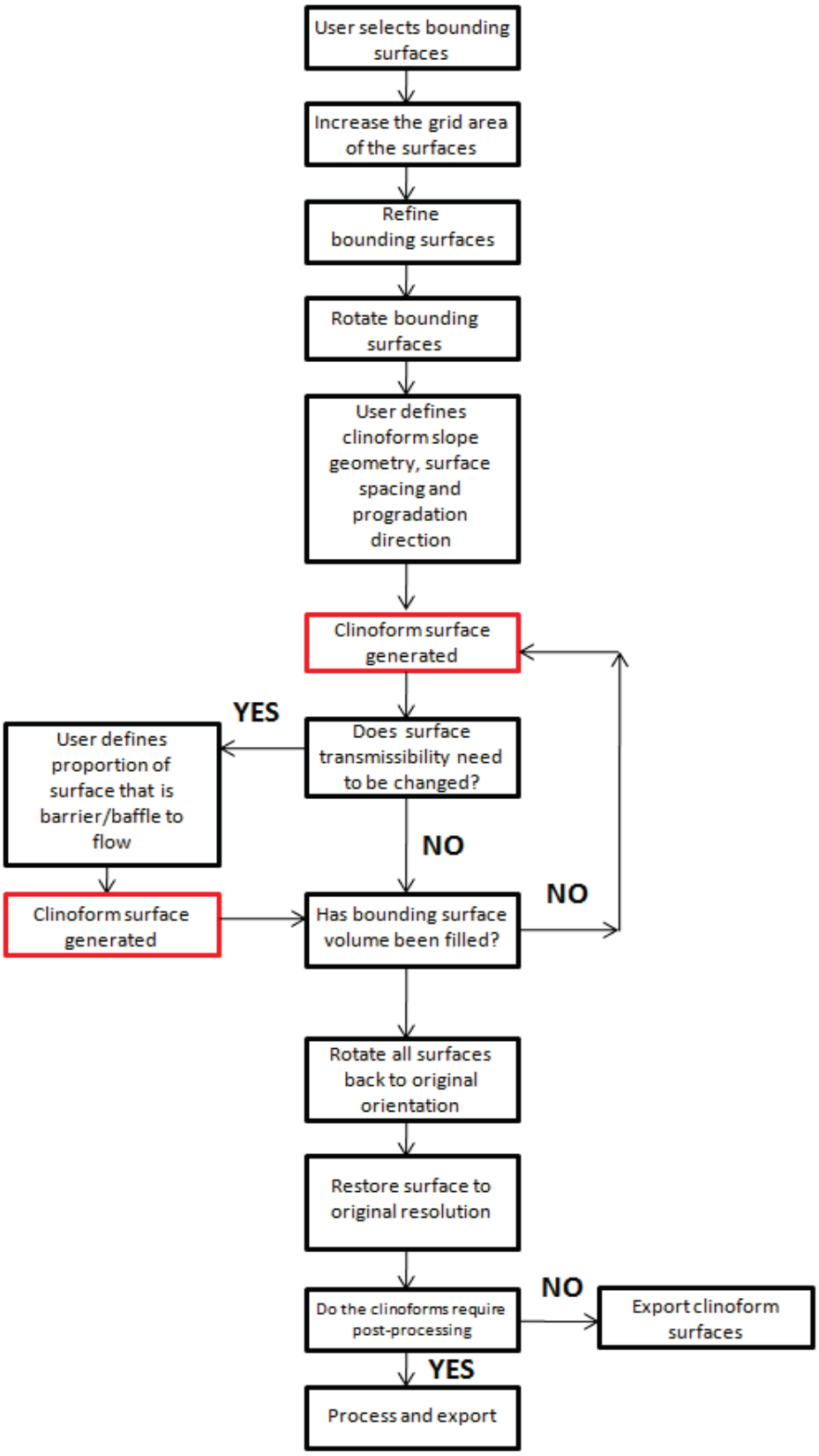


Fig. A1.1

Flowchart depicting the stages required to generate clinoform surfaces and surfaces that represent the heterogeneity along clinoforms. Utility functions are shown in black while the subroutines shown in this Appendix are shown in red.

A1.1 Generating clinoform surfaces

```
!creates clinoform surfaces
!first part of subroutine initiates arrays used in subsequent subroutines
subroutine create_clinoform_surfaces(ROTATION, nonvalue, n_regrid, m_regrid, resolx, xmin, xmax, ymin, ymax,
user_angle, A)

    interface
     subroutine rotate_back(CLINOFORM, AGAIN, resolx, nonvalue, n_regrid, m_regrid, xmin, xmax, ymin, ymax,
user_angle, B, Petrel)
     character :: B*5
     integer :: n_regrid, m_regrid, Petrel
     real :: resolx, nonvalue, xmin, xmax, ymin, ymax, user_angle
     real, allocatable :: CLINOFORM(:,:)
     real, allocatable :: AGAIN(:,:)
     end subroutine
    end interface

    interface
     subroutine rotate_back_bounding(ROTATION, AGAIN, resolx, nonvalue, n_regrid, m_regrid, xmin, xmax, ymin, ymax,
user_angle, B, Petrel)
     character :: B*5
     integer :: n_regrid, m_regrid, Petrel
     real :: resolx, nonvalue, xmin, xmax, ymin, ymax, user_angle
     real, allocatable :: ROTATION(:,:,:)
     real, allocatable :: AGAIN(:,:)
     end subroutine
    end interface

    interface
     subroutine muddraperef(passagemud,n_regrid,m_regrid,resolx,routa,routb,rina,rinb, B,nonvalue, coordicenter,
coordjcenter, dimi, dimj)
     character :: B*5
     integer :: n_regrid, m_regrid, coordicenter, coordjcenter, dimi, dimj
     real :: resolx, nonvalue,routa,routb,rina,rinb
     real, allocatable :: passagemud(:,:)
```

```
      end subroutine
     end interface

     interface
      subroutine mud_surface(passagemud,ROTATION,ROTATION_ADJUSTED,CLINOFORM_ADJUSTED,MUD, n_regrid,m_regrid, nonvalue,
h, j0, coordicenter, coordjcenter,xmin,xmax,ymin,ymax, dimi, dimj, resolx,routa,routb,rina,rinb)
      character :: temp_name*28
      integer :: n_regrid, m_regrid, nbcontrol, h, j0, coordicenter, coordjcenter, i, j, k, dimi, dimj
      real :: nonvalue, coordiinf, coordjinf,xmin,xmax,ymin,ymax, resolx, routa,routb,rina,rinb
      real, allocatable :: passagemud(:,:)
      real, allocatable :: CLINOFORM_ADJUSTED(:,:)
      real, allocatable :: ROTATION(:,:,:)
      real, allocatable :: ROTATION_ADJUSTED(:,:,:)
      real, allocatable :: MUD(:,:)
      end subroutine
     end interface

     interface
      subroutine rotate_back_mud(MUD,AGAIN, resolx, nonvalue, n_regrid, m_regrid, xmin, xmax, ymin, ymax, user_angle,
B, Petrel)
      character :: B*5
      integer :: n_regrid, m_regrid, Petrel
      real :: resolx, nonvalue, xmin, xmax, ymin, ymax, user_angle
      real, allocatable :: MUD(:,:)
      real, allocatable :: AGAIN(:,:)
      end subroutine
     end interface

     interface
      subroutine alter_clinoform(ROTATION, ROTATION_ADJUSTED,n_regrid, m_regrid, nonvalue, alteration_value,
CLINOFORM_ADJUSTED, xmin, xmax, ymin, ymax)
      integer :: n_regrid, m_regrid
      real :: nonvalue, alteration_value, xmin, xmax, ymin, ymax
      real, allocatable :: ROTATION(:,:,:)
      real, allocatable :: CLINOFORM_ADJUSTED(:,:)
      real, allocatable :: ROTATION_ADJUSTED(:,:,:)
      end subroutine
     end interface
```

```
   interface
     subroutine write_zmap_file(CLINOFORM_ADJUSTED_TEMP,temp_name,n,m,k,xmin,xmax,ymin,ymax)
     character :: temp_name*28
     integer :: n,m,k
     real :: xmin, xmax, ymin, ymax
     real, allocatable :: CLINOFORM_ADJUSTED_TEMP(:,:,:)
     end subroutine
   end interface

    character :: parameters_input*28, dummy*28, B*5, temp_name*28
    integer :: n, m, numsurf, n_regrid, m_regrid, h, pl, j0, A, length, compteur, limit_sup, limit_inf, nblines, k
    integer :: Petrel, coordicenter, coordjcenter, dimi, dimj
    real :: nonvalue, resolx, routa, routb, rina, rinb, dist1, dist2, ipole1, jpole1, jpole2, ipole2, ipole3, jpole3
    real :: radiusmax, radiusmin, xmin, xmax, ymin, ymax, jpole4, ipole4, heightbis, height, r, axis, user_angle,
alteration_value
    real, allocatable :: ROTATION(:,:,:)
    real, allocatable :: CLINOFORM(:,:)
    real, allocatable :: CLINOFORM_ADJUSTED(:,:)
    real, allocatable :: CLINOFORM_ADJUSTED_TEMP(:,:,:)
    real, allocatable :: ROTATION_ADJUSTED(:,:,:)
    real, allocatable :: CLINOFORM_PAST(:,:)
    real, allocatable :: AGAIN(:,:)
    real, allocatable:: passagemud(:,:)
    real, allocatable :: MUD(:,:)

!-----------------------------------------------------------------------------------------------------------------------
!read in of user defined parameters fro the clinoform-modelling algorithm
    print*, "Press 1 for Petrel or 2 for RMS"
    read*, Petrel
    write(*,*)"Enter the exponent of the clinoform shape function"
    read(*,*) pl
    write(*,*)"Enter the axis of progradation percentage"
    read(*,*) axis
    write(*,*)"Enter the filename for the clinoform parameters"
    read(*,*) parameters_input
    write(*,*)"Enter the value for bounding surfaces to be altered by"
    read(*,*) alteration_value
```

```
      allocate (CLINOFORM(n_regrid,m_regrid))
      allocate (CLINOFORM_ADJUSTED(n_regrid,m_regrid))
      allocate (CLINOFORM_PAST(n_regrid,m_regrid))
      allocate (AGAIN(n_regrid,m_regrid))
      allocate (MUD(n_regrid,m_regrid))

     routa_past=0
     routb_past=0
     rina_past=0
     rinb_past=0

      open(6, file=parameters_input)
        read(6,*)dummy
      read(6,*) routa, routb, rina, rinb
      close(unit=6)
      routa= routa/resolx
      rina= rina/resolx
      routb= routb/resolx
      rinb= rinb/resolx
      axis=axis/100

       numsurf=1
       j0 = (m_regrid*axis)
      if (routa>routb.or.routb==routa) then;
       length=routa
      else if(routb>routa)then;
       length=routb
      end if
       h=1-length

       A=0
       nblines=0

       !Begin clinform calc
do while (h<n_regrid+1)
```

```
  open(unit=6,file=parameters_input)
  read(6,*) dummy
  do i = 1,A+1
   read(6,*) routa, routb, rina, rinb
  end do
  close(unit=6)
  routa= routa/resolx
  rina= rina/resolx
  routb= routb/resolx
  rinb= rinb/resolx


 if (routa>routb.or.routb==routa) then;
 length=routa
 else if(routb>routa)then;
 length=routb
 end if

if(routb>routa)then;
 ipole1 = SQRT((rinb**2)-(rina**2))
 ipole1 = h +ipole1
 jpole1 = j0
 ipole2 = SQRT((rinb**2)-(rina**2))
 ipole2 = h-ipole2
 jpole2 = j0

 ipole3 = SQRT((routb**2)-(routa**2))
 ipole3 = h+ipole3
 jpole3 = j0
 ipole4 = SQRT((routb**2)-(routa**2))
 ipole4 = h-ipole4
 jpole4 = j0
end if

if(routa>routb.or.routb==routa)then;
 ipole1 = h
 jpole1 = SQRT((rina)**2-(rinb)**2)
 jpole1 = j0+jpole1
```

```
      ipole2 = h
      jpole2 = SQRT((rina)**2-(rinb)**2)
      jpole2 = j0-jpole2

      ipole3 = h
      jpole3 = SQRT((routa)**2-(routb)**2)
      jpole3 = j0+jpole3
      ipole4 = h
      jpole4 = SQRT((routa)**2-(routb)**2)
      jpole4 = j0-jpole4
     end if

      compteur=0
        limit_sup=h+(length)
      limit_inf=h
        if(limit_inf<1) then;
      limit_inf=1
      end if
        if(limit_sup>n_regrid.or.limit_sup<1) then;
      limit_sup=n_regrid
      end if

!Calculates clinform surface from 1 to limit_inf-1
      do i= 1, limit_inf-1
        do j=1,m_regrid
          if (ROTATION(1,i,j)>nonvalue) then;
              dist1 = SQRT((ipole3*1.-h*1.)**2+(jpole3*1.-j*1.)**2)+SQRT((ipole4*1.-h*1.)**2+(jpole4*1.-j*1.)**2)
              dist2 = SQRT((ipole1*1.-h*1.)**2+(jpole1*1.-j*1.)**2)+SQRT((ipole2*1.-h*1.)**2+(jpole2*1.-j*1.)**2)
              if (routa>routb.or.routb==rina) then;
                  if (dist2<=2*routa.and.dist1<=2*routa)then;
                  CLINOFORM(i,j)=ROTATION(2,i,j)
                  end if
                  if(dist2>=2*rina.and.dist1<=2*routa) then;
                  radiusmin=rina
                  radiusmax=routa
                  height=ROTATION(2,i,j)-ROTATION(1,i,j)
                  r=SQRT((((h-h)**2)*1.)+(((j0-j)**2)*1.))
                  !(Height function Eq. 2.1 Chapter 2)
```

```
                heightbis= height-((r-radiusmin)*height)/(radiusmax-radiusmin)
                !(Clinoform shape function Eq. 2.8 Chapter 2)
                CLINOFORM(i,j)=ROTATION(1,i,j)+((ABS((radiusmax-r)**(pl))/ABS((radiusmax-radiusmin)**(pl)))*heightbis)
                compteur=compteur+1
                end if
                if (dist2>=2*routa.and.dist1>=2*routa) then;
                CLINOFORM(i,j)=ROTATION(1,i,j)
                end if
            else;
                if (dist2<=2*routb.and.dist1<=2*routb)then;
                CLINOFORM(i,j)=ROTATION(2,i,j)
                end if
                if(dist2>=2*rinb.and.dist1<=2*routb) then;
                radiusmin=rina
                radiusmax=routa
                height = ROTATION(2,i,j)-ROTATION(1,i,j)
                r = SQRT((((h-h)**2)*1.)+(((j0-j)**2)*1.))
                heightbis= height-((r-radiusmin)*height)/(radiusmax-radiusmin)
                CLINOFORM(i,j)=ROTATION(1,i,j) +((ABS((radiusmax-r)**(pl))/ABS((radiusmax-
radiusmin)**(pl)))*heightbis)
                compteur=compteur+1
                end if
                if (dist2>=2*routa.and.dist1>=2*routb) then;
                CLINOFORM(i,j)=ROTATION(1,i,j)
                end if
            end if
          else;
          CLINOFORM(i,j)=nonvalue
          end if
        end do
      end do

!calc clinoform surface
   do i=limit_inf,limit_sup
    do j=1,m_regrid
     if (ROTATION(1,i,j)>nonvalue) then;
        dist1 = SQRT((ipole3*1.-i*1.)**2+(jpole3*1.-j*1.)**2)+SQRT((ipole4*1.-i*1.)**2+(jpole4*1.-j*1.)**2)
        dist2 = SQRT((ipole1*1.-i*1.)**2+(jpole1*1.-j*1.)**2)+SQRT((ipole2*1.-i*1.)**2+(jpole2*1.-j*1.)**2)
```

```
        if (routa>routb.or.routb==routa) then;
           if (dist2<=2*routa.and.dist1<=2*routa)then;
           CLINOFORM(i,j)=ROTATION(2,i,j)
           end if
           if(dist2>=2*rina.and.dist1<=2*routa) then;
           !print*, dist1, dist2
           radiusmin=(rina*rinb)/(SQRT(((rina**2)*(((i-h)**2)*1.)+(rinb**2)*(((j-j0)**2)*1.))/(((i-h)**2+(j-
j0)**2))*1.))
           radiusmax=(routa*routb)/(SQRT(((routa**2)*(((i-h)**2)*1.)+(routb**2)*(((j-j0)**2)*1.))/(((i-h)**2+(j-
j0)**2))*1.))
           height = ROTATION(2,i,j)-ROTATION(1,i,j)
           !(radius of clinofrom relative to clinoform origin Eq. 2.4 Chapter 2)
           r = SQRT((((h-i)**2)*1.)+(((j0-j)**2)*1.))
           !(Height function Eq. 2.1 Chapter 2)
           heightbis= height-((r-radiusmin)*height)/(radiusmax-radiusmin)
           !(Clinoform shape function Eq. 2.8 Chapter 2)
           CLINOFORM(i,j)=ROTATION(1,i,j)+((ABS((radiusmax-r)**(pl))/ABS((radiusmax-radiusmin)**(pl)))*heightbis)
           compteur=compteur+1
           end if
           if (dist2>=2*routa.and.dist1>=2*routa) then;
           CLINOFORM(i,j)=ROTATION(1,i,j)
           end if
        else;
           if (dist2<=2*routb.and.dist1<=2*routb)then;
           CLINOFORM(i,j)=ROTATION(2,i,j)
           end if
           if(dist2>=2*rinb.and.dist1<=2*routb) then;
           !(Eq. 2.5 Chapter 2, maximum radius of top ellipse)
           radiusmin=(rina*rinb)/(SQRT(((rina**2)*(((i-h)**2)*1.)+(rinb**2)*(((j-j0)**2)*1.))/(((i-h)**2+(j-
j0)**2))*1.))
           !(Eq. 2.6 Chapter 2, maximum radius of base ellipse)
           radiusmax=(routa*routb)/(SQRT(((routa**2)*(((i-h)**2)*1.)+(routb**2)*(((j-j0)**2)*1.))/(((i-h)**2+(j-
j0)**2))*1.))
           height = ROTATION(2,i,j)-ROTATION(1,i,j)
           !(radius of clinofrom relative to clinoform origin Eq. 2.4 Chapter 2)
           r = SQRT((((h-i)**2)*1.)+(((j0-j)**2)*1.))
           !(Height function Eq. 2.1 Chapter 2)
           heightbis= height-((r-radiusmin)*height)/(radiusmax-radiusmin)
```

```
            !(Clinoform shape function Eq. 2.8 Chapter 2)
            CLINOFORM(i,j)=ROTATION(1,i,j) +((ABS((radiusmax-r)**(pl))/ABS((radiusmax-radiusmin)**(pl)))*heightbis)
            compteur=compteur+1
            end if
            if (dist2>=2*routa.and.dist1>=2*routb) then;
            CLINOFORM(i,j)=ROTATION(1,i,j)
            end if
          end if
        else;
        CLINOFORM(i,j)=nonvalue
        end if
       end do
       if (compteur>1) then;
       nblines=nblines+1
       end if
       compteur=0
     end do

!Ensures all clinoform values outside volume are nonvalue
    if (limit_sup<n_regrid) then;
     do i=limit_sup+1,n_regrid
       do j=1,m_regrid
        CLINOFORM(i,j)=ROTATION(1,i,j)
       end do
     end do
    end if

   if (A>1) then;
    do i=1,n_regrid
       do j=1,m_regrid
        if (CLINOFORM(i,j)>nonvalue+1)then;
        if (CLINOFORM(i,j)>CLINOFORM_PAST(i,j))then;
        CLINOFORM(i,j)=CLINOFORM_PAST(i,j)
        end if
        end if
       end do
     end do
    end if
```

```
  do i=1,n_regrid
    do j=1,m_regrid
     CLINOFORM_PAST(i,j)=CLINOFORM(i,j)
    end do
  end do

    do i=1,n_regrid
      do j=1,m_regrid
         CLINOFORM_ADJUSTED(i,j)=CLINOFORM(i,j)
      end do
   end do

if (nblines>1) then;
    A=A+1

   open(unit=40, file="listing.txt")
    do i=1,A
      read(40,*) B
     end do
    close(unit=40)

     if (A>0)then;
        print*, "Generating clinoform surface",trim(B)

    end if

    ! subroutine that rotates clinoform surface to orientation of original bounding surfaces, but honour the user
specified progradation direction
    call rotate_back(CLINOFORM, AGAIN, resolx, nonvalue, n_regrid, m_regrid, xmin, xmax, ymin, ymax, user_angle, B,
Petrel)
    ! modifies the clinoform surfaces if user wishes to add grid layers above or below clinoforms
    call alter_clinoform(ROTATION,ROTATION_ADJUSTED,n_regrid, m_regrid, nonvalue,alteration_value, CLINOFORM_ADJUSTED,
xmin, xmax, ymin, ymax)
    ! calculates the positions of the heterogeneity along clinoform surfaces
    call muddraperef(passagemud,n_regrid,m_regrid,resolx,routa,routb,rina,rinb, B,nonvalue, coordicenter,
coordjcenter, dimi, dimj)
    ! creates a surface representing the heterogeneity along clinoforms
```

```
    call mud_surface(passagemud,ROTATION,ROTATION_ADJUSTED,CLINOFORM_ADJUSTED,MUD,n_regrid,m_regrid, nonvalue, h, j0,
coordicenter, coordjcenter,xmin,xmax,ymin,ymax, dimi, dimj, resolx,routa,routb,rina,rinb)
   ! subroutine that rotates surfaces representing the heterogeneity along clinoforms to orientation of original
bounding surfaces,
   ! but honours the user specified progradation direction
    call rotate_back_mud(MUD,AGAIN, resolx, nonvalue, n_regrid, m_regrid, xmin, xmax, ymin, ymax, user_angle, B,
Petrel)
end if

call xpath(h,z,A, parameters_input)
     z=z/resolx
     h=h+z

    if (A>1)then;

    call ypath(j0,q, A, parameters_input)
      q=q/resoly
      j0=j0+q
    end if

     nblines=0
     numsurf=numsurf+1

end do

    ! subroutine that rotates bounding surfaces back to their original orientation
    call rotate_back_bounding(ROTATION, AGAIN, resolx, nonvalue, n_regrid, m_regrid, xmin, xmax, ymin, ymax,
user_angle, B, Petrel)

    deallocate (CLINOFORM)
    deallocate (CLINOFORM_PAST)
    deallocate (CLINOFORM_ADJUSTED)
    deallocate (AGAIN)
    deallocate (MUD)

return
end subroutine create_clinoform_surfaces
```

A1.2 Modelling heterogeneity along clinoform surfaces

```
!-----------------------------------------------------------------------------------------------------------------------
! calculates the positions of the heterogeneity along clinoform surfaces
subroutine muddraperef(passagemud,n_regrid,m_regrid,resolx,routb_P,routa_P,rinb_P,rina_P, B,Nonvalue, coordicenter,
coordjcenter, dimi, dimj)

real, allocatable :: passagemud(:,:)
integer :: P, max,n,m,dimi,dimj,coordicenter, coordjcenter, n_regrid, m_regrid
real:: ipole1, jpole1, ipole2, jpole2, imin, imax, jmin, jmax, coordireal, coordjreal, dist, pi,Nonvalue
integer :: A_P,A_P1,h_P, j0_P, nbpointsdoneround, nbpointsdoneline, nbpointsell,k,nbpointsline,nbpointsround
real :: routa_P, routb_P, rina_P, rinb_P, resol, paramG, paramH, paramK, proportion, ell, ref, pos, mud, angle,
h_Preal,j0_Preal
real:: radius, radiusmax, major, minor,xmin,xmax,ymin,ymax,radiusmin
parameter (pi=3.14159265)
character:: name*50, B*5, temp_name*28

    paramG=1.00354
    paramH=9.65442
    paramK=-4.3162

    proportion=80.5
    ell=150

    n=n_regrid
    m=m_regrid

    resol=resolx
    routa_P=routa_P*resol
    routb_P=routb_P*resol
    rina_P=rina_P*resol
    rinb_P=rinb_P*resol

    dimi=((routa_P+SQRT((n*resol)**2+(m*resol)**2))/resol)+1
    dimj=(routb_P*2)/resol+1
    coordicenter=(1+ceiling(routa_P/resol))
```

```
coordjcenter=(1+ceiling(routb_P/resol))

xmin=-(dimi-1)*resol/2
xmax=-xmin
ymin=-(dimj-1)*resol/2
ymax=-ymin

if (allocated(passagemud)) then;
deallocate(passagemud)
end if
allocate(passagemud(dimi,dimj))

nbpointsround=0
nbpointsline=0

do i=1,dimi
    do j=1,dimj
    if(i<=coordicenter) then;
        if(((coordicenter-i)*resol/routa_P)**2+((coordjcenter-j)*resol/routb_P)**2<=1) then;
            if(((coordicenter-i)*resol/rina_P)**2+((coordjcenter-j)*resol/rinb_P)**2<=1) then;
            passagemud(i,j)=Nonvalue
            else;
            nbpointsround=nbpointsround+1
            passagemud(i,j)=0
            end if
        else;
        passagemud(i,j)=1
        end if
    else;
        if (SQRT(((coordjcenter-j)*1.)**2)<=routb_P/resol) then;
            if (SQRT(((coordjcenter-j)*1.)**2)<=rinb_P/resol) then;
            passagemud(i,j)=Nonvalue
            else;
            nbpointsline=nbpointsline+1
            passagemud(i,j)=0
            end if
        else;
        passagemud(i,j)=1
```

```
        end if
    end if
    end do
end do

nbpointsdoneround=0
nbpointsdoneline=0

do while(nbpointsdoneround<nbpointsround*proportion/100)

    pos=2
    ref=0
    mud=1

    do while(ref<mud)
    call random_number(angle)
    angle=angle*pi
    call random_number(pos)
    radiusmax=routb_P*routa_P/SQRT((routb_P*sin(angle))**2+(routa_P*cos(angle))**2)
    radiusmin=rinb_P*rina_P/SQRT((rinb_P*sin(angle))**2+(rina_P*cos(angle))**2)
    !distance from clinoform pinch out, Eq. 3.2, Chapter 3)
    radius=(1-pos)*(radiusmax-radiusmin)+radiusmin
    coordireal=coordicenter-(radius)*sin(angle)/resol
    coordjreal=coordjcenter+(radius)*cos(angle)/resol
    !Frequency function Eq. 3.1, Chapter 3)
    ref=paramG/(1+exp(paramH*(pos)+paramK))
    call random_number(mud)
    end do

    nbpointsell=0

    do while (nbpointsell<10)

            nbpointsell=0
            call random_number(major)
            major=ell*major*(radiusmax-radiusmin)/200
            call random_number(minor)
            minor=minor*major
```

```
                ipole1=(SQRT(major**2-minor**2))/resol
                jpole1=0
                ipole2=-ipole1
                jpole2=-jpole1
                imin=-(major/resol)-1
                imax=(major/resol)+1
                jmin=-(minor/resol)-1
                jmax=(minor/resol)+1

                do i=imin,imax
                    do j=jmin,jmax
                    dist=SQRT(((ipole1*1.-i*1.)*resol)**2+((jpole1*1.-j*1.)*resol)**2)+SQRT(((ipole2*1.-
i*1.)*resol)**2+((jpole2*1.-j*1.)*resol)**2)
                    if (dist<2*major) then;
                    nbpointsell=nbpointsell+1
                    end if
                    end do
                end do

        end do


        jpole1=coordjreal+(ipole1)*sin(angle)
        jpole2=coordjreal+(ipole2)*sin(angle)
        ipole1=coordireal+(ipole1)*cos(angle)
        ipole2=coordireal+(ipole2)*cos(angle)


        imin=floor(coordireal-(major/resol))
        if(imin<1) then;
        imin=1
        end if
        imax=ceiling(coordireal+(major/resol))
        if(imax>dimi) then;
        imax=dimi
        end if
        jmin=floor(coordjreal-(major/resol))
```

```
        if(jmin<1) then;
        jmin=1
        end if
        jmax=ceiling(coordjreal+(major/resol))
        if(jmax>dimj) then;
        jmax=dimj
        end if

        do i=imin,imax
            do j=jmin,jmax
                if (passagemud(i,j)<0.5.and.passagemud(i,j)-1>Nonvalue) then;
                dist=SQRT(((ipole1-i)*resol)**2+((jpole1-j)*resol)**2)+SQRT(((ipole2-i)*resol)**2+((jpole2-
j)*resol)**2)
                    if (dist<2*major) then;
                    passagemud(i,j)=1
                        if (i<=coordicenter) then;
                        nbpointsdoneround=nbpointsdoneround+1
                        else;
                        nbpointsdoneline=nbpointsdoneline+1
                        end if
                    end if
                end if
            end do
        end do

    end do

    do while(nbpointsdoneline<nbpointsline*proportion/100)

        pos=2
        ref=0
        mud=1
        angle=pi

        do while(ref<mud)
        call random_number(coordireal)
        coordireal=coordireal*(dimi-coordicenter)+coordicenter
        call random_number(coordjreal)
```

```
        coordjreal=coordjreal*(dimj-1)+1
        pos=1-(SQRT(((coordjcenter-coordjreal)*resol)**2)-rinb_P)/(routb_P-rinb_P)
        radiusmax=routb_P
        radiusmin=rinb_P
        radius=(1-pos)*(radiusmax-radiusmin)
        ref=paramG/(1+exp(paramH*pos+paramK))
        call random_number(mud)
        end do


        nbpointsell=0

        do while (nbpointsell<10)

                nbpointsell=0
                call random_number(major)
                major=ell*major*(radiusmax-radiusmin)/200
                call random_number(minor)
                minor=minor*major

                ipole1=(SQRT(major**2-minor**2))/resol
                jpole1=0
                ipole2=-ipole1
                jpole2=-jpole1
                imin=-(major/resol)-1
                imax=(major/resol)+1
                jmin=-(minor/resol)-1
                jmax=(minor/resol)+1

                do i=imin,imax
                    do j=jmin,jmax
                    dist=SQRT(((ipole1*1.-i*1.)*resol)**2+((jpole1*1.-j*1.)*resol)**2)+SQRT(((ipole2*1.-
i*1.)*resol)**2+((jpole2*1.-j*1.)*resol)**2)
                    if (dist<2*major) then;
                    nbpointsell=nbpointsell+1
                    end if
                    end do
                end do
```

```
        end do


        jpole1=coordjreal+(ipole1)*sin(angle)
        jpole2=coordjreal+(ipole2)*sin(angle)
        ipole1=coordireal+(ipole1)*cos(angle)
        ipole2=coordireal+(ipole2)*cos(angle)


        imin=floor(coordireal-(major/resol))
        if(imin<1) then;
        imin=1
        end if
        imax=ceiling(coordireal+(major/resol))
        if(imax>dimi) then;
        imax=dimi
        end if
        jmin=floor(coordjreal-(major/resol))
        if(jmin<1) then;
        jmin=1
        end if
        jmax=ceiling(coordjreal+(major/resol))
        if(jmax>dimj) then;
        jmax=dimj
        end if

        do i=imin,imax
            do j=jmin,jmax
                if (passagemud(i,j)<0.5.and.passagemud(i,j)-1>Nonvalue) then;
                dist=SQRT(((ipole1-i)*resol)**2+((jpole1-j)*resol)**2)+SQRT(((ipole2-i)*resol)**2+((jpole2-
j)*resol)**2)
                    if (dist<2*major) then;
                    passagemud(i,j)=1
                        if (i<=coordicenter) then;
                        nbpointsdoneround=nbpointsdoneround+1
                        else;
                        nbpointsdoneline=nbpointsdoneline+1
```

```
                        end if
                    end if
                end if
            end do
        end do

    end do

 return
 end subroutine muddraperef
 !-------------------------------------------------------------------------------------------------------------
 ! creates a surface representing the heterogeneity along clinoforms
subroutine mud_surface(passagemud,ROTATION,ROTATION_ADJUSTED,CLINOFORM_ADJUSTED,MUD, n_regrid,m_regrid, nonvalue, h,
j0, coordicenter, coordjcenter,xmin,xmax,ymin,ymax, dimi, dimj, resolx,routa,routb,rina,rinb)

    character :: temp_name*28
    integer :: n_regrid, m_regrid, nbcontrol, h, j0, coordicenter, coordjcenter, i, j, k, dimi, dimj, c
    integer :: icoordinate, jcoordinate,last_value, icoordinate_2, jcoordinate_2, fci, fcj, lci, lcj
    real :: nonvalue,xmin,xmax,ymin,ymax, coordiinf, coordjinf, resolx,routa,routb,rina,rinb, radiusmax, radiusmin
    real, allocatable :: passagemud(:,:)
    real, allocatable :: CLINOFORM_ADJUSTED(:,:)
    real, allocatable :: ROTATION_ADJUSTED(:,:,:)
    real, allocatable :: MUD(:,:)
    real, allocatable :: MUD_TEMP(:,:,:)
    real, allocatable :: ROTATION(:,:,:)

  do i=1,n_regrid
   do j=1,m_regrid
    coordiinf=floor(coordicenter*1.-(i*1.-h*1.))
    coordjinf=floor(coordjcenter*1.-(j*1.-j0*1.))
    if (coordiinf<1.or.coordjinf<1.or.coordiinf+1>dimi.or.coordjinf+1>dimj) then;
    MUD(i,j)=CLINOFORM_ADJUSTED(i,j)
    else;

nbcontrol=passagemud(coordiinf,coordjinf)*100+passagemud(coordiinf,coordjinf+1)*1000+passagemud(coordiinf+1,coordjinf)
*1+passagemud(coordiinf+1,coordjinf+1)*10
```

```
if(nbcontrol==1001.or.nbcontrol==110.or.nbcontrol==1.or.nbcontrol==10.or.nbcontrol==100.or.nbcontrol==1000.or.nbcontro
l==0) then;
    MUD(i,j)=nonvalue
    else;
    MUD(i,j)=CLINOFORM_ADJUSTED(i,j)
    end if
    end if
   end do
  end do

do i=1,n_regrid
 do j=1,m_regrid
 if (i>1.and.i<(n_regrid-2))then;
    if (MUD(i,j)>ROTATION(2,i,j))then;
        if(MUD(i+2,j)==nonvalue) then;
            MUD(i,j)=nonvalue
        end if
    end if
 end if
 end do
end do

deallocate(ROTATION_ADJUSTED)

return
end subroutine mud_surface
```

A2 Stochastic input parameters algorithm

This section of the appendix contains the code for stochastically generating input parameters that can be used with the clinoform-modelling algorithm (Table 2.1). The user can specify the mean and standard deviation to constrain a random normal distribution using a Box-Muller transform (Box and Muller, 1958), as described in Chapter 2, Section 2.3.5. The output file from this algorithm is used as an input file for the clinoform-modelling algorithm.

```
program stochastic_parameter_population

implicit none

interface
    subroutine random_normal(random_normal_1, random_normal_2)
    double precision :: random_normal_1, random_normal_2
    end subroutine
end interface

double precision :: theta, po, P, tw, ssf, tl, L, Sx, Sy, mean, sigma,random_normal_1, random_normal_2
integer :: theta_int,P_int, i, tw_int, tl_int, L_int, bw_int, bl_int, Sx_int, Sy_int
character :: dummy1*1

call random_seed()

open (unit=12,file="Stochastic input parameters for clinoform modeling algorithm.txt")
close(unit=12, STATUS='DELETE')

theta=-1.0
do while (theta<0.0.or.theta>360.0)
    call random_normal(random_normal_1, random_normal_2)

    open(unit=1,file="clinoform progradation angle.txt")
        read(1,*) dummy1
        read(1,*) mean, sigma
    close(unit=1)

    if(random_normal_1<1)then;
        theta=mean+(sigma*random_normal_1)
    else if(random_normal_2<1)then;
        theta=mean+(sigma*random_normal_2)
    end if

    open(unit=2,file="Stochastic clinoform progradation angle output.txt")
    write(2,*)'!clinoform progradation angle'
    theta_int=theta
    write(2,*) theta_int
    close(unit=2)
end do
```

```
po=-1.0
do while (po<0.0.or.po>1.0)
    call random_normal(random_normal_1, random_normal_2)

    open(unit=3,file="clinoform axis of progradation.txt")
        read(3,*) dummy1
        read(3,*) mean, sigma
    close(unit=3)

    if(random_normal_1<1)then;
        po=mean+(sigma*random_normal_1)
    else if(random_normal_2<1)then;
        po=mean+(sigma*random_normal_2)
    end if

    open(unit=4,file="Stochastic clinoform axis of progradation output.txt")
    write(4,*)'!clinoform axis of progradation'
    write(4,"(1F10.2)") po
    close(unit=4)
end do

P=-1.0
do while (P<0.0)
    call random_normal(random_normal_1, random_normal_2)

    open(unit=5,file="clinoform shape function exponent.txt")
        read(5,*) dummy1
        read(5,*) mean, sigma
    close(unit=5)

    if(random_normal_1<1)then;
        P=mean+(sigma*random_normal_1)
    else if(random_normal_2<1)then;
        P=mean+(sigma*random_normal_2)
    end if

    open(unit=6,file="Stochastic clinoform shape function exponent.txt")
        write(6,*)'!clinoform shape function exponent'
            P_int=P
        write(6,*) P_int
    close(unit=6)
```

```
end do


do i=1,200
        tw=0
        ssf=-1
        L=0
        Sx=0
        Sy=0
    do while(tw<1)
        call random_normal(random_normal_1, random_normal_2)

        open(unit=7,file="length of top ellipse in depositional strike.txt")
            read(7,*) dummy1
            read(7,*) mean, sigma
        close(unit=7)

        if(random_normal_1<1)then;
            tw=mean+(sigma*random_normal_1)
        else if(random_normal_2<1)then;
            tw=mean+(sigma*random_normal_2)
        end if
    end do

   do while(ssf<0)
        call random_normal(random_normal_1, random_normal_2)

        open(unit=8,file="shoreline shape.txt")
            read(8,*) dummy1
            read(8,*) mean, sigma
        close(unit=8)

        if(random_normal_1<1)then;
            ssf=mean+(sigma*random_normal_1)
        else if(random_normal_2<1)then;
            ssf=mean+(sigma*random_normal_2)
        end if
    end do

    tl=tw/ssf
```

```
do while(L<1)
     call random_normal(random_normal_1, random_normal_2)

     open(unit=9,file="clinoform length.txt")
          read(9,*) dummy1
          read(9,*) mean, sigma
     close(unit=9)

     if(random_normal_1<1)then;
          L=mean+(sigma*random_normal_1)
     else if(random_normal_2<1)then;
          L=mean+(sigma*random_normal_2)
     end if
 end do

   tw_int=tw
   tl_int=tl
   L_int=L
   bw_int=tw_int+L_int
   bl_int=tl_int+L_int

 do while(Sx<1)
     call random_normal(random_normal_1, random_normal_2)

     open(unit=10,file="clinoform spacing in x.txt")
          read(10,*) dummy1
          read(10,*) mean, sigma
     close(unit=10)

     if(random_normal_1<1)then;
          Sx=mean+(sigma*random_normal_1)
     else if(random_normal_2<1)then;
          Sx=mean+(sigma*random_normal_2)
     end if
 end do

 do while(Sy<1)
     call random_normal(random_normal_1, random_normal_2)

     open(unit=11,file="clinoform spacing in y.txt")
          read(11,*) dummy1
```

```
            read(11,*) mean, sigma
        close(unit=11)

        if(random_normal_1<1)then;
            Sy=mean+(sigma*random_normal_1)
        else if(random_normal_2<1)then;
            Sy=mean+(sigma*random_normal_2)
        end if
    end do

        Sx_int=Sx
        Sy_int=Sy

    open(unit=12,file="Stochastic input parameters for clinoform modeling algorithm.txt",ACCESS='APPEND')
    if (i==1)then;
        write(12,*)'!clinoform geometry and spacing parameters'
    end if
        write(12,*) bw_int, bl_int, tw_int, tl_int, Sx_int, Sy_int
    close(unit=12)
end do

write(*,*) 'Press return to exit program'
read(*,*)

stop
end program
!-----------------------------------------------------------------------------------------------------------
subroutine random_normal(random_normal_1, random_normal_2)

implicit none

double precision :: u, v, random_normal_1, random_normal_2, s
real :: pi
parameter (pi=3.14159265358979323846264338327950288419716939937510)

call random_seed()

s=2
random_normal_1=2
random_normal_2=2
```

```
do while(s>1)
    call random_number(u)
    call random_number(v)
    s=(u**2)+(v**2)
end do

    random_normal_1=SQRT(-2*LOG(u))*(sin(2*pi*v))
    random_normal_2=SQRT(-2*LOG(u))*(cos(2*pi*v))

return
end subroutine random_normal
```

Appendix B

B1 Example Eclipse® data file

```
---------------------------------------------------------------------
RUNSPEC
---------------------------------------------------------------------
DEBUG
51*0/

SAVE
/

TITLE
 FerronPSS1_100_90D_PERMBASE_NOFCF

DIMENS
-- Nx   Ny   Nz
  34  148  3897/

-- Phases present
-- Only dead oil and water above bubble point at all time
OIL
WATER

METRIC
-- Note units used throughout .DATA file

START
  01 'jan' 2005 /

UNIFIN
UNIFOUT

WELLDIMS
-- NWMAX NWMAXZ NGMAX NWGMAX
  20    200     2    100 /

TABDIMS
-- NTSFUN NTPVT NSSFUN NPPVT
  3     1     100    50 /

NSTACK
  80/

MESSAGES
  500000 500000 100000 100000 100000 100000 100000 100000 100000 100000 /
```

```
-- All else is defaulted

MEMORY
1428 /

----------------------------------------------------------------------
GRID
----------------------------------------------------------------------
NEWTRAN
-- Use NEWTRAN for irregular grids and OLDTRAN for Cartesian grids

PSEUDOS
--Write restart file containing initial water saturations etc.

--Switch off output to the PRT file during grid loading for easier debugging
NOECHO

--Include file containing COORD, ZCORN, PORO, PERMX, PERMY, PERMZ data
INCLUDE
'Includes/PSS1_100MD_NOFCF.GRDECL' /

-- PORO, PERMX etc. data may be included in separate files in later runs

INCLUDE
  'Includes/PORO_PSS1_NOFCF.GRDECL' /

INCLUDE
  'Includes/PERMX_BASE_PSS1_NOFCF.GRDECL' /

INCLUDE
  'Includes/PERMZ_BASE_PSS1_NOFCF.GRDECL'/

COPY
 PERMX PERMY /
/

--Include MULTZ data (if calcite cement present)
INCLUDE
  'Includes/MULTX_90_PSS1_NOFCF.GRDECL'/
INCLUDE
  'Includes/MULTY_90_PSS1_NOFCF.GRDECL'/
INCLUDE
  'Includes/MULTZ_90_PSS1_NOFCF.GRDECL'/

-- Set up NNC's across pinched-out cells
PINCH
0.01 'GAP' /

-- Produce initial file for GRAF
INIT
```

```
-----------------------------------------------------------------
PROPS
-----------------------------------------------------------------
-- oil/water relative permeability and capillary pressure are tabulated as
-- a function of water saturation

--        SMB
--Sw     krw      kro      Pc (Bar)
SWOF
0.2      0        0.7      0.168109639
0.25     0.003    0.567    0.02831031
0.3      0.012    0.448    0.00915982
0.35     0.027    0.343    0.003771691
0.4      0.048    0.252    0.002155252
0.45     0.075    0.175    0.001077626
0.5      0.108    0.112    0.000808219
0.55     0.147    0.063    0.000538813
0.6      0.192    0.028    0.000269406
0.65     0.243    0.007    5.38813E-05
0.7      0.3      0        0  /

--        pDF
--Sw     krw      kro      Pc (Bar)

0.2      0        0.7      0.316990576
0.25     0.003    0.567    0.053382432
0.3      0.012    0.448    0.017271922
0.35     0.027    0.343    0.007111968
0.4      0.048    0.252    0.004063982
0.45     0.075    0.175    0.002031991
0.5      0.108    0.112    0.001523993
0.55     0.147    0.063    0.001015995
0.6      0.192    0.028    0.000507998
0.65     0.243    0.007    0.0001016
0.7      0.3      0        0  /

--        dDF
--Sw     krw      kro      Pc (Bar)

0.2      0        0.7      2.046165368
0.25     0.003    0.567    0.344582118
0.3      0.012    0.448    0.11148978
0.35     0.027    0.343    0.045907556
0.4      0.048    0.252    0.026232889
0.45     0.075    0.175    0.013116445
0.5      0.108    0.112    0.009837334
0.55     0.147    0.063    0.006558222
0.6      0.192    0.028    0.003279111
0.65     0.243    0.007    0.000655822
0.7      0.3      0        0  /
```

```
--        OS
--Sw     krw      kro      Pc (Bar)

0.2      0        0.7      2.046165368
0.25     0.003    0.567    0.344582118
0.3      0.012    0.448    0.11148978
0.35     0.027    0.343    0.045907556
0.4      0.048    0.252    0.026232889
0.45     0.075    0.175    0.013116445
0.5      0.108    0.112    0.009837334
0.55     0.147    0.063    0.006558222
0.6      0.192    0.028    0.003279111
0.65     0.243    0.007    0.000655822
0.7      0.3      0        0   /
/

-- Specify fluid properties
--       OIL      WATER      GAS
--     (KG/M3)   (KG/M3)   (KG/M3)
DENSITY
       650     950      0.0 /

-- Specify rock properties
--     REF.PRES   ROCK-COMPRESSIBILITY
--      (BAR)        (1/BAR)
ROCK
       100      0.000000000001  /

-- Dead oil PVT table (FVF and Viscosity must vary with pressure)
--    Oil phase press.   Oil FVF   Oil compressibility  Oil Viscosity
--       (BAR)       (Rm3/Sm3)        (1/bars)         (CPoise)
PVCDO
        100      1.00000009    0.0001000000       0.7000000000   0.0 /

-- Water PVT table
--    Ref. press.  FVF-WATER  Compressibility  Viscosity  Viscosibility
--     (BAR)      (RM3/SM3)     (1/BAR)     (CPoise)      (1/BAR)
PVTW
      100         1.0         0.00001         0.30         0.0  /

------------------------------------------------------------------------
REGIONS
------------------------------------------------------------------------
INCLUDE
'Includes/SATNUM_PSS1_NOFCF.GRDECL' /

------------------------------------------------------------------------
SOLUTION
------------------------------------------------------------------------

-- DATA FOR INITIALISING FLUIDS TO POTENTIAL EQUILIBRIUM
EQUIL
```

```
-- DATUM    PRESSURE    DEPTH    OWC    DEPTH    GOC    INIT    INIT    INTE
-- DEPTH    @ DATUM     OWC      CAP    GOC      CAP    TYPE    TYPE    N
--                      PRESS          PRE    LO     DO
   1142      100       1892                   0 /

-----------------------------------------------------------------------
SUMMARY
-----------------------------------------------------------------------
DATE

-- Specify creation of summary file
RPTSMRY
 1 /

-- Specify summary file in LOTUS format
LOTUS

-- Specify output of producer wells to summary file
GOPR
 'P' /
GWPR
 'P' /
WBHP
 'P1' /
WBHP
 'P2' /
WBHP
 'P3' /
WBHP
 'P4' /
WBHP
 'P5' /
WBHP
 'P6' /
WBHP
 'I1' /
WBHP
 'I2' /
WBHP
 'I3' /
WBHP
 'I4' /
GWCT
 'P' /
GWIT
 'I' /

-- Specify output of oil and water in place to summary file
FOIP
FWIP
FOPT
FOPR
FWPT
```

```
FWPR
FWCT
FWPR
FLPR
FOE

--well oil production total
WOPT
 'P1' /
WOPT
 'P2' /
WOPT
 'P3' /
WOPT
 'P4' /
WOPT
 'P5' /
WOPT
 'P6' /

--water prod total
WWPT
 'P1' /
WWPT
 'P2' /
WWPT
 'P3' /
WWPT
 'P4' /
WWPT
 'P5' /
WWPT
 'P6' /

--well BHP
WBHP
  /

--water inj total
WWIT
 'I1' /
WWIT
 'I2' /
WWIT
 'I3' /
WWIT
 'I4' /
```

```
----------------------------------------------------------------------
SCHEDULE
----------------------------------------------------------------------
-- CONTROLS ON OUTPUT AT EACH REPORT TIME
RPTSCHED
 'FIP=1' 'WELLS'  'SUMMARY=2'  /
-- 'FIP=1' 'WELLS'  'SUMMARY=2' 'RS' 'SGAS'  'SOIL'  'SWAT' 'PRESSURE'  /

RPTRST
  'BASIC=2'  /

INCLUDE
  'Includes/WELSPECS-EXAMPLE-DOWN-3kmNOFCF.txt' /

GCONPROD
-- NAME  PROD  OIL  WAT  GAS  LIQ  PROCE  FREE  GRP  DEF  PROC  PROC  PROC  RES
PROD
--      RATE  TAR  TAR  TAR  TAR  EXC  RES  PRO  GUI  EXCW  EXCG  EXCL  FLU  BAL
   'P'  'LRAT'  3*          350  /
/

GCONINJE
-- NAME  PHA  INJ  WAT  RES  RINJ  TOTAL  FREE  GRP  DEF
--          MODE  TAR  VOL  TAR  VOID  RES  INJ  GUI
   'I'  'WATER' 'RATE' 350  /
/

WCONPROD
-- NAME  STATUS  CONTMODE  OILT  WATT  GAST  LIQT  RESVT  BHPT TOHT  PROVFP  ART
  'P1'  'OPEN'   'GRUP'  3*          1589   1*      50/
  'P2'  'OPEN'   'GRUP'  3*          1589   1*      50/
  'P3'  'OPEN'   'GRUP'  3*          1589   1*      50/
  'P4'  'OPEN'   'GRUP'  3*          1589   1*      50/
  'P5'  'OPEN'   'GRUP'  3*          1589   1*      50/
  'P6'  'OPEN'   'GRUP'  3*          1589   1*      50/
/

WCONINJE
-- NAME  INJPHASE  OP/SH  CONTMODE  SURFLOWRATE  RESFLOWRATE  BHPLIMIT
THPTARGET  VFPTABLE  RS/OR/RV
  'I1'    'WATER'  'OPEN'  'GRUP'   1589      1*      150 /
  'I2'    'WATER'  'OPEN'  'GRUP'   1589      1*      150 /
  'I3'    'WATER'  'OPEN'  'GRUP'   1589      1*      150 /
  'I4'    'WATER'  'OPEN'  'GRUP'   1589      1*      150 /
/

ECHO

TUNING
1.0 10 0.1 0.15 3.0 0.3 0.1 1.25/
/
2* 100/
```

```
DATES
1 JAN 2006/
1 JAN 2007/
1 JAN 2008/
1 JAN 2009/
1 JAN 2010/
1 JAN 2011/
1 JAN 2012/
1 JAN 2013/
1 JAN 2014/
1 JAN 2015/
/

END
```

Appendix C

C1 Photomodeler Scanner® workflow

Collecting an outcrop dataset suitable for creating a digital outcrop model using stereophotogrammetry, such as outcrop coordinate data and photographs, is described in detail in Section 4.5 of Chapter 4 and demonstrated via its application to distal lower shoreface deposits exposed at outcrop (G2 parasequence, Grassy Member, Blackhawk Formation, Utah, USA). This appendix contains a detailed workflow for using the Photomodeler Scanner® software after the outcrop data has been collected, and is used to create the dense point clouds described in Chapter 4 (Figs. 4.8, Fig. 4.9).

C1.1 Camera calibration

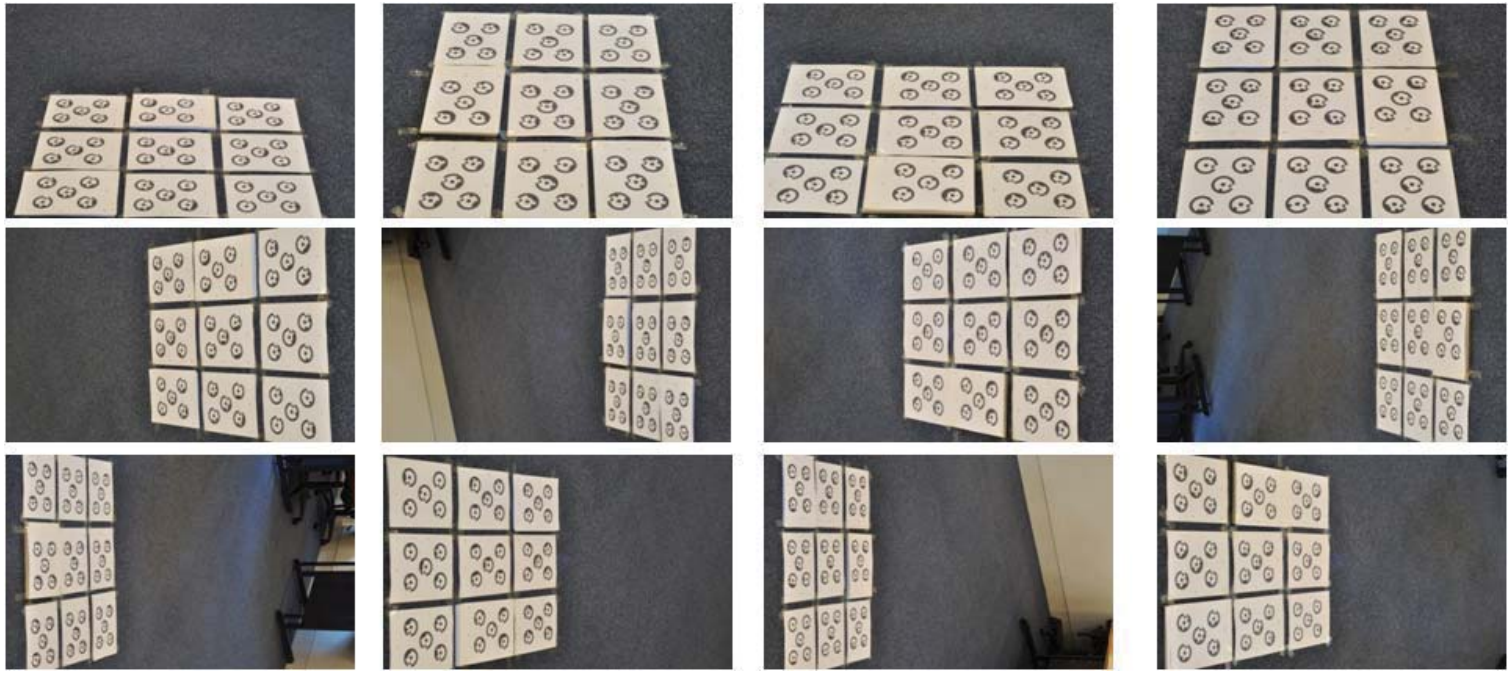


Fig. C1.1

Camera calibration is the process of accurately determining the internal parameters of the camera (such as its focal length, principal point, format aspect, and lens distortion) and is important for achieving accurate results. Camera calibration requires a set of photographs of calibration sheets at a range of heights as shown in Fig. C1.1. Photographs should be taken at each side of the square with the camera oriented in landscape view (4 photographs), rotated 90 degrees to the right for portrait view (4 photographs) and then 90 degrees to the left for portrait view (4 photographs). The camera settings when taking project photos should match the settings of the camera during calibration. Features such as image stabilization, auto-rotation, and sharpening should be disabled when taking project or calibration photos.

C1.2 Triangulation

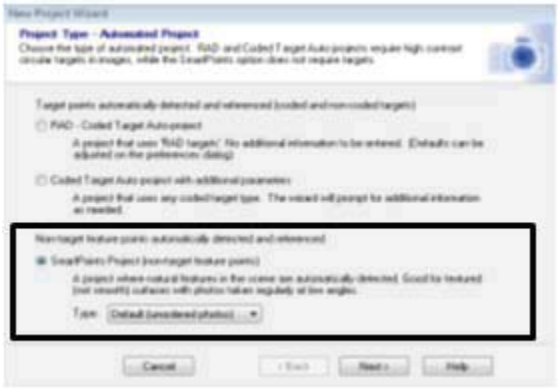


Fig. C1.2



Fig. C1.3

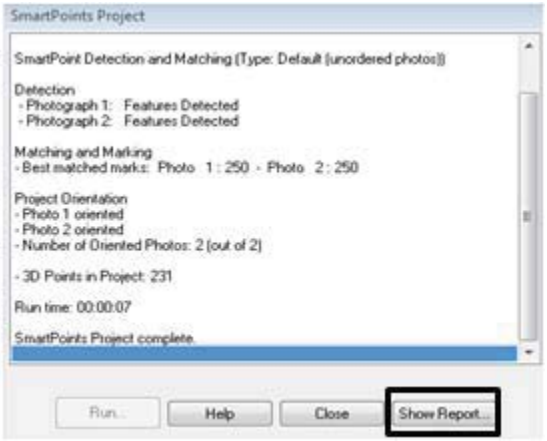


Fig. C1.4

Triangulation is the process of determining the camera position and orientation in 3D and creating 3D points reconstructed from the original 2D photographs. We position and orient the camera and photographs in 3D as follows:

1. Select automated project when prompted on start up.

2. Choose smart point project when prompted (Fig C1.2) and load the photographs to be stereomatched. If calibration has been completed (Section C1.1) a prompt informing that the photographs have been matched with a calibrated camera will appear (Fig C1.3).

3. Select run smart points. This locates the 3D position and orientation of the cameras and orientation of the photographs in 3D. Around 200 smartpoints indicates a good triangulation of camera positions and photographs. If the number of points is low (<100) select new photographs to stereomatch. View the report after smart points has run to check the quality of the triangulation (Fig. C1.4).

C1.3 Dense point cloud

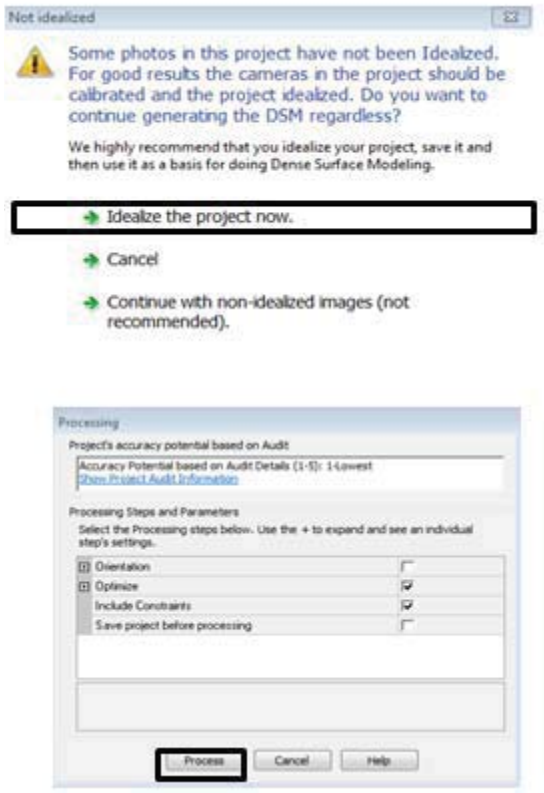


Fig. C1.5

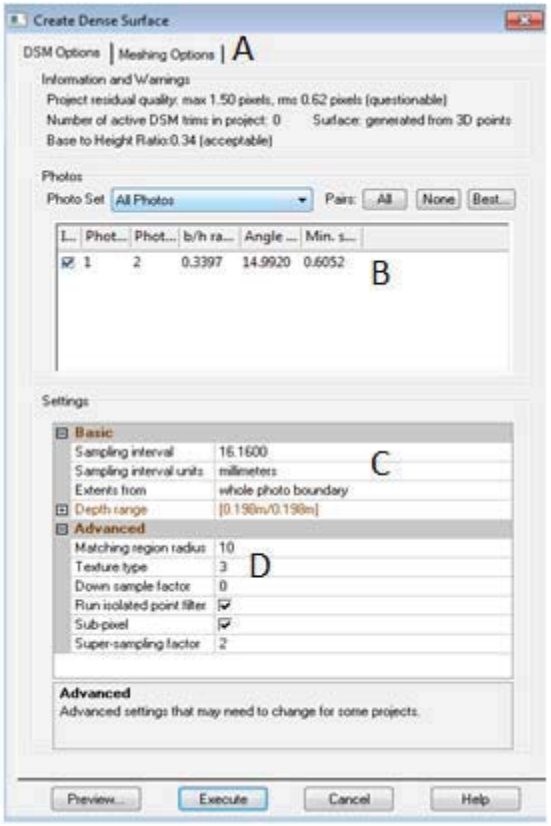


Fig. C1.6

In section C1.2 we oriented the positions of the camera and photographs in 3D. We now use this information to triangulate the positions of more points in the 2D photographs in order to create a dense point cloud as follows:

1. From the menu options select Dense surface->create dense surface. You will be prompted to idealize the project (Fig. C1.5). This step prompts us to re-process the project to reduce residuals (Fig. C1.5) where residuals are the difference between the points in the 2D photographs and the 3D projection (see project report C1.5).

2. We can now create the dense point cloud. There are two options shown in the tabs in Figure C1.6A, where we can create a dense point cloud or a triangulated mesh. Only dense point clouds were considered in this project so that the resulting digital outcrop model could be exported to conventional reservoir modelling software. We can alter the input parameters to customise the dense point cloud to our requirements (Fig. C1.6). Figure C1.6B indicates which photographs are to be matched, which in this case is photographs 1 and 2. This section also highlights the minimum sampling interval that can be achieved with this pair of photographs (i.e. the minimum distance between points in the dense point cloud) and the base to height ratio (b/h ratio), which indicates the difference in perspective between the two photographs. The b/h ratio should be between 0.1 and 0.5 for optimum results.

3. We can change the minimum sampling interval shown in Figure C1.6C. A useful first step is to select a minimum sampling interval at c. 20 mm, to first check the quality of the resulting point clouds. Once the photographs have been demonstrated to capture the point cloud of interest, the user can go back and select a finer sampling interval.

4. Figure C1.6D shows two further important parameters. Increasing the matching region radius reduces the number of holes in the point cloud, but if the matching radius is set too high it can reduce the ultimate density of the point cloud. If there are smooth surfaces in the images, the texture type can be reduced to minimize the number of holes in the dense point cloud.

5. To texture the resulting dense point cloud select: 3D viewer Options->Surface types->Display style->Quality textures.

C1.4 Georeferencing

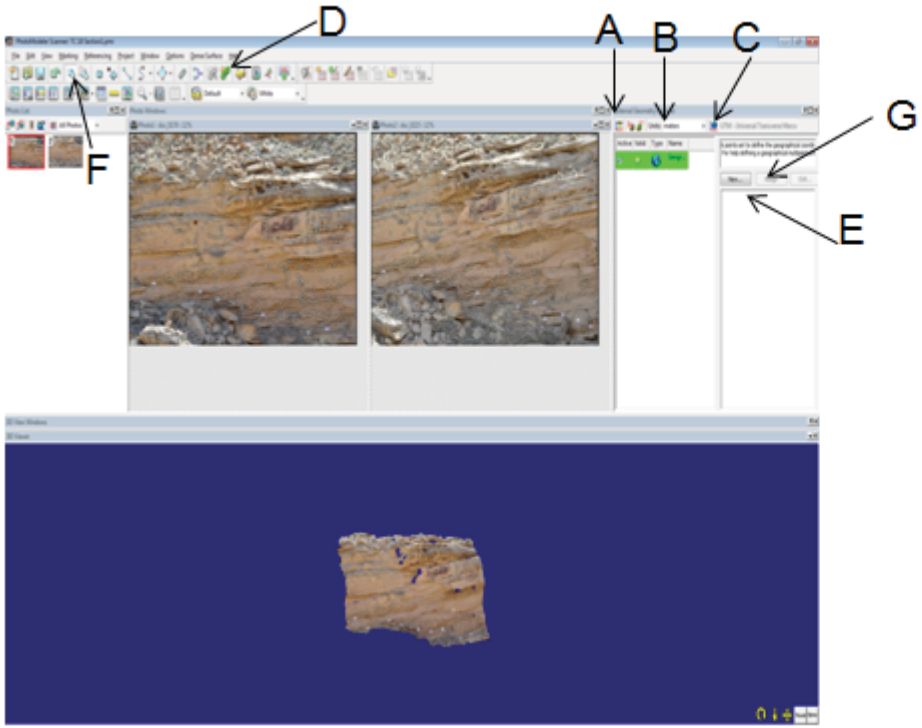


Fig. C1.7

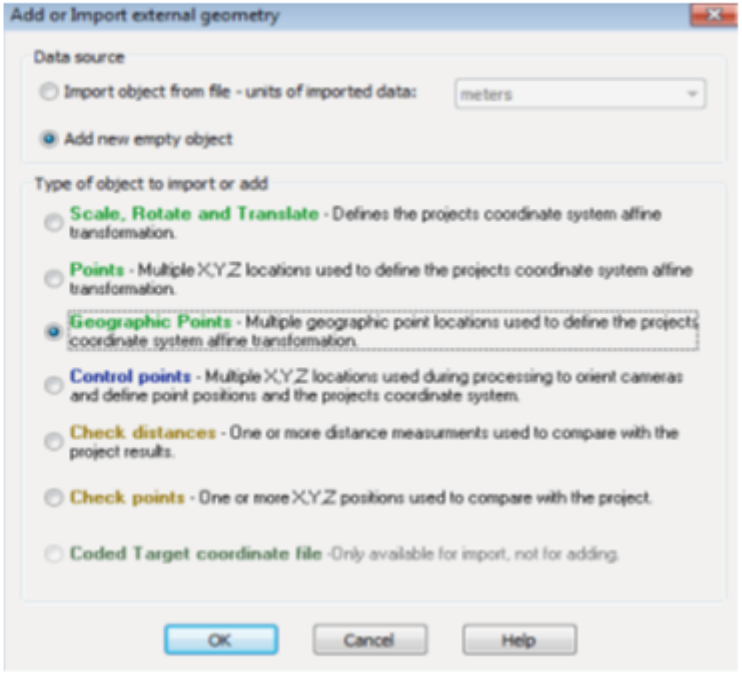


Fig. C1.8

We can now assign the dense point clouds to a “real world” coordinate system. This step allows us to accurately position multiple discrete dense point clouds in space.

1. Select View->External Geometry Explorer.

2. Select button shown in Figure C1.7A (add/import external geometry). The resulting prompt is shown in Figure C1.8. Select add new empty object and geographic points. The user can change project units using the button shown in Figure C1.7B, in this project the units were set to metres. Select button shown in Figure C1.7C to define the geographic coordinate system. In this project we used: UTM coordinates, Datum WGS84, Zone 12N although this is subject to change with respect to outcrop location.

3. Select referencing mode (Fig. C1.7D). Using this select a point on photo 1 which has a known location such as an outcrop target (e.g. Fig. 4.9A, B). Then select the same point in photo 2. Do this for at least 3 points.

4. Using the button shown in Fig. C1.7E, select create new points and do this for each point referenced in step 3. For each point created, enter the coordinates and the point name. Use the pointer tool (Fig. C.1.7F) to select a referenced point in a photo, then hit assign (Fig. C1.7G). Repeat this for a least three referenced points to put the project into "real world" coordinates, however the greater number of assigned coordinate positions will result in a more accurately positioned point cloud Assigned points will have a green tick if successful.

C1.5 Export

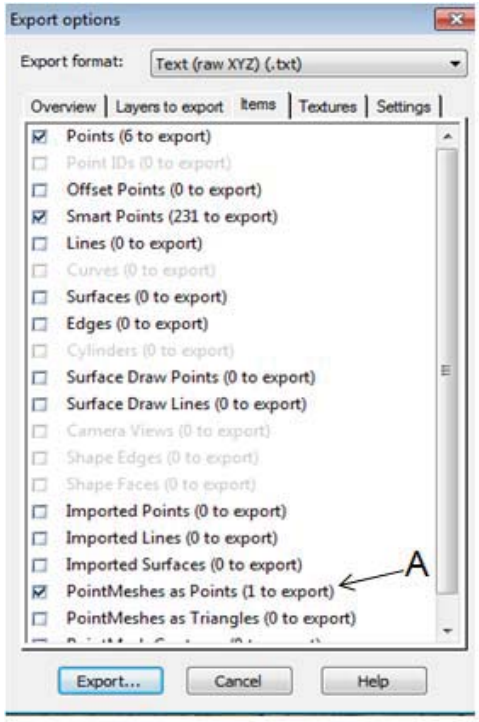


Fig. C1.9

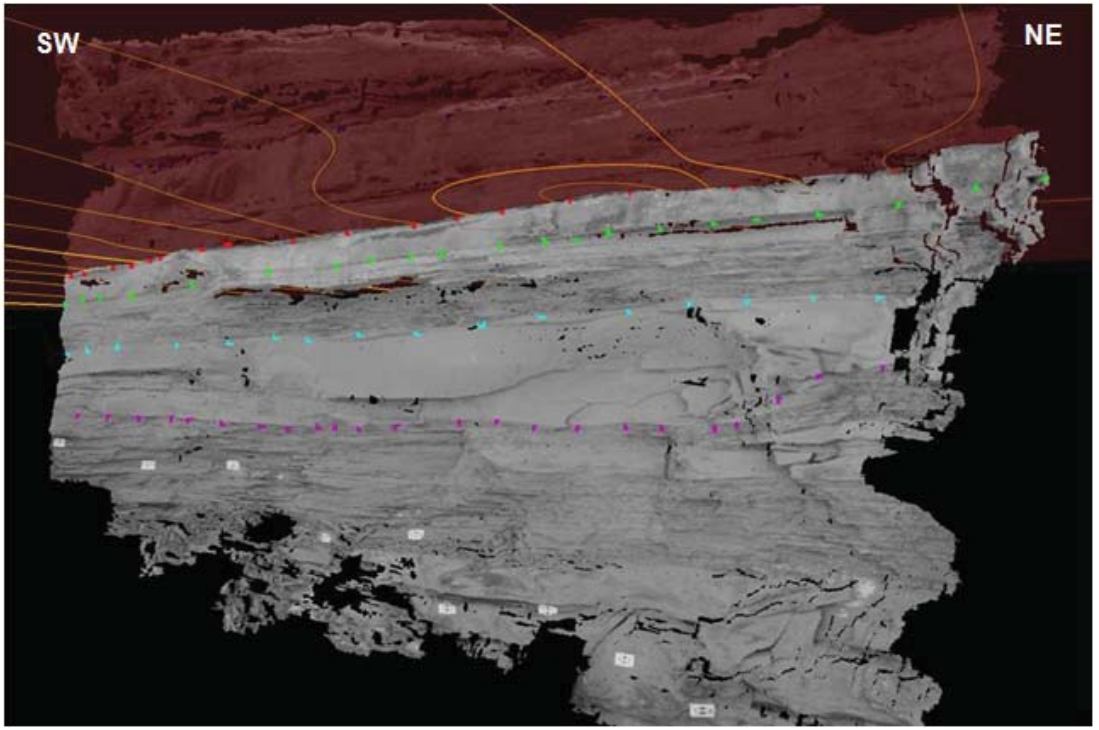


Fig. C1.10

We can now export the georeferenced point cloud to conventional reservoir modelling software packages:

1. Select File->Exports->Export model and choose the export format shown in Fig. C1.9A. The dense point cloud that has been exported can now be interpreted upon using points, surfaces and polygons in conventional reservoir modelling software packages (e.g. Fig. C1.10 corresponding to Fig. 4.9B).